Dankwoord

Wouter and Sonja, first of all thank you very much for giving me the opportunity to start a PhD. I enjoyed my time at UHasselt. I would also like to thank you for all the guidance, discussions, reading and of course all the corrections in function of my PhD. Thank you and good luck with the future of NuTeC!

My dear PhD colleagues! Kenny, let's start with you (order is chronologic not by importance ;)). I will never forget my first moments at our office. My thoughts at the moment "Where the hell did I end up?" - for the record these thoughts never disappeared. I enjoyed our numerous discussions on (international) politics. In the end, I need to admit, you were right with your advices (Niels and I made sure to spread them). Good luck with Act&Sorb and don't forget Antwerp is the industrial heart of Belgium ;). Niels, we shared a lot of pleasant times and interesting discussions on life, self-development and career paths. I really appreciated our open communication, feedback and way of approaching problems. I look forward to work together afterwards. Katrijn, thank you for the nice talks and the funny moments. Bram, thank you for the well thought out discussions. Niels, Katrijn and Bram good luck with your PhD! Lukas and Inva it was really nice meeting you! I hope the both of you are doing well!

Ida, héél erg bedankt voor de plezante tijden in het labo, voor alle lesverplaatsingen, voor het piekfijne labomateriaal dat altijd klaar stond,… maar vooral bedankt voor de leuke babbels!

Diana, bedankt voor de ontelbare gezellige babbels, zowel op het secretariaat in Hasselt, als op het vliegtuig en elders in Europa. Bedankt voor alle administratieve ondersteuning voor de conferenties, mijn doctoraat,… en voor er telkens te staan wanneer het nodig was!

Indy and Ruben, het was een leuke en leerrijke ervaring om jullie te begeleiden als Masterstudent. Ik wil jullie beiden bedanken voor jullie bijdrage aan mijn doctoraat.

I also would like to thank the doctoral school team. Following all these well organized and interesting workshops was an added value to me and my PhD!

I would like to thank everybody of the RN-group of JRC-Geel. My PhD would never have been the same without the provided equipment and knowledge. I am very very very grateful for the granted Eufrat-projects which allowed me accessing the facilities of JRC-Geel. Working at JRC-Geel was also a stimulus for my BMI; uncountable are the cakes, cookies, chocolates, … I ate during the

breaks. First of all, I am very thankful to Mikael. Mikael gave me the chance to perform my experiments and measurements. He was always open to questions and helped me a lot with the development of the attenuation set-up. Next, I would like to thank the famous "Chief Complaint Officer" of JRC-Geel; also known as Gerd Marissens. Gerd, I had a lot of fun and enjoyed our lunches together. I am very grateful for all the help, for the sample preparations we performed together, for all the drawings of the attenuation set-up and for a thousand more things! Guillaume, where to start? You not only expanded my French vocabulary but also my skills and knowledge of gamma-ray spectrometry. Amused, I look back at the lunches with or without candle light. The uncountable pages you print for me, left me with an unpayable debt at my Visa card. Next time you visit Antwerp, it will be champagne! Heiko, I would like to thank you for the support in the measurements and the lovely talks about going on holiday! Jan, we should develop our own crypto currency! Faidra, Kasia and Maria, you were the force behind all the cakes and sweets, thank you! Mira, thank you for your enthusiasm and off course for my new nickname. Viktor, I will never forget the Treicep conference! Petya, thank you for all the nice talks and the care! Raf and Stefaan, thank you for the interesting conversations.

Danny, Mark, Eddy and Stephaan, thank you so much for all your hard and dedicated work! The workplace of JRC is an absolute asset for performing research! Without you, chapter 7 and 8 would never been written!

Yiannis, thank you for all the nice discussions and for your critical view. Thank you for letting me work in the laboratories of KULeuven. Remus, thank you for all the guidance in the field, for teaching me how to make geopolymers, work with the equipment at KULeuven and so much more. I enjoyed our philosophical talks about life and travelling.

I would like to thank Cristina, Federica and Rosabianca for their hospitality. The warm welcome in their institute in combination with lovely pizza was the perfect recipe for a fruitful collaboration. Spending two weeks in Rome was a privilege that I will never forget. I had a good time in one of the most beautiful cities of the world. Rome was an absolute top experience for me. Thanks to the COST action for the financial support.

I would like to thank the secondary smelter facility for providing the samples.

Pavel and Sasha, thank you for the nice collaboration. It was a pleasure working with you.

Mama, héél erg bedankt voor alles! Dankzij jouw goede zorgen, doorzettingsvermogen, goede opvoeding en nog zoveel meer heb ik een mooie universitaire carrière achter de rug. Dit alles heeft voor mij het verschil gemaakt voor de rest van mijn leven, ik ben je dan ook ontzettend dankbaar!

Evelyn, de ups en downs van een doctoraat heb jij mee mogen ervaren. Ik wil je ontzettend bedanken voor alle steun doorheen mijn hele doctoraat. De combinatie doctoraat, postgraduaat en scouts was niet gelukt zonder jou. Bedankt om er telkens weer te staan! Ik vond je bezoekje aan Rome geweldig! Hoewel het soms anders leek, pendelde ik met plezier om samen met jou in het fantastische Antwerpen te wonen ;). Ik kijk uit naar onze toekomst als team Dr. Mercroy!

Bedankt NMBS, hoe mooi kan een haat-liefde verhouding zijn.

Table of Contents

LIST OF FIGURES

List of Figures

List of Tables

List of Abbreviations

AAM	Alkali activated material
AC	Activity concentration
ACI	Activity concentration index
ACI_{BM}	Activity concentration index for building materials
ACI_{SP}	Activity concentration index for streets and playgrounds
B	Build-up factor
BA	Barite
BM	Basalt-magnetite
BR	Bauxite residue
CPR	Construction product regulation
CR	Count rate
D_A	Absorbed dose rate in air
D_d	Direct dose
DDEP	Decay Data Evaluation Project
D_s	Scattered dose
D_t	Total external effective dose
EC	European Commission
EGDA	Expanded gamma dose assessment
EU-BSS	Euratom basic safety standerds
FEP	Full efficiency peak
FS	Fayalite slag
FSIP	Fayalite slag based inorganic polymer
FWHM	Full width at half maximum
GP	Geopolymer
GUM	Guide to the expression of uncertainty in measurement
HDC	High density concrete
HPGe	High purity germanium
HS	Hematite-serpentine
IL	Ilmenite-limonite
IP	Inorganic polymer
IT	Ilmenite-limonite
JRC	Joint Research Centre

KNUCA	Kiev National University of Construction and Architecture
KULeuven	Katholieke Universiteit Leuven
MCS	Monte Carlo simulation
MDA	Minimum detectable activity concentration
NFFS	Non-ferrous fayalite slag
NIRS	Japanese National Institute of Radiological Sciences
NIST	National Institute of Standards and Technology
NOR	Naturally occurring radionuclide
NORM	Naturally occurring radioactive material
OPC	Ordinary Portland cement
OR	Ordinary
RP	Radiation protection
SCFS	Slowly cooled fayalite slag
SCM	Supplementary cementitious material
SM	Steel magnetite
SPR	Scatter to peak ratio
SS	Steel scrap
$T_{1/2}$	Half-life
USGS	United States Geological Surveys
VITO	Vlaamse Instelling Technologisch Onderzoek
WQFS	Water quenched fayalite slag
XRD	X-ray diffraction
XRF	X-ray fluorescence
Z	Atomic number
Z_{eff}	Effective atomic number

Outline

Naturally occurring radionuclides (NORs) are spread in variable concentrations in the earth's crust. Due to industrial processing of primary or secondary raw materials, NORs can concentrate or dilute in the produced (by-) products (also called residues). In this work, industrial by-products are being used or investigated for usage in the production of construction materials. Examples of these by-products are metallurgical slags, bauxite residue, phosphogypsum, fly and bottom ashes. Due to their possible enrichment in NORs, these products are sometimes called NORM (naturally occurring radioactive material)-residues[1]. This work focusses on the NORs that are of main interest in the case of construction materials i.e. ^{40}K and radionuclides part of the ^{238}U, ^{235}U or ^{232}Th decay chains. It must be noted that radon is outside the scope of this thesis and will not be handled in detail.

Certain by-products have proven to be promising precursors in the development of construction materials via a novel process named alkali activation. The process of alkali activation allows using high volumes of residues, consequently tackling the environmental challenges of stockpiling or re-processing these residues. In addition, the resulting alkali activated materials (AAMs) aim at substituting environmentally burdensome conventional cement and concrete materials. It has also been shown that AAMs can have superior properties over conventional construction materials. The chemical, physical and microstructural properties of the processed residues are crucial for the final application. In terms of valorizing and commercializing the usage of alkali activated construction materials, niche applications can prove to be valuable in the step towards the implementation of these construction materials in public usage and space. One such niche application can be as a structural gamma-ray shielding material, which is studied in this thesis.

In the development of AAMs for public use, the radiological characteristics need to be properly addressed. This aspect is considered in the European basic safety standards (EU-BSS) (Council Directive 2013/59/Euratom). The EU-BSS introduces a legislative framework and sets a dose criterion for construction

[1] The term TENORM (Technically Enhanced Naturally Occurring Radioactive Material) was used to distinguish between NOR containing materials produced in industry and those found in nature. The European Commission's radiation protection 122 report only uses the term NORM, no matter how the material was produced (anthropogenically of primordally).

materials. An accurate assessment of the effective dose is therefore of utmost importance to assure safe reuse of by-products in AAMs.

This thesis deals with the radiological assessment of Fe-rich industrial by-products in construction materials. Different topics over several scientific disciplines are studied; i.e. NORs, gamma-ray dose modelling, gamma-ray attenuation and production of AAM construction materials.

The thesis is divided in 8 chapters starting with an introductory framework, the objectives, an introduction followed by the methodology and the different (published) articles, presented here as individual chapters. The thesis ends with a general conclusion. The thesis is structured such that the reader can better understand the published articles i.e. Chapters 4 to 8. Therefore the introduction deals with the different aspects brought about in each article. The methodology provides additional information to the information provided in Chapters 4 to 8.

In Chapter 1, the objectives and the other chapters are described. The main focus of this thesis is on the radiological aspect.

Chapter 2 introduces a literature overview of the different topics dealt with in Chapters 4 to 8. This chapter starts with framing the "waste to material" research in case of construction materials, followed by presenting the industrial by-products handled in this thesis. Then, the use of these industrial by-products in construction materials is handled. In what follows, the focus is on the radiological aspect of the usage of industrial by-products in building materials. First, the presence of naturally occurring radionuclides (NORs) in industrial by-products is discussed. Consequently, the legislative framework regarding the usage of by-products containing NORs, whether or not, in building materials is handled, followed by a discussion on the dose calculation inside rooms constructed out of these materials. The introduction ends with providing an understanding of gamma-ray shielding and the conventional structural shielding materials used.

Chapter 3 deals with materials and methods used in the studies of Chapters 4 to 8. The chapter starts with describing the studied samples. Next, the preparation steps and sample characterization are described. As gamma-ray spectrometry is a major analytical technique used in this thesis, the analysis and calculations are discussed in detail.

Chapter 4 and 5 deal with the radiological characterization of bauxite residue containing concretes and fayalite slag by means of gamma-ray spectrometry, respectively. Chapter 4 focusses on the public exposure from building materials and roads containing high levels of bauxite residue. Additionally, the impact on construction workers is assessed. Chapter 5 starts with providing an overview of the activity concentration of different NORs in slags available in the literature.

The slag output of an industrial facility is followed during a one-month production period. The variation of NORs in the facility is discussed and an assessment of its usage as building material.

In Chapter 6, different room dose models for external gamma radiation are compared and a new model is developed using an expanded set of gamma emission lines. In this comparison, the main focus is the number of gamma lines and the gamma emission data used. Next, a sensitivity analysis of the developed model is performed. Finally, an additional comparison is performed of the most used index and dose calculations relevant for the dose assessment within the European legislative framework applicable towards building materials.

Chapter 7 deals with a detailed discussion on the developed narrow beam set-up to experimentally determine the linear attenuation coefficient.

In Chapter 8, the performance of a fayalite slag based inorganic polymers is evaluated in function of its gamma-ray shielding capabilities. Monte Carlo simulations are performed of this inorganic polymer and of conventional high density concretes. The linear attenuation coefficient is also determined experimentally for a set of gamma-rays.

The thesis ends with the general conclusion written in English and Dutch, respectively, followed by the list of publications.

CHAPTER 1: OBJECTIVES

Chapter 1: Objectives

The overarching aim of this work is to contribute to the transition towards a sustainable society by supporting a change of practice from stockpiling certain industrial residue to enabling their safe use in valuable construction products. This thesis deals with the valorization of Fe-rich industrial by-products in construction materials and considers specifically a radiological point of view. The work conducted includes gamma-ray spectrometry of naturally occurring radionuclides (NORs), gamma dose modelling and production and characterization of alkali activated materials (AAMs). As a specific application for AAMs, their use as gamma-ray shielding material is studied. Consequently, the thesis addresses a diverse set of topics, which are all linked to the usage of by-products in construction materials. This leads to four objectives which are handled within different chapters of this thesis.

1) Investigate the radiological aspects of selected bauxite residues (BRs) and non-ferrous fayalite slags (FSs).

The activity concentration of ^{238}U, ^{235}U, ^{232}Th (including decay products) and ^{40}K were determined in bauxite residue (BR) containing concretes and in fayalite slags (FSs) and is presented in Chapter 4 and 5, respectively. In Chapter 4, the impact of the different amounts of BR in BR based concretes is studied. Whereas in Chapter 5, the NOR content of slags is followed during a one-month production period. The determination of the radiological characteristics is important to assess the possible reuse options and to which extent implementation of NOR-containing by-products is in line with the legislation. Both by-products can be incorporated or converted into construction materials. The activity concentrations obtained are used as input in different dose calculations, required for objective 2.

2) Investigate the potential use and valorization of these residues in construction materials from a radiological point of view.

Based on the determined activity concentrations, different valorization pathways can be investigated by means of dose calculation models. Dose calculation models are aimed towards a specific usage, for example as road base or as a material for public usage like houses, hospitals, etc. In addition, a distinction is made between occupational exposure and public exposure. Chapter 4 studies the exposure of the BR based concretes both for public exposure and occupational exposure for usage as road or material for public usage. Whereas, Chapter 5 studies the material in terms of public exposure in case of fayalite slags.

3) Improve existing dose assessments to better estimate the radiological impact of these building materials on public exposure.

A variety of dose assessment models exist to assess the public exposure from building materials in terms of the effective gamma dose. The official dose index calculation proposed by the European legislation is not able to take into account building material specific parameters, (like for example density and thickness), which are impacting the effective gamma dose. Other developed models take into account these parameters that vary between different building materials and their specific use. However, the complete gamma emission intensity linked to ^{40}K and the decay series of ^{238}U, ^{235}U and ^{232}Th is not considered. In Chapter 6, the impact of the gamma emission intensity linked to the corresponding gamma emission energies is studied and a comparison is made between the most used index and dose calculations relevant for the dose assessment within the European legislative framework applicable to building materials containing naturally occurring radionuclides.

4) Investigate the use of building materials based on non-ferrous fayalite slag as gamma-ray shielding material.

Fayalite slag is a Fe-rich dense material, which is suitable for producing inorganic polymer building materials constructed solely out of fayalite slag. These characteristics possibly allow producing a gamma- and X-ray shielding material without the usage of cement or other raw materials. In order to check the shielding capabilities of such inorganic polymers, a dedicated set-up was developed in Chapter 7 to experimentally determine linear attenuation coefficients. Chapter 8 studies the shielding capabilities of a fayalite slag based inorganic polymer and compares the results with conventional high density concretes.

Chapter 2: Introduction

2.1. Waste to Material Research

The transition from a society based on conventional consumption towards a sustainable society is proving to be an arduous task, but is necessary to avoid further pollution, depletion of natural resources and expansion of landfills. With the global population expected to grow to around 10 billion people by 2050, Europe recognizes the necessity to take action [1,2]. The European Commission (EC) published in 2011 a report and in 2014 a communication dealing with this issue in the construction sector [2,3]. This underlines the initiatives of the EC to work towards a circular economy which aims at keeping added value in products as long as possible, eliminating waste and running on renewable energy.

The past decade, the global cement production has nearly doubled from 2.5 billion tons in 2006 to 4.2 billion tons in 2016 [4]. Currently, it is estimated that the cement sector contributes between 5 to 8 % to the global anthropogenic CO_2 emission [5]. The largest amount of CO_2 emissions is linked to the chemical reaction of cement production implying that the CO_2 burden of cement is intrinsically linked to its production process and unavoidable [6]. In addition, raw material exploitation for cement production puts a lot of environmental pressure on our planet. The intensity in research towards novel sustainable binding materials as alternatives for cement has increased in recent years due to the huge market potential [6–8].

Several industrial by-products have properties that are suitable for conversion to or incorporation in construction materials [6,9]. Nevertheless, a wide range of these industrial by-products is dumped as waste or processed in low-value applications [9]. Using these by-products as a raw material allows reducing landfilling and the exploitation of natural raw materials for cement production. One example is alkali activated materials (AAMs). The CO_2 emissions linked to these AAMs are up to 80% lower on a binder-to-binder comparison [6,10–14]. In addition, these AAMs can possess technical characteristics that are superior in comparison to cement e.g. acid resistance, resistance against freeze-thaw, fire resistance etc. [6].

The incorporation of by-products into (novel) construction materials allows the reduction of waste and generation of added value. This perfectly fits with the waste to material philosophy needed for keeping the planet healthy for future generations. This thesis deals with two Fe-rich by products i.e. bauxite residue (BR) and fayalite slag (FS).

References at page 63

2.2. By-Products

2.2.1. Bauxite Residue (BR)

Bauxite residue (BR), also known as red mud, is a major by-product that is produced during the refining of the bauxite ore by means of the Bayer process, shown in Figure 2-1 [15]. Aluminum is extracted from the bauxite ores by pressure leaching, followed by a series of separation steps. In addition to the recovery of Al, a highly alkaline residue rich in Fe-oxides remains - mentioned in Figure 2-1 as "residue disposal". The alkalinity originates from the entrained NaOH in the residue whereas the Fe-oxides result in a red color of the residue leading to the name "red mud" [15]. Typically, 1-1.5 tonnes of BR are generated for every tonne of produced alumina [16]. In 2015, the annual production rate was estimated at 150 million tonnes per year [16]. In China alone, about 30 million tonnes of BR was generated in 2009. The reuse of BR is limited to a few percent of the annual production rate [15,16]. Consequently, it is estimated that over 2.7 billion tonnes of BR are currently stockpiled and it is expected that this number will increase [15]. BR is typically stored in large basins and the disposal costs in different countries may add up to 5 % to the alumina production cost [17]. Furthermore, improper storage of BR can lead to harmful contamination of water, land and air in the surrounding area. This was dramatically proven by the accident at the Ajka alumina refinery in Hungary in October 2010. Between 600 000 to 800 000 m^3 of BR flooded the village of Kolontar and flowed into the Torna Creek, Marcal, and Raba rivers [18].

The chemical composition of BR varies from one production site to another. An overview of the chemical composition of BR is shown in Table 2-1 [16]. It can be observed that the chemical composition can vary largely for the different main components, for example the Fe_2O_3 mass fraction can differ from 5 % to 60 %. These variations are linked to the bauxite feed and the nature of the Bayer refinery circuit [15].

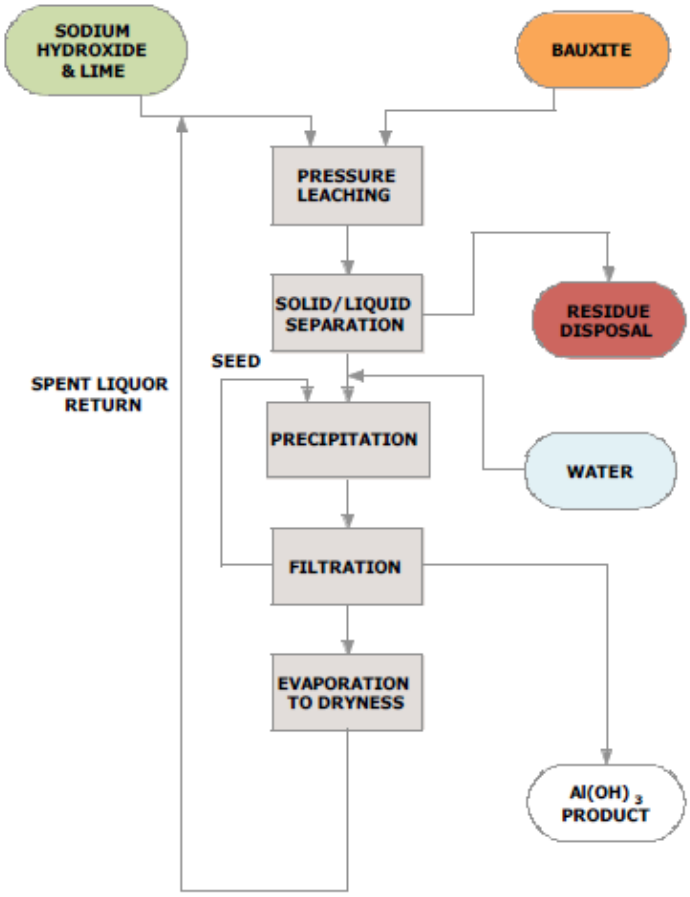

Figure 2-1: Schematic overview of the patented leach process of Bayer also known as "the Bayer process". Figure from Klauber (2009) [15].

Table 2-1: Chemical composition, expressed as oxides, commonly found in BR. Data from Evans (2016) [16].

Component	Typical range (mass%)
Fe_2O_3	5-60
Al_2O_3	5-30
TiO_2	0.3-15
CaO	2-14
SiO_2	3-50
Na_2O	1-10
LOM	5-20

In addition, BR is identified as a residue with potentially enhanced levels of NORs (Naturally Occurring Radionuclides) [19]. The radionuclide content of the BR varies depending on the production process and the origin of the ores. Nuccetelli et al. (2015) made an overview of the radionuclide content of BR in different countries, shown in Table 2-2 [19]. A wide range in the activity concentrations of ^{226}Ra, ^{232}Th and ^{40}K is observed between the BR producing countries. For ^{226}Ra, ^{232}Th and ^{40}K the activity concentrations vary between 97 and 1047 Bq/kg, 115 and 1350 Bq/kg, and 15 and 583 Bq/kg, respectively.

The treatment and utilization of BR is both of environmental and economic significance. The large quantities of stockpiled BR are a problem due to their high content of heavy metals (e.g. Cr and As) and of radionuclides, high alkalinity and not straightforward storage. Nevertheless, these large quantities can become a (future) resource via the right (pre-) processing steps. For example, the mining of rare earth minerals from BR is investigated [20]. Other options, which are used or investigated, use BR as a substituent of clay in the brick and tile industry, as glass ceramics, as soil remediation, as road base, as landfill barrier or cover, as backfilling of abandoned bauxite mines or as source for iron production [15,21]. In addition, research is performed to convert this material into a construction material via the incorporation of BR in the binding agent or as an aggregate in construction materials [15]. The most widespread use of BR is as an iron source for the clinker production [15]. Nevertheless, in 1999 this reuse pathway only accounted for 1% of the annual BR production [15]. In addition, the production of BR containing alkali activated construction materials is studied [22]. However, the limited availability of Al makes the use of BR in AAM challenging – Al is a typical component of AAMs as discussed in Section 2.3.2 [6]. Consequently, the usage of BR as the single binding component has been mainly unsuccessful [6]. In order to produce BR containing AAMs, a blend with Al-containing raw materials is necessary [6]. Blends are performed with metakaolin, calcined oil shale, fly ash and blast furnace slags [6]. BR incorporated structures can be used for the production of tiles, bricks but also casted structures. Chapter 4 deals with the application of BR concrete as

road construction material and as building material for public use and approaches these applications from a radiological point of view.

Table 2-2: Activity concentration in Bq/kg of ^{226}Ra, ^{232}Th and ^{40}K determined in BR of different countries. When available, uncertainties are reported. Data from Nuccetelli et al. (2015) [19].

Country	^{226}Ra (Bq/kg)	^{232}Th (Bq/kg)	^{40}K (Bq/kg)
Australia A	310 ± 20	1350 ± 40	350 ± 20
Australia B	326	1129	30
Brazil	139 ± 1	350 ± 19	45 ± 1.9
China A	477	705	153
China B	225 ± 16	422 ± 42	164 ± 15
China C	478 ± 24	555 ± 56	401 ± 32
China D	350 ± 21	414 ± 41	583 ± 47
China E	370 ± 22	437 ± 44	505 ± 40
Germany	122	183	n.r.
Greece A	379 ± 43	472 ± 23	21 ± 11
Greece B	232 ± 46	344 ± 33	45 ± 12
Hungary - Neszmely RM tailings pond A	300	260	n.r.
Hungary - Neszmely RM tailings pond B	250	400	n.r.
Hungary - Ajka and Almásfüzitó	347	283	48
Italy	97	118	15
Jamaica A	370	328	265
Jamaica B	1047	350	335
Turkey	210 ± 6	539 ± 18	112 ± 7

n.r.: Not reported.

2.2.2. Slags

Metallurgical slags are a by-product from metal producing facilities. The two main classes of metallurgical slags are non-ferrous and ferrous slags [23]. Non-ferrous (from production of Ag, Cu, Ni, Pb, Sn, Zn) slags typically consist mainly of Fe and Si whereas the ferrous (steel and blast furnace) slags are typically rich in Ca and Si [23]. Table 2-3 shows that the average CaO content is 36 mass%, 35 mass%, 3.3 mass% and 7.1 mass% for iron -, steel-, nickel sulfide and copper slags, respectively. In case of FeO; iron-, steel-, nickel sulfide and copper slags contain on average 1.6 mass%, 23 mass%, 45 mass% and 33 mass%, respectively. In case of SiO_2; iron-, steel-, nickel sulfide and copper slags contain on average 32 mass%, 17 mass%, 37 mass% and 36 mass%, respectively (Table 2-3). Each year over 400 million tonnes of metallurgical slags are produced and the production of non-ferrous slag accounts for

approximately 12 % of the total worldwide slag production [24]. Reuse and valorization options for metallurgical slags are of great importance [23,25–27]. The reuse and recycle applications depend on the chemical composition, cooling path, availability, price, etc. [23,28]. Usage of metallurgical slag in tiles, in railway ballast, in roofing materials, in colored glass, in cementitious material, as sand blasting material, as reprocessing material for secondary metal recovery and in environmental remediation is reported [23,25,29–31]. The main usage is as a raw material in asphalt and concrete mixtures for road construction [23,28,32–34]. Although a diverse range of applications for slags exists, still some of these by-products currently end up in landfills – especially for non-ferrous slags [29]. According to the USA Federal Highway Administration, this is due to the remoteness from the potential market [29]. Consequently, stockpiling is limited and the main incentive for research is to look for applications with higher added values. The application of metallurgical slag as a binder to produce alkali activated building materials (see Section 2.3.2), a promising alternative for ordinary Portland cement (OPC-) based constructions, proves to be an interesting valorization pathway [35,36].

Looking at the radiological aspect, the radionuclide content in slags is very different for different types of slags and even within the same type of slag large variability exists. Table 5-1 of Chapter 5 (Section 5.2) shows the radiological content present in different slags [37]. A wide range is observed in the activity concentrations of ^{226}Ra, ^{232}Th and ^{40}K; i.e. between 0.004-69 kBq/kg, 0.002-130 kBq/kg and 0.002-23 kBq/kg for ^{226}Ra, ^{232}Th and ^{40}K, respectively. Chapter 5 focusses in more detail on this aspect. Next to the radiological aspect, the presence of potentially toxic elements, such as As, Ba, Cd, Pb and Zn introduces environmental concerns that need to be evaluated before a specific reuse practice can be accepted [23,38]. Barna et al. (2004) assessed the leaching of road materials containing lead and zinc slags [39]. Piatak et al. (2004) investigated the leaching of non-ferrous metals from slags originating from different mines in the USA [40]. An extensive overview of studies focusing on leaching aspects of slag can be found in Piatak et al. (2015) [23].

Non-ferrous Fayalite slag

In this thesis, the focus will be on non-ferrous fayalite slags (FS). Chapter 5 deals with the radiological aspects of FS. Fayalite (Fe_2SiO_4) is the main crystalline phase of copper slag. 2.2 – 3 tonnes of FS are produced per tonne Cu [41]. The global production through mining of Cu was 19.4 million tonnes in 2016, leading to millions of tonnes of FS by-products every year [4]. These FSs are used as low added value material in a diverse range of applications i.e. as abrasive tools, roofing granules, cutting tools, tiles, glass, road base construction, rail-road ballast, pavements, and as cement additive and aggregate in concrete [25,42,43]. In fact, FSs are considered as an ideal raw material in construction materials due to the large amounts in which they are

produced [41]. Despite applications in the cement and concrete industry, FSs are an ideal precursor for the production of more environment-friendly alkali activated based construction materials. The production of FS based AAMs with competitive mechanical properties has been published [41]. Specialized applications as a high strength material, as a structural lightweight material and as a high temperature resistance material have been described [41,44]. The leaching properties of FS AAMs have been studied recently by Iacobescu et al. (2017) [45]. FSs are rich in Fe, therefore, the potential of an environment-friendly gamma-ray shielding material can be another application providing a high added value. This aspect is studied in Chapter 8. Details on the FS used in this thesis are described in Chapter 5.

Table 2-3: Overview of chemical composition of Fe, steel, Ni sulfite and Cu slags Data from Piatak et al. (2015) [23]. With min: minimum value, max: maximum value, n1: number of samples, n2 number of studies that have values.

Component	Fe-slag					Steel slag				
	Min (mass%)	**Max (mass%)**	**Average (mass%)**	**n1**	**n2**	**Min (mass%)**	**Max (mass%)**	**Average (mass%)**	**n1**	**n2**
Al_2O_3	5.86	41.2	14.3	41	13	0.02	44.3	7.49	60	25
CaO	0.15	93.4	36.1	38	12	1.63	70.1	34.9	62	25
FeO total	0.02	13.6	1.6	37	11	1.07	50.9	22.9	61	25
K_2O	0.08	5.06	0.99	33	10	0.01	3.89	0.24	29	13
MgO	1.66	19.6	8.78	41	13	0.43	19.9	7.22	58	25
MnO	0.01	26	1.9	34	10	0.2	21.5	4.32	55	25
Na_2O	0.09	2.65	0.49	33	12	0.02	0.57	0.16	31	16
S	0.38	3.15	1.27	26	6	0.03	1.06	0.22	30	8
SiO_2	26.6	46.1	35.3	41	13	0.03	61.1	16.9	56	23
TiO_2	0.02	3.7	0.63	36	9	0.12	1.98	0.66	37	20
LOI	0.1	4.52	1.86	5	3	0.2	11.2	3.55	16	7
	Min (mg/kg)	**Max (mg/kg)**	**Average (mg/kg)**	**n1**	**n2**	**Min (mg/kg)**	**Max (mg/kg)**	**Average (mg/kg)**	**n1**	**n2**
As	0.5	25	6.5	7	2	0.5	244	24.6	16	8
Ba	180	1110	557	9	4	24	1800	366	32	10
Cd	–	–	–	–	–	0.1	128	14.7	21	7
Co	0.03	33	9.447	10	4	0.8	36	7.88	27	8
Cr	0.1	9580	1032	17	6	4	32700	4798	44	13
Cu	0.13	54	15.9	17	6	3	540	114	33	9
Ni	0.3	68	14.4	11	6	0.9	3180	153	31	9
Pb	0.2	150	21.7	13	4	2	1040	126	31	9
Zn	0.15	320	79.5	15	4	1	11000	748	41	14

Table 2-3 (Continuation): Overview of chemical composition of Fe, steel, Ni sulfite and Cu slags Data from Piatak et al. (2015) [23]. With min: minimum value, max: maximum value, n1: number of samples, n2 number of studies that have values.

Component	Ni Sulfide slag					Cu slag				
	Min (mass%)	**Max (mass%)**	**Average (mass%)**	**n1**	**n2**	**Min (mass%)**	**Max (mass%)**	**Average (mass%)**	**n1**	**n2**
Al_2O_3	6.72	7	6.87	6	1	0.01	18.9	6.17	97	13
CaO	2.74	3.96	3.03	7	2	0.15	21.9	7.06	97	13
FeO total	42.8	47.7	45.2	7	2	0.67	62	33.1	107	14
K_2O	–	–	–	–	–	0.01	4.83	1.35	95	12
MgO	1.56	3.2	2.88	7	2	0.09	6.45	1.79	96	12
MnO	0.06	0.06	0.06	6	1	0.03	6.55	0.54	94	11
Na_2O	–	–	–	–	–	0.01	4.31	0.45	95	12
S	0.99	1.03	1.01	6	1	0.01	6.51	1.4	91	11
SiO_2	29	39.3	36.9	7	2	9.82	70.7	35.9	93	12
TiO_2	0.23	0.24	0.24	6	1	0.1	1.66	0.39	88	11
LOI	–	–	–	–	–	0.1	11.8	1.73	25	4
	Min (mg/kg)	**Max (mg/kg)**	**Average (mg/kg)**	**n1**	**n2**	**Min (mg/kg)**	**Max (mg/kg)**	**Average (mg/kg)**	**n1**	**n2**
As	–	–	–	–	–	0.8	75865	3315	74	9
Ba	–	–	–	–	–	28	29000	2226	66	8
Cd	–	–	–	–	–	0.43	14000	1055	41	11
Co	1210	1400	1293	6	1	15	24104	3317	53	7
Cr	–	–	–	–	–	13	7510	455	61	6
Cu	110	180	140	6	1	1400	353580	25088	97	11
Ni	2600	2960	2762	6	1	2	935	70.9	65	8
Pb	–	–	–	–	–	6.2	183800	14205	92	10
Zn	180	190	187	6	1	44	280000	36314	95	10

2.3. Use of By-products in Construction Materials

Industrial by-products are often used for the production of construction materials. This section distinguishes their use in cement based construction materials (Section 2.3.1) and in alkali activated construction materials (Section 2.3.2).

2.3.1. Cement Based Construction Materials

The worldwide cement production in 2016 is estimated at around 4.2 billion tonnes [4]. It is expected that the usage of cement will further increase in the future to over 5 billion tonnes by 2050 [46]. The best known cement produced today is ordinary Portland cement (OPC) [47]. The production of cement is a CO_2 intensive process contributing to 5-8% of the total anthropogenic CO_2 emission worldwide [7]. The main contribution originates from the conversion of lime stone ($CaCO_3$) to CaO and CO_2, 0.78 tonnes of CO_2 is produced per tonne CaO [7]. Next to lime stone, clay, silica sand and an iron oxide source are mixed in a kiln at 1450°C to produce clinker, shown in Figure 2-2. The clay and silica sand act as an Al and Si source. The clinker is mixed with calcium sulfate source (typically gypsum) to produce cement. The energy consumption in the cement production process is estimated at 0.34 tonnes CO_2 per tonne cement [7]. Consequently, the production ratio of CO_2 and cement is approximately 1:1. Nevertheless, the cement industry tries to lower the CO_2 emissions by means of increasing energy efficiency, usage of alternative fuels and raw materials and reducing the cement clinker ratio [48]. In addition, carbon capture and storage of CO_2 emissions from cement production are being developed [48].

A typical OPC chemical composition is (in mass%) CaO: 65 ± 3; SiO_2: 21 ± 2; Al_2O_3: 5 ± 1.5; Fe_2O_3: 3 ± 1; MgO <5 [47]. When cement is mixed with water diverse hydrated reaction products are formed over time. Although cement has been used for decades, the exact fundamental mechanism and structures leading to strength development are still under discussion [7,49–51]. The main and most important reaction products are calcium silicate hydrates as a result of the hydration of calcium silicates. In addition, also calcium hydrates are produced.

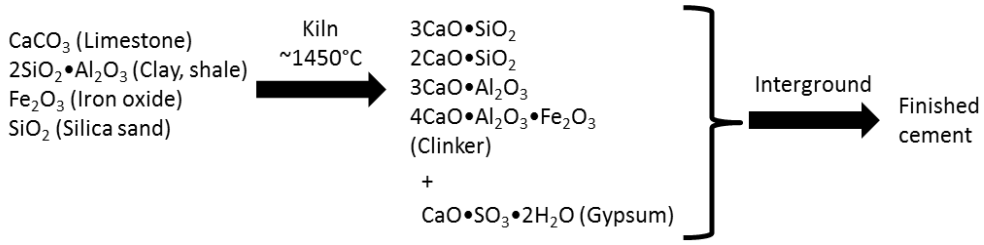

Figure 2-2: Schematic overview of cement production process.

Next to binding agents consisting of pure cement, also blended cement can be used to bind sand and coarse aggregates. Blended cement consists of a mixture of pure cement with by-products from other industries, leading to the replacement of cement and a reduction in CO_2 emissions. Typically, fly ash or ground granulated blast furnace slag is used [47]. These supplementary cementitious materials (SCMs) are estimated to make up 515 million tons of the 3.7 billion tons of cement (in 2012) [47]. The blast furnace slag reserves (290 million tons in 2012 production) are nearly entirely used whereas nearly one-third of the fly ash reserves (670 million tons in 2012 production) are used [47]. Complete usage of the fly ash reserves can further reduce the CO_2 emissions of the cement industry [36]. The heterogeneity and low quality (overall low reactivity) of the remaining fly ash reserves can lead to practical issues [47]. In addition, it is expected that blast-furnace slag and fly ash production will decrease in the long term due to more efficient processes in their corresponding industries [52]. Consequently, other by-products like non-ferrous slags, BR and municipal solid waste ashes are investigated for usage in cements [6,47]. Next to the necessary technical aspects that blended cement requires, the local availability of these by-products is crucial in their production. Nevertheless, the produced concrete from these blends can have better properties than when conventional OPC is used [7]. The lower reactivity of these cements can become a disadvantage in winter. The different chemistry of cement and SCMs leads to different reactions by the addition of water. For example, SCMs react with the calcium hydroxide released by the hydration of cement to produce calcium silicate hydrates.

Cement is widespread and cheap, but not sustainable. Although blended cement is more sustainable, the intrinsic CO_2 production linked to the conversion of lime stone is not sustainable. Greener alternatives, which produce less CO_2, are needed and exist like calcium sulfoaluminate cements and alkali activated materials (AAMs) [47].

2.3.2. Alkali Activated Construction Materials

Alkali activated construction materials are a novel type of construction materials. The basic production principle is explained by Figure 2-3. In essence, an alumina silicate source (metakaolin) dissolves in an alkaline solution (NaOH) and reorganizes its structure to produce an amorphous 3D network of Si-O-Al chains [8]. This section will first address the reason and benefits for the development of a novel type of construction materials. The following section deals with the nomenclature since there is a lot of confusion around this aspect. Sections 2.3.2.3 and 2.3.2.4 deal with the formation process and constituents of AAM, respectively.

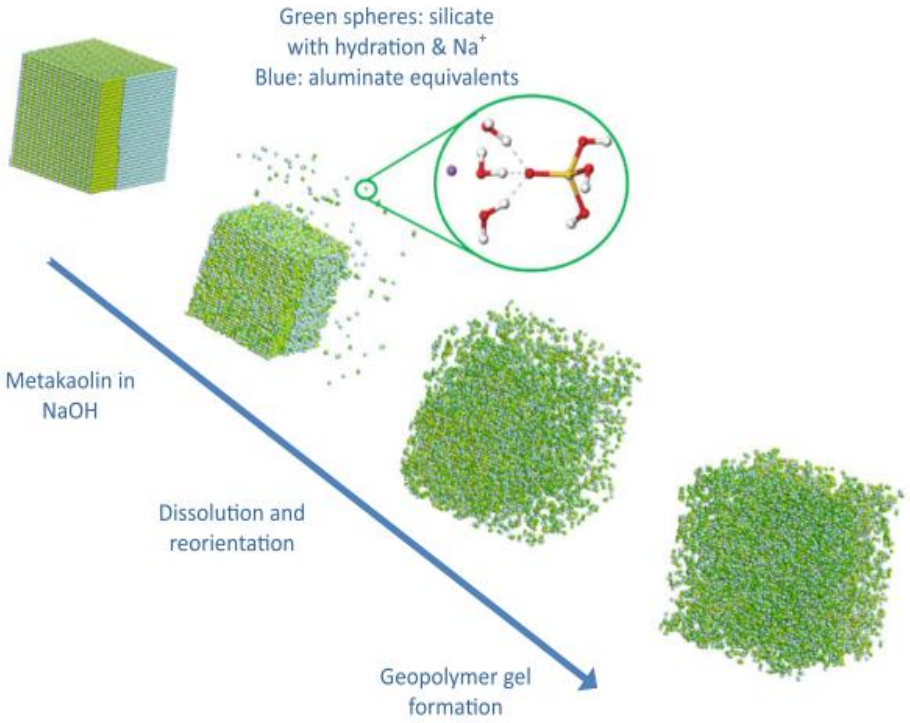

Figure 2-3: Graphical representation of the formation of a geopolymer from metakaolin in NaOH. Figure from Provis (2014) [8].

2.3.2.1. Alkali Activated Materials: Why?

In section 2.3.1 it is described that the CO_2 production linked to cement production is high. AAM binders are investigated and even used as an alternative binder to cement [7]. Life cycle analyses show that the CO_2 reduction varies between 30 and 80% in comparison to cement production [6,10–14]. The CO_2 reduction mainly originates from omitting the energy intensive calcination step in the cement production process [6,7]. Looking further than only CO_2 emissions, life cycle analysis also showed that AAMs perform better in terms of fossil depletion and climate change [53]. Next, AAMs are identified with other potential advantages over cement. AAMs allow the use of by-products, which are now treated as waste, leading to a decrease in the exploitation of raw materials [6]. The emission of heavy metals is considered to be lower in AAM production than in cement production. This is due to omitting the heat intensive kiln step and due to a better capture of heavy metals in AAMs [6]. From a technical point of view, AAMs can perform better than OPC-based building materials. This is especially valid in terms of acid, chemical and fire resistance [6]. AAMs are used

in or under investigation for other applications, like for example as a high strength material, a toxic waste-immobilizer or a heat insulating material [44,54,55]. From an economic and technical point of view, the AAMs need to be able to compete with OPC-based structures. As OPC is a relatively cheap and widespread product, several economic incentives need to push the usage of AAMs. This can be driven by the better performance of the AAMs in niche applications. Another (future) incentive is the possible carbon taxes and the market of CO_2 emissions which can stimulate the usage of CO_2 friendly cement alternatives. The willingness of people to pay a premium for environmental friendly products can also be an incentive. So why are AAM not yet widespread? The historically grown large scale production of cement has given cement a competitive advantage regarding the logistic aspects and low cost [7]. Limestone for cement production is available in the earth's crust in sufficient quantities in most places [7]. The supply chains for AAM need to be (further) developed and the availability of an appropriate activating solution is not straightforward, especially in developing countries. In addition, OPC is a well-known material for construction which has proven to be trustful. AAMs are relatively new and the durability needs to be investigated in more detail. Although this can be tested by extrapolating short term durability tests; it only gives indications of the "real" performance over a longer period [7]. Additionally, the current standards are often based on cement chemistry and not (yet) adapted to novel products like AAMs. Also, the awareness of the general public regarding these novel building materials is limited. Nevertheless, the usage of "green" products in the building industry is promoted by several initiatives in the EU [2,3]. Commercializing of AAM as building or construction material has taken off in several countries, for example in Australia. The Australian company E-Crete™ has produced several construction and building materials based on the alkali activation process like pavements, fire-resistant and fibre-reinforced tunnel segments, bridge retaining walls and pre-cast panels for a library [6].

2.3.2.2. Nomenclature of AAM

Many names are given to AAMs in the literature e.g. inorganic polymers (IPs), geopolymers (GPs), mineral polymers, inorganic polymer glasses, etc. GP is the most-known name. Nevertheless, these names do not all imply the same precursor composition. Figure 2-4 shows a simplified schematic overview of the classification based on the Ca and Al content. It must be noted that the chemistry of AAMs is complex and other elements like for example Fe, Si and Na play a role in the final chemistry of the end product. 'AAM' is considered as the most general classification. AAM is essentially any binder system derived by the reaction of an alkaline salt (solid or dissolved) with a solid silicate powder [56]. Deventer et al. (2010) [7] summarize "This solid can be a calcium silicate as in alkali activation of more conventional clinkers, or a more aluminosilicate-rich precursor such as a metallurgical slag, natural pozzolan, fly ash or bottom ash. The alkaline salts used can include alkali hydroxides, silicates, carbonates,

sulfates, aluminates or oxides—essentially any soluble substance which can raise the pH of the reaction mixture and accelerate the dissolution of the solid precursor". Reactions between water and fly ash and slags are not considered in this definition [6]. IPs are a subclass of AAMs. The primary binding phase is a disordered silicate network. IPs are characterized by a lower available Ca content. Consequently, the ratio of (SiO_2 + Al_2O_3)/(CaO + Na_2O) is higher in comparison to OPC and leading to the higher silicate connectivity [7]. GPs are a subclass of IPs and are characterized by an even lower available Ca content. The binding phase is nearly exclusively an aluminosilicate network [7]. Typical raw materials for GPs are low calcium fly ashes and calcined clays [7].

Although this classification still exists different names are used and the different names are still mixed.

In Chapter 4 dealing with FS, the nomenclature of IP is used.

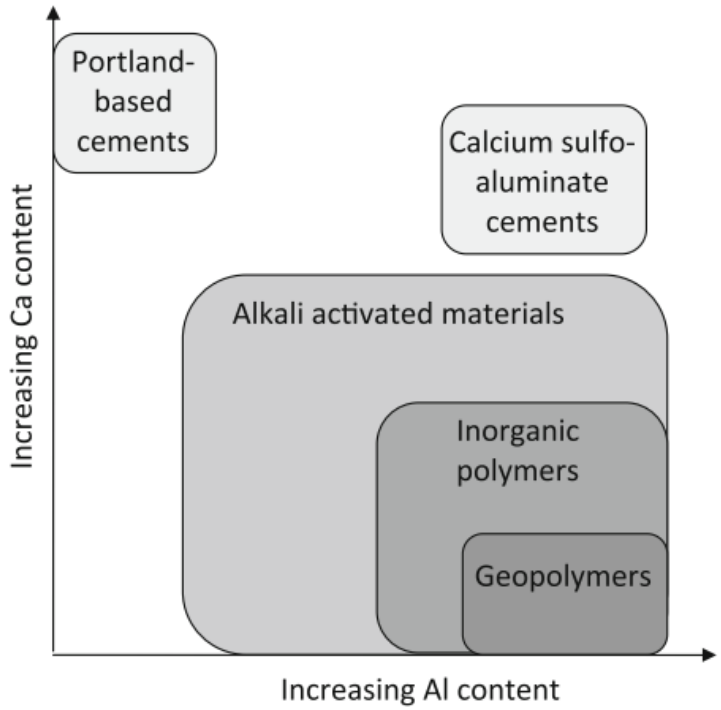

Figure 2-4: Classification of different subsets of AAMs, with comparisons to OPC and calcium sulfoaluminate binder chemistry. Shading indicates approximate alkali content; darker shading corresponds to higher concentrations of Na and/or K. Figure from Deventer et al. (2010) [7].

Fe-Rich Subclass

Alkali aluminosilicate structures are well known [20,21]. A lesser known structure is the branch in which Fe is incorporated in the structure [20,21,57]. Natural precursors for the production of this type of IP are a specific set of rocks i.e. peridodites and dunites [44]. In addition, different types of non-ferrous slags are investigated for use as starting materials for Fe-rich IP structures i.e. lead slag, FeNi slag, and copper slag or FS [35,44,58–62]. These slags are typified by a high iron content (FeO or Fe_2O_3 > 30 mass%) with limited aluminum content (Al_2O3 < 10 mass%). Also, they are semi-vitreous and the iron oxidation state is mostly bivalent. These Fe-rich IPs show competitive mechanical properties in comparison to cement based structures. Nevertheless, the understanding on the role of Fe remains limited and is still investigated [57,63–67].

2.3.2.3. Formation of the Aluminosilicate Network in AAMs

The formation processes of AAMs are still not completely understood, nevertheless, a general conceptual model for the processes of the formation of the aluminosilicate network has been described (Figure 2-5). From an aluminosilicate source, aluminate and silicate is brought into solution by an alkaline hydrolysis which consumes water. This dissolution occurs rapidly at high pH. The alumina and silica form together with OH^--groups tetrahedral structures of $Al(OH_4)$- and $Si(OH_4)$. These structures are regarded as monomers. The solution is currently a complex mixture of silicate, aluminate and aluminosilicate structures and oligomers are formed during the gelation phase leading to the release of water. This condensation reaction continues and large networks of Al-O-Si chains are formed which are considered as an inorganic polymer network. As this network expands and reorganizes itself a 3D aluminosilicate network, attributed to GP, is formed. Although Figure 2-5 shows a linear sequence, the different steps occur simultaneously.

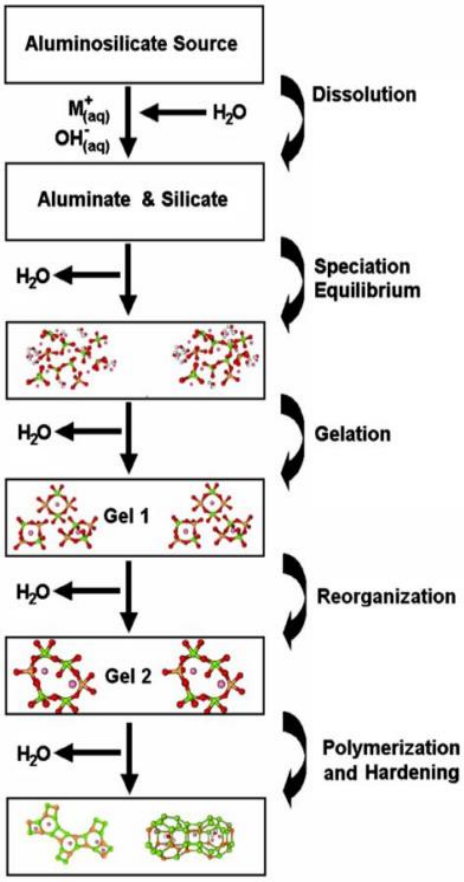

Figure 2-5: Schematic overview of conceptual model for formation of 3D aluminosilicate network. Figure from Duxson et al. (2006) [68].

Figure 2-6 shows the chemical structure of the 3D-network. The tetrahedral Al-structures have negatively charged cations which are counterbalanced by cations, typically Na^+ or K^+ (K^+ in Figure 2-6). These cations are captured in the network.

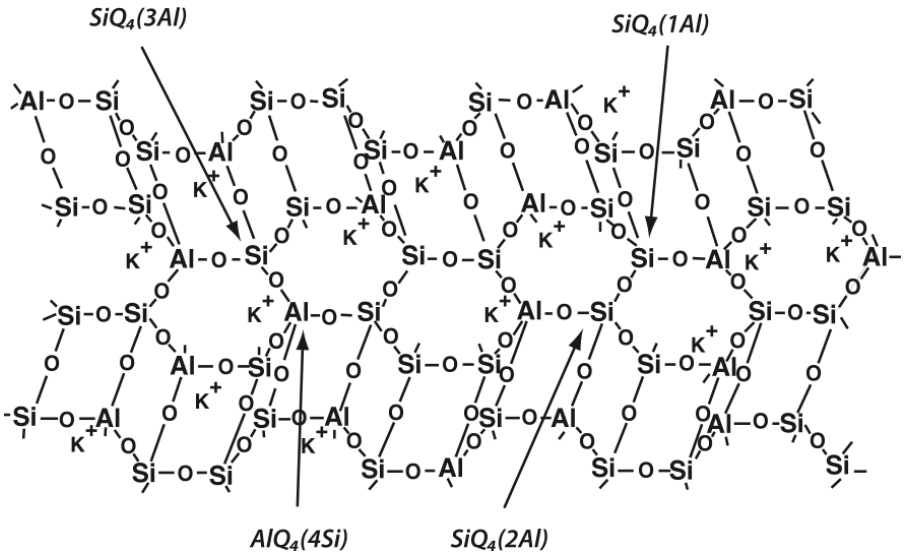

Figure 2-6: Overview of 3D aluminosilicate network. Figure from Geopolymer Institute 2012 [69].

2.3.2.4. Components of AAM

AAMs consist typically of two or three components depending if a paste/gel, mortar or concrete is produced. These structures vary from each other:

Paste/gel = Binder + activating solution

Mortar = Binder + activating solution + fine aggregate (particle size 8µm till 2000-4000 µm)

Concrete = Binder + activating solution + coarse aggregate (particle size 4000 µm till 24 mm)

So the necessary components are the binder, the aggregate and the activating solution. Each component affects the final physical and chemical properties of the AAM.

Binder

The function of the binder – as the name indicates - is to bind all the materials together like cement does. The binder is the source of Al and Si and

consequently, it is typically rich in Si and Al. The availability of both elements also influences the reactivity of the binder so both Al and Si need to be able to be dissolved by the activating solution. Pontikes et al. (2013) showed that for Fe-rich precursors the presence of an Al- and Si-rich amorphous phase in the slags is crucial for dissolving the Al and Si [35]. The Al:Si ratio influences the final characteristics of the produced AAM [6]. This ratio can be adapted by the activating solution. The particle size of the precursor also influences the reactivity and the final mechanical properties.

Aggregates

The aggregates don't have a binding function and their interaction with the alkaline activating solution is typically limited. In mortar, the aggregate is typically sand whereas in concrete typically sand and gravel is used. The aggregates allow additionally diversifying the final parameters of the end-product for example enhanced strength, fire resistance, radiological protection etc [70]. In the case of radiological protection, minerals like barite or magnetite are typically used. Nevertheless, not solely primary raw materials can be used as an aggregate but also by-products, for example crystalline metallurgical slags (low amorphous content) or BR.

Activating Solution

The activating solution is responsible for dissolving the Al and Si framework of the precursor. A wide range of activating solutions exists and the most used are NaOH and KOH. The activating solution affects the final physical and chemical properties of the AAM. In case of FS, it has been shown that the compressive strength at 28 days curing is higher in case of KOH than when NaOH is used as activating solution [71]. The molarity of the activating solution affects the compressive strength of the AAM. A higher molarity also impacts the viscosity of the binder/activating solution mixture. The solid to liquid ratio (S:L) also affects the viscosity of the mixture which can lead to the production of pores. A higher molarity can lead to thermal stresses due to the exothermic reaction. The Al:Si ratio can be adapted by combining the activating solution with a sodium silicate solution (Na_2SiO_3). The sodium silicate solution acts as a secondary source of Si.

In addition to parameters linked to the binder, aggregate or activating solution external factors can influence the final properties of the AAM. Examples are the curing temperature and moisture content [45]. In relation to gamma-ray shielding, both parameters are not expected to impact the linear attenuation coefficient.

2.4. Naturally Occurring Radionuclides in Industrial Residues

2.4.1. Naturally Occurring Radionuclides (NORs)

NORs are radionuclides of natural origin and are found in water, minerals, living organisms etc. NORs can be classified as primordial radionuclides or cosmogenic radionuclides, depending on their origin.

The primordial radionuclides exist because their half-life ($T_{1/2}$) is in correspondence with the age of the earth i.e. 4.5 billion years and originate from stellar processes like nucleosynthesis. The most relevant primordial radionuclides are ^{238}U ($T_{1/2}$= 4.468 x 10^9 a), ^{235}U ($T_{1/2}$=7.04 x 10^8 a), ^{232}Th ($T_{1/2}$= 1.405 x 10^{10} a) and ^{40}K ($T_{1/2}$ = 1.251 x 10^9 a). ^{238}U, ^{235}U and ^{232}Th are each head of a decay chain (shown in Figure 2-7) and decay via a series of alpha and beta decays until a stable Pb isotope is reached. ^{40}K decays to stable ^{40}Ca and ^{40}Ar nuclides.

The cosmogenic radionuclides are produced due to the interaction of cosmic radiation with atoms and molecules in e.g. the atmosphere. ^{14}C and ^{7}Be are typical examples of cosmogenic radionuclides.

2.4.1.1. Definition of NORM and NORM-residue

The IAEA safety glossary defines NORM as: "Radioactive material containing no significant amounts of radionuclides other than naturally occurring radionuclides" where "significant amounts of naturally occurring radionuclides" would be defined by a regulator [72]. In addition, the safety glossary also mentions: "Material in which the activity concentrations of the naturally occurring radionuclides have been changed by a process is included in naturally occurring radioactive material (NORM)." To identify NORM the European Commission specified a list of certain industrial sectors of concern and set levels to represent "the significant amount of naturally occurring radionuclides". Details on the involved industrial sectors and the levels are discussed in Section 2.5. Schroeyers and Kovler (2017) defined a NORM-residue as "a material that remains from a process, which contains more than 1 kBq/kg of ^{238}U, ^{232}Th (or any of their decay products) or more than 10 kBq/kg of ^{40}K." [73]. The term NORM by-product is introduced meaning a by-product from an industrial process, which contains more than 1 kBq/kg of ^{238}U, ^{232}Th (or any of their decay products) or more than 10 kBq/kg ^{40}K [73]. In the continuation of this thesis, the residues/by-products discussed here are not necessary NORM since their activity concentrations can be below the threshold levels. The focus is on the containment of NORs in by-products and construction materials produced out of these by-products.

2.4.1.2. Radioprotection Aspects of NORs

Regarding the radioprotection aspects of NORs, solely ^{40}K and radionuclides of the ^{238}U, ^{235}U and ^{232}Th decay chains are of interest and are defined as NORs throughout this thesis. These NORs are distributed heterogeneously in the earth's crust. Concentrations of these radionuclides can vary depending on the location but also on the geological media they are captured in [74]. Table 2-4 shows the activity concentration of ^{238}U, ^{232}Th and ^{40}K in different rocks, the continental upper crust and the soil. The activity concentrations vary between the different rock types but also between continental upper crust and the soil. For example, the ^{40}K activity concentration is a factor two higher in the continental upper crust than in the soil. These varying concentrations are due to physical and geochemical processes which affect the different radionuclides differently. This can lead to disequilibria states in the decay chain. More information on the decay chains of ^{238}U, ^{235}U and ^{232}Th and a discussion on the disequilibria are provided further in this section.

Table 2-4: Summary of activity concentrations of NORs in rocks, continental upper crust and soils. Data from IAEA [74].

	^{238}U (Bq/kg)	**^{232}Th (Bq/kg)**	**^{40}K (Bq/kg)**
Rocks			
Basalt (crustal average)	7–10	10–15	300
Granite (crustal average)	40	70	>l000
Shale, sandstones	40	50	800
Carbonate rocks	25	8	70
Continental upper crust (average)	36	44	850
Soils	66	37	400

NORs are present in minerals used for the production of industrial products such as different types of metals, however the activity concentration is very dependent on the type of the considered material (Table 2-5). For example, in the case of ores for phosphate production, activity concentrations ranging between 100 to 4000 Bq/kg, 600 to 3000 Bq/kg and 15 to 150 Bq/kg are observed for ^{238}U, ^{226}Ra and ^{232}Th, respectively. In the case of using secondary raw materials, variations are also observed even for materials of the same class and originating from the same facility [37]. In the processing of these input materials towards end products, the NORs present undergo several chemical and physical processes which can lead to enrichments in specific (by-) products or following a specific industrial pathway. The individual NORs can be affected differently and the availability of NORs for release in the biosphere is, in comparison with the original mineral state, altered due to industrial processing, which can have detrimental effects on the environment and human health. In addition, elevated levels of NORs in (by-) products can also lead to radiological

problems. These (by-) products with elevated NORs levels are often considered as waste or as low-value products by the producer. Nevertheless, this "waste" often possesses useful properties for other industries like for example the construction industry and the residues could, after a critical evaluation and study of the environmental impact, be used for novel applications. Therefore, these materials are classified in this thesis not as waste but as by-products or residues meaning they are secondary raw materials that can still find use.

Table 2-5: NORs in mineral resources. Data from IAEA (2003) [74].

Element/mineral	Source	^{238}U (Bq/kg)	^{226}Ra (Bq/kg)	^{232}Th (Bq/kg)
Aluminium	**Ore**	250		
	Bauxitic limestone, soil		100-400	30-130
	Tailings		70–100	
Copper	**Ore**	30–100000		20-110
Phosphate	**Ore**	100–4000	600-3000	15-150
Titanium (rutile, ilmenite)	**Ore**	30-750	30–750	35-750
Uranium	**Ore**	150000		
	Slimes		100000	
	Tailings		10000-20000	
Zirconium	**Sands**	4000	4000-7000	600

The radiological risk for workers and the general public associated with the presence and the processing of NOR containing materials is also acknowledged by the regulators via a series of legislative documents. Recently, the European Commission listed the industrial sectors involving NORM and set exemption and clearance levels for further reuse, recycling, incineration and disposal of these materials. In addition, specific legislation dealing with NORs in building materials is developed by the European Commission and is complementary with initiatives taken to stimulate the valorization of (by-) products in the building industry. The legislative aspect regarding NORs is discussed in Section 2.5.

The radiological consequences in terms of dose associated with the presence of NORs in building materials should be well determined. Different dose assessment calculations exist to estimate the effective dose. This is discussed in Section 2.6.

2.4.1.3. Radionuclides of the Natural Decay Chains of ^{238}U, ^{235}U and ^{232}Th

The decay chains of ^{238}U, ^{235}U and ^{232}Th are shown in Figure 2-7. These three radionuclides decay via a series of alpha and beta decays to a stable Pb isotope. A consequence of the alpha and beta decay can be the emission of gamma-rays. The underlined radionuclides are measurable via gamma-ray spectrometry. The activity of two or more radionuclides is equal in case of secular equilibrium throughout the decay chain. Due to above named processes, disequilibria can occur. The time frame in which a disequilibrium is present depends on the half-life of the involved radionuclides. As a rule of thumb, an equilibrium state (transient or secular[2]) is reinstalled over time i.e. after 3 half-lives of the daughter 87.5% of equilibrium is reached and after 5 half-lives 97%, given that the daughter half-life is shorter than the mother's. Consequently, disequilibrium between consecutive radionuclides can be measurable via gamma-ray spectroscopy in a select number of cases leading to different activities in specific parts of the decay chain separated by long-lived daughters. The ^{238}U decay chain can be divided into ^{238}U-part (^{238}U to ^{230}Th), ^{226}Ra-part (^{226}Ra to ^{214}Po) and ^{210}Pb-part (^{210}Pb to ^{206}Pb). The ^{232}Th decay chain can be divided into ^{232}Th-part (only ^{232}Th), ^{228}Ra-part (^{228}Ra to^{228}Ac) and ^{228}Th-part (^{228}Th to ^{208}Pb). In this thesis, no attention is payed to disequilibria in the ^{235}U decay chain as they are generally hard to measure via gamma-ray spectrometry in NORM unless complex and cumbersome radiochemical methods are employed. Special attention is required for the radionuclides ^{222}Rn and ^{220}Rn of the ^{238}U and ^{232}Th decay chains, respectively. Radon is a noble gas and can escape from the material bearing it, affecting the equilibrium state. The consequences for gamma-ray spectrometry and the dose assessments calculations are addressed in Chapter 4 and 5, respectively. Radon is discussed in more detail in the next section.

---

[2] In secular equilibrium the daughter activity equals the parent activity [109]. It is a necessary pre-requisite that the daughter's half-life is shorter than the mother's for equilibrium to be established [109]. If the daughter half-life is > 10 000 times shorter than the mother's half-life, secular equilibrium will eventually be reached.
In transient equilibrium the ratio of daughter to parent activities in a given radioactive decay is constant [109]. The daughter's half-life should be less than 10 000 times that of the mother's. When transient equilibrium will eventually be established, the daughter's activity is that of the mother's multiplied by the factor $T_{½\ mother}/(T_{½\ mother} - T_{½\ daughter})$. The ratio of the activities will be constant and the daughter apparently decays with the half-life of the mother.
Transient and secular equilibrium can be determined using the Bateman equation. More information regarding this can be found in [109,111].

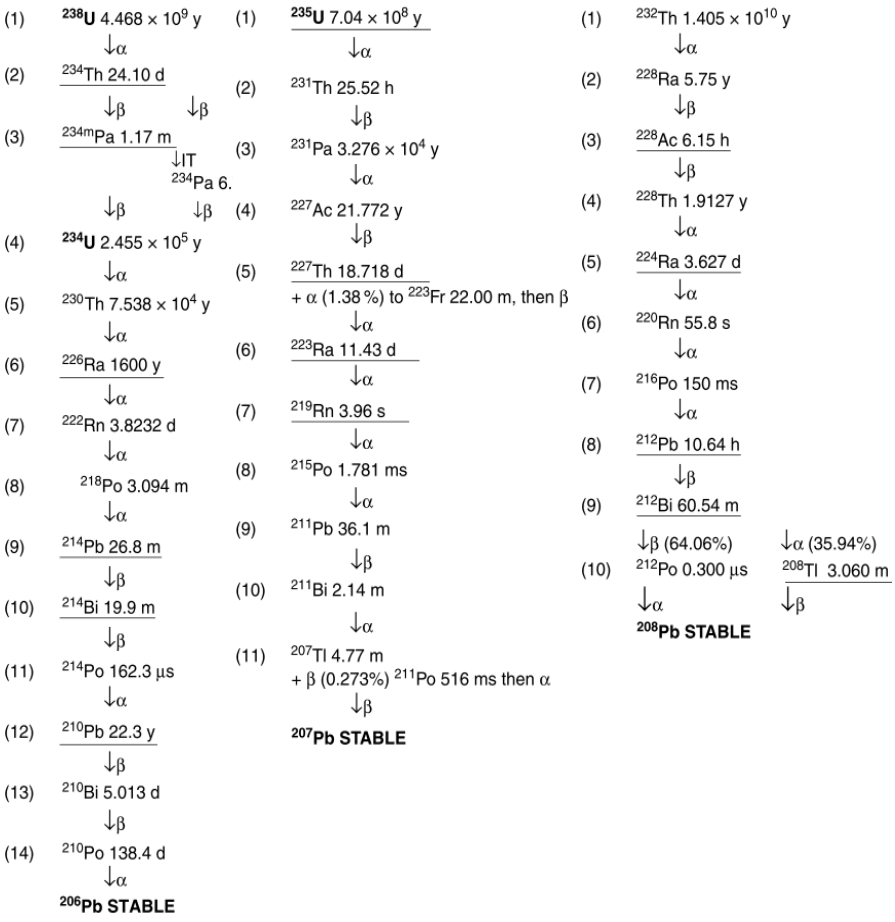

Figure 2-7: Decay scheme of ^{238}U, ^{235}U and ^{232}Th. Underlined radionuclides emit gamma-rays, principal gamma lines used in gamma-ray spectrometry are shown in Table 4-2 in Section 4.3.2. Figure from Gilmore (2008) [75].

2.4.1.4. Radon

Radon is a radioactive noble gas which accounts for approximately 40 % of the annual exposure (i.e. 3 mSv) [76]. Five naturally occurring isotopes of radon exist i.e. ^{222}Rn ($T_{1/2}$ = 3.82 days), ^{220}Rn ($T_{1/2}$ = 55.6 s) and ^{219}Rn ($T_{1/2}$ = 3.98 s) ^{218}Rn ($T_{1/2}$ = 36 10^{-3} s), ^{217}Rn ($T_{1/2}$ = 0.54 10^{-3} s) [77]. Due to difference in half-life the main concern for radiation protection is focused on ^{222}Rn. Rn is able to migrate from the soil or a building material into the indoor air [76]. Consequently, Rn and its progeny (Figure 2-7) can be inhaled and become a source of ionizing radiation. The radon progeny can be deposited and accumulated in the bronchi and the lungs as well on dust particles which can be inhaled. Although the outdoor concentration of Rn is 10 Bq/m^3, Rn can

accumulate in buildings – with values varying between tens of Bq/m^3 up to several kBq/m^3 - and consequently form a radiation risk. Generally spoken the main contribution comes from the ground below the house [76]. Building materials containing Ra are also a source of Rn – typical indoor radon concentration from building materials is 10-20 Bq/m^3.

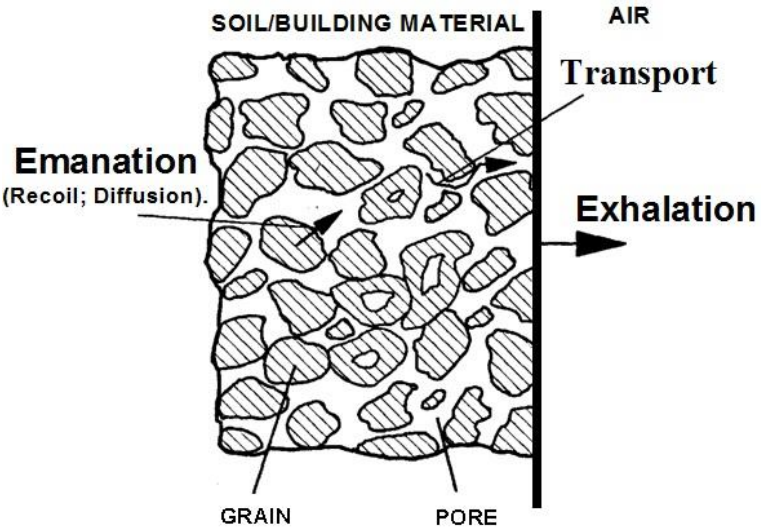

Figure 2-8: Overview of emanation, exhalation and transport of Rn in the soil or a building material [78].

Figure 2-8 shows the radon transport in a building material.

The characteristics of the building material like for example porosity, Ra concentration, thickness, etc. will impact the radon release from the building material into indoor air [76].

2.5. Legislative Aspects regarding Radiological Considerations for Reuse of Industrial Residues

In the European legislative framework, NORM, building materials and construction materials are handled differently from a radiological perspective.

Regulation (EU) No 305/2011, also called the construction products regulations (CPR), was published in 2011 and lays down essential requirements for construction works in general. According to this regulation, the construction works must be designed and built in such a way that the emission of dangerous radiation will not be a threat to the health of the occupant or neighbors.

It must be noted that in the CPR, the term construction products is defined as "any product or kit which is produced and placed on the market for incorporation in a permanent manner in construction works or parts thereof and the performance of which has an effect on the performance of the construction works with respect to the basic requirements for construction works". In addition, the term construction works is defined as meaning "buildings and civil engineering works". This means that a construction product consists of building materials and materials related to civil engineering works like roads and bridges. In this thesis the term construction material is used instead of construction product in order to not confuse with the term by-products.

In case of building materials the radiological safety requirements are specified by the Council Directive 2013/59/EURATOM, laying down basic safety standards for protection against the dangers arising from exposure to ionizing radiation, also named the European basic safety standards (EU-BSS) [79]. This directive was developed to establish basic standards, applicable to EU member states, for the protection against exposure of ionizing radiation for workers and the general public. This directive must be transposed to national law by EU Member States before February 2018. Also the term building material is specified in this directive meaning "any construction product for incorporation in a permanent manner in a building or parts thereof and the performance of which has an effect on the performance of the building with regard to exposure of its occupants to ionizing radiation".

This section deals with the European legislative framework regarding the usage of building materials, the radon aspect in case of building materials, construction materials and the clearance of solid materials.

2.5.1. Legislation regarding Building Materials

Mineral based building materials contain NORs and consequently are responsible for the most significant part of the external gamma dose indoors [80]. Requirements for regulating the gamma dose of building materials are specified in article 75 of the EU-BSS, which states "The reference level applying to indoor external exposure to gamma radiation emitted by materials, in addition to outdoor external exposure, shall be 1 mSv per year" [79]. An indicative list of building materials that should be considered in the framework of article 75 is listed in annex XIII of the EU-BSS and is shown here in List 1. A distinction is made between materials of natural origin and materials incorporating residues from industries processing NORM. Nevertheless, this list is not exhaustive and the dose criterion is valid for the whole building.

In order to assess in practice the 1 mSv/a reference level, a screening tool is implemented in the directive in annex VIII and shown in Equation 2-13 (Section 2.6.5.1.). This screening tool is also called the activity concentration index

(ACI). The ACI was introduced as a conservative screening tool to identify materials that need supplementary investigations. The index is valid for building materials, not the separate constituents. Consequently, annex VIII of the EU-BSS states: "The index relates to the gamma radiation dose, in excess of typical outdoor exposure, in a building constructed from a specified building material. The index applies to the building material, not to its constituents except when those constituents are building materials themselves and are separately assessed as such. For application of the index to such constituents, in particular residues from industries processing naturally occurring radioactive material recycled into building materials, an appropriate partitioning factor needs to be applied. The activity concentration index value of 1 can be used as a conservative screening tool for identifying materials that may cause the reference level laid down in Article 75 (1) to be exceeded. The calculation of dose needs to take into account other factors such as density, thickness of the material as well as factors relating to the type of building and the intended use of the material (bulk or superficial)." The technical aspects of the ACI are discussed in more detail in Section 2.6.

Section 2.5.3 provides information on the exemption and clearance when recycling of (NORM)-residues in building materials is not an option due to the 1 mSv threshold.

List 1: Indicative list of types of building materials considered with regard to their emitted gamma radiation as referred to in Article 75 of the EU-BSS [79].

1. Natural materials
(a) Alum-shale.
(b) Building materials or additives of natural igneous origin, such as:
— granitoides (such as granites, syenite and orthogneiss),
— porphyries;
— tuff;
— pozzolana (pozzolanic ash);
— lava.
2. Materials incorporating residues from industries processing naturally-occurring radioactive material, such as [79]:
fly ash;
phosphogypsum;
phosphorus slag;
tin slag;
copper slag;
red mud (residue from aluminium production);
residues from steel production

2.5.1.1. Legislation regarding Radon in case of Building Materials

Radon exposure is treated separately by the EU-BSS in article 74. The EU-BSS states that "Member States shall establish national reference levels for indoor radon concentrations. The reference levels for the annual average activity concentration in air shall not be higher than 300 Bq/m^3." [79]. So the radon concentration from building materials is not regulated.

Friedmann et al. (2017) give a detailed discussion on how to estimate the contribution from building materials to the indoor radon concentration [81]. They state that a ^{226}Ra concentration of 100 Bq/kg for a non-highly porous material should not lead to a radon concentration beyond the reference level of 300 Bq/m^3. A detailed discussion on the radon issue can be found in [81,82]. It must be noted that according to the UNSCEAR report of 2008 the annual exposure originating from radon is 1.26 mSv/a [83]. Typically the soil is the largest contributor to radon exposure. It must be noted that the annual radon exposure of 1.26 mSv/a is larger than the threshold value of 1 mSv/a, set by the EU-BSS in terms of indoor external exposure to gamma radiation emitted by materials.

2.5.2. Legislation regarding Construction Materials

In case of construction materials - so excluding building materials – no specific regulations are set currently. Nevertheless, according to the CPR, construction works must be designed and built in such a way that the emission of dangerous radiation will not be a threat to the health of the occupant or neighbors. However, no specific requirements are set by the CPR. Other regulatory documents allow providing guidelines. Markkanen (1995) developed a dose calculation index in case of streets and playgrounds with a reference level of 0.1 mSv/a, see Section 4.3.3 [84]. RP-122 specifies an exposure scenarios in case of road construction with a reference level of 0.3 mSv/a, see Section 4.3.4 [85].

2.5.3. Legislation regarding the Clearance of Solid Materials for Reuse, Recycling, Conventional Disposal or Incineration

In annex VII of the EU-BSS exemption clearance levels are set regarding the reuse, recycling, conventional disposal and incineration of NORs in solid materials (so applicable to industrial residues). The EU-BSS exemption/clearance levels were chosen in accordance with the exemption/clearance levels of the IAEA "Application of the concepts of exclusion, exemption and clearance". A global level benefits the industries processing and transporting these materials from an administrative and legislative point of view. These EU-BSS | IAEA levels are 1 kBq/kg for natural radionuclides from the ^{238}U and ^{232}Th decay series and 10 kBq/kg for ^{40}K (Table 2-6).

Table 2-6: Values for exemption or clearance as described in the EU-BSS for NORs in solid materials in secular equilibrium with their progeny. Data from EC (2013) [79].

Radionuclides	**Exemption or clearance level (kBq/kg)**
Natural radionuclides from the ^{238}U series	1
Natural radionuclides from the ^{232}Th series	1
^{40}K	10

Nevertheless, these levels are only applicable if secular equilibrium in the decay series is obtained. The EU-BSS allows higher values in case of disequilibrium but does not specify which levels are recommended. Radiation Protection (RP)-122 proposed values that also could be used in case of disequilibrium and applies a summation rule for the radiological evaluation (Equation 2-1) [85]. In this summation rule, the sum of the ratios of the activity concentration of each

individual radionuclide over its clearance level is calculated. If this sum is less than one, the material complies with the clearance requirements.

Equation 2-1 defines the summation rule to cope with disequilibria situations as defined in RP-122 [85].

$$\sum_{i=1}^{n} \frac{AC_i}{AC_{Li}} \leq 1.0$$

Equation 2-1

With AC_i the total activity in the structure per unit mass of radionuclide *i* expressed in Bq/g, AC_{Li} the clearance level of radionuclide *i* expressed in Bq/g, and *n* the number of radionuclides in the mixture.

The individual clearance levels are shown in Table 2-7. In case of wet sludges from oil and gas industries, the levels are higher than for the other materials. This is because the inhalation pathway is omitted in the calculation of these levels. In addition, the "+" sign indicates that the derived clearance level also includes the daughter nuclides (when applicable). Details on which daughter radionuclides are included can be found in RP-122 [85].

Table 2-7: Rounded clearance and exemption levels according to RP-122 for the ^{238}U, ^{232}Th decay series and its components and ^{40}K [85].

Nuclides*	**All materials (kBq/kg)**	**Wet sludges from oil and gas industry (kBq/kg)**
$^{238}U_{sec}$ incl. $^{235}U_{sec}$**	0.5	5
U nat **	5	100
^{230}Th	10	100
^{226}Ra+	0.5	5
^{210}Pb+	5	100
^{210}Po	5	100
$^{235}U_{sec}$***	1	10
^{235}U+***	5	50
^{231}Pa	5	50
^{227}Ac+	1	10
$^{232}Th_{sec}$	0.5	5
^{232}Th	5	100
^{228}Ra+	1	10
^{228}Th+	0.5	5
^{40}K	5	100

* For radionuclides considered to be in secular equilibrium.

** $^{238}U_{sec}$ and $^{235}U_{sec}$ are in their fixed natural ratio (99.275 and 0.72 % atomic fraction).

*** Separate values for radionuclides of ^{235}U series are given here only for information. For NORM these values are never limiting as ^{238}U and ^{235}U are always in their fixed natural ratio.

In addition, article 23 of the EU-BSS deals with the usage of NORM from a legislative perspective and identifies a list of sectors involving NORM. Article 23 states that "Member States shall ensure the identification of classes or types of practice involving naturally–occurring radioactive material and leading to exposure of workers or members of the public which cannot be disregarded from a radiation protection point of view [79]. Such identification shall be carried out by appropriate means taking into account industrial sectors listed in Annex VI (List 2)".

List 2: List of industrial sectors involving naturally-occurring radioactive material as referred to in article 23 [79].

When applying article 23, the following list of industrial sectors involving naturally-occurring radioactive material, including research and relevant secondary processes, shall be taken into account:

— Extraction of rare earths from monazite
— Production of thorium compounds and manufacture of thorium-containing products
— Processing of niobium/tantalum ore
— Oil and gas production
— Geothermal energy production
— TiO_2 pigment production
— Thermal phosphorus production
— Zircon and zirconium industry
— Production of phosphate fertilizers
— Cement production, maintenance of clinker ovens
— Coal-fired power plants, maintenance of boilers
— Phosphoric acid production,
— Primary iron production,
— Tin/lead/copper smelting,
— Ground water filtration facilities,
— Mining of ores other than uranium ore.

In the light of recycling or reuse of the materials listed in annex VI (List 2), related to article 23, RP-122 part II deals with the assessment of the exposure for workers and the general public for different exposure scenarios [79,85]. The RP-122 scenarios are discussed in more detail in section 2.6.5.3. It should be noted that the EU-BSS did not incorporate these recommendations but the system proposed by RP-122 can still be useful in case of disequilibrium.

Member states are allowed to implement a more stringent regulation in comparison to the EU-BSS. In addition, the legislative aspects are also valid for future recycling steps whether or not in building materials [86].

2.6. Dose Assessment

Different dosimetric calculation methods are used in Chapter 4, 5 and 6. The methodology regarding the dosimetric calculations is extensively discussed in the methodology section of the corresponding chapter. Chapter 6 deals with the improvement of the existing integration calculation model of Markkanen (Section 2.6.4.1; Equation 2-8 and Equation 2-9). The improved model is called the Expanded Gamma Dose Assessment (EGDA) model. The theory and reasoning behind the calculation method and the way the method was improved are

discussed here briefly and extensively in Chapter 6. In addition, an in depth comparison of the different characteristics of the dosimetric room models is performed. Section 2.6 gives extensive background information regarding these different dosimetric models.

The considered dose assessment calculations attempt to estimate the effective external gamma exposure of persons living in a room that originates from the used building materials. These dose assessments allow assessing whether a building material is, from a radiological perspective, safe to use or not in a specific environment/application and allow verifying whether a residue is adequate for valorization via a building material pathway or not. In addition, they allow estimating the external indoor exposure without performing measurements, which is practical for rooms that still need to be constructed. From a legislation perspective, dose assessments are important to assess whether the requirements of article 75 of the EU-BSS are fulfilled or if further steps should be taken as was discussed in Section 2.5. The adequateness of the dose assessments is of utmost importance.

Many parameters linked to the simulated room and the building material affect the final estimated dose. They are discussed in more detail in Section 2.6.2. Special attention is payed to the number of gamma lines as this is a key aspect studied in Chapter 6.

The calculation of the dose from a building material is in essence a calculation of the radiation transport through an attenuating medium and in fact an application of shielding calculations. Three methods are common in the literature to assess the effective dose originating from building materials i.e. (1) via Monte Carlo simulations (MCSs) (Section 2.6.3), (2) via an integration method (Section 2.6.4), and (3) via (simplified) index or dose formulas (Section 2.6.5). The methods vary in complexity, flexibility and user friendliness towards non-nuclear industries. (1) The MCS method allows calculating complex systems in a flexible way. The drawback of this calculation method is the complexity and the specialized knowledge needed in order to work with specialized codes. (2) The calculation based on integration allows performing flexible calculations and typically rectangular shapes are simulated. Different variations, on how the integration is performed, exist. (3) The simplified index or dose formulas are derived from the integration method or MCS method. These formulas allow performing easy calculations; however the flexibility towards non-standard rooms is often limited. It must be noted that next to the 3 methods described above, other calculations methods dealing with the transport of photons exist, for example: discrete ordinates method, using spherical harmonics, invariant embedding technique etc. Detailed information on these calculation techniques can be found in Stevens and Trubey (1968) [87].

The 3 calculation methods will be discussed hereafter with focus on the integration method, based on the build-up and attenuation methodology, and on the method that involves simplified indexes and dose formulas. These 2 methods are also used and studied in Chapter 6. Prior to the discussion, the basic principle (Section 2.6.1) is explained and the parameters (Section 2.6.2) which impact the dose rate are discussed.

2.6.1. Basic Principle

The total external effective dose (D_t) from gamma radiation originating from a building material can be divided into the direct dose (D_d) and the scattered dose (D_s) [88].

$$D_t = D_d + D_s$$

Equation 2-2

In the case of the direct dose, the gamma rays originating from the building material do not interact with the building material before reaching the measurement point. In the case of the scattered dose, the gamma-rays contributing to the dose are scattered before reaching the measurement point. It is the scattering process that complicates the dose calculations. The dose is dependent on the strength and energy of the source, the material it crosses, the distance between the measurement point and the source point. These aspects are discussed in more detail in the Section 2.6.4, dealing with the integration method.

Throughout the thesis different dose concepts like absorbed dose and effective dose are used. A detailed explanation of these dose concepts can be found in the UNSCEAR 2000 report [80]. In addition, the focus of this thesis is on the dose originating from gamma-rays emitted by building materials. Consequently, the term external gamma dose is used.

2.6.2. Room and Building Parameters affecting the Effective Dose

Physical parameters of the room and the building material can affect the total effective external gamma dose from a building material. The extent of the impact is depending on the adoptive parameters which are discussed below. In general, developed dose calculations in the literature are reported together with a sensitivity analysis of the handled parameters. Nevertheless, it must be noted that not all dose assessment methods are able to take different parameters into account. Typically, index and dose formula calculations only allow adapting a limited set of parameters.

In order to check to which extent a parameter affects the external dose, a comparison standard should be present. Koblinger (1978) defined a standard SiO_2 room measuring 400 cm x 500 cm x 280 cm, with the presence of neither windows nor doors [89]. The point of detection is set at the middle of the room. A standard thickness of walls, floor and ceiling of 20 cm and a density of 2320 kg/m^3 is set. Deviations on the standard exist, RP-112 suggests a density of 2350 kg/m^3 and instead of a SiO_2 composition, often the composition of concrete is set as the standard [89,90]. In addition, it is also assumed that the walls are homogeneous and the radionuclides are spread homogeneously in the walls.

The sensitivity analysis for all the parameters described below, except position in the room, radon and neighboring structures, is performed for the proposed EGDA model and presented in Chapter 6.

Wall Thickness

It has been observed that with increasing wall thickness, the dose rate increases rapidly; however, from a certain thickness on, this increase stagnates [88,89,91–94]. For example, Righi et al. (2016) found that when the wall thickness increases from 5 cm to 40 cm, the absorbed dose rate in air more than doubles in case of ^{238}U and ^{232}Th [88]. Whereas from 40 cm to 60 cm wall thickness, the absorbed dose rate in air raises only with 1 % in case of ^{238}U and ^{232}Th [88]. Risica et al. (2001) subscribed this stagnation to self-absorption effects [91].

Density

It is observed by various studies that with increasing density, the absorbed dose rate in air increases [88,89,91,92]. For example, Risica et al. (2001) observed that in case of ^{40}K, the absorbed dose rate in air of a concrete room with a density of 2350 kg/m^3 is approximately 40 % higher than of a room with a density of 1000 kg/m^3 [91].

Room Size

Risica et al. (2001) showed that with increasing room size the absorbed dose rate in air increases [91]. The absorbed dose rate in air increases with approximately 10 % when the room volume is increased from 11.2 m^3 to 280 m^3. De Jong and Van Dijck (2008) observed that the absorbed dose rate in air increases with 3% when the room volume increases from 56 m^3 to 200 m^3 [92].

Presence of Windows and Doors

The presence of windows and doors inside the wall, floor or ceiling of a room decreases the absorbed dose rate in air [91,92]. Risica et al. (2001) observed a decrease of 6 % in the absorbed dose in air due to the presence of door (1.5 x 2 m^2) in a tuff room (5.4 x 4.8 x 3 m^3) [91]. For a typical Dutch house this was approximately 5% [92].

Wall Composition

Koblinger (1978), and De Jong and van Dijck (2008) found that the chemical composition did not significantly influence the dose rate in case of SiO_2, concrete and gypsum with equal densities [89,92]. Van der Graaf et al. (2001) stated that the gamma emission energies of NORs mainly transfer energy via the Compton effect, which is almost independent from the mass number and thus also from the chemical composition [75,95]. To take the sample composition into account via the linear attenuation factor a correction factor (Equation 2-12) was used by Righi et al. (2016) and Mustonen (1984) [88,96]. Maduar and Hiromoto (2004) calculated the attenuation coefficients by interpolation using the data from Hubbell and Seltzler (1995) [93,97].

Position in the Room

Risica et al. (2001) concluded that the absorbed dose rate in air increases when the point of detection approaches thicker or longer walls [91]. An increase up to 10 % was found with distances up to 1 m from the walls in comparison to the center of the room [91]. In contrast, a decrease of the absorbed dose rate in air is observed when the point of detection moves towards windows or doors. In the literature, it is generally accepted that the middle of the room is considered to be representative for the assessment of the external dose originating from building materials [88,89,92].

Radon

Radon can escape from the building material. This escape is driven by the radon concentration gradient between the material and the open air [82]. Consequently, radon and its progeny can have a lower concentration than ^{226}Ra in the building material as radon escapes from the building material and finally the room due to ventilation [92,96]. This can lead to a lower external gamma-ray exposure from the building material. De Jong and Van Dijck (2008) calculated that the external absorbed gamma dose rate in air decreased on average with 9 % and 5 % for gypsum and concrete, respectively, used in the Netherlands [92]. Radon is often treated separately from external exposure from gamma-rays for simplification reasons. In addition, the EU-BSS also treats radon separately, see section 2.5.1.1 [79]. Nevertheless, the Austrian and Israeli index

as well as the dose calculation of De Jong and Van Dijck allow taking into account radon via a correction factor [92,98,99].

Neighboring Structures

The presence of neighboring structures, like for example in multi-story apartments or neighboring rooms, increases the absorbed dose rate in air. Toth (1983) assumes a 10 % increase in dose rate due to photons coming from neighboring rooms [100]. De Jong and Van Dijck (2008) found a 12 % increase in the dose rate in case of a room in a multi-story apartment [92]. Koblinger (1978) reported that the influence of neighboring structures is negligible when the wall thickness is 30 cm due to shielding of the gamma rays originating from the neighboring rooms [89].

Number of Gamma Lines and Emission Intensity

A large set of gamma-rays, which originate from the ^{238}U and ^{232}Th decay series, exists. Nevertheless, this set of gamma-rays is often not fully used or the set has been narrowed down to a limited number of (weighted averaged) gamma lines and their respective (summed) gamma emission intensities. This approach is widespread and has been maintained in models from the 80's up to now [88,89,94,96,101,102] because a lot of gamma emission intensities are very low and the number of gamma lines is very high. In addition, often gamma lines with similar emission energy are present. This approach simplifies the model and calculations. However, no uniformity exists on how many gamma lines are used. For example, in case of the ^{238}U decay series, Stranden et al. (1979) used 4 gamma lines (Table 2-8), Markkanen (1995) used 1 gamma line (Table 2-9 of Section 2.6.4.1), Righi et al. (2016) also used 1 gamma line, Koblinger (1978) used 24 gamma lines and Nuccetelli et al. (2015) used a set of 19 averaged gamma lines [88,89,94,101,102]. According to Righi et al. (2016), the validity of this weighted average approach is based on the fact that the differences in mass energy absorption coefficients in air are negligible in the energy range of 240-1800 keV [88]. Nevertheless, it must be noted that the effect of using different gamma emission energies can influence the dose rate significantly. Koblinger (1984) reported that for the same individual gamma emission line, different emission energies and different emission intensities were reported [103]. The differences could be up to several percent. These differences lead to deviations up to 30 percent in the dose rate calculated by the same model [100,103]. Therefore, it is important not to use old gamma line libraries [103]. Consequently, the newest nuclear data available is implemented in the EGDA model of Chapter 6 and the impact on the dose due to usage of weighted averaged gamma intensities or with limited gamma emission intensity is discussed.

Table 2-8: Overview of gamma emission energies and corresponding intensities used in the dose calculation of Stranden (1979) [94].

Nuclide	Energy (keV)	Gamma emission intensity
^{238}U	2240	0.078
	1740	0.241
	1230	0.333
	650	0.537
	310	0.64
^{232}Th	2610	0.359
	1570	0.113
	930	0.596
	760	0.141
	560	0.43
	340	0.194
	230	0.636
^{40}K	1460	0.11

2.6.3. Monte Carlo Simulation (MCS) Method

In Monte Carlo Simulations (MCSs), the photon transport in the walls of the room and the air inside a room is simulated. Typically, in a MCS, the path and interaction of a photon originating from a predefined volume source is followed until it is absorbed or leaves the predefined system. Starting from the source, the photon energy, photon direction and source position are selected, considering the defined spatial distribution of the source, the energy spectrum and the isotropic direction distribution. Consequently, the free path length, i.e. the distance a photon can travel before interaction is defined by the MCS. Here, the attenuation, linked to the material it is travelling in, influences the free path length. At the point of interaction of the photon with the material, the interaction is selected from the cross sections linked to the interaction. This interaction can be a photoelectric interaction, scattering interaction or pair production (Section 2.7.1). In case of scattering, a new energy and direction is given to the photon considering the scattering events distribution.

In MCSs, it is assumed that the radioactive sources are distributed uniformly in the different walls, floor and ceiling and that the photons are emitted isotropically. Jun et al. (2014) used the MCNPX code [104]. Here, energy lines above 10 keV with emission intensities above 1 % are considered. MCSs allow taking into account all specific room and building material properties.

2.6.4. The Integration Method

This method is based on calculating the dose rate coming from the building material via an integral.

The direct dose rate (D_d in Equation 2-2) from a gamma-ray source can be written as:

$$D_d = k \frac{\mu_a(E)}{\rho_a} E \Phi(E)$$

Equation 2-3

With k a proportionality constant, $\mu_a(E)/\rho_a$ the mass attenuation coefficient in air expressed in cm^2/g, E the photon energy and $\Phi(E)$ the flux density of photons in photons/m^2s. The flux density of photons of a point source in a medium is written as:

$$\Phi(E) = \frac{C}{4\pi l^2} e^{-\mu_m(E)s}$$

Equation 2-4

With C the activity of the source, $\mu_m(E)$ the linear attenuation of the medium in cm^{-1}, l the distance between the source the point of observation in cm, s the distance a photon travels through the medium in cm. In case the source is a volume source, the flux density can be written as

$$\Phi(E) = \frac{C}{4\pi} \int_0^V \frac{1}{l^2} e^{-\mu_m(E)s} dV$$

Equation 2-5

If the source is uniformly distributed in a given volume having a defined activity concentration AC (in Bq/kg) and a set of n energy lines with energy E_i (in MeV) and corresponding emission intensities I_i, D_d can be written as:

$$D_d = \frac{kAC}{4\pi} \sum_{i=1}^{n} \frac{\mu_a(E_i)}{\rho_a} E_i I_i \int_0^V \frac{1}{l^2} e^{-\mu_m(E_i)s} dV$$

Equation 2-6

In this expression the scattered fraction is not taken into account.

The calculation of the scattered fraction (D_s in Equation 2-2) can be implemented in the dose rate in different ways with varying complexity: (1) via the implementation of modified attenuation coefficients, (2) via a build-up factor (B) and (3) via Monte Carlo simulations.

Toth et al. (1983) incorporated the scattered dose via the implementation of modified attenuation coefficients in case of the medium (μ_m) in Equation 2-6 [100]. These modified attenuation coefficients are lower than the ones used to solely calculate the direct dose.

Another method involves the implementation of a build-up factor (*B*) in Equation 2-6, representing the scattering of the photons in the wall. So *B* is incorporated as a multiplication factor in Equation 2-6. Different ways of calculating B exist, for example, Stranden (1979) calculates the absorbed dose rate in air via linear approximation as shown in Equation 2-7 whereas Mustonen (1984) and Markkanen (1995) used the Berger equation to calculate the B (Equation 2-9). The usage of build-up factors in the dose calculation from building materials is widespread and the method is often called "build-up and attenuation" method.

$$B(E, \mu_m s) = 1 + a_l(E, \mu_m s)$$

Equation 2-7

With *B* the build-up factor, *E* the incident photon energy, μ_m the linear attenuation coefficient of the medium, *s* the distance the photon travels through the medium and a_l the fitting parameter.

A third method to calculate the scattered fraction is via Monte Carlo simulation (MCS). Koblinger (1984) calculated the scattered gamma-rays via a so-called adjoint MCS [103]. This means that photons are simulated starting from the point of detection and a reverse path is traversed to the source region (the walls). At every collision the energy is increased instead of decreased [103]. Zeeshan et al. (2007) used MCS to simulate the scattering that takes place in the wall [105]. This scattering is converted to a flux which is used to further perform calculations via integration.

Integration Models Studied in Chapter 6

In Chapter 6, the Markkanen model [101], the Mustonen model [96], the ISS room model [91] and the developed EGDA models are discussed. Each model is characterized by a specific set of gamma emission energies and intensities. The details of each model are discussed in Section 6.3 which provides an overview of the details in Table 6-1. In the next sections (Sections 2.6.4.1 to 2.6.4.3) background information on the discussed models is provided. The Markkanen model is discussed in more detail since the mathematical calculations of the EGDA models are based on the calculations of the Markkanen model.

2.6.4.1. Study of Markkanen

The Markkanen model [101] was at the base of the development of the ACI [79,90] (Section 2.6.5.1) and the consecutive legislative framework implemented by the EU. The model developed by Markkanen became a standard in the field of dose assessments [79,90,101].

The geometry used in the study of Markkanen is shown in Figure 2-9 and is also applied in the other studies, except when mentioned differently. Figure 2-9 shows a wall with height "a", width "b" and depth "h" The point "P(x_p, y_p, z_p)" is the position in which the dose rate is calculated. Point Q(x, y, z) is the point of integration. The distance between Point "Q" and point "P" is marked by "l" in Figure 2-9. Consequently, "s" is the fraction of "l" within the wall. The wall is defined by a certain density, sample composition and activity concentrations of the radionuclides of the ^{238}U and ^{232}Th decay series and ^{40}K. All this information is put together to calculate the dose rate coming from this wall in Equation 2-8.

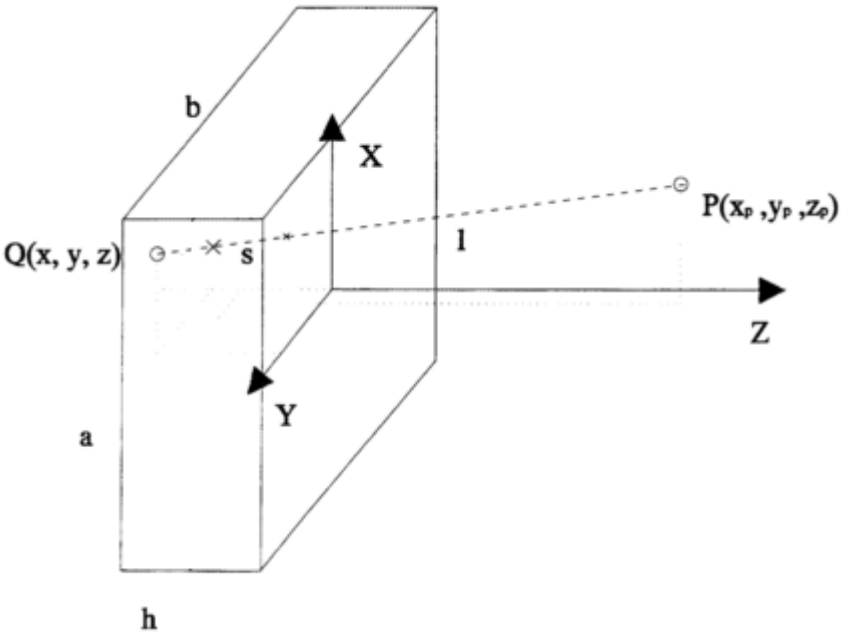

Figure 2-9: Graphical representation of the geometry used in calculating the external gamma dose. Figure (modified) from Markkanen (1995) [101].

$$D_A = 5.77x10^{-7}\ \frac{AC\rho}{4\pi}\sum_i \gamma_i(\frac{\mu_{en}}{\rho})_i\, E_i \int B_i \frac{e^{-\mu_i s}}{l^2}\, dV$$

Equation 2-8

With D_A the absorbed dose rate in air, *AC* the activity concentration of the material in Bq/kg, ρ the density of the material in kg/m^3, γ_i the gamma intensity of gamma line *i*, $(\mu_{en}/\rho)_i$ the energy absorption coefficient in air for gamma energy E_i in cm^2/g, E_i the photon energy in MeV, μ_i the linear attenuation coefficient of the material for gamma energy E_i in cm^{-1}, B_i the dose build up factor (Equation 2-9), *l* the distance from the point where the dose is calculated and the point of integration in cm (Equation 2-11), *s* the fraction of *l* within the top layer in cm (Equation 2-10). The build-up factor is calculated via the formula of Berger (Equation 2-9) and is only considered in the wall, ceiling or floor not in the air. The values of the energy depended *C* and *D* parameters are listed in Table 2-9.

$$B_i = 1 + C(E_i)\mu_i s e^{D(E_i)\mu_i s}$$

Equation 2-9

$$s = \left|\frac{z}{z_p - z}\right| l$$

Equation 2-10

$$l = \sqrt{(x_p - x)^2 + (y_p - y)^2 + (z_p - z)^2}$$

Equation 2-11

The total absorbed dose rate in air is the sum of the absorbed dose rate in air calculated from ceiling, floor and each wall.

In order to convert the absorbed dose in air to an effective dose a conversion factor of 0.7 Sv/Gy is used. This conversion factor is used for all gamma emitters and originates from the UNSCEAR 2000 report [80].[3]

Markkanen used a set of 5 gamma emission energies to calculate the dose coming from the building materials (Table 2-9). The 810 keV energy line of ^{238}U and the 587 keV energy line of ^{232}Th are averaged gamma lines. The data used to compose these averaged gamma lines originates from the study of Mustonen (1984) [96]. In case of 810 keV (^{238}U) 24 gamma lines were used whereas in case of 587 keV (^{232}Th) 19 gamma lines were used. These 43 gamma lines are shown in Table 2-10. In addition, both studies assume that the decay chains are

[3] The 0.7 Sv/Gy conversion factor was reported in the UNSCEAR report of 1982 [112] and has been used in several dose models since then. However, it must be noted that conversion factor is depended on several parameters like energy, body size etc. [113]. More information regarding this aspect can be found in the UNSCEAR reports and corresponding references and in [80,112,113].

in equilibrium. ^{137}Cs is also considered by Markkanen in the light of nuclear fall-out of the Tsjernobyl accident of April 1986. In fact, all radionuclides of interest can be implemented when necessary. The source of the linear attenuation coefficients, mass attenuation coefficient of air and the *C* and *D* Berger parameters are not specified in Markkanen (1995). Markkanen performed the calculations using the Fortran program MATERIA. Righi et al. (2016) updated the model of Markkanen in the FORTRAN 77 code [88]. The developed computer model allows the user to modify the dimensions of the room, the thickness of the walls, the point of absorption in the room, the density of the material and the activity concentration of ^{238}U, ^{232}Th and ^{40}K.

Finally it must be noted that Markkanen also proposed a dose calculation for multilayered walls. More info can be found in Markkanen (1995) [84].

Table 2-9: Overview of input data as used in the dosimetric calculation of Markkanen (1995) [101].

Nuclide	Energy (keV)	Gamma emission intensity	μ (cm^{-1})	μ/ρ_{air} (cm^2/g)	C	D
^{238}U	810	2.12	0.166	0.0285	1.161	0.144
^{232}Th	587	2.05	0.193	0.0295	1.279	0.19
^{232}Th	2615	0.356	0.0927	0.0217	0.734	0.0234
^{40}K	1461	0.107	0.0257	0.0257	0.946	0.0755
^{137}Cs	662	0.852	0.183	0.0293	1.237	0.1737

2.6.4.2. Study of Mustonen

The study of Mustonen (1984) calculates the absorbed dose rate in air via Equation 2-8 and the *B* of Berger shown in Equation 2-9 [96]. The *C* and *D* parameters of concrete are used, taking into account 7 mean free paths – being the average distance a photon travels between collisions with atoms of the target material - defined in the report of Trubey (1966).

$$\mu_{mat} = \frac{\mu_{con}\,\rho_{mat}}{\rho_{con}}$$

Equation 2-12

With μ_{mat} the linear attenuation coefficient of the material, μ_{con} the linear attenuation coefficient of concrete, ρ_{mat} the density of the material and ρ_{con} the density of concrete.

Mustonen proposed to address sample compositions differing from that of concrete via a correction factor, shown in Equation 2-12. Mustonen used a set of 24 and 20 gamma lines to represent the ^{238}U and ^{232}Th decay chains

respectively (Table 2-10). This set of 44 gamma lines was converted by Markkanen (1995) to a smaller set of 3 gamma lines.

Table 2-10: Overview of input data as used in the dosimetric calculation of Mustonen (1984) [96]. Equilibrium is assumed in the ^{238}U and ^{232}Th decay series. Data from Mustonen (1984) [96].

Nuclide	Energy (keV)	Gamma emission intensity	μ (cm^{-1})	μ/ρ_{air} (cm^2/g)
^{238}U	47	0.04	0.925	6.84E-05
	53	0.022	0.76	5.68E-05
	186	0.04	0.299	3.39E-05
	242	0.084	0.272	3.59E-05
	273	0.059	0.262	3.66E-05
	295	0.207	0.253	3.70E-05
	352	0.348	0.236	3.78E-05
	395	0.012	0.225	3.82E-05
	470	0.021	0.214	3.83E-05
	609	0.43	0.188	3.82E-05
	666	0.029	0.181	3.79E-05
	773	0.077	0.169	3.74E-05
	806	0.021	0.165	3.73E-05
	934	0.036	0.154	3.65E-05
	1120	0.159	0.14	3.53E-05
	1246	0.083	0.133	3.46E-05
	1390	0.092	0.127	3.37E-05
	1509	0.037	0.122	3.30E-05
	1661	0.02	0.117	3.23E-05
	1760	0.18	0.113	3.17E-05
	1848	0.027	0.11	3.13E-05
	2118	0.011	0.104	3.02E-05
	2204	0.062	0.103	2.99E-05
	2435	0.024	0.096	2.91E-05

Table 2-10 (Continuation): Overview of input data as used in the dosimetric calculation of Mustonen (1984) [96]. Equilibrium is assumed in the ^{238}U and ^{232}Th decay series. Data from Mustonen (1984) [96].

Nuclide	**Energy (keV)**	**Gamma emission intensity**	**μ (cm^{-1})**	**μ/ρ_{air} (cm^2/g)**
^{232}Th	925	0.015	1.270	9.29E-05
	760	0.023	0.397	2.97E-05
	299	0.034	0.355	3.15E-05
	272	0.045	0.287	3.48E-05
	262	0.45	0.274	3.57E-05
	253	0.032	0.262	3.65E-05
	236	0.057	0.254	3.70E-05
	225	0.19	0.242	3.78E-05
	214	0.019	0.222	3.82E-05
	188	0.046	0.211	3.83E-05
	181	0.086	0.203	3.83E-05
	169	0.3	0.191	3.82E-05
	165	0.072	0.174	3.77E-05
	154	0.091	0.168	3.74E-05
	140	0.051	0.16	3.69E-05
	133	0.26	0.156	3.66E-05
	127	0.172	0.151	3.64E-05
	1588	0.066	0.119	3.25E-05
	1626	0.041	0.118	3.24E-05
	2615	0.352	0.092	2.85E-05
^{40}K	1460	0.107	0.123	3.33E-05

2.6.4.3. The ISS-room Model

The ISS-room model is based on the calculation method of Markkanen (1995) [91]. The main difference is the implementation of a larger set of gamma lines with a larger total gamma emission intensity shown in Table 6-1 (Section 6.3.). For example in case of ^{238}U, the total gamma emission intensity is 2.41 and 2.12 for the ISS-room model and the Markkanen model, respectively. It must be noted that most of these gamma lines are weighted averaged gamma lines except for dedicated cases, like for example the 2614 keV line of ^{208}Tl (^{232}Th). The attenuation coefficients and the build-up factor (B) of concrete are used. The Bs are based on the best-fit of the values of Markkanen shown in Table 2-9. The density and thickness corrected index calculation I(ρd) and dose calculation D(ρd), discussed in Section 2.6.5.2, are based on the ISS-room model.

2.6.5. Index and Dose Formulas Method

The third method for assessing the dose originating from building materials is via a (simple) index and dose formula calculation. This method is characterized by its straightforward use and is therefore often used by legislators. However, the results don't always necessarily match with reality. The formulas are derived from the Monte Carlo simulation (MCS) method or from the integration calculation method. A lot of indexes and tools exist, Trevisi et al. (2013) reviewed official and non-official indexes in Europe and outside Europe (Australia, Israel) [106].

In Chapter 6 of this thesis, the activity concentration index (ACI) and density and thickness corrected index I(ρd) and dose D(ρd) calculation are compared with the studied integration methods (Section 2.6.4.1 to 2.6.4.3). These formula calculations were selected based on their usage in (upcoming) legislation. The ACI is a screening tool listed in the EU-BSS. In addition to the ACI and I(ρd), there is an online calculation tool provided by NIRS (Japanese National Institute of Radiological Sciences) based on the Radiation Protection-122 (RP-122) report of the European Commission. RP-122 deals with dose assessment for the public and workers in different scenarios; several are used in Chapter 4. Background information on the discussed index and dose formulas is provided in Sections 2.6.5.1 to 2.6.5.3

2.6.5.1. Activity Concentration Index (ACI)

The ACI is a screening index defined in annex VIII of the EU-BSS to identify materials that need supplementary investigations (See List 1). The index is considered as a fast and conservative screening tool for building materials and is not valid for the components of the building material. The index was originally developed by Markkanen (1995) and is derived from the Markkanen calculation method using numerical integration for the calculation of a standard room, as

described in section 2.6.2 [84]. The index uses the activity concentration of ^{226}Ra, ^{232}Th (or ^{228}Ra), ^{40}K as input. The index calculation is shown in Equation 2-13. The denominator values were chosen by Markkanen in that way that the 1 mSv threshold (taking into account a background dose; 50 nGy/h in case of RP-112, 70 nGy/h in case of Markkanen 1995) will not be exceeded [90,101]. The denominator values were rounded for simplicity reasons. If the ACI is below one, it is supposed that the exposure is below the 1 mSv per year limit.

Table 6-2 (Section 6.3.4) shows information on the parameters, linked to concrete, assumed for the ACI calculation. The ACI however solely uses fixed physical and chemical parameters. As discussed in Section 2.6.2 variations in the physical parameters of the room and building material can affect the total effective external gamma dose. Consequently, a one-size-fits-all-approach can provide wrong insights.

$$ACI = \frac{AC_{226\mathrm{Ra}}}{300\ Bq/kg} + \frac{AC_{232\mathrm{Th}}}{200\ Bq/kg} + \frac{AC_{40\mathrm{K}}}{3000\ Bq/kg}$$

Equation 2-13

With AC_i the activity concentration of the mentioned radionuclide *i* expressed in Bq/kg.

Uncertainty of the ACI is calculated like in Equation 2-14

$$\Delta(ACI) =$$

$$\sqrt{\left(\frac{1}{300}\right)^2 \Delta(\mathrm{AC}_{226\mathrm{Ra}})^2 + \left(\frac{1}{200}\right)^2 \Delta(AC_{232Th})^2 + \left(\frac{1}{3000}\right)^2 \Delta(AC_{40K})^2}$$

Equation 2-14

With $\Delta(AC_i)$ the uncertainty of the activity concentration of the mentioned radionuclide *i*.

To address one of the shortcomings of the ACI calculations a novel index was developed by Nuccetelli et al. (2015) which allows taking into account density and thickness of the building material [102]. These parameters were identified by Risica et al. (2001) as the most important parameters to be considered [91].

2.6.5.2. Density Corrected Index I(ρd)and Dose D(ρd)

The density corrected index $I(\rho d)$ developed by Nuccetelli et al. (2015) is derived from the ISS-room model calculations. The gamma dose rates per unit of activity concentration (nGy/h per Bq/kg) for ^{238}U, ^{232}Th and ^{40}K are calculated for a large set of densities and thicknesses. The best fit of these results is converted to a function for individually ^{238}U, ^{232}Th and ^{40}K. The same values for

non-sample specific parameters; such as exposure time, conversion coefficient and background reduction, are used for the ACI calculation and implemented in the calculation. The *I(ρd)* is based on the standard room size. The index is defined in such a way that an *I(ρd)* index value of 1 corresponds to a dose of 1 mSv/a. In order to calculate the index value, the activity concentrations of ^{226}Ra, ^{232}Th and ^{40}K are used. The formula is shown in Equation 2-15. In addition to the index calculation, Nuccetelli et al. (2015) developed a related formula which is able to calculate the annual effective dose, Equation 2-16 [102]. In this dose formula, the background reduction of 0.245 mSv/a is mentioned explicitly.

$$I(\rho d) = \frac{AC_{Ra226}(\rho d)^2}{182[(\rho d)^2+267(\rho d)+5128]} + \frac{AC_{Th232}(\rho d)^2}{140[(\rho d)^2+285(\rho d)+4928]} + \frac{AC_{K40}(\rho d)^2}{1969[(\rho d)^2+325(\rho d)+4440]}$$

Equation 2-15

With I the density and thickness depended index, ρ the density of the building material in kg/m^3, d the thickness of the building material in m, AC_{Ra226} the activity concentration of ^{226}Ra in Bq/kg, AC_{Th232} the activity concentration of ^{232}Th in Bq/kg and AC_{K40} the activity concentration of ^{40}K in Bq/kg.

$$\mathrm{D}(\rho d) = \left[\frac{AC_{Ra226}(\rho d)^2}{170[(\rho d)^2+156(\rho d)+11477]} + \frac{AC_{Th232}(\rho d)^2}{130[(\rho d)^2+173(\rho d)+11226]} + \frac{AC_{K40}(\rho d)^2}{1870[(\rho d)^2+194(\rho d)+11610]}\right] - 0.245$$

Equation 2-16

With *D* the annual effective dose rate in mSv/a.

2.6.5.3. Dose Assessment Scenarios of Radiation Protection 122

The technical guide radiation protection (RP)-122 (part II) describes a series of exposure scenarios for the general public and workers [85]. The parameters of the dose assessment scenarios vary per scenario and in specific scenarios differentiation is made for different materials [85]. These scenarios deal with transport, storage, disposal and landfill of NORM, and with the application in road (construction) and building material (construction). The Japanese National Institute of Radiological Sciences (NIRS) developed an online tool which allows simulating the different scenarios [107]. This tool allows setting several input parameters linked to the different dose assessment scenarios like: dilution factor, average dust concentration, direct ingestion and the activity concentrations of ^{226}Ra, ^{232}Th and ^{40}K. The model does not allow altering the density and thickness of the building materials. In addition, it is assumed that the decay chains are in equilibrium. In case of disequilibrium the highest activity

concentration of the decay chain should be selected. RP-122 (part II) lists the radionuclides that are considered for the modelling but does not specify the gamma emission lines. The online tool can give insight into the dose of different scenarios in which NORM-residues could be used. The scenarios named in part 4.2. of RP-122 part II as "Road constructions" and "Building construction with NORM containing building materials" are applied in Chapter 4 of this thesis. Both scenarios are aimed at workers. It must be noted that the room size parameters and the number of walls are different than in the case of ACI and the I(ρd). More details on the above mentioned scenarios can be found in Chapter 4 or in RP-122 part II [85].

2.7. Gamma-Ray Shielding

Gamma-ray shields are used to protect an object from external radiation coming from a source which could cause irreparable damage. This object can be a person but could be anything that is sensitive to ionizing radiation. Gamma-ray shields are not designed to protect against internal radiation and/or contamination. These shields find their application in nuclear facilities, medical facilities and storage facilities and are mainly used to protect people from the damaging effects of gamma-rays on the body [70].

2.7.1. Interaction of Gamma-Rays with Matter

Unlike alpha and beta radiation, gamma-rays have a low rate of interaction with the material they cross [70]. In theory, any material can be used as a shielding material but dense materials consisting of elements with high atomic number are preferred against gamma-rays [70].

In the interaction of gamma-rays with electrons and nuclei of the crossing material, 3 interactions are the most important: i.e. photoelectric effect, Compton scattering and pair production. Each of these interactions between a photon and a nucleus or an electron has a certain probability to occur. This probability is expressed by the cross section (σ) which is defined by Kaplan (1989) as "the probability of an interaction of a particle or photon with one target nucleus, or electron, per unit volume of the shielding medium" [70]. The cross section is conceived as an area and is expressed in barn (10^{-24} cm^2). The total cross section is the sum of the cross sections of the photoelectric effect, Compton scattering and pair production shown in Equation 2-17. Figure 2-10 shows the dominant interaction process as function of energy and absorber. For example the photoelectric effect at an atomic number of 20 and 60 is dominant between 0.01 and 0.1 MeV, and between 0.01 and 0.5 MeV, respectively.

$$\sigma_{tot,a} = \sigma_{ph} + \sigma_{cs} + \sigma_{pp}$$

Equation 2-17

With σ_{ph} the photoelectric cross-section, σ_{cs} the Compton scattering cross-section and σ_{pp} the pair production cross-section.

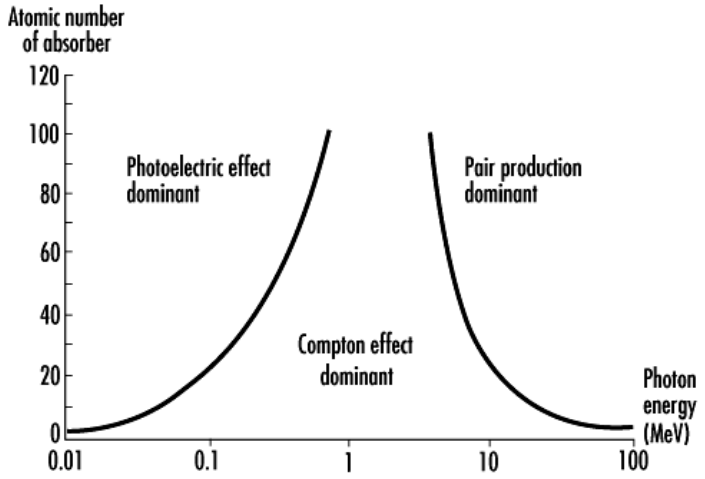

Figure 2-10: Graphical overview of dominant interaction process af gamma radiation with matter. From Robert and Cherry [108].

2.7.1.1. Photoelectric Effect

When a photon collides with an orbital electron and the photon possesses energy higher than the binding energy of the orbital electron, the orbital electron can be ejected from the atom, as shown in Figure 2-11. This electron is than classified as a photoelectron containing a kinetic energy equivalent to the energy difference of the initial photon and the binding energy. The cross section of the photoelectric effect is proportional to Z^{ζ}/E^{ζ} with Z the atomic number, E the photon energy and the exponent ζ a number in the range between 3 and 5. The exponent depends on the energy and different combinations have been proposed [109]. So the photoelectric effect increases with increasing Z and decreases with increasing E, also shown schematically in Figure 2-10. Due to the ejected orbital electron, a vacancy in the electron shell is created which can be occupied by electrons of higher shells leading to X-rays or Auger electrons. These X-rays are typically of low energy and are not of importance for shielding designs, shown in Figure 2-12.

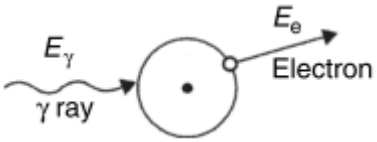

Figure 2-11: Schematic overview of photoelectric effect. From Gilmore (2008) [75].

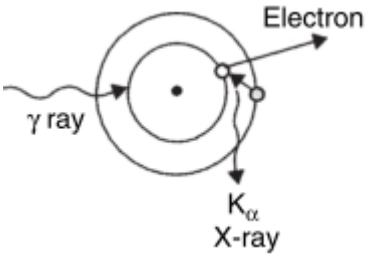

Figure 2-12: Schematic overview of vacancy filled by higher orbital electron leading to emission of characteristic X-rays. From Gilmore (2008) [75].

2.7.1.2. Compton Scattering

In a Compton scattering process, a photon elastically collides with a free or weekly bound electron resulting in a recoil electron and a scattered photon, shown in Figure 2-13. The scattered photon is deflected from its original path and has transferred a part of its energy to the recoil electron. The transferred energy is dependent on the initial energy and the scattering angle. The cross section of the Compton scattering is approximately proportional to *Z* of the absorber material.

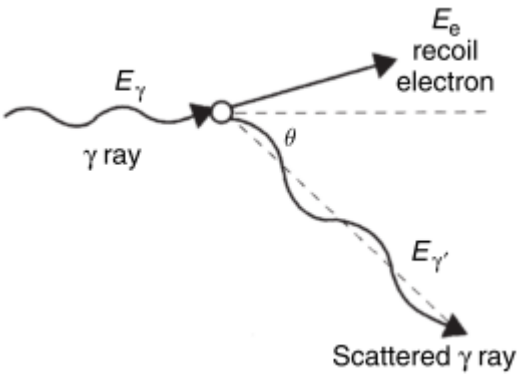

Figure 2-13: Schematic overview of Compton scattering process. From Gilmore (2008) [75].

2.7.1.3. Pair Production

In the pair production process a photon is converted into a positron and an electron in the Coulomb field of an atomic nucleus, as shown in Figure 2-14. All the photon's energy is converted into creation of the pair and their kinetic energy, meaning that the full energy of the photon is absorbed. The pair now contains energy and will lead to secondary radiation. This secondary radiation

consists of two photons with energy of 511 keV coming from the annihilation process between the produced positron and an electron.

Only photons possessing an energy higher than 1022 keV can induce pair production effects – next to photoelectric effects and Compton scattering - since the rest mass of an electron/positron is equivalent to an energy of 511 keV ($E=mc^2$). The pair production process is more likely to occur in materials with a higher Z and at higher energies. In fact this effect is the dominant interaction effect of photons with matter at high energies (see Figure 2-10). The cross section is proportional to Z^2.

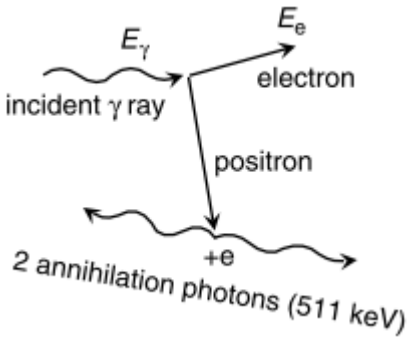

Figure 2-14: Schematic overview of pair production process. From Gilmore (2008) [75].

2.7.2. Expression of the Probability of Gamma-Ray Interaction with a Material

2.7.2.1. Linear Attenuation Coefficients μ

Kaplan (1989) defines the linear attenuation coefficient as "The probability of an atomic particle or photon (X-ray or gamma-ray) interacting in a particular way with a given material per unit path length" [70]. Consequently, the linear attenuation coefficient is expressed in cm^{-1} and symbolized as μ. μ depends on the type and energy of the radiation, the type of interaction, the density and the composition of the interacting material [70]. Figure 2-15 shows the variation of μ in function of energy for different materials (thus different Z). μ is proportional to the number of atoms per unit volume (N) and is expressed as $\mu = \sigma * N$. Linear attenuation coefficients are dependent on the density. This effect is obviated by defining a mass attenuation coefficient of a material which is symbolized as μ/ρ expressed in cm^2/g [70]. The linear attenuation coefficient or mass attenuation coefficient of compounds or mixtures can be obtained from the coefficients of the elemental constituents by means of weighted average as shown in Equation 2-18 and Equation 2-19.

$$\mu = \sum \mu_i = \sum N_i \sigma_i$$

Equation 2-18

With μ the linear attenuation coefficient of the compound or mixture in cm^{-1}, μ_i the linear attenuation coefficient of the *i*th constituent in cm^{-1}, N_i the atoms per unit volume of the *i*th constituent and σ_i the cross section of the *i*th constituent in cm^2.

$$\frac{\mu}{\rho} = \sum W_i (\frac{\mu}{\rho})_i$$

Equation 2-19

With μ/ρ the mass attenuation coefficient of the compound or mixture in cm^2/g, W_i the weighing factor of the *i*th constituent and $(\mu/\rho)_i$ the mass attenuation coefficient of the *i*th constituent in cm^2/g.

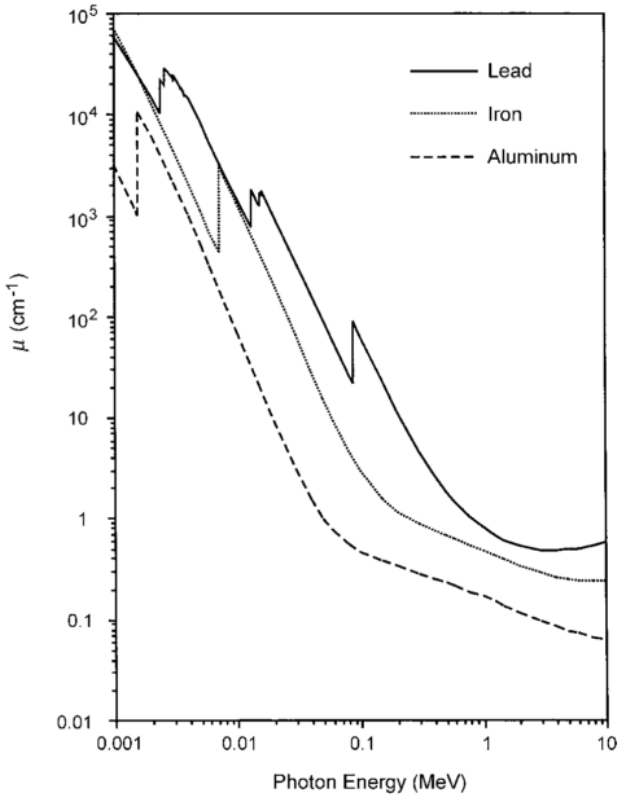

Figure 2-15: μ in function of the photon energy for different materials. From Martin (2006) [110].

2.7.2.2. Determination of the Linear Attenuation Coefficient

The determination of the attenuation of photons is a complex problem in which the experimental set-up plays a crucial role. In an absorber material of thickness *dx* the fractional reduction in the photon intensity I is related to the linear attenuation coefficient μ as expressed in Equation 2-20 [110].

$$-\frac{dI}{I} = \mu dx$$

Equation 2-20

The linear attenuation coefficient needs to be determined in a so called "narrow beam set-up" in order to be representative. A schematic overview of a narrow beam (or so called good geometry) and a broad beam set-up (or so called poor geometry) are shown in Figure 2-16.

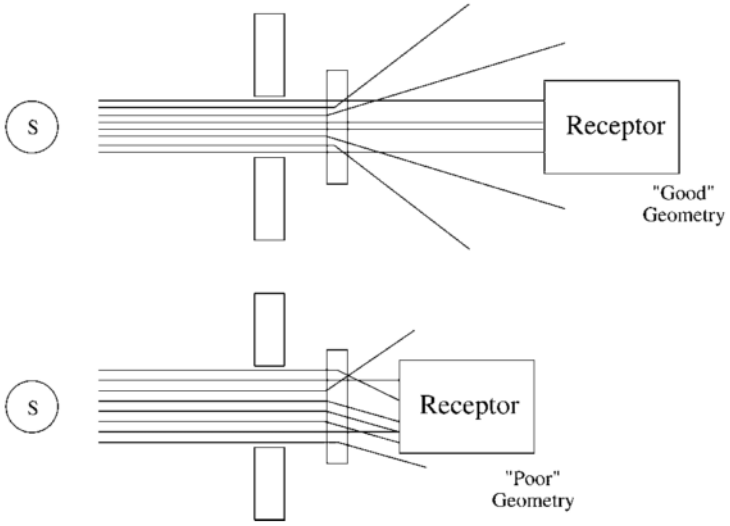

Figure 2-16: Schematic overview of narrow beam geometry or so called good geometry and of broad beam geometry or so called poor geometry. Figure from Martin (2006) [110].

In narrow beam geometry every photon that interacts with the absorber is absorbed or scattered out of the reach of the detector [110]. Consequently, only the photons that passed through the absorber without interaction will reach the detector, still having their initial energy. A narrow beam of "original" photons will only reach the detector. Measurements performed with the narrow beam set-up with and without absorber allow calculating the μ by the fraction of photons that

were removed from the narrow beam [110]. This calculation is performed by the Lambert-Beer equation (Equation 2-21).

$$I = I_0 \, e^{-\mu x}$$

Equation 2-21

With I the photon intensity after passing through an absorber, I_o the initial photon intensity, x the thickness of the absorber material in cm and μ the linear attenuation coefficient in cm^{-1}.

In contrast, in the case of a broad beam geometry scattered photons, in addition to the transmitted photons, will reach the active volume of the detector as shown in Figure 2-16. The scattered photons reaching the detector will lead to a more complex energy spectrum [110]. It must be noted that poor geometry will occur in practical applications of shielding materials whereas good geometry is obtained on lab scale in order to accurately calculate μ [110]. In order to deal with broad beam geometries a build-up factor (B), is incorporated in Equation 2-21 leading to Equation 2-22. This B allows taking into account scattered radiation and can be estimated via a set of approximating formulas like for example the linear approximation formula of Equation 2-7 or the Berger approximation formula of Equation 2-9.

$$I = I_0 B \, e^{-\mu x}$$

Equation 2-22

Converting Equation 2-22 to calculate μ gives Equation 2-23

$$\mu = B \frac{\ln(\frac{I_0}{I})}{x}$$

Equation 2-23

In case of a narrow beam, B is equal to 1 whereas in broad beam geometry this factor becomes larger than 1 [110]. Consequently, determination of linear attenuation coefficients is nearly always performed in narrow beam geometries since determining B is cumbersome.

2.7.3. Materials Used for Gamma-Ray Shielding

Shielding materials are designed to protect against damaging radiation. Theoretically every material can be used as shielding material as long as the absorber is thick enough [70].

In addition to the shielding capacities, the economical and mechanical properties of the material need to be considered [70]. Lead shields would only require a

limited thickness but the structural properties of lead do not allow its use as a structural material [70]. In addition, lead is also sensitive to high temperatures [70]. The usage of concrete as shielding material is currently widespread and concrete-based shielding structures are used in nuclear power plants, particle accelerators, research reactors, medical facilities and laboratory hot cells [70]. Concrete is regarded as an inexpensive structural material of which the shielding characteristics can be adapted by different cements and aggregates [70]. In case of gamma ray shielding, the aggregate plays the major role in the shielding capacities and aggregates of high density rich in Fe or Ba are typically used to produce high density concretes i.e. with a density above 2.6 g/cm^3 [70]. A major disadvantage of concrete-based structures is the low thermal conductivity which can lead to thermal stresses and temperature gradients [70].

2.7.3.1. High Density Concrete

The properties of high density concretes (HDCs) are determined by their aggregate. Table 2-11 shows the chemical composition, density, type and drawbacks of the aggregates that are typically used but in addition other types of aggregates can be used [70]. The attenuation properties of the different concretes listed here are discussed in Section 8.4.4. A high density is preferred as this typically lowers the thickness resulting in space optimization [70].

The aggregates used in the production of HDC are Fe- or Ba-containing minerals from natural origin except for ferrophosphorus and steel which are from industrial origin (Table 2-11). The density of the aggregates varies between 2.7 and 7.5 g/cm^3. No aggregate is free of drawbacks making the production of HDC complex. The most used HDC is based on magnetite [70]. HDC is not always developed using one specific aggregate and often mixtures of the above mentioned aggregates are used. The density and compressive strength are shown in Table 2-12. The density varies between 2.96 and 6.3 g/cm^3. The density of the resulting concretes (Table 2-12) is lower than of the pure aggregates on which it is based (Table 2-11). The compressive strength varies between 16 and 76 MPa. According to Kaplan (1989) the compressive strength of concrete for radiation shielding will depend on circumstances it is used in, but a 28-day strength of 20 MPa is generally adequate [70]. The linear attenuation coefficients of these HDC at different photon energies are shown in Table 8-5 of Section 8.4.4. Other mechanical properties like thermal conductivity, thermal expansion and resistance against radiation induced damage are not dealt with in this thesis as the focus is on the shielding properties. Nevertheless, these properties together with the practicability are important as well. Mechanical properties of the above listed HDC are described in Kaplan (1989) [70].

Table 2-11: Overview of high density concrete aggregates and their characteristics data from Kaplan (1989) [70].

	High density concrete aggregates						
	Barite	**Ilmenite**	**Limonite**	**Hematite**	**Ferrophosphorus**	**Magnetite**	**Steel**
Chemical composition	$BaSO_4$	$FeTIO_3$	$2Fe_2O_3.3H_20$	Fe_2O_3	Fe_3P, Fe_2P, FeP	Fe_3O_4	Fe
Density (g/cm^3)	4.0-4.4	4.2-4.8	2.7-4.3	4.9-5.3	5.7-6.5	4.6-5.2	6.5-7.5
Type	Mineral	Mineral	Mineral	Mineral	Industrial	Mineral	Industrial
Drawbacks	Sensitive to abrasion, weak, harmful impurities	Friable	Soft, not usable as coarse aggregate	Soft, flaky	Disintegrate, production of inflammable gasses	Magnetic attraction of fine Fe-containing aggregate	Expensive, suitable size and shape required

Table 2-12: Overview of density and compressive strength of different types of high density concrete. Data from Kaplan (1989) [70].

	Type concrete						
	Barite	**Ilmenite**	**Limonite**	**Hematite**	**Ferrophosphous**	**Magnetite**	**Steel**
Density (g/cm^3)	3.5-3.7	3.49-3.92	2.96	3.73-4.2	4.65	3.41-4.38	6.3
Compressive strength (MPa)	24.8-42.2	20.6-75.3	40.4	16.2-89.3	30.4	19.2-41.8	76

The material costs of different minerals are shown in Table 2-13. These prices originate from the corresponding USGS mineral reports, data are from 2012 and 2016 [4].

Table 2-13: Overview cost for different minerals. Data from USGS (2017) [4].

Mineral	Cost of mineral 2012 (dollars per ton)	Cost of mineral 2016 (dollars per ton)
Cement	89.5	111
Barites	187	198
Iron-scrap	367	192
Ilmenite	300	105
Sand and gravel	7.65	8.8
Iron-ore	116.48	82.41
Iron and steel slag	17	19.5

The cost price of HDC differs largely from aggregate to aggregate and generally spoken, the higher the density, the higher the price. The mineral prices are market dependent, from 2012 to 2016 price decreases and increases are observed. Nevertheless, the cost of high density minerals like barite, iron scrap and ilmenite are a factor 23, 22 and 12, respectively, more expensive than sand and gravel (2016 data). A HDC structure comes with a higher cost than an ordinary concrete structure. The usage of slags to produce HDC structures can be an interesting pathway from an economical point of view.

2.7.3.2. Inorganic Polymers as Structural Gamma-Ray Shielding Material

As described in Section 2.3, the production process of cement and consequently concrete produces high quantities of CO_2. The conventional aggregates used in HDC are typically minerals which require exploitation of natural resources. In addition, these aggregates are expensive. An alternative for these HDCs could be Fe-rich inorganic polymers (IPs) based on inexpensive non-ferrous slags. In this way, a valorization pathway of these slag materials can be created. In addition, usage of IPs in niche markets can be a trigger towards a breakthrough of the general use of IP as building material. The usage of IPs as shielding material is a new and unexplored field which will be dealt with in Chapter 8 with focus on fayalite slag based inorganic polymers (FSIPs) as possible alternative.

2.8. References

[1] United Nations, World population prospects key findings & advance tables ESA/P/WP/248, 2017.

[2] European Commission, Communication from the commission to the european Parliament, the council, the european economic and social committee and the committee of the regions Roadmap to a resource efficient Europe COM(2011) 571 final, (2011).

[3] European Commission, Communication from the commission to the european parliament, the council, the european economic and social committee and the committee of the regions on resource efficiency opportunities in the building sector COM(2014) 445 final, (2014) 1–10.

[4] USGS, Commodity Statistics and Information - nonfuel minerals, (2017). https://minerals.usgs.gov/minerals/pubs/commodity/ (accessed October 1, 2017).

[5] K.L. Scrivener, R.J. Kirkpatrick, Innovation in use and research on cementitious material, Cem. Concr. Res. 38 (2008) 128–136. doi:10.1016/j.cemconres.2007.09.025.

[6] J.L. Provis, J.S.J. van Deventer, Alkali Activated Materials State-of-the-Art Report, RILEM TC 224-AAM, 1st ed., Springer Dordrecht Heidelberg New York London, 2014. doi:10.1007/978-94-007-7672-2.

[7] J.S.J. Van Deventer, J.L. Provis, P. Duxson, D.G. Brice, Chemical research and climate change as drivers in the commercial adoption of alkali activated materials, Waste and Biomass Valorization. 1 (2010) 145–155. doi:10.1007/s12649-010-9015-9.

[8] J.L. Provis, Geopolymers and other alkali activated materials: why, how, and what?, Mater. Struct. 47 (2014) 11–25. doi:10.1617/s11527-013-0211-5.

[9] W. Schroeyers, Naturally Occurring Radioactive Materials in Construction Integrating Radiation Protection in Reuse (COST Action Tu1301 NORM4BUILDING), 1st ed., Woodhead Publishing, 2017.

[10] E. von Weizsäcker, K. Hargroves, M.H. Smith, C. Desha, P. Stasinopoulos, Factor Five: Transforming the Global Economy Through 80% Improvements in Resource Productivity., 1st ed., Earthscan, London, 2009.

[11] B. Tempest, O. Sansui, J. Gergely, V. Ogunro, D. Weggel, Compressive strength and embodied energy optimization of fly ash based geopolymer concrete., in: World Coal Ash, 2009.

[12] A. Buchwald, K. Dombrowki, M. Weil, Evaluation of primary and secondary materials under technical, ecological and economic aspects for

the use as raw materials in geopolymeric binders., in: 2nd Int. Symp. Non- Tradit. Cem. Concr. Brno, Czech Repub., 2005: pp. 32–40.

[13] B.C. McLellan, R.P. Williams, J. Lay, A. van Riessen, G.D. Corder, Costs and carbon emissions for geopolymer pastes in comparison to ordinary portland cement, J. Clean. Prod. 19 (2011) 1080–1090. doi:10.1016/j.jclepro.2011.02.010.

[14] T. Stengel, J. Reger, D. Heinz, Life cycle assessment of geopolymer concrete – what is the environmental benefit?, in: Concr. Solut. 09, Sydney, 2009.

[15] C. Klauber, M. Gräfe, G. Power, Review of Bauxite Residue " Re-use " Options. Project ATF-06-3: "Management of Bauxite Residues", Department of Resources, Energy and Tourism (DRET), (2009).

[16] K. Evans, The History , Challenges , and New Developments in the Management and Use of Bauxite Residue, J. Sustain. Metall. 2 (2016) 316–331. doi:10.1007/s40831-016-0060-x.

[17] S. Kumar, R. Kumar, A. Bandopadhyay, Innovative methodologies for the utilisation of wastes from metallurgical and allied industries, Resour. Conserv. Recycl. 48 (2006) 301–314. doi:10.1016/j.resconrec.2006.03.003.

[18] W. Mayes, I. Burke, Risks, remediation and recovery: lessons for bauxite residue management from Ajka., in: Bauxite Residue Valorization Conf., 2015: pp. 35–45.

[19] C. Nuccetelli, Y. Pontikes, F. Leonardi, R. Trevisi, New perspectives and issues arising from the introduction of (NORM) residues in building materials: A critical assessment on the radiological behaviour, Constr. Build. Mater. 82 (2015) 323–331. doi:10.1016/j.conbuildmat.2015.01.069.

[20] C.R. Borra, B. Blanpain, Y. Pontikes, K. Binnemans, T. Van Gerven, Recovery of Rare Earths and Major Metals from Bauxite Residue (Red Mud) by Alkali Roasting , Smelting , and Leaching Recovery of Rare Earths and Major Metals from Bauxite Residue, J. Sustain. Metall. (2016). doi:10.1007/s40831-016-0103-3.

[21] E. Balomenos, P. Davris, Y. Pontikes, D. Panias, Mud2Metal : Lessons Learned on the Path for Complete Utilization of Bauxite Residue Through Industrial Symbiosis, J. Sustain. Metall. (2016). doi:10.1007/s40831-016-0110-4.

[22] Y. Pontikes, G.N. Angelopoulos, Bauxite Residue in Cement and Cementitious Applications : Current Status and a Possible Way Forward, "Resources, Conserv. Recycl. 73 (2013) 53–63. doi:10.1016/j.resconrec.2013.01.005.

[23] N.M. Piatak, M.B. Parsons, R.R. Seal, Applied Geochemistry

Characteristics and environmental aspects of slag : A review, Elsevier Ltd, 2015. doi:10.1016/j.apgeochem.2014.04.009.

[24] National Slag Association, Common uses for slag, (2013). http://www.nationalslag.org/common-uses-slag (accessed May 22, 2016).

[25] B. Gorai, R.K. Jana, Characteristics and utilisation of copper slag - a review, Resour. Conserv. Recycl. 39 (2003) 299–313. doi:10.1016/S0921-3449(02)00171-4.

[26] U.S. Department of Transportation Federal Highway Administration, User guidelines for waste and byproduct materials in pavement construction, (2012) 1–10.

[27] S. Esfahani, M. Barati, Current status of heat recovery from granulated slag, 3rd Int. Symp. High Temp. Metall. Process. (2012) 337–348.

[28] National Cooperative Highway Research Program, SYNTHESIS 435 Recycled Materials and Byproducts in Highway Applications— summary report volume 1, 2013.

[29] U.S. Department of Transportation Federal Highway Administration, User Guidelines for Waste and Byproduct Materials in Pavement Construction, (2016) 1–8. http://www.fhwa.dot.gov/publications/research/infrastructure/structures/97148/nfs1.cfm (accessed May 22, 2016).

[30] K.S. Al-jabri, A.H. Al-saidy, R. Taha, Effect of copper slag as a fine aggregate on the properties of cement mortars and concrete, Constr. Build. Mater. 25 (2011) 933–938. doi:10.1016/j.conbuildmat.2010.06.090.

[31] H. Shen, E. Forssberg, An overview of recovery of metals from slags, Waste Manag. 23 (2003) 933–949. doi:10.1016/S0956-053X(02)00164-2.

[32] I. Barišić, S. Dimter, I. Netinger, Possibilities of application of slag in road construction, Teh. Vjesn. – Tech. Gaz. 4 (2010) 523–528.

[33] National Slag Association, Properties and uses of iron and steel slags MF 182-6, 1992.

[34] B. Das, S. Prakash, P.S.R. Reddy, V.N. Misra, An overview of utilization of slag and sludge from steel industries, Resour. Conserv. Recycl. 50 (2007) 40–57. doi:10.1016/j.resconrec.2006.05.008.

[35] Y. Pontikes, L. Machiels, S. Onisei, L. Pandelaers, D. Geysen, P.T. Jones, B. Blanpain, Slags with a high Al and Fe content as precursors for inorganic polymers, Appl. Clay Sci. 73 (2013) 93–102. doi:10.1016/j.clay.2012.09.020.

[36] P. Duxson, J.L. Provis, G.C. Lukey, J.S.J. van Deventer, The role of inorganic polymer technology in the development of "green concrete," Cem. Concr. Res. 37 (2007) 1590–1597. doi:10.1016/j.cemconres.2007.08.018.

[37] T. Croymans, I. Schreurs, M. Hult, G. Marissens, H. Stroh, G. Lutter, S. Schreurs, W. Schroeyers, Variation of natural radionuclides in non-ferrous fayalite slags during a one-month production period, J. Environ. Radioact. 172 (2017) 63–73. doi:10.1016/j.jenvrad.2017.03.004.

[38] N.M. Piatak, R.R. Seal Ii, Applied Geochemistry Mineralogy and the release of trace elements from slag from the Hegeler Zinc smelter , Illinois (USA), Appl. Geochemistry. 25 (2010) 302–320. doi:10.1016/j.apgeochem.2009.12.001.

[39] R. Barna, P. Moszkowicz, C. Gervais, Leaching assessment of road materials containing primary lead and zinc slags, Waste Manag. 24 (2004) 945–955. doi:10.1016/j.wasman.2004.07.014.

[40] N.M. Piatak, R.R.S. Ii, J.M. Hammarstrom, Mineralogical and geochemical controls on the release of trace elements from slag produced by base- and precious-metal smelting at abandoned mine sites, Appl. Geochemistry. 19 (2004) 1039–1064. doi:10.1016/j.apgeochem.2004.01.005.

[41] M. Marangoni, L. Arnout, L. Machiels, L. Pandelaers, E. Bernardo, P. Colombo, Y. Pontikes, C. Jantzen, Porous, Sintered Glass-Ceramics from Inorganic Polymers Based on Fayalite Slag, J. Am. Ceram. Soc. 99 (2016) 1–7. doi:10.1111/jace.14224.

[42] M. De Schepper, P. Verlé, I. Van Driessche, N. De Belie, Use of Secondary Slags in Completely Recyclable Concrete Use of Secondary Slags in Completely Recyclable Concrete, (2014). doi:10.1061/(ASCE)MT.1943-5533.0001133.

[43] R.S. Edwin, M. De Schepper, E. Gruyaert, N. De Belie, Effect of secondary copper slag as cementitious material in ultra-high performance mortar, Constr. Build. Mater. 119 (2016) 31–44. doi:10.1016/j.conbuildmat.2016.05.007.

[44] L. Machiels, L. Arnout, P.T. Jones, B. Blanpain, Y. Pontikes, Inorganic polymer cement from fe-silicate glasses: Varying the activating solution to glass ratio, Waste and Biomass Valorization. 5 (2014) 411–428. doi:10.1007/s12649-014-9296-5.

[45] R.I. Iacobescu, V. Cappuyns, T. Geens, L. Kriskova, S. Onisei, P.T. Jones, Y. Pontikes, The influence of curing conditions on the mechanical properties and leaching of inorganic polymers made of fayalitic slag, Front. Chem. Sci. Eng. (2017) 208–213. doi:10.1007/s11705-017-1622-6.

[46] M. Taylor, C. Tam, D. Gielen, Energy Efficiency and CO2 Emissions from

the Global Cement Industry, Energy Effic. CO2 Emiss. Reduct. Potentials Policies Cem. Ind. IEA, Paris, 4-5 Sept. 2006. (2006) 1–13.

[47] Y. Pontikes, R. Snellings, Cementitious binders incorporating residues, in: Handb. Recycl., 2014: p. 219–229,. doi:10.1016/B978-0-12-396459-5.00016-7.

[48] European Cement Research Academy, Deployment of CCS in the Cement Industry - report: 2013/19, 2013.

[49] I.G. Richardson, The nature of C–S–H in hardened cements., Cem. Concr. Res. 29 (1999) 1131–1147.

[50] A.G. Kalinichev, J. Wang, R.J. Kirkpatrick, Molecular dynamics modeling of the structure, dynamics and energetics of mineral-water interfaces: application to cement materials, Cem. Concr. Res. 37 (2007) 337–347.

[51] A.J. Allen, J.J. Thomas, H.M. Jennings, Composition and density of nanoscale calcium–silicate–hydrate in cement., Nat. Mater. 6 (2007) 311–316.

[52] J.S. Damtoft, J. Lukasik, D. Herfort, D. Sorrentino, E.M. Gartner, Sustainable development and climate change initiatives, Cem. Concr. Res. 38 (2008) 115–127. doi:10.1016/j.cemconres.2007.09.008.

[53] A. Peys, L. Arnout, B. Blanpain, H. Rahier, K. van Acker, Y. Pontikes, Mix-design Parameters and Real-life Considerations in the Pursuit of Lower Environmental Impact Inorganic Polymers, Waste and Biomass Valorization. 0 (2017) 1–11. doi:10.1007/s12649-017-9877-1.

[54] J.G.S.V.A.N. Jaarsveld, J.S.J.V.A.N. Deventer, A. Schwartzman, The potential use of geopolymeric materials to immobilise toxic metals : part II. Material and leaching characteristics, Miner. Eng. 12 (1999) 75–91.

[55] J. Davidovits, Geopolymer chemistry and applications, 3rd ed., Institut Geopolymere, 2011.

[56] C. Shi, P. V. Krivenko, D. Roy, alkali activated cements and concretes, Taylor & Francis, NY, USA, 2006.

[57] S. Simon, G.J.G. Gluth, A. Peys, S. Onisei, D. Banerjee, Y. Pontikes, The fate of iron during the alkali-activation of synthetic (CaO-)FeO_x-SiO_2 slags: An Fe *K* -edge XANES study, J. Am. Ceram. Soc. (2017) 1–12. doi:10.1111/jace.15354.

[58] K. Komnitsas, D. Zaharaki, V. Perdikatsis, Geopolymerisation of low calcium ferronickel slags, J. Mater. Sci. 42 (2007) 3073–3082.

[59] I. Maragkos, I.P. Giannopoulou, D. Panias, Synthesis of Ferronickel slag-based geopolymers, Miner. Eng. 22 (2009) 196–203.

[60] S. Onisei, Y. Pontikes, T. Van Gerven, G.N. Angelopoulos, T. Velea, V.

Predica, P. Moldovan, Synthesis of inorganic polymers using fly ash and primary lead slag., J. Hazard. Mater. 205–206 (2012) 101–10. doi:10.1016/j.jhazmat.2011.12.039.

[61] S. Onisei, K. Lesage, B. Blanpain, Y. Pontikes, Early Age Microstructural Transformations of an Inorganic Polymer Made of Fayalite Slag, J. Am. Ceram. Soc. 9 (2015) 1–9. doi:10.1111/jace.13548.

[62] M.B. Ogundiran, H.W. Nugteren, G.J. Witkamp, Immobilisation of lead smelting slag within spent aluminate-fly ash based geopolymers., J. Hazard. Mater. 248–249 (2013) 29–36. doi:10.1016/j.jhazmat.2012.12.040.

[63] D.S. Perera, J.D. Cashion, M.G. Blackford, Z. Zhang, E.R. Vance, Fe speciation in geopolymers with Si/Al molar ratio of ~2, J. Eur. Ceram. Soc. 27 (2007) 2697–2703. doi:10.1016/j.jeurceramsoc.2006.10.006.

[64] J.L. Bell, W.M. Kriven, Formation of an iron-based inorganic polymer (geopolymer), in: D. Singh, W.M. Kriven (Eds.), Mech. Properites Perform. Eng. Ceram. Compos. IV., John Wiley & Sons, 2010: pp. 301–311.

[65] K.C. Gomes, G.S.T. Lima, S.M. Torres, S. De Barros, I.F. Vasconcelos, N.P. Barbosa, Iron Distribution in Geopolymer with Ferromagnetic Rich Precursor, Mater. Sci. Forum. 643 (2010) 131–138. doi:10.4028/www.scientific.net/MSF.643.131.

[66] P.N. Lemougna, K.J.D. MacKenzie, G.N.L. Jameson, H. Rahier, U.F. Chinje Melo, The role of iron in the formation of inorganic polymers (geopolymers) from volcanic ash: a 57Fe Mössbauer spectroscopy study, J. Mater. Sci. 48 (2013) 5280–5286. doi:10.1007/s10853-013-7319-4.

[67] A. Peys, L. Arnout, T. Hertel, R.I. Iacobescu, S. Onisei, L. Kriskova, H. Rahier, B. Blanpain, Y. Pontikes, The use of ATR-FTIR spectroscopy in the analysis of iron-silicate inorganic polymers, in: 5th Int. Slag Valoris. Symp. | Leuven / 3-5/04/2017, 2017: pp. 1–4.

[68] P. Duxson, a. Fernández-Jiménez, J.L. Provis, G.C. Lukey, a. Palomo, J.S.J. Deventer, Geopolymer technology: the current state of the art, J. Mater. Sci. 42 (2006) 2917–2933. doi:10.1007/s10853-006-0637-z.

[69] Geopolymer Institute, Examples of geopolymer frameworks, (2012). https://www.geopolymer.org/science/examples-geopolymer-frameworks/ (accessed August 16, 2017).

[70] M.F. Kaplan, Concrete radiation shielding, 1st ed., Longman Scientific & Technical, 1989.

[71] V. Hallet, A. Peys, A. Katsiki, H. Rahier, S. Onisei, Y. Pontikes, The influence of activating solution on the kinetics and compressive strength of an iron- rich slag paste, in: 5th Int. Slag Valoris. Symp. | Leuven / 3-5/04/2017, 2017: pp. 1–4.

[72] IAEA, IAEA Safety Glossary Terminology Used in Nuclear Safety and Radiation Protection 2016 Revision, 2016.

[73] W. Schroeyers, K. Kovler, Chapter 2 Introduction, in: Nat. Occur. Radioact. Mater. Constr. Integr. Radiat. Prot. Reuse (COST Action Tu1301 NORM4BUILDING), 2017: pp. 5–11.

[74] IAEA, Extent of Environmental Contamination by Naturally Occurring Radioactive Material (NORM) and Technological Options for Mitigation - Technical reports series no. 419, 2003.

[75] G.R. Gilmore, Gamma Spectrometry of Naturally Occurring Radioactive Materials (NORM), in: Pract. Gamma-Ray Spectrom., 2nd ed., 2008: pp. 1–389.

[76] K. Kovler, H. Friedmann, B. Michalik, W. Schroeyers, A. Tsapalov, S. Antropov, T. Bituh, D. Nicolaides, Chapter 3 Basic aspects of natural radioactivity, in: Nat. Occur. Radioact. Mater. Constr. Integr. Radiat. Prot. Reuse (COST Action Tu1301 NORM4BUILDING), 2017: pp. 13–36.

[77] Laboratoire national Henri Becquerel, Decay Data Evaluation Project, (2016). http://www.nucleide.org/DDEP.htm (accessed May 22, 2016).

[78] J. Porstendorfer, Properties and behavior of radon and thoron and their decay products in the air, J. Aerosol Sci. 25 (1994) 219–263.

[79] European Commission, Laying down basic safety standards for protection against the dangers arising from exposure to ionising radiation, and repealing directives 89/618/Euratom, 90/641/Euratom, 96/29/Euratom, 97/43/Euratom and 2003/122/Euratom, Off. J. Eur. Union. (2014) 1–73.

[80] United Nations, Sources and Effects of Ionizing Radiation United Nations Scientific Committee on the Effects of Atomic Radiation UNSCEAR 2000 Report to the General Assembly, with Scientific Annexes VOLUME I: SOURCES, 2000.

[81] H. Friedmann, C. Nuccetelli, B. Michalik, M. Anagnostakis, G. Xhixha, K. Kovler, G. de With, C. Gasco, W. Schroeyers, R. Trevisi, S. Antropov, A. Tsapalov, C. Kunze, N.P. Petropoulos, Chapter 5 Measurement of NORM, in: Nat. Occur. Radioact. Mater. Constr. Integr. Radiat. Prot. Reuse (COST Action Tu1301 NORM4BUILDING), 2017: pp. 61–133.

[82] J. Porstendorfer, Properties and behavior of radon and thoron and their decay products in the air, J. Aerosol Sci. 25 (1994) 8502.

[83] United Nations, Sources and effects of ionizing radiation United Nations Scientific Committee on the Effects of Atomic Radiation UNSCEAR 2008 Report Volume I: SOURCES Report to the General Assembly Scientific Annexes A and B, 2008.

[84] M. Markkanen, Radiation Dose Assessments for Materials with Elevated Natural Radioactivity, Finish Cent. Radiat. Nucl. Safety. Rep. STUK-B-STO

32. (1995) 1–41.

[85] European Commission, Radiation protection 122 practical use of the concepts of clearance and exemption Part II application of the concepts of exemption and clearance to natural radiation sources, 2002.

[86] C. Nuccetelli, G. de With, R. Trevisi, N. Vanhoudt, S. Pepin, H. Friedmann, G. Xhixha, W. Schroeyers, J. Aguiar, J. Hondross, B. Michalik, K. Kovler, A. Janssens, R. Wiegers, Chapter 4 Legislative aspects, in: Nat. Occur. Radioact. Mater. Constr. Integr. Radiat. Prot. Reuse (COST Action Tu1301 NORM4BUILDING), 2017: pp. 37–60.

[87] P.N. Stevens, D.K. Trubey, Chapter 3. Methods for Calculating Neutron and Gamma-ray Attenuation, in: Weapons Radiat. Shield. Handb., 1968: pp. 1–119.

[88] S. Righi, S. Verità, P.L. Rossi, M.F. Maduar, A dose calculation model application for indoor exposure to two-layer walls gamma irradiation: the case study of ceramic tiles, Radiat. Prot. Dosimetry. 171 (2016) 545–553. doi:10.1093/rpd/ncv476.

[89] L. Koblinger, Calculation of exposure rates from gamma sources in walls of dwelling rooms, Health Phys. 34 (1978) 459–463.

[90] European Commission, Radiation protection 112 Radiological protection principles concerning the natural radioactivity of building materials, (1999) 1–16.

[91] S. Risica, C. Bolzan, C. Nuccetelli, Radioactivity in building materials: room model analysis and experimental methods., Sci. Total Environ. 272 (2001) 119–126.

[92] P. de Jong, W. van Dijk, Modeling gamma radiation dose in dwellings due to building materials., Health Phys. 94 (2008) 33–42. doi:10.1097/01.HP.0000278509.65704.11.

[93] M.F. Maduar, G. Hiromoto, Evaluation of indoor gamma radiation dose in dwellings, Radiat. Prot. Dosimetry. 111 (2004) 221–228. doi:10.1093/rpd/nch329.

[94] E. Stranden, Radioactivity of building materials and the gamma radiation in dwellings, Phys. Med. Biol. 24 (1979) 921–930.

[95] E.R. van der Graaf, L.E.J.J. Schaap, G. Bosmans, Radiation performance index for Dutch dwellings: consequences for some typical situations, Sci. Total Environ. 272 (2001) 151–158.

[96] R. Mustonen, Methods for evaluation of doses from building materials, Radiat. Prot. Dosimetry. 7 (1984) 235–238.

[97] J.H. Hubbell, S.M. Seltzer, Tables of X-Ray mass attenuation coefficients and mass energy-absorption coefficients 1 keV to 20 MeV for Elements

Z=1 to 92 and 48 Additional substances of Dosimetric Interest., Http://Physics.Nist.Gov/Xaamdi. (1996). doi:http://physics.nist.gov/xaamdi.

[98] Austrian Standards, Önorm S 5200. Radioaktivität in Baustoffen, 2009.

[99] K. Kovler, Legislative aspects of radiation hazards from both gamma emitters and radon exhalation of concrete containing coal fly ash, Constr. Build. Mater. 25 (2011) 3404–3409. doi:10.1016/j.conbuildmat.2011.03.031.

[100] A. Toth, A lakossag természetes sugarterhelése Natural Radiation Burden of the Population, 1983.

[101] M. Markkanen, Radiation dose assessments for materials with elevated natural radioactivity, 1995.

[102] C. Nuccetelli, F. Leonardi, R. Trevisi, A new accurate and flexible index to assess the contribution of building materials to indoor gamma exposure, J. Environ. Radioact. 143 (2015) 70–75. doi:10.1016/j.jenvrad.2015.02.011.

[103] L. Koblinger, Mathematical models of external gamma radiation and congruence of measurements, Radiat. Prot. Dosimetry. 7 (1984) 227–234.

[104] J. Deng, L. Cao, X. Su, Monte Carlo simulation of indoor external exposure due to gamma-emitting radionuclides in building materials, Chinese Phys. C. 38 (2014) 108202. doi:10.1088/1674-1137/38/10/108202.

[105] M. Zeeshan Anjum, S.M. Mirza, M. Tufail, N.M. Mirza, Z. Yasin, Natural radioactivity in building materials: dose determination in dwellings using hybrid Monte Carlo-deterministic approach, Int. Conf. Nucl. Data Sci. Technol. (2007) 1–4. doi:10.1051/ndata:07187.

[106] R. Trevisi, C. Nuccetelli, S. Risica, Screening tools to limit the use of building materials with enhanced/elevated levels of natural radioactivity: Analysis and application of index criteria, Constr. Build. Mater. 49 (2013) 448–454. doi:10.1016/j.conbuildmat.2013.08.059.

[107] Research Center for Radiation Protection, National Institute of Radiological Sciences, NIRS NORM database., (n.d.). http://www.nirs.qst.go.jp/ENG/index.html (accessed May 5, 2017).

[108] N. Robert, J. Cherry, Chapter 48 -Radiation: ionizing, (n.d.). http://www.ilocis.org/documents/chpt48e.htm (accessed May 17, 2017).

[109] G.R. Gilmore, Practical gamma-ray spectrometry, 2nd ed., John Wiley& Sons, 2008.

[110] J.E. Martin, Physics for radiation protection, 2nd ed., WILEY-VCH Verlag

GmbH & Co. KGaA, 2006.

[111] H. Bateman, The solution of a system of differential equations occurring in the theory of radioactive transformations, Proc. Cambridge Philos. Soc. 15 (1910) 423–427.

[112] United Nations Scientific Committee on the Effects of Atomic Radiation, Ionizing Radiation: Sources and Biological Effects United Nations Scientific Committee on the Effects of Atomic Radiation 1982 Report to the General Assembly, with annexes, 1982.

[113] K. Saito, N. Petoussi-Henss, M. Zankl, Calculation of the effective dose and its variation from environmental gamma ray sources., Health Phys. 74 (1998) 698–706. doi:10.1097/00004032-199806000-00007.

Chapter 3: Materials and methods

Figure 3-1 gives an overview of the materials and methods used in this thesis, which will be discussed in the forthcoming sections or in the corresponding chapters. In addition, gamma-ray spectrometry will be handled in detail in this chapter.

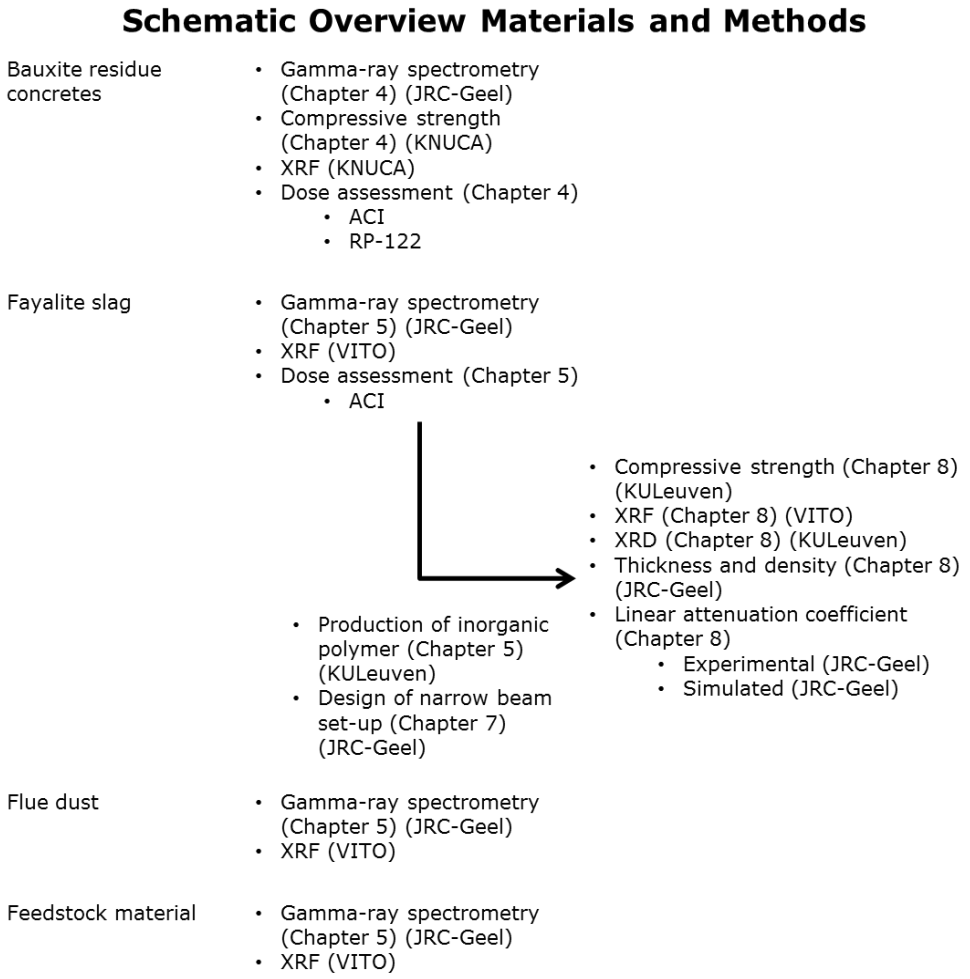

Figure 3-1: Schematic overview of materials and methods with corresponding chapters. KNUCA: Kiev National University of Construction and Architecture, VITO: Vlaamse Instelling Technologisch Onderzoek, JRC-Geel: Joint Research Centre Geel and KULeuven: Katholieke Universiteit Leuven.

References at page 90

3.1. Metrological Considerations

A large part of the experimental work in this thesis was conducted at the JRC's Radionuclide Metrology Laboratory in Geel. It is represented since many years at Bureau International de Poids et Mesures's Consultative Committee for Ionizing Radiation (BIPM's CCRI(II)). BIPM is an international organization established by the Metre Convention, which focuses on measurement science and measurement standards. Therefore, at JRC-Geel, particular attention is payed to metrological aspects, which includes correct naming of units and entities as well as careful assessment of parameters affecting measurements and uncertainty-budgets. Prior to the continuation a few metrological aspects are handled.

Activity Concentration vs. Specific Activity

According to the International Standard Organization (ISO) activity concentration is expressed in bequerel per unit volume (Bq/m^3). The Council Directive 2013/59/EURATOM, laying down basic safety standards for protection against the dangers arising from exposure to ionizing radiation, also named the European Basic Safety Standards (EU-BSS) uses the term activity concentration to express Bq per unit of mass (Bq/kg) [1]. ISO defines the specific activity, *a*, as shown in Equation 3-1 [2]. With *A* the activity of a sample and *m* its mass. This is also called massic activity. Since the EU-BSS forms a major topic of this thesis, the terminology linked to this document is followed so activity concentration here is expressed in Bq/kg. In future legislative documents, the terminology could be adapted to be in line with the ISO standards.

$$a = \frac{A}{m}$$

Equation 3-1

Mass Fraction vs. Weight Fraction

The terms weight fraction or percentage by weight (wt%) are used frequently (but somewhat incorrectly) in literature. In this thesis, the terms percentage by mass or mass fraction (mass%) will be used – even when the original reference reports wt%. The weight of an object is depending on the gravitational force at the place of weighing, whereas the mass of an object is independ of the gravity. kg is the official SI-unit of mass whereas weight is expressed by Newtons.

3.2. Samples for Gamma-Ray spectrometry

3.2.1. Bauxite Residue (BR) Concretes

In Chapter 4, different bauxite residue (BR) concretes are studied by means of gamma-ray spectrometry. BR concretes with different mass% of BR

incorporated are produced, as shown in Table 4-1 in Section 4.3.1. The concretes were dried at 110 °C until no mass difference was observed, prior to storage into sealed Teflon® containers. X-ray Flourescence (XRF) data measured using an Saturn-2 instrument of all the major elements of the BR concretes was provided. The input composition for the Monte Carlo simulation (MCS) was calculated from the individual components taken the mass% as weighing factor. Further information regarding the sample preparation and radiological analysis is provided in Section 4.3.

3.2.2. Fayalite Slag (FS)

In Chapter 5, a study of 33 fayalite slag (FS) samples analysed by means of gamma-ray spectrometry is presented. All samples originated from one industrial facility. The FS samples were received dry and milled from the company. For each slag sample XRF analysis was performed by Vlaamse Instelling Technologisch Onderzoek (VITO) (Mol, Belgium) with a high performance energy dispersive XRF spectrometer with polarized X-ray excitation geometry (HE XEPOS, Spectro Analytical Systems, Kleve, Germany). This instrument was equipped with a 50 W tungsten end-window tube (max. 60 kV, 2 mA) and a Silicon Drift Detector. The XRF-data was normalized and used as input for the MCS. More details on the FS samples are provided in Section 5.3.1.1.

3.2.3. Flue Dust

In Chapter 5, a study of 9 different flue dust samples analysed by means of gamma-ray spectrometry is presented. All samples originated from one industrial facility (same as the FS). All flue dust samples were provided by the company as dry powders. For each flue dust sample a XRF analysis was performed by VITO (Mol, Belgium) with the same instrument as mentioned in Section 3.2.2. More details on the flue dust samples are provided in Section 5.3.1.2.

3.2.4. Feedstock Samples

In Chapter 5, a study of 5 feedstock samples analysed by means of gamma-ray spectrometry is presented. All samples originated from one industrial facility. All feedstock samples were provided by the company as a mixture of powders and

fine granules, with a diameter up to 5 mm. All samples were provided dry. Prior to XRF analyses the samples were milled by means of a ball mill by VITO (Mol, Belgium). XRF analysis were performed by VITO (Mol, Belgium) using the same instrument as mentioned in Section 3.2.2. More details on the feedstock samples are provided in Section 5.3.1.3.

3.3. Samples for Compressive Strength Testing and Determination of Linear Attenuation Coefficients

3.3.1. Preparation of Precursor Materials

Water-quenched (WQFS) and slowly cooled fayalite slags (SCFS) were used for the production of inorganic polymers. The difference between both slags was the cooling path, leading to a higher crystalline phase for the SCFS. WQFS samples were milled using an attritor mill (Wiener & Co N.V.) and sieved afterwards with a vibratory sieve shaker AS 200 (Retsch) equipped with 80 µm sieve. D(50) of the milled powder was 8.65 µm and determined by laser scattering (Mastersizer Micro Plus; Malvern, Worcestershire, UK). The SCFS were reduced in size by hand until they were small enough to fit in a disk mill pulverisette 13 (Fritsch). The milled fraction was sieved according to the EN 196-1 norm by a vibratory sieve shaker AS 200 (Retsch). For both slags samples a XRF analysis was performed by VITO (Mol, Belgium) using the same instrument as mentioned in Section 3.2.2.

3.3.2. Production of Inorganic Polymer (IP)

The WQFS were used as binder due to high amorphous content; the SCFS were used as aggregate. The FSs were activated using a 50-50 mass% 6M sodiumhydroxide-sodiumsilicate activating solution and mixed in binder/aggregate/activating solution ratios of 1/4.2/0.4. They were then pressed with a hydraulic laboratory press MIGNON SSN/EA (Nannetti) at 100 bar into 3 cuboid and 8 cylindrical shapes.

The cuboid samples were stored for 28 days at 20 °C and 60% humidity and used for compressive strength testing. Average dimensions of these samples were 50.3 ± 0.1 mm, 50.2 ± 0.1 mm, and 19.3 ± 0.4 mm. The cuboid samples were polished prior to the uniaxial compressive strength test, performed with a Schenck Trebel apparatus with head displacement of 1 mm/s.

The cylindrical samples were selected for experimental determination of the attenuation factor and no specific requirements of temperature and humidity were chosen for storage. The height of the cylindrical samples varied between 6.43 ± 0.05 mm and 18.86 ± 0.03 mm and these samples had a typical diameter of 50.0 ± 0.1 mm. The density of the produced FSIPs varied between 2.96 ± 0.02 g/cm^3 and 3.10 ± 0.01 g/cm^3. The highest density was observed for

the thickest samples. The density was calculated from the dimensions, measured with a Vernier caliper (precision of 0.03 mm) or Mitutoyo Micrometer (precision of 0.001 mm), and the mass with an analytical balance (Sartorius MSX (SE EA)) (precision of 0.1 mg).

From the produced batch, 1 sample was milled by means of a mortar and pestle. XRF-analysis was performed on this powder by Vlaamse Instelling Technologisch Onderzoek (VITO) (Mol, Belgium) using the same instrument as mentioned in Section 3.2.2.

3.3.3. Compressive Strength

The compressive strength is the tension which a material can withstand when a pressure load tends to reduce its size. The compressive strength is measured by compressing a sample from both sides until it breaks. The compressive strength will reach a maximum before breaking. The compressive strength tests were performed with a Schenck Trebel apparatus with head displacement of 1 mm/s. All samples were polished prior to the uni-axial compressive strength test.

3.3.4. XRD Analysis

The mineral composition of the WQFS and SCFS was determined using X-ray diffraction (XRD). The sample for XRD analysis consisted of 2.7 g of each slag samples (<160 µm) and 0.3 g of Al_2O_3 standard. This sample was further crushed using a McCrone micronising mill for 5 min. Ethanol was used to prevent sticking of the slag to the plastic container wall. After milling, the XRD sample was transferred to a ceramic bowl by rinsing the milling containers with ethanol. The ethanol evaporated at room temperature leaving behind a fine powder which was analysed by a Philips Analytical PW 1710 diffractometer with Cu Kα radiation operating at 45 kV and 30 mA. The measurement included a stepwise scan over a range of 5-70° 2θ with steps of 0.02° 2θ per 2 seconds. Qualitative analysis was performed by "X'pert HighScore Plus" PANalytical software (PANalytical, Almelo, The Netherlands). Quantitative results were obtained adopting the Rietveld method using the "Topas® Academic" software.

3.4. Gamma-Ray Spectrometry

In order to quantify the activity concentration of NORs present in a sample gamma-ray spectrometry was used. Gamma-ray spectrometry is a non-destructive method by which one can choose to measure samples with none or very simple sample preparation techniques. The gamma-ray spectra of NORs-containing samples are usually complex due to the long decay chains and some radionuclides with many gamma-rays. In order to unambiguously identify the different radionuclides, a high resolution spectrum is required, which allows resolving gamma-lines separated by only a keV or two. Consequently, high-

purity germanium (HPGe) detectors were used, being the most suitable instrument for this purpose and with a resolution more than a factor 10 superior to e.g. $LaBr_3$ or NaI-detectors.

Chapter 4 and 5 describes work that involved measuring radionuclides occurring in the natural decay series of ^{238}U and ^{232}Th as well as ^{235}U and ^{40}K. The measured nuclides and their corresponding energies and probabilities of gamma emission and the technical aspects of the measurement are provided in the corresponding chapters. In what follows an overview and additional information (not described in Chapter 4 and 5) is provided with respect to the methodology used for the analysis.

3.4.1. Activity Concentration Formula

The activity of the listed radionuclides is calculated based on individual selected gamma-rays (*i*) of the radionuclides (*x*) using the following formula:

$$A_{ix} = \frac{C_{TOT\,i} - C_{Bkg\,i} - C_{Continuum\,i}}{\varepsilon_{ref_i}^{exp} \frac{\varepsilon_{sample_i}^{MC}}{\varepsilon_{ref_i}^{MC}} P_{\gamma i} t_l} \cdot e^{\lambda_x t_d} \cdot \frac{\lambda_x t_m}{1 - e^{-\lambda_x t_m}} \cdot K_{\mathrm{CS}} \cdot K_{\mathrm{BC}} K_{\mathrm{EC}}$$

Equation 3-2

where C_{TOT} is the number of counts in the peak of gamma-ray *i* (plus the continuum under the peak) in the sample spectrum, C_{Bkg} is the number of counts of the same peak in the background spectrum of gamma-ray *i*, $C_{Continuum}$ is the number of counts in the continuum under the peak in the sample spectrum of gamma-ray *i*, λ is the decay constant, P_γ is the gamma-ray emission probability, t_l, the live time, t_d, the decay time (i.e. the time between the measurement date and the reference date), t_m, the real time (the coordinated universal time (UCT)) of the measurement, ε *is* the full energy peak (FEP) efficiency either calculated using Monte Carlo (MC) simulation or determined experimentally (exp) on a sample or a reference (ref), K_{CS} is the coincidence summing correction factor, K_{BC} *is* the branching correction factor and K_{EC} is the equilibrium correction factor. The activity concentration is obtained by dividing the activity by the mass of the sample and is expressed in Bq/kg.

For each radionuclide with multiple gamma-rays, a weighted mean was calculated taken into account the activity of the different gamma-rays. The nuclear decay data originates from the database of the Decay Data Evaluation Project (DDEP), which is hosted at the website of Laboratoire National Henri Becquerel [3]. This database provides continuously updated information on the gamma emission lines of a wide range of radionuclides. It is the recommended database by the ICRM (International Committee for Radionuclide Metrology) due

to the "advanced" evaluation procedures which includes e.g. expert assessment of the quality of a reported measurement and its uncertainty budget.

3.4.2. Uncertainty on the Activity Concentration Calculation

In the uncertainty calculation on the activity (ΔA) for a single gamma-ray a difference was made between type A and type B uncertainties [4]. Type A uncertainties are due to counting statistics whereas type B uncertainties are uncertainty estimates from another source of uncertainty e.g. from calibration sources or manufacturer's specifications. As a consequence of Equation 3-2 (and neglecting the uncertainty of the decay corrections), the uncertainty of the massic activity was calculated as the root sum of the squares of the relative type A and relative type B uncertainty. No correlation was taken into account between the uncertainties.

$$\Delta A = A \cdot \sqrt{\left(\Delta A^{rel}_{type\ A}\right)^2 + \left(\Delta A^{rel}_{type\ B}\right)^2}$$

Equation 3-3

Type A uncertainties ($\Delta A_{type\ A}$):

$$\Delta A_{type\ A} = \sqrt{\sum_j \left(\delta_{j\ type\ A}\right)^2}$$

Equation 3-4

with j as being the statistical uncertainty on the counts. $\sqrt{\left(\delta N_{sample}\right)^2 + \left(\delta N_{background}\right)^2}$

Equation 3-5

Type B uncertainties ($\Delta A_{type\ B}$):

$$\Delta A_{type\ B} = A \cdot \sqrt{\sum_j \left(\delta^{rel}_{j\ type\ B}\right)^2}$$

Equation 3-6

with j as being the uncertainty on the mass sample, uncertainty on the measurement time, uncertainty on the full energy peak efficiency, uncertainty on radionuclide half-life $T_{1/2}$, uncertainty on the emission probability P_γ. It must

be noted that uncertainty of the decay during the measurement was neglected when measuring long-lived radionuclides.

In case a radionuclide has more than one gamma-ray, which was used in the activity calculation; the weighted mean activity *A'* was reported. The weighted mean activity *A'* calculation, for a given radionuclide with (N) gamma-rays is:

(N) activities: $A^1, A^2, \dots, A^i, \dots, A^N$

(N) $\Delta A_{type\ A}$: $\Delta A^1_{type\ A}, \Delta A^2_{type\ A}, \dots, \Delta A^i_{type\ A}, \dots, \Delta A^N_{type\ A}$

(N) $\Delta A_{type\ B}$: $\Delta A^1_{type\ B}, \Delta A^2_{type\ B}, \dots, \Delta A^i_{type\ B}, \dots, \Delta A^N_{type\ B}$

$$A' = \frac{\sum_{i=1}^{i=N} A_i \cdot \left(\frac{1}{\Delta A^i_{type\ A}}\right)^2}{\sum_{i=1}^{i=N} \left(\frac{1}{\Delta A^i_{type\ A}}\right)^2}$$

Equation 3-7

Equation 3-7 calculates the weighted mean activity concentration with the inverse of the statistical uncertainty of each peak as a weighting factor in order to limit the contribution of small peaks with high uncertainties.

The total uncertainty of the weighted mean activity concentration of a radionuclide was calculated as the root sum of squares of the type A and type B uncertainty (Equation 3-8).

$$\Delta A' = A' \cdot \sqrt{\left(\Delta A'^{rel}_{type\ A}\right)^2 + \left(\Delta A'^{rel}_{type\ B}\right)^2}$$

Equation 3-8

With

$$\Delta A'_{type\ A} = \sqrt{\frac{1}{\sum_{i=1}^{i=N} \left(\frac{1}{\Delta A^i_{type\ A}}\right)^2}}$$

Equation 3-9

The type A uncertainty of the weighted mean activity concentration is shown in Equation 3-9. The sum of the inverse of the type A activity concentrations was taken in in order to limit the contribution of small peaks with high uncertainties.

$$\Delta A'_{type\ B} = Min_{i=1}^{i=N}\left(\Delta A^{i}_{type\ B}\right)$$

Equation 3-10

In Equation 3-10 the type B uncertainty on the weighted mean activity concentration was the minimum observed uncertainty of the type B uncertainty of N gamma-rays. The minimum was taken in order to not obtain too large and unrealistic uncertainties.

In case the uncertainty calculation of a mother radionuclide was calculated from different daughter radionuclides, the weighted mean calculation and uncertainty calculation was performed as for a radionuclide with different gamma emission lines. So the weighted mean activity A' calculation, for a given mother radionuclide with (N) daughter radionuclides was calculated via Equation 3-7, with the activities of (N) daughter radionuclides: $A^1, A^2, \dots, A^i, \dots, A^N$. Equation 3-8 to Equation 3-10 were used for the uncertainty calculations of the activity concentration.

3.4.3. Measurement of Sample

The activity concentration of samples was determined via gamma-ray spectrometry. For this measurement technique, knowledge of the geometry, composition and density of the sample were crucial in order to obtain accurate results. In order to obtain a well-defined sample geometry, samples are milled to a fine powder and dried. The powder was then transferred to a radon tight Teflon® container and stored. Measurement of the sample was done at least 21 days after storage in order to reach secular equilibrium between ^{226}Ra and its daughters. After this period the sample was ready for measurement and was placed on a holder on top of the endcap of the detector. The technical characteristics of the detectors are provided in Chapter 4 and 5.

Canberra's Genie 2000 software was used for acquiring and analysing the energy spectrum of a sample. The acquired spectrum was analyzed using a combination of the Canberra Genie 2000 software and the "GLysis" calculation sheet developed by Lutter et al. 2017 [5] (see Section 3.4.5). Using Genie 2000 the peaks were located in the spectrum using the "Unidentified 2nd difference" method. In this method an algorithm calculates a significance value for each considered peak. Peaks which exceed a set significance threshold are selected. The significance value of the peak is higher when the peak is larger with respect to the continuum. This method is best suited for cases in which the expected peaks in the spectrum are unknown. A search region was defined in which all possible peaks were distinguished from the continuum based on the 2nd difference function.

Next the "Sum/non-linear least squares fit" method of Genie 2000 determined the peak's region limits together with the region of interest. The method also identifies if a peak is a single peak or is part of a multiplet. Next the net peak area was determined by subtracting the continuum (the background is subtracted in a later phase). Then, the "interactive peak fit" software of Genie 2000 was used to inspect and, if necessary, corrected the fit provided by Genie 2000. This function also allows deconvolutionizing peaks and adding peaks which were not identified by the peak locate function.

3.4.4. Full Energy Peak (FEP) Efficiency Calculation

Not all the gamma-rays emitted by the source reach the detector and deposit all their energy in the active media (here germanium) of the detector. Consequently, only a fraction of the emitted gamma-rays were registered in the detector which is taken into account by the full energy peak (FEP) efficiency, ε_{FEP}, as shown in Equation 3-11. The FEP efficiency can be derived from Equation 3-2 by solving it for ε_{ref}^{exp} and assuming all other parameters are known. By neglecting effects like decay during measurement, coincidence summing etc., one can formulate an expression in a simplified way. It is the ratio between the count rate, *CR*, in the FEP and the activity of the radionuclide, *A*, that emits those gamma rays. The emission probability (P_γ) of the corresponding gamma ray needs to be taken into account in the denominator of Equation 3-11. Consequently, the FEP efficiency is energy dependent and needs to be determined for each gamma-ray energy. In addition, the geometry of the whole measurement set-up, as well as the properties of the sample affect the FEP efficiency.

$$\varepsilon_{FEP} = \frac{CR}{A\,P_\gamma}$$

Equation 3-11

The FEP efficiency can be calculated by means of a matrix equivalent reference source, i.e. a source with the exact same characteristics (density, chemical composition and geometry) as the measured sample. Obtaining or producing sources that resemble the sample can be difficult or labor-intensive to achieve. Another method to obtain the FEP efficiency of the measured sample is by means of MC simulations and was used here. The complete measurement set-up per sample was simulated using a computer model that includes the detector, sample, sample container and shield. The simulation as performed for the radionuclides of interest taking into account their decay schemes. Performing MC simulations requires a high calculation power as a high number of events need to be simulated to obtain proper counting statistics (preferentially statistical uncertainty <1%). In Chapter 4 and 5 the MC simulations are calculated via the "hpge3" code using the Electron Gamma-ray Shower National Research Council

of Canada (EGSnrc) Monte Carlo code framework [5,6]. Hpge3 was developed by Lutter et al. (2017) and offers a validated MC simulation approach [5]. EGSnrc simulates the transport of electrons and photons and allows using C++ packages to construct the measurement set-up (detector, shield, sample, sample container) [5,6]. Figure 3-2 shows the code written to describe the geometry of a Teflon® sample container and a bauxite sample i.e. the model file. A separate material file described the chemical composition and density of the media – in Figure 3-2 the media is "Bauxite" for the bauxite sample.

```
#Container139
    :start geometry:
        library = egs_cones
        type    = EGS_ConeStack
        axis    = 0.0 0.0 0.0 0.0 0.0 1.0
        name    = Container
        :start layer:
            thickness   = 0.2
            top radii   = 3.83
            bottom radii    = 3.83
            media       = TEFLON
        :stop layer:
        :start layer:
            thickness   = 3.8
            top radii   = 2.5325 3.83
            bottom radii    = 2.5325 3.83
            media       = AIR521ICRU TEFLON
        :stop layer:
        :start layer:
            thickness   = 0.5
            top radii   = 3.83
            bottom radii    = 3.83
            media       = TEFLON
        :stop layer:
    :stop geometry:

#Sample Bauxite
   :start geometry:
        library = egs_cones
        type    = EGS_ConeStack
    axis    = 0.0 0.0 0.2 0.0 0.0 1.0
    name = BAUXITE
        :start layer:
            thickness    = 3.8
            top radii    = 2.5325
            bottom radii = 2.5325
        media        = Bauxite
        :stop layer:
   :stop geometry:
```

Figure 3-2: Screenshot of code of model file to describe the geometry of the different components of a gamma-ray measurement set-up.

Figure 3-3 shows the home screen of the material file composer (i.e. the pegs data file composer) in which sample composition and density can be defined. This file contains the details behind the defined media of Figure 3-2. Such material file was constructed per component of the measurement set-up.

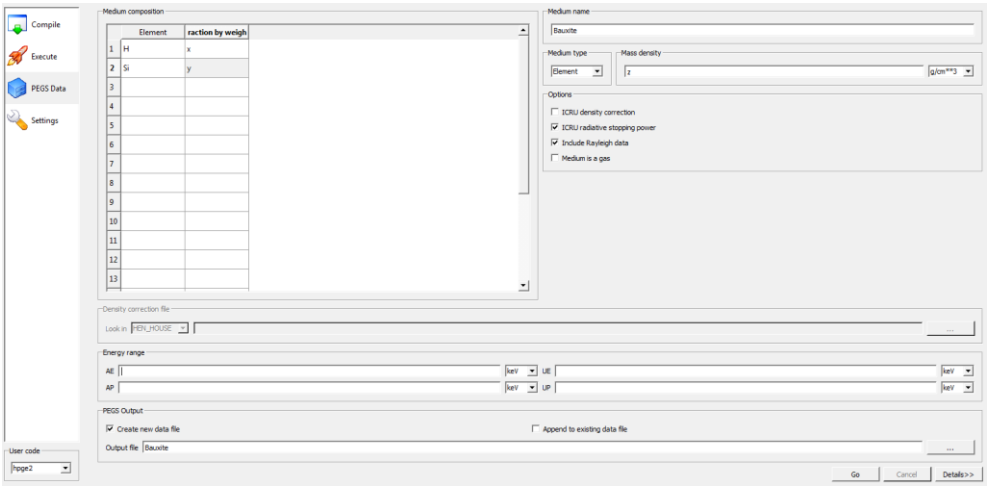

Figure 3-3: Screenshot of home screen of the material file composer (i.e. pegs data file composer).

A graphical scheme of the T5 detector set-up, based on the model file, is shown in Figure 3-4. Each individual media has an individual color code in Figure 3-4. In the code also a source was described. For example in Figure 3-5 the source is "Bauxite" and the active material is "Germanium". Here, the simulation of the source occurs isotropic and uncorrelated meaning that source will emit gamma-rays in all directions from different points in the defined source region and the direction of one gamma-ray has no influence on the direction of other gamma-rays from the same decay.

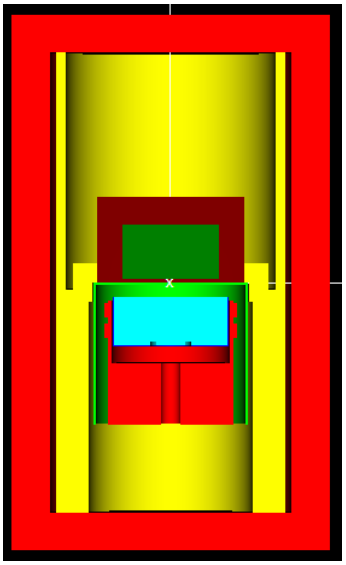

Figure 3-4: EGSnrc MC simulation of HPGe detector set-up "T5".

```
:start source definition:
    :start source:
    library = egs_isotropic_source
    name = Bauxite
        :start shape:
            type = cylinder
            radius = 2.5325
            height = 3.8
            midpoint = 0.0 0.0 2.1
        :stop shape:
        charge = 0
    :start spectrum:
            type = decay
            nucl = Bi214
    :stop spectrum:
    :stop source:

    simulation source = Bauxite
:stop source definition:

:start active material definition:
     name = Germanium
:stop active material definition:
```

Figure 3-5: Screenshot of code of model file to describe the source volume (here bauxite) and the active volume (here germanium) of the gamma-ray measurement set-up.

Figure 3-6 shows that the starting point - represented by black dots - of the gamma-rays are chosen random in the source region. In addition, also an active material was defined. In the active material the deposited energy originating from a gamma-ray was registered, taken the characteristics of the active material into account.

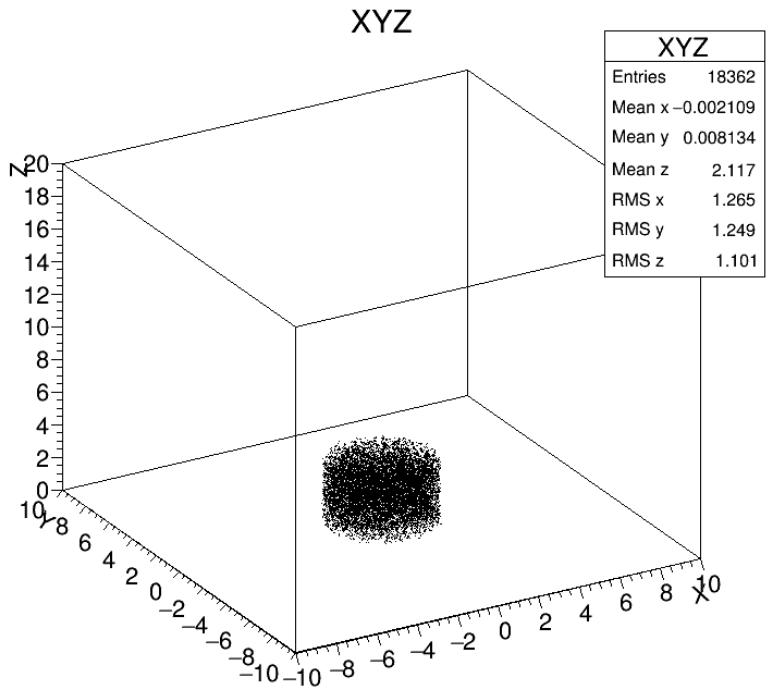

Figure 3-6: Graphical representation of the starting points, represented by black dots, in the disk- or cylinder-shaped source volume. Here 1000 events are simulated.

3.4.5. Calculation of the Activity Concentration

The data obtained via the spectrum analysis and efficiency calculation was imported in a dedicated MS Excel® based calculation sheet developed by Lutter et al. (2017), named "GLysis" [5]. Both the sample's spectrum as well as the background spectrum were imported. The background spectrum was subtracted from the sample's spectrum. Prior to subtraction, the background spectrum was normalized to match the measurement time of the sample's spectrum. GLysis contains a database with nuclear information, coming from the Decay Data Evaluation Project (DDEP) website, regarding radionuclides relevant for measurement of environmental samples [3]. GLysis allows the user selecting only the radionuclides of the user's interest and generates a sample specific analysis sheets, using the aforementioned information to calculate the massic

activity and uncertainty for each gamma line and radionuclide of interest. This sheet allows the user to manually update the information when needed (for example in case of interferences). All calculations were performed according to the ISO11929 2010 version. A full description of the GLysis analysis sheet is outside the scope of this thesis and can be found in Lutter et al. (2017) [5].

The measured nuclides and their corresponding energies and probabilities of gamma emission are mentioned in the corresponding Chapters 4 and 5.

3.5. References

[1] European Commission, Laying down basic safety standards for protection against the dangers arising from exposure to ionising radiation, and repealing directives 89/618/Euratom, 90/641/Euratom, 96/29/Euratom, 97/43/Euratom and 2003/122/Euratom, Off. J. Eur. Union. (2014) 1–73.

[2] ISO, ISO 80000-10 Quantities and units - part 10: Atomic and nuclear physiscs Grandeurs et unités - Partie 10: Physique atomique et nucléaire, 2009.

[3] Laboratoire national Henri Becquerel, Decay Data Evaluation Project, (2016). http://www.nucleide.org/DDEP.htm (accessed May 22, 2016).

[4] S. Bell, A Beginner's Guide to Uncertainty of Measurement, Meas. Good Pract. Guid. 11 (2001) 1–33.

[5] G. Lutter, M. Hult, F. Tzika, H. Stroh, G. Marissen, Gamma-ray spectrometry analysis software environment, Appl. Radiat. Isot. (2017) 1–5. doi:10.1016/j.apradiso.2017.06.045.

[6] I. Kawrakow, E. Mainegra-Hing, F. Tessier, B.R.B. Walters, The EGSnrc C++ class library, NRC Rep. PIRS-898 (Rev A). (2009).

Chapter 4: Radiological Characterization and Evaluation of High Volume Bauxite Residue Alkali Activated Concretes

The results of this chapter have been published:

T. Croymans, W. Schroeyers, P. Krivenko, O. Kovalchuk, A. Pasko, M. Hult, G. Marissens, G. Lutter, S. Schreurs, Radiological characterization and evaluation of high volume bauxite residue alkali activated concretes, J. Environ. Radioact. 168 (2017) 21–29.

Link with objectives: This chapter fits within objectives 1 and 2 of this thesis and is focused on bauxite residue (BR). The activity concentrations (ACs) of the decay series of ^{238}U, ^{235}U and ^{232}Th and ^{40}K were determined and used as input to assess the occupational exposure for construction workers constructing roads and building. In addition, the public exposure for the concretes used as road and as housing was assessed based on the determined activity concentrations. Based on this radiological assessment recommendations were made towards the usage of these BR concretes from a radiation protection point of view.

4.1. Abstract

Bauxite residue (BR), also known as red mud, can be used as an aggregate in concrete products. The study involves the radiological characterization of different types of concretes containing bauxite residue from Ukraine. The activity concentrations of radionuclides from the ^{238}U, ^{232}Th decay series and ^{40}K were determined for concrete mixture samples incorporating 30, 40, 50, 60, 75, 85 and 90 mass% of bauxite residue using gamma-ray spectrometry with a HPGe detector. The studied bauxite residue can, from a radiological point of view using activity concentration indexes developed by Markkanen, be used in concrete for building materials and in road construction, even in percentages reaching 90 mass%. However, when also occupational exposure is considered it is recommended to incorporate up to 60 mass% of Ukrainian bauxite residue for the construction of buildings in order to keep the dose to workers below the dose criterion used by Radiation Protection (RP-) 122 (0.3 mSv/a). Considering RP-122 for evaluation of the total effective dose to workers no restrictions are required for the use of the Ukrainian bauxite residue in road construction.

References at page 113

4.2. Introduction

Bauxite residue, also known as red mud, is a major by-product that is produced during the refining of the aluminum ore by means of the Bayer process. For every tonne of alumina produced, 1-1.5 tonnes of bauxite residue is generated. It is estimated that about 120 million tonnes of bauxite residue were produced worldwide in 2007 [1]. In China alone, about 30 million tonnes of bauxite residue was generated in 2009, of which only 4 % was utilized [2]. The disposal-costs may add up to 5 % of the alumina production cost [3]. Furthermore, improper storage of bauxite residue can lead to harmful contamination of water, land and air in the surrounding area because of its high alkalinity. Strong environmental concerns are linked to the disposal of bauxite residue. The treatment and utilization of bauxite residue is both of environmental and economic significance.

In recent years, many studies have investigated different application possibilities for bauxite residue. Several studies focus on the reuse of bauxite residue as an additive for construction materials and among other on the use in ceramics cements [4–11]. However, due to low chemical activity of bauxite residue its application in membranes is limited and in several cases, an energy intensive preliminary pre-treatment is required [4,5].

Early studies already reported that the use of alkali activation can allow for a considerable increase in bauxite residue incorporation rates for cements and concretes without reducing their physio- mechanical characteristics [12–14]. The properties of alkali activated cements and concretes are highly competitive to traditional cement concretes.

To make the reuse practices economically viable, a sufficiently high fraction of bauxite residue needs to be incorporated in the concrete. In the current work it is demonstrated that it becomes possible to formulate high volume bauxite residue alkali activated cements and concretes with incorporation rates of bauxite residue in the concretes reaching 90 mass%.

An important aspect that needs to be dealt with when incorporating larger percentages of bauxite residue in concrete, concerns the radiological properties. The UNSCEAR report (2000) reported activity concentrations for the bauxite ore of 400 to 600 Bq/kg for individual radionuclides from the ^{238}U-series and 300 to 400 Bq/kg for individual radionuclides from ^{232}Th-series. For Hungarian bauxite ore, activity concentrations up to 800 Bq/kg ^{226}Ra and up to 500 Bq/kg ^{232}Th were published [15,16]. The average activity concentrations of bauxite residues produced in several European and non-European countries were reported by Nuccetelli et al. (2015) [17]. For the considered bauxite residues, an overall average activity concentration of 340 Bq/kg ^{226}Ra, 480 Bq/kg ^{232}Th and 210 Bq/kg ^{40}K was obtained. For Ukrainian bauxite residue, activity concentrations of

160 Bq/kg ^{226}Ra, 330 Bq/kg ^{232}Th and 53 Bq/kg ^{40}K were reported [18]. In general, most authors consider the activity concentrations of ^{226}Ra, ^{232}Th and ^{40}K for the radiological evaluation of bauxite residue and construction materials based on the bauxite residue [16,19–24]. Other radionuclides in the decay chains are rarely evaluated to assess the secular equilibrium in the decay chains. Since for NORM containing construction materials in general the secular equilibrium will be disturbed this aspect will be dealt with in this study in detail by analyzing a broad selection of radionuclides using gamma spectrometric analysis.

For the synthesized concretes based on bauxite residue aggregates the current work aims to investigate the radiological properties in order to control and prevent radiological problems upon large scale application. Therefore, this study will verify if the reuse meets the requirements of the new Euratom basic safety standards (EU-BSS) and occurs according to the principles set by the construction products regulations (CPR) [25]. The EU-BSS covers the issue of naturally occurring radioactive materials (NORM) in industrial applications and the reuse of by-products from NORM processing industries in building materials. The EU-BSS uses an index developed by Markkanen (1995) for the screening and evaluation of the public exposure from building materials that are permanently incorporated in buildings [26]. The CPR lays down essential requirements for construction works in general. According to the CPR, the construction works must be designed and built in such a way that the emission of dangerous radiation will not be a threat to the health of the occupant or neighbors. Methodology for dose assessment and classification of construction materials in view of their gamma emitting properties, linked to the implementation of the CPR, is still under development. Markkanen (1995) proposed another index specifically to evaluate the exposure to the public caused by "materials used for constructing streets and playgrounds" [26]. Both indexes, developed by Markkanen and part of the Finnish legislation on natural radiation, are used to assess the public exposure and will be used in the current study [27]. For the evaluation of the occupational exposure this study will follow the approach proposed by Radiation Protection (RP-) 122 part II [28].

4.3. Materials and Methods

4.3.1. Description of the Studied Concrete Samples and their Constituents

Cylindrical concrete specimens (d= typically 50 mm for P-series samples and typically 46 mm for C-series samples; h= typically 30 mm for P-series and typically 37 mm for C-series) with various incorporation rates of bauxite residue were prepared. Bauxite residue, in its state as it was produced as part of fine aggregate to produce alkali activated concrete, was incorporated directly in the

specimen. In both casted (C-series) and semi-pressed (P-series) concrete specimens the aluminosilicate component was represented by a granulated blast-furnace slag with basicity modulus of 1 and content of glassy phase of 80 %. The compositions of concrete mixtures produced by the semi-dry pressing technique (P1 – P5) and by the high slump casting technique (C1-C4) are given in Table 4-1. The pressing technique allows production of prefabricated products like tiles, bricks, etc. The casting technique allows production of pre-casted and on-site casted construction materials and is often applied for concrete structures on the basis of Portland cement and concrete. The different types of samples are representative for the most common ways that concretes are produced and applied. Two different samples with the same red mud bauxite concentration (P5 and C3 contain both 40 mass% red mud; P4 and C2 contain both 50 mass% red mud) were characterized by gamma-ray spectrometry to demonstrate that the impact of the production (casting or pressing) method is negligible from a radiological point of view.

A cement of the following composition was chosen: 87 mass% slag (Ground-granulated blast-furnace slag), 5 mass% ordinary Portland Cement (OPC), 4 mass% Na_2CO_3 and 4 mass% $Na_2O{\cdot}SiO_2{\cdot}5H_2O$. All cement constituents were milled until a Blaine fineness of 350-450 m^2/kg (specific surface) was obtained.

Bauxite residue from Ukraine was used in the experiments. It has the following mineralogical composition: 25-27 % hematite, 25-28 % goethite, 4.5-6.5 % rutile and anatase, 15-17 % hydrogarnets, 6-7 % sodium aluminosilicate hydrate and 2.5-3.0 % calcite.

Local river sand with maximum grain size of 1.2 mm and bauxite residue with particle sizes varying from 50 to 1000 μm were used as aggregates.

Table 4-1: Concrete mixture design for semi-dry pressing (P=30 MPa) and slump casting.

	Concrete mixture design, mass%; (100 % corresponds to dry mass)				
Sample	**Cement**	**Bauxite red mud**	**Sand**	**H_2O**	**Compressive strength (MPa)**
P1	10	90	-	17	6.78
P2	15	85	-	17	5.45
P3	25	75	-	16	5.05
P4	25	50	25	14	10
P5	25	40	35	12	14
C1	25	60	15	32.5	15
C2	25	50	25	25.5	17.5
C3	25	40	35	23.5	23.5
C4	25	30	45	11.25	25

4.3.2. Radiological Analysis

Bauxite residue samples for gamma-ray spectrometry were transferred to radon tight Teflon® containers and stored for at least 21 days for secular equilibrium to be established between ^{226}Ra and its daughters. The sample mass ranged from 111 to 136 g (dry mass). The sample density ranged from 1.9 to 2.2 g/cm^3. The sample containers were positioned on a holder 11.4 mm from the top of a HPGe-detector. This detector is located in the above ground Radionuclide Metrology Laboratory at the European Commission's Joint Research Centre in Geel, Belgium. The HPGe detector is a coaxial detector with a relative efficiency of 46 % (FWHM: 1.41 at 662 keV and 1.86 at 1332 keV) with a shield composed of 4 mm Cu and 10 cm low-activity Pb. The measured percent dead time ranged from 0.02 % to 0.04 % for all samples. The samples were measured for a period ranging from 3 to 8 days.

Data acquisition and spectrum analysis were performed using Canberra's Genie 2000 software. The full energy peak efficiencies, ε, were calculated using Monte Carlo simulations with the EGSnrc Monte Carlo code [29]. The computer model of the detector has been validated through participation in proficiency testing exercises. The model uses measured dimensions of the sample, composition of the sample and the detector as input. The simulations assume that the gamma-ray emissions are isotropic and uncorrelated. All calculations assume that the radionuclides are homogeneously distributed in the sample and that the sample material is homogeneously distributed in the sample container. The use of Monte Carlo calculations has the additional benefit that the correction for coincidence

summing which occurs in decays with cascading gamma-rays is obtained in the same calculation as the FEP efficiency.

Gamma-rays emitted by the radionuclides occurring in natural decay series of ^{238}U and ^{232}Th as well as ^{235}U and ^{40}K were investigated. An overview of the investigated emission lines is given in Table 4-2. For each radionuclide with multiple gamma-rays, a weighted mean of the activity was calculated taking into account the activity of the different gamma-rays. The nuclear decay data were taken from the Decay Data Evaluation Project (DDEP) tables [30]. The ^{208}Tl activity has been divided with the branching factor (0.3594).

The 186 keV peak is a doublet with contributions from ^{235}U and ^{226}Ra. The activity of ^{235}U is calculated after subtracting the contribution from ^{226}Ra to the 186 keV peak. The ^{226}Ra activity was determined by its daughters, ^{214}Pb and ^{214}Bi. The activity concentration (in this paper meaning the activity per unit mass) was determined by dividing the final activity determined for each radionuclide (the mother radionuclide in cases with short-lived daughters) by the measured dry mass of the sample.

The uncertainties of the obtained activity concentrations are the combined standard uncertainties calculated according to the Guide to the expression of uncertainty in measurement (GUM) [31]. When combining several gamma-rays to one radionuclide and several daughters to one mother radionuclide using weighted means, the correlated parameters were added separately in quadrature in order not to obtain unrealistic and far too low final uncertainties.

Table 4-2: Overview of the investigated gamma lines with data obtained from DDEP [30].

Nuclide	Energy (keV)	Emission probability (%)	Nuclide	Energy (keV)	Emission probability (%)
^{234}Th	63.3	3.75	^{228}Ac	209.248	3.97
	92.38	2.18		328.004	3.04
	92.8	2.15		409.46	2.02
^{234m}Pa	766.361	0.323		463.002	4.45
	1001.026	0.847		755.313	1.03
^{214}Pb	241.997	7.268		772.291	1.52
	295.224	18.414		794.942	4.31
	351.932	35.6		911.196	26.2
^{214}Bi	609.312	45.49		968.96	15.9
	768.356	4.892		1588.2	3.06
	806.174	1.262		1630.618	1.52
	934.061	3.1	^{224}Ra	240.986	4.12
	1120.287	14.91	^{212}Pb	238.632	43.6
	1155.19	1.635	^{212}Bi	1620.738	1.51
	1238.111	5.831	^{208}Tl	277.37	6.6
	1280.96	1.435		583.187	85
	1377.669	3.968		763.45	1.8
	1401.5	1.33		860.53	12.4
	1407.98	2.389		2614.511	99.755
	1509.228	2.128	^{235}U	143.767	10.94
	1729.595	2.844		185.72	57
	1764.494	15.31		163.356	5.08
	1847.42	2.025		205.316	5.02
	2118.55	1.158	^{40}K	1460.822	10.55
	2204.21	4.913	^{137}Cs	661.652	84.99
	2447.86	1.548			
^{210}Pb	46.539	4.252			

4.3.3. Activity Concentration Indexes as Screening Tools for Public Exposure

The activity concentration index for building materials (ACI_{BM}), proposed by Markkanen and implemented in the council directive 2013/59/EURATOM (EU-BSS), is calculated using the activity concentration of ^{226}Ra, ^{232}Th and ^{40}K (Equation 4-1) [26,32]. The activity concentration index for materials used for streets and playgrounds (ACI_{SP}), as defined by Markkanen, is calculated using the activity concentration of ^{226}Ra, ^{232}Th, ^{40}K and ^{137}Cs (Equation 4-2) [26]. More information on the models used for both indexes is shown in Table 4-3. Note that an $ACI_{BM} > 1$ indicates an effective gamma dose larger than 1 mSv/a whereas an ACI_{SP} indicates an effective gamma dose larger than 0.1 mSv/a: both indexes were designed for different dose models. To calculate the ACIs secular equilibrium is assumed between ^{232}Th and ^{228}Ra and between ^{226}Ra and its two daughters ^{214}Pb and ^{214}Bi. The used activity concentration of ^{232}Th is in reality the activity concentration of ^{228}Ac and the activity concentration of ^{226}Ra is in reality the weighted mean between the activity concentrations of ^{214}Pb and ^{214}Bi. ^{40}K and ^{137}Cs were directly measured using their respective gamma emission lines at 1460.8 keV and 661.6 keV.

$$ACI_{BM} = \frac{AC_{226Ra}}{300\ Bq/kg} + \frac{AC_{232Th}}{200\ Bq/kg} + \frac{AC_{40K}}{3000\ Bq/kg}$$

Equation 4-1

$$ACI_{SP} = \frac{AC_{226Ra}}{700\ Bq/kg} + \frac{AC_{232Th}}{500\ Bq/kg} + \frac{AC_{40K}}{8000\ Bq/kg} + \frac{AC_{137Cs}}{2000\ Bq/kg}$$

Equation 4-2

With AC as activity concentration of the mentioned radionuclide expressed in Bq/kg.

The uncertainty on the activity concentration indexes (Δ) is calculated using Equation 4-3 and Equation 4-4.

$$\Delta(ACI_{BM}) = \sqrt{\left(\frac{1}{300}\right)^2 \Delta(Ac_{226Ra})^2 + \left(\frac{1}{200}\right)^2 \Delta(Ac_{232Th})^2 + \left(\frac{1}{3000}\right)^2 \Delta(Ac_{40K})^2}$$

Equation 4-3

$$\Delta(ACI_{SP}) = \sqrt{\left(\frac{1}{700}\right)^2 \Delta(AC_{226Ra})^2 + \left(\frac{1}{500}\right)^2 \Delta(AC_{232Th})^2 + \left(\frac{1}{8000}\right)^2 \Delta(AC_{40K})^2 + \left(\frac{1}{2000}\right)^2 \Delta(AC_{137Cs})^2}$$

Equation 4-4

Where $\Delta(AC_{226Ra})$ is the uncertainty on the activity concentration of ^{226}Ra, $\Delta(AC_{232Th})$ is the uncertainty on the activity concentration of ^{232}Th, $\Delta(AC_{40K})$ is the uncertainty on the activity concentration of ^{40}K, and $\Delta(AC_{137Cs})$ is the uncertainty on the activity concentration of ^{137}Cs.

4.3.4. Dose Assessment for Occupational Exposure

Following RP-122 (part II) dose assessments were performed that consider the impact of concrete containing bauxite residues following different scenarios for workers active in building construction and road construction. All calculations of the different scenarios were performed using the NIRS (Japanese National Institute on Radiological Sciences) database dose assessment tool [33]. The scenarios named in part 4.2. of RP-122 part II as "4.2.6. Road constructions" and "Building construction with NORM containing building materials" are listed on the NIRS website as "Road construction" and "Building construction", respectively, under "Dose assessment for workers who handle NORM (including ores and building materials)" [28]. Each scenario is characterized by specific parameters listed in Table 4-3. In both scenarios the highest activity concentrations of all measured radionuclides from the ^{238}U decay series, from ^{232}Th decay series and for ^{40}K were taken for different percentages of incorporated bauxite residue. RP-122 uses as dose criterion 0.3 mSv/year. In this case the total effective dose (external, inhalation and ingestion dose) is calculated.

Important sources of uncertainty in the dose analysis are the uncertainty on the occupation time, on the dust concentration and on the ingestion rate which are unknown. The models used for the dose assessment are simplified models that do not correspond to actual situations. The uncertainty shown in the results originates from the uncertainty on the activity concentration of the selected radionuclide with the highest activity concentration.

Table 4-3: Field of application and relevant parameters that define the underlying models for the activity concentration indexes and the dose assessments based on RP-122.

	ACI_{BM}	**ACI_{SP}**	**RP-122 BC**	**RP-122 RC**
Geometry	Floor, ceiling, 4 walls	Plane	Floor, ceiling, 2 walls	Plane
Size geometry (m)	4 x 5 x 2.8 with thickness 0.2*	20 x 20 Thickness not specified	3 x 4 x 2.5 with thickness 0.2	100 x 10 with thickness 0.4
Density (kg/m^3)	2350	2350	2300	2000
Dilution factor	/	/	1	1
Exposure time (h)	7000	500	1800	1800
Dust concentration (mg/m^3)	/	/	0.5	1
Breathing rate (m^3/h)	/	/	1.2	1.2
Direct ingestion (mg/h)	/	/	10	10
Dose criterion (mSv/y)	1	0.1	0.3	0.3
Exposure to Workers/public:	Public	Public	Workers	Workers
Field of application:	Building materials	Streets, playgrounds and roads	Building construction	Road construction
Reference(s)	EC 2014 [32]; RP-112 [34]	Markkanen (1995) [26], STUK (2010) [27]	RP-122 [28], NIRS database [33]	RP-122 [28], NIRS database [33]

* In Markkanen 1995 size is 12 x 7 x 2.8 m with thickness of 0.2 m

4.4. Results and Discussion

Even at high incorporation rates of bauxite red mud, reaching 90 mass%, the strength of the resulting concrete remains rather high (Table 4-1), allowing from a mechanical point of view to manufacture such construction products as bricks for various applications, tiles, plates, etc. using the technology of semi-dry pressing. Alternatively, concrete constructions can be precasted or made on site by the casting technique.

A stepwise approach is used for the radiological evaluation of the considered applications of the newly synthesized concretes that contain bauxite residues as an aggregate: (1) The activity concentrations of several radionuclides occurring in the natural decay series of ^{238}U and ^{232}Th as well as ^{235}U and ^{40}K were determined using gamma-ray spectrometry while monitoring the secular equilibrium. (2) Activity concentration indexes are then used for initial screening of the public exposure regarding the use of the newly produced concretes as building materials or for constructing streets and playgrounds. (3) In addition, in order to also evaluate the occupational exposure, a dose assessment for construction workers, based on RP-122 part II, is performed.

4.4.1. Study of the Activity Concentrations

As mentioned in the introduction, average activity concentrations of 165 Bq/kg ^{226}Ra, 328 Bq/kg ^{232}Th and 53 Bq/kg ^{40}K are reported in Ukrainian national studies for the Ukrainian bauxite residue [18]. The results of the gamma spectrometric analysis of bauxite residue containing concrete mixtures produced by semi-dry pressing and casting are shown in Table 4-4 and Table 4-5. When studying the ^{238}U decay series (Table 4-4) for all samples and when comparing the activity concentrations of each radionuclide to the nearest decay product measurable via gamma-ray spectrometry (^{234}Th to ^{234m}Pa; ^{234m}Pa to ^{214}Pb; ^{214}Pb to ^{214}Bi and ^{214}Bi to ^{210}Pb) secular equilibrium seems to be present in all samples when considering the measurement uncertainty. Only minor deviations from secular equilibrium can be observed in the ^{238}U decay series, for example for the sample P1, when comparing the activity concentration of ^{234}Th to the activity concentration of ^{214}Pb or ^{214}Bi. Generally speaking, for the studied concrete mixtures the whole ^{238}U decay series is in equilibrium or there are only minor deviations from equilibrium. Focusing on the ^{232}Th decay series (Table 4-5) also in this case, no disequilibrium could be observed when studying the individual samples. The uncertainty on the activity concentration of ^{212}Bi is higher in comparison with the other radionuclides of the chain. This is due to the fact that a limited number of counts is registered in the 1620.7 keV peak of ^{212}Bi, leading to limited counting statistics.

For all samples, the $^{238}U/^{235}U$ activity ratio shows no deviation from the expected value of 21.6 which indicates natural isotopic abundance. The measured ^{235}U activity concentrations are shown in Table 4-4.

In none of the samples ^{137}Cs was detected and the MDA (minimum detectable activity concentration) was in all cases below 1 Bq/kg.

Table 4-4: Activity concentrations (Bq/kg, dry mass) of radionuclides from the ^{238}U decay as well as for ^{235}U (k=2) for the 9 test samples.

Series	**^{238}U**					**^{235}U**
Sample(mass% bauxite residue)	**^{234}Th (Bq/kg)**	**^{234m}Pa (Bq/kg)**	**^{214}Pb (Bq/kg)**	**^{214}Bi (Bq/kg)**	**^{210}Pb (Bq/kg)**	**^{235}U (Bq/kg)**
P1 (90 %)	(11 ± 2)×10	(9 ± 2)×10	69 ± 8	70 ± 6	(12 ± 4)×10	3.8 ± 0.5
P2 (85 %)	(10 ± 1)×10	(8 ± 2)×10	68 ± 6	68 ± 6	(12 ± 6)×10	4.3 ± 0.5
P3 (75 %)	(9 ± 2)×10	(8 ± 2)×10	66 ± 6	66 ± 6	(12 ± 6)×10	3.8 ± 0.5
P4 (50 %)	(7 ± 1)×10	(7 ± 1)×10	53 ± 6	52 ± 4	(7 ± 2)×10	3.3 ± 0.4
P5 (40 %)	(7 ± 1)×10	(6 ± 1)×10	46 ± 4	46 ± 4	(5 ± 2)×10	2.9 ± 0.4
C1 (60 %)	(8 ± 1)×10	(7 ± 1)×10	49 ± 6	48 ± 2	(8 ± 3)×10	3.5 ± 0.4
C2 (50 %)	(7 ± 2)×10	(6 ± 1)×10	51 ± 5	49 ± 5	(6 ± 2)×10	2.6 ± 0.3
C3 (40 %)	(6 ± 1)×10	(5 ± 1)×10	42 ± 4	40 ± 4	(4 ± 2)×10	2.5 ± 0.3
C4 (30 %)	(5 ± 2)×10	(5 ± 1)×10	39 ± 4	37 ± 4	(2 ± 2)×10	1.6 ± 0.3

Table 4-5: Activity concentrations (Bq/kg, dry mass) of radionuclides from the ^{232}Th decay series as well as for ^{40}K (k=2) for the 9 test samples.

Series	**^{232}Th**					**^{40}K**
Sample(mass% bauxite residue)	**^{228}Ac (Bq/kg)**	**^{224}Ra (Bq/kg)**	**^{212}Pb (Bq/kg)**	**^{212}Bi (Bq/kg)**	**^{208}Tl (Bq/kg)**	**^{40}K (Bq/kg)**
P1 (90 %)	(12 ± 1)×10	(12 ± 1)×10	(12 ± 1)×10	(12 ± 2)×10	(12 ± 1)×10	(8 ± 2)×10
P2 (85 %)	(12 ± 1)×10	(12 ± 1)×10	(12 ± 1)×10	(11 ± 2)×10	(12 ± 1)×10	(8 ± 2)×10
P3 (75 %)	(10 ± 1)×10	(10 ± 1)×10	(10 ± 1)×10	(12 ± 2)×10	(11 ± 1)×10	(9 ± 2)×10
P4 (50 %)	77 ± 8	80 ± 8	78 ± 8	(7 ± 1)×10	78 ± 6	(8 ± 2)×10
P5 (40 %)	65 ± 6	63 ± 8	66 ± 6	(6 ± 1)×10	65 ± 6	(8 ± 2)×10
C1 (60 %)	83 ± 8	(8 ± 1)×10	83 ± 8	(7 ± 2)×10	82 ± 8	(6 ± 1)×10
C2 (50 %)	69 ± 7	71 ± 9	70 ± 7	(6 ± 1)×10	70 ± 7	(6 ± 1)×10
C3 (40 %)	58 ± 6	56 ± 7	59 ± 6	(5 ± 1)×10	58 ± 6	(6 ± 1)×10
C4 (30 %)	48 ± 5	49 ± 7	49 ± 5	(4 ± 1)×10	48 ± 5	(6 ± 1)×10

4.4.2. Public Exposure

Two ACIs, as described by Markkanen, are used to verify whether the bauxite concrete mixtures are safe to use considering public exposure [26]. Figure 4-1 shows the results of the ACI_{BM}, which focusses on building materials and is used by the council directive 2013/59/EURATOM (EU-BSS) [32], discussed in Section 4.4.2.1. Figure 4-2 shows the results of the ACI_{SP}, which focusses on streets and playgrounds, discussed in Section 4.4.2.2

4.4.2.1. The Activity Concentration Index for Building Materials

All the calculated ACI_{BM}s are below the EU-BSS threshold level of 1 and therefore from a radiological point of view the materials can be accepted for use as building materials considering external exposure to the public. If, according to the EU-BSS, the ACI_{BM} exceeds this threshold level, the indoor external exposure to gamma radiation emitted by building materials in addition to outdoor external exposure, of 1 mSv per year needs to be verified.

When considering concrete for bulk applications in building materials, as is the case here, then the ACI is a reliable screening tool since it was designed for this type of scenario. For other types of materials next to concrete or for thin layer application it is advisable to use a density and thickness corrected index [17].

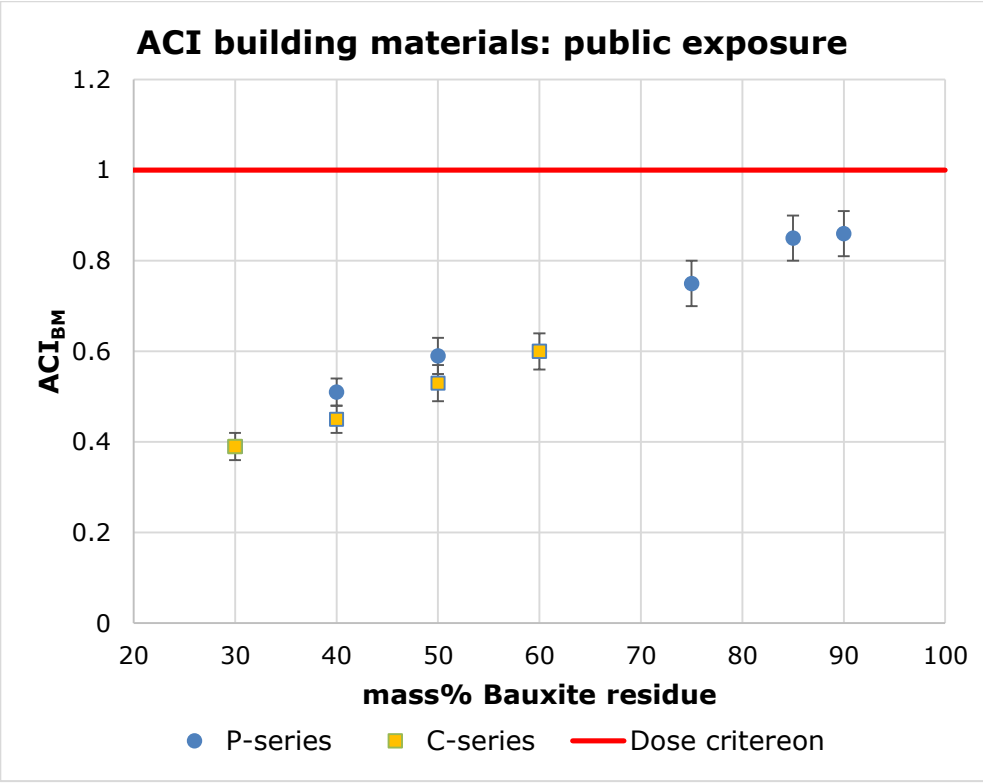

Figure 4-1: Activity concentration index for building materials (ACI_{BM}) for different bauxite concrete mixtures with different mass% of bauxite residue incorporation. Red line indicates dose criterion/threshold value of 1. (k=2).

4.4.2.2. The Activity concentration Index for Streets and Playgrounds

All the calculated ACI_{SP}s are well below the threshold level of 1. This threshold level, proposed by Markkanen and used in the Finnish radiation protection regulation, corresponds to a dose criterion of 0.1 mSv per year.

This implies that from a radiological point of view, the mixtures are safe for public use as road, street and playground considering external exposure [26,27]. The ACI_{SP} developed by Markkanen involves, next to the naturally occurring radionuclides, also ^{137}Cs in the evaluation.

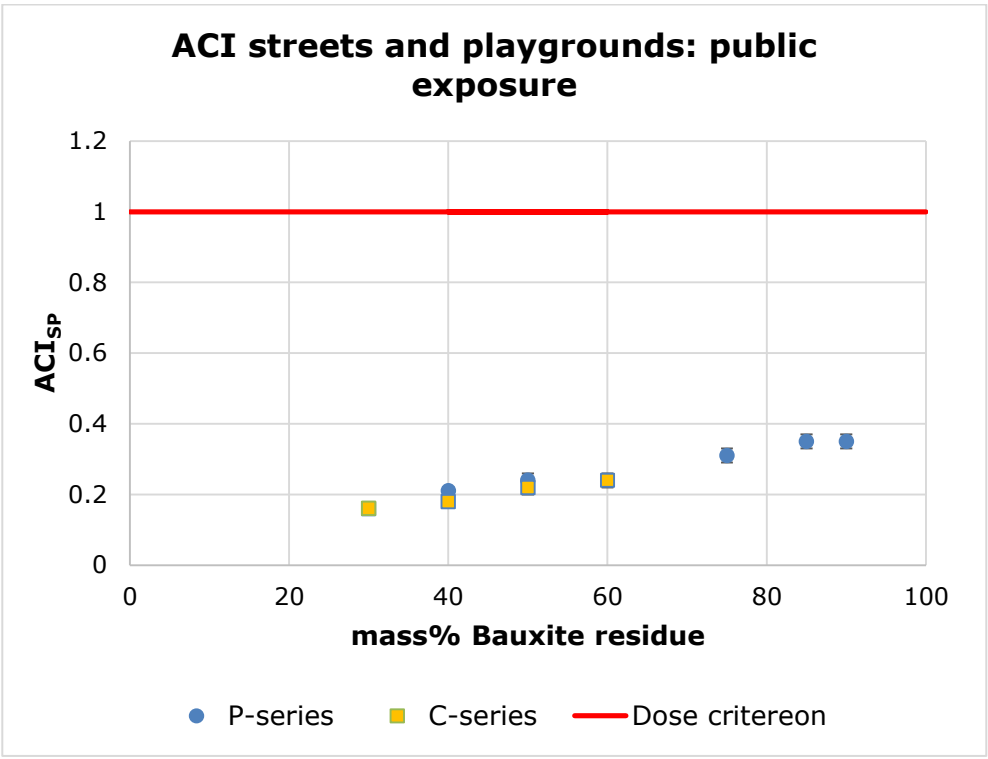

Figure 4-2: Activity concentration index for streets and playgrounds (ACI_{SP}) for different bauxite concrete mixtures with different mass% of bauxite residue incorporation. Red line indicates dose criterion/threshold value of 1. (k=2).

4.4.3. Occupational Exposure

Following RP-122 (part II), a simplified dose assessment was made that considered the impact of concrete containing bauxite residue on building and road construction workers. The results of the simulation are shown in Figure 4-3 and Figure 4-4. In this case the total effective dose (external, inhalation and ingestion dose) was considered. The dose criterion used by RP-122 is 0.3 mSv/a.

4.4.3.1. Dose Assessment for Building Construction Worker

The mass incorporation of 75 % bauxite in the concrete mixtures already leads to effective doses above the dose criterion of 0.3 mSv/a (Figure 4-3). From the dose calculations it can be assessed that an incorporation rate of 60 mass% provides an acceptable incorporation level to assure that the dose to the workers will not be higher than the dose criterion proposed by RP-122. Typically, 95 % of the calculated total dose could be assigned as external dose.

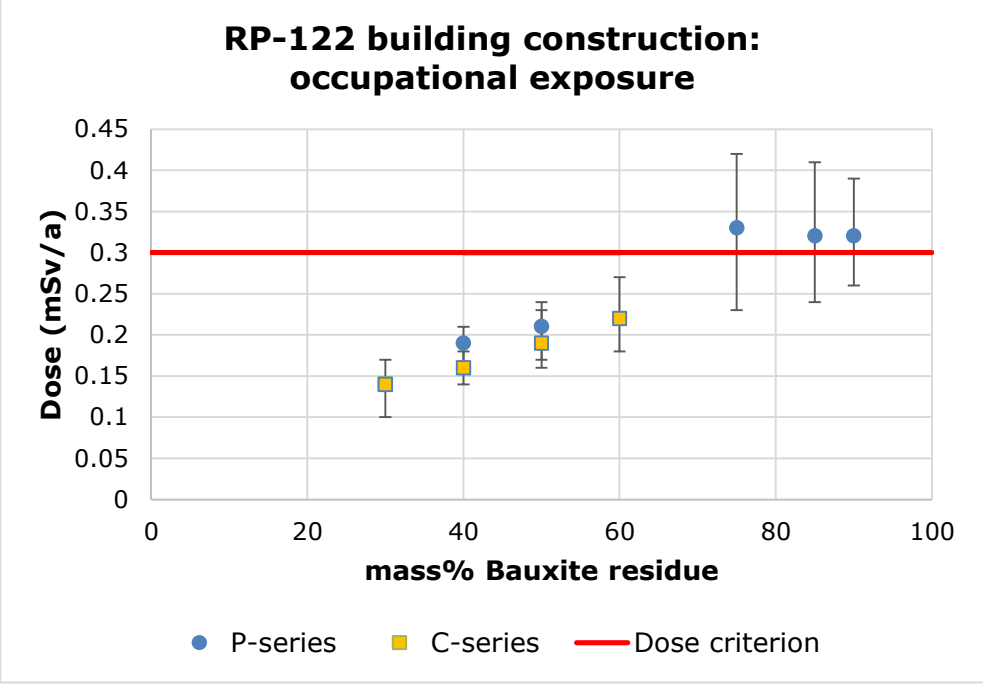

Figure 4-3: Total effective dose for workers active in building construction in function of the different bauxite concrete mixtures with different mass% of bauxite residue incorporation. Dose criterion of 0.3 mSv/a proposed by RP-122. (k=2).

4.4.3.2. Dose Assessment for Road Construction Worker

Even when using high incorporation rates of 90 mass% for road construction the dose criterion of 0.3 mSv/a is not exceeded (Figure 4-4). From a radiological point of view, road construction workers are able to safely use bauxite concrete mixtures with high contents of bauxite red mud. In this case typically 85 % of the calculated total dose could be assigned as external dose.

As reported by Nuccetelli et al. (2015) [19], average activity concentrations of bauxite residue are origin and therefore country dependent. For European countries activity concentrations for bauxite residue of up to 379 ± 43 Bq/kg ^{226}Ra, 472 ± 23 Bq/kg ^{232}Th and 21 ± 11 Bq/kg ^{40}K (Greece) were found. In the world even activity concentrations of 1047 Bq/kg ^{226}Ra, 350 Bq/kg ^{232}Th and 335 Bq/kg ^{40}K are reported (Jamaica). When assuming a dilution factor of 0.9 (90 mass% incorporation of the bauxite residue) total doses up to 0.64 mSv/a (Greece) and 0.89 mSv/a (Jamaica) can be calculated for road construction workers. Also in this case, the external dose is the main contributing factor (0.58 mSv/a for workers in Greece; 0.8 mSv/a for workers in Jamaica) to the total dose of the workers. Therefore, an adapted monitoring strategy, taking into consideration the way that variations in the origin of the incoming material occur over time, is required to ensure that the dose criteria are met.

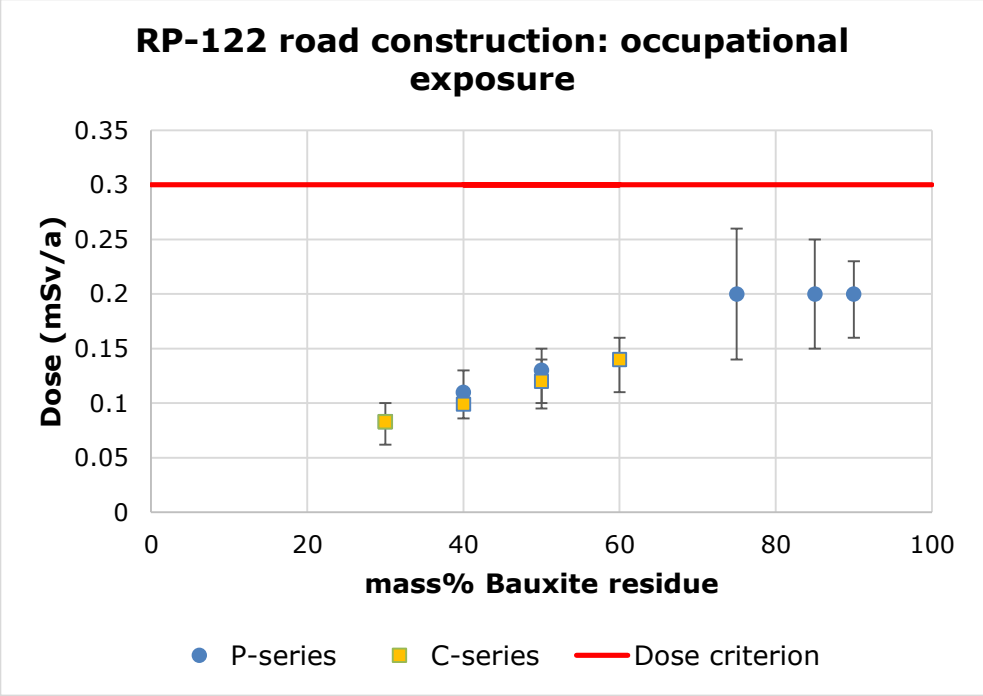

Figure 4-4: Total effective dose of workers active in road construction in function of the different bauxite concrete mixtures with different mass% of bauxite residue incorporation. Dose criterion of 0.3 mSv/a proposed by RP-122. (k=2).

4.5. Conclusion

The current study demonstrates that the studied Ukrainian bauxite residue can, based on the ACI_{BM} defined by the EU-BSS and the ACI_{SP} defined by Markkanen for streets and playgrounds, be used for building materials and for road construction, even in percentages reaching 90 mass% incorporation.

However, when also considering occupational exposure and using the dose assessment models of RP-122 (part II) for building construction workers it becomes advisable to incorporate less than 75 mass% of bauxite red mud. Upon incorporating 75 mass% bauxite residue or more a total effective dose higher than the dose criterion proposed by RP-122 (0.3 mSv/a) was found. 60 mass% of bauxite residue incorporation was found to be acceptable for building construction. For the case of road construction, based on the model proposed by RP-122, 90 mass% bauxite residue incorporation can be accepted also from the perspective of occupational exposure.

Considering the large variation in the activity concentration of the bauxite ore and resulting bauxite residues and considering that the ores accepted by

industries and the processing of the ores will vary over time, the authors recommend that screening of the bauxite residues should determine the possible applications.

In order to evaluate reuse options for NORM residues, the COST Action NORM4Building recommends to use a holistic approach and to consider all aspects that can determine whether a specific reuse practice becomes possible. A holistic approach can only function if chemical, radiological, physical and mechanical data is available for a specific type of residue or construction material. Therefore, in addition to this paper, a detailed study of the chemical, physical and mechanical properties of the discussed concretes is in preparation [35].

4.6. Acknowledgements

The authors would like to acknowledge networking support by the COST Action TU1301. This work was supported by the European Commission within HORIZON2020 via the EURATOM project EUFRAT.

4.7. References

[1] G. Power, M. Gräfe, C. Klauber, Bauxite residue issues: I. Current management, disposal and storage practices, Hydrometallurgy. 108 (2011) 33–45. doi:10.1016/j.hydromet.2011.02.006.

[2] G. Power, M. Gräfe, C. Klauber, Review of Current Bauxite Residue Management, Disposal and Storage: Practices, Engineering and Science CSIRO Document DMR-3608 May, 2009.

[3] S. Kumar, R. Kumar, A. Bandopadhyay, Innovative methodologies for the utilisation of wastes from metallurgical and allied industries, Resour. Conserv. Recycl. 48 (2006) 301–314. doi:10.1016/j.resconrec.2006.03.003.

[4] V.M. Sglavo, R. Campostrini, S. Maurina, G. Carturan, M. Monagheddu, G. Budroni, G. Cocco, Bauxite "red mud" in the ceramic industry. Part 1: thermal behaviour, J. Eur. Ceram. Soc. 20 (2000) 235–244. doi:10.1016/S0955-2219(99)00156-9.

[5] V.M. Sglavo, S. Maurina, A. Conci, A. Salviati, G. Carturan, G. Cocco, Bauxite "red mud" in the ceramic industry. Part 2: production of clay-based ceramics, J. Eur. Ceram. Soc. 20 (2000) 245–252. doi:10.1016/S0955-2219(99)00156-9.

[6] Y. Pontikes, P. Nikolopoulos, G.N. Angelopoulos, Thermal behaviour of clay mixtures with bauxite residue for the production of heavy-clay ceramics, J. Eur. Ceram. Soc. 27 (2007) 1645–1649. doi:10.1016/j.jeurceramsoc.2006.05.067.

[7] P.E. Tsakiridis, S. Agatzini-Leonardou, P. Oustadakis, Red mud addition in the raw meal for the production of Portland cement clinker, J. Hazard. Mater. 116 (2004) 103–110. doi:10.1016/j.jhazmat.2004.08.002.

[8] J. Pascual, F.A. Corpas, J. López-Beceiro, M. Benítez-Guerrero, R. Artiaga, Thermal characterization of a Spanish red mud, J. Therm. Anal. Calorim. 96 (2009) 407–412. doi:10.1007/s10973-008-9230-9.

[9] Z. Pan, L. Cheng, Y. Lu, N. Yang, Hydration products of alkali-activated slag-bauxite red mud cementitions materials, Cem. Concr. Res. 32 (2002) 357–362.

[10] Z. Pan, L. Dongxu, Y. Jian, N. Yang, Properties and microstructure of the hardened alkali-activated bauxite red mud slag cementitions material, Cem. Concr. Res. 33 (2003) 1437–1441.

[11] X. Ke, N. Ye, S. a. Bernal, J.L. Provis, J. Yang, Preparation of one-part geopolymer from thermal alkali activated bauxite red mud, in: Proc. Second Int. Conf. Adv. Chem. Mater. June 13, Chang. P.R.China, Pp. 204-211., 2014: pp. 204–211.

[12] P. Krivenko, O. Petropavlovsky, G. Rostovskaya, Patent of Ukraine UA 10286 a, C 04 B7/06, 7/06, 25.12.96, Bulletin No 4., 1996.

[13] G. Rostovskaya, Alkaline binders based on bauxite residues, in: First Int. Conf. Alkaline Cem. Concr. Kyiv, Ukr. 1, 1994: pp. 329–346.

[14] V.D. Glukhovsky, Durability of concrete: aspects of admixtures and industrial by-products., in: Berntsson, Swedish Counc. Build. Res. Stock. Sweden, 1989: pp. 53–61.

[15] United Nations, Sources and Effects of Ionizing Radiation United Nations Scientific Committee on the Effects of Atomic Radiation UNSCEAR 2000 Report to the General Assembly, with Scientific Annexes VOLUME I: SOURCES, 2000.

[16] J. Somlai, V. Jobbágy, J. Kovács, S. Tarján, T. Kovács, Radiological aspects of the usability of red mud as building material additive, J. Hazard. Mater. 150 (2008) 541–545. doi:10.1016/j.jhazmat.2007.05.004.

[17] C. Nuccetelli, F. Leonardi, R. Trevisi, A new accurate and flexible index to assess the contribution of building materials to indoor gamma exposure, J. Environ. Radioact. 143 (2015) 70–75. doi:10.1016/j.jenvrad.2015.02.011.

[18] P. Krivenko, O. Petropavlovsky, G. Rostovskaya, Synthesis of Analogs to Natural Minerals and Development of Technological Parameters and Selection of Equipment for Ecologically Friendly Localization of Toxic and Radioactive Wastes in Building Materials and Compounds, 1995.

[19] C. Nuccetelli, Y. Pontikes, F. Leonardi, R. Trevisi, New perspectives and issues arising from the introduction of (NORM) residues in building materials: A critical assessment on the radiological behaviour, Constr. Build. Mater. 82 (2015) 323–331. doi:10.1016/j.conbuildmat.2015.01.069.

[20] Ş. Turhan, I.H. Arikan, H. Demirel, N. Güngör, Radiometric analysis of raw materials and end products in the Turkish ceramics industry, Radiat. Phys. Chem. 80 (2011) 620–625. doi:10.1016/j.radphyschem.2011.01.007.

[21] Ş. Turhan, Y. Gündüz, A. Varinlioğlu, Gamma spectrometric characterization of refractory products used in Turkey, Radiat. Phys. Chem.

97 (2014) 1–5. doi:10.1016/j.radphyschem.2013.10.015.

[22] G. Viruthagiri, B. Rajamannan, K. Suresh Jawahar, Radioactivity and associated radiation hazards in ceramic raw materials and end products, Radiat. Prot. Dosimetry. 157 (2013) 383–391. doi:10.1093/rpd/nct149.

[23] T. Kovacs, Z. Sas, J. Somlai, V. Jobbagy, G. Szeiler, Radiological investigation of the effects of red mud disaster, Radiat. Prot. Dosimetry. 152 (2012) 76–79. doi:10.1093/rpd/ncs192.

[24] T. Kovacs, Z. Sas, V. Jobbagy, A. Csordas, G. Szeiler, J. Somlai, Radiological aspects of red mud disaster in Hungary, Acta Geophys. 61 (2013) 1026–1037.

[25] European commission, REGULATION (EU) No 305/2011 OF THE EUROPEAN PARLIAMENT AND OF THE COUNCIL of 9 March 2011 laying down harmonised conditions for the marketing of construction products and repealing Council Directive 89/106/EEC, Off. J. Eur. Union. (2011) 5–43. papers3://publication/uuid/BD5A1031-4234-4755-80B7-C824AAEA8F82.

[26] M. Markkanen, Radiation Dose Assessments for Materials with Elevated Natural Radioactivity, Finish Cent. Radiat. Nucl. Safety. Rep. STUK-B-STO 32. (1995) 1–41.

[27] STUK, The radioactivity of building materials and ash GUIDE ST 12.2, 2010.

[28] European Commission, Radiation protection 122 practical use of the concepts of clearance and exemption Part II application of the concepts of exemption and clearance to natural radiation sources, 2002.

[29] I. Kawrakow, D. Rogers, The EGSnrc code system: Monte Carlo simulation of electron and photon transport., 2011.

[30] Laboratoire national Henri Becquerel, Decay Data Evaluation Project, (2016). http://www.nucleide.org/DDEP.htm (accessed May 22, 2016).

[31] JCGM WG1, Evaluation of measurement data — Guide to the expression of uncertainty in measurement, 2008.

[32] European Commission, Laying down basic safety standards for protection against the dangers arising from exposure to ionising radiation, and repealing directives 89/618/Euratom, 90/641/Euratom, 96/29/Euratom, 97/43/Euratom and 2003/122/Euratom, Off. J. Eur. Union. (2014) 1–73.

[33] Research Center for Radiation Protection, National Institute of Radiological Sciences, NIRS NORM database., (n.d.). http://www.nirs.qst.go.jp/ENG/index.html (accessed May 5, 2017).

[34] European Commission, Radiation protection 112 Radiological protection principles concerning the natural radioactivity of building materials, (1999) 1–16.

[35] P. Krivenko, O. Kovalchuk, A. Pasko, T. Croymans, M. Hult, G. Lutter, N. Vandevenne, S. Schreurs, W. Schroeyers, Development of alkali activated cements and concrete mixture design with high volumes of red mud, Constr. Build. Mater. 151 (2017) 819–826.

Chapter 5: Variation of Naturally Occurring Radionuclides in Non-Ferrous Fayalite Slags During a One-Month Production Period

The results of this chapter have been published:

T. Croymans, I. Schreurs, M. Hult, G. Marissens, H. Stroh, G. Lutter, S. Schreurs, W. Schroeyers, Variation of natural radionuclides in non-ferrous fayalite slags during a one-month production period, J. Environ. Radioact. 172 (2017) 63–73.

Link with objectives: This chapter fits within objectives 1 and 2 of this thesis and is focused on fayalite slag (FS). FS has a range of reuse options as mentioned in Section 2.2.2. In addition, FS is a suitable precursor to produce inorganic polymer (IP) building materials which allows creating a higher added value. The focus of this chapter is on the study of the suitability of fayalite slag based inorganic polymer (FSIP) as building material from a radiological point of view. As discussed in Section 2.2.2., the radionuclide content can vary significanly between different types of slags but also between slags of the same class. The same was observed for other by-products like BR as discussed in Section 2.2.1. This chapter studies the variability in the activity concentrations of radionuclides from the decay series of ^{238}U, ^{235}U and ^{232}Th and ^{40}K of FS originating from one industrial facility during a one-month production period. The obtained results were used as input for the assessment of the public exposure via the ACI. In addition, flue dust and feedstock samples were studied and the these results were used to assess the transport of radionuclides and explain (dis)equilibria situations.

5.1. Abstract

The European basic safety standards (EU-BSS) describes a set of naturally occurring radioactive materials (NORM-) processing industries that produce residues known to be possibly enriched in naturally occurring radionuclides (NORs). These residues can be used as a component in building materials aimed for public usage. The industrial processes, in which the residues are produced, are often complex and total monitoring can be challenging especially when the origin of the used raw materials varies. In this study, the NORs present in non-ferrous fayalite slags of a secondary smelter facility, a NORM-processing

References at page 143

industry according to the EU-BSS, were monitored daily during a one-month production period. In addition, flue dust samples and feedstock samples, known

to contain elevated levels of NORs, of the same period were measured. The survey involved the gamma-ray spectrometric analysis of the decay products from the ^{238}U and ^{232}Th decay chains, ^{235}U and ^{40}K using HPGe detectors. Secular equilibrium was observed for the slags, flue dust and feedstock samples in the ^{232}Th decay chain, in contrast to the ^{238}U decay chain. During the month in question the ratios of maximum over minimum activity concentration were 3 ± 1 for ^{40}K, 4.0 ± 1.0 for ^{238}U, 5.9 ± 0.7 for ^{226}Ra, 13 ± 7 for ^{210}Pb, 4.5 ± 0.6 for ^{228}Ra and 4.7 ± 0.5 for ^{228}Th for the slags. Even with the activity concentration of the feedstock material ranging up to 2.1 ± 0.3 kBq/kg for ^{238}U, 1.6 ± 0.2 kBq for ^{226}Ra, 22 ± 7 kBq/kg for ^{210}Pb, 2.1 ± 0.2 kBq/kg for ^{228}Ra and 2.0 ± 0.4 kBq/kg for ^{228}Th, none of the slag samples exceeded the exemption/clearance levels of the EU-BSS and RP-122 part II, which can provide guidance under equilibrium and in absence of equilibrium, respectively. As each NORM-processing industry has its own complexity and variability, the observed variations point out that one should approach one-time measurements or low frequency monitoring methods cautiously. Low frequency measurements should be optimized depending on the discharge of the batches. A follow up of the industrial process and its output can provide important insights to assure a limited public exposure upon application of these industrial residues.

Finally, a comparison was made with reported data on other metallurgical slags and the use of the slags in building materials was evaluated using the activity concentration index (ACI) proposed by the EU-BSS.

5.2. Introduction

Each year over 400 million tonnes of metallurgical slags, a by-product from metal producing industries, are produced world-wide [1]. Due to the presence of naturally occurring radionuclides (NORs) in the raw materials used by the metallurgical industries the produced metallurgical slag can contain enhanced concentrations of NORs. In Table 5-1 an overview is given on the activity concentrations of ^{226}Ra, ^{232}Th and ^{40}K for different types of metallurgical slags reported in the literature. These activity concentrations are found in the intervals 0.004-69 kBq/kg, 0.002-130 kBq/kg and 0.002-23 kBq/kg for ^{226}Ra, ^{232}Th and ^{40}K, respectively. It must be noted that this list is not exhaustive and some data originate from samples of the 1980's. In several cases the number of measured samples is not specified and not all considered NORs (^{226}Ra, ^{232}Th and ^{40}K) are reported. The data and nomenclature are shown as mentioned in the corresponding reference. Data on other radionuclides mentioned in the corresponding reference is not shown in Table 5-1. The two main classes of metallurgical slags are non-ferrous and ferrous slags [2].

Especially for non-ferrous slags such as Sn, Nb and Cu slags, higher activity concentrations can be found reaching up to (Table 5-1):

- 69 kBq/kg ^{226}Ra, 130 kBq/kg ^{232}Th and 23 kBq/kg ^{40}K for Sn slag,
- 5 kBq/kg ^{226}Ra and 118 kBq/kg ^{232}Th for Nb slag
- 2.1 kBq/kg ^{226}Ra, 0.1 kBq/kg ^{232}Th and 1.3 kBq/kg ^{40}K for Cu slag.

Non-ferrous slags typically consist mainly out of Fe and Si whereas the ferrous slags are typically rich in Ca and Si [2]. The production of non-ferrous slag is limited to approximately 12 % of the total worldwide slag production [3]. Non-ferrous industries that process niobium ores or work on tin, lead or copper smelting and therefore produce Nb, Sn, Pb and Cu slags are specifically considered in Council directive 2013/59/Euratom, known as the European basic safety standards (EU-BSS), as practices involving naturally occurring radioactive materials (NORM). This is also true for residues of steel production. In Table 5-1, it is also demonstrated that a large range of activity concentrations can be found for a given type of metallurgical slag. For example, for Sn slag, the activity concentrations range from 0.5 - 69 kBq/kg for ^{226}Ra, 0.2 - 130 kBq/kg for ^{232}Th and 0.3 - 23 kBq/kg for ^{40}K. The measured activity concentrations for different non-ferrous slags were in several cases higher than the activity concentrations for exemption or clearance of NORs in solid materials in secular equilibrium with their progeny, proposed by the EU-BSS [4]. The EU-BSS exemption/clearance levels were chosen in accordance with the exemption/clearance levels of the IAEA "Application of the concepts of exclusion, exemption and clearance". A global level benefits the industries processing and transporting these materials from an administrative and legislative point of view. These EU-BSS | IAEA levels are 1 kBq/kg for natural radionuclides from the ^{238}U and ^{232}Th decay series and 10 kBq/kg for ^{40}K (Table 5-2) however these levels are only applicable if secular equilibrium in the decay series is obtained. The EU-BSS allows higher values in case of disequilibrium but does not specify which levels are recommended. Radiation Protection (RP)-122 specifies these values and applies a summation rule for the radiological evaluation (Table 5-2).

Table 5-1: Overview of the activity concentrations of ^{226}Ra, ^{232}Th and ^{40}K in metallurgical slags in Bq/kg. N is the number of samples.

Slag type	N	^{226}Ra	^{232}Th	^{40}K	Slag origin	Reference
Tin slag*	/	1100	/	/	Germany	Leopold and Weiss, 2003 [5]
Tin slag◇	/	/	11000		United Kingdom - The Netherlands	Ryan et al., 2004 [6]
Tin slag	/	2000	/	/	Malaysia	Omar, 2000 [7]
Tin slag	12	492 - 1153	720 - 1532	11230 - 23183	Malaysia	Ismail et al., 2011 [8]
Tin slag	4	/	12100 - 14200	/	United Kingdom	Gilmore and Jackson, 1992 [9]
Tin slag	3	500 - 3400	800 - 7300	/	Malaysia	Omar et al., 2008 [10]
Tin slag	/	4570	420	/	Malaysia	Kontol et al., 2007 [11]
Tin slag	3	20000 - 69000	34000 - 130000	/	Brazil	Garcia, 2009 [12]
Tin slag	/	1000	4000	/	United Kingdom	European Commission, 1997 [13]
Tin slag	/	1000 - 1200	230 - 340	330	Germany	Lehmann, 1996 [14]
Tin melting slag*	/	5500	15000	/	Germany	Leopold and Weiss, 2003 [5]
Nickel smelt slag	3	16.7 -364	7.9 - 82	78.1 - 888	Poland	Zak et al., 2008 [15]
Nickel slag	/	52	78	76	Germany	Lehmann, 1996 [14]
Niobium slag	/	/	80000	/	/	European Commission, 1997 [13]
Niobium slag	/	3300 - 5000	17000 - 118000	/	Brazil	Pires do Rio et al., 2002 [16]

Table 5-1 (Continuation): Overview of the activity concentrations of ^{226}Ra, ^{232}Th and ^{40}K in metallurgical slags in Bq/kg. N is the number of samples.

Slag type	N	^{226}Ra	^{232}Th	^{40}K	Slag origin	Reference
Lead slag	/	270	36	200	Germany	Lehmann, 1996 [14]
Copper slag*	/	2000	/	/	Germany	Leopold and Weiss, 2003 [5]
Copper slag	8	287 - 401	44 - 73	674 - 900	Poland	Zak, 1995 [17]
Copper smelt slag•	80	236.6 - 517.8	25.7 - 183	615.4 - 1250.6	Poland	Zak et al., 2008 [15]
Copper slag*	/	530	183	1459	Poland	Skowronek et al., 2004 [18]
Copper slag	23	237 - 336	26 - 76	615 -1251	Poland	Zak et al., 1993 [19]
Copper slag (old production)	/	861 - 2100	18 - 78	300 - 730	Germany	Lehmann, 1996 [14]
Copper slag (new production	/	490 - 940	41 - 60	530 - 760	Germany	Lehmann, 1996 [14]
Copper slag primary process	/	/	13	/	/	RP-122 part II [20]
Copper slag secondary process	/	17	15	/	/	RP-122 part II [20]
Steel slag	/	88	49	/	United Kingdom	Crockett et al., 2003 [21]; Hughes and Harvey, 2008 [22]
Steel Slag	1	8.62	3.73	5.14	Romania	Ene and Pantelica, 2011 [23]
Steel slag	/	/	150	/	The Netherlands	Van Der Steen, 2004 [24]

Table 5-1 (Continuation): Overview of the activity concentrations of ^{226}Ra, ^{232}Th and ^{40}K in metallurgical slags in Bq/kg. N is the number of samples.

Slag type	N	^{226}Ra	^{232}Th	^{40}K	Slag origin	Reference
Steel slag	1	62	21	51	China	Wendling et al., 2013 [25]
Steel slag	3	184 - 213	156 - 182	<17 - 25	Qatar	Taha et al., 2014 [26]
Steel slag	10	15.2 - 21.4	12.9 - 15.1	45.3 - 62.9	Croatia	Sofilic et al., 2011 [27]
Steel slag	/	5 - 31	0 - 5	/	/	RP-122 part II [20]
Steel slag	/	100 -600	/	/	Slovenia	Smodis et al., 2006 [28]
Steel and Iron slag	/	150	150	/	/	European Commission, 1997 [13]
Steel slag□	/	196	29.6	148	Romania	Tanase and Tanase, 2003 [29]
Steel slag	5	51 - 114	28.6 - 35.5	118 - 145	Romania	Sahagia et al., 2014 [30]
Non-Iron slag	/	20 -30	10 - 15	20	South Korea	Jeong et al., 2014 [31]
Iron slag	2	107.4 - 113.9	95.2 - 109.6	2.27 - 18.9	Saudi Arabia	Alamoudi and Almehmadi, 2013 [32]]
Iron slag	/	10 - 220	10 - 90	10 - 150	South Korea	Jeong et al., 2014 [31]
Iron slag	12	15 - 22	/	/	Scandinavia	Broden et al., 2001 [33]
Iron slag	/	64 - 380	30 - 98	/	/	RP-122 part II [20]
Iron slag	6	4 - 234	2 - 196	8 - 105	Slovenia	NORM4Building database, 2016 [34]
EAF slag	3	14.6 - 17.1	6.7 - 13.1	15.3 - 36.9	Croatiä	Sofilic et al., 2010 [35]

Table 5-1 (Continuation): Overview of the activity concentrations of ^{226}Ra, ^{232}Th and ^{40}K in metallurgical slags in Bq/kg. N is the number of samples.

Slag type	N	^{226}Ra	^{232}Th	^{40}K	Slag origin	Reference
EAF slag	12	18.3 -21.6	12.3 - 15.4	45.3 - 63.8	Croatia	Sofilic et al., 2010 [36]
EAF slag	/	25	5	10	Greece	Xirouchakis and Manolakou, 2011 [37]
Blast furnace slag	/	160 - 165	35-40	/	Belgium	Vanmarcke et al., 2010 [38]
Blast furnace slag	40	13.7 - 310.1	3.8 - 330	18.1 - 290.1	Turkey	Ugur et al., 2013 [39]
Blast furnace slag	1	166	47.6	232.3	Spain	Chinchon-Paya et al., 2011 [40]
Blast furnace (boiler) slag	368	12.4 - 351.1	2.2 - 115	18.0 - 1400	Poland	Zak et al., 2008 [15]
Blast furnace slag	4	116 - 223	83 - 141	136 - 196	China	Wendling et al., 2013 [25]
Blast furnace slag	12	8 -308	1.6 - 337.3	18.4 - 388.9	Turkey	Turhan, 2008 [41]
Blast furnace slag	/	251.2	24.8	361.7	Croatia	Sofilic et al., 2011 [42]
Blast furnace slag	2	143.4 - 150.9	45.6 - 45.8	75.7 - 76.8	/	Puertas et al., 2015 [43]
Blast furnace slag	5	105 - 129	32.4 - 102	97.2 - 209	Finland	Mustonen, 1984 [44]
Blast furnace slag	5	323 ± 18.6	39.8 ± 7.2	158 ± 16	Egypt	Sharaf et al., 1999 [45]
Blast furnace slag	/	88.3 - 142.0	26.8 - 46.0	188 - 269	Hungary	Gallyas and Torok, 1984 [46]
Blast furnace slag	/	186.69 ± 2.38	35.87 ± 1.67	295.91 ± 9.08	Turkey	Baltas et al., 2014 [47]

Table 5-1 (Continuation): Overview of the activity concentrations of ^{226}Ra, ^{232}Th and ^{40}K in metallurgical slags in Bq/kg. N is the number of samples.

Slag type	N	^{226}Ra	^{232}Th	^{40}K	Slag origin	Reference
Blast furnace slag†	4200%	18.5 - 458.8	/	225.7 - 2227.4	Poland	Pensko et al., 1980 [48]
Blast furnace slag*	/	2100	340	1000	/	RP-112 [49]
Blast furnace slag◇	/	270	70	240	/	RP-112 [49]
Blast furnace slag	/	131 - 139	4	157 - 177	Ukraine	NORM4Building database, 2016 [34]
Metallurgical slag	/	251	115	1400	Poland	Skowronek and Dulewski, 2005 [18]
Metallurgical slag	6	41 - 124	41 - 106	166 - 395	Slovakia	Cabanekova, 1996 [50]
Metallurgical slag	2	162 - 173	25 - 52	179 - 219	Romania	Muntean et al., 2014 [51]
Metallurgical slag	40	13 - 341	2 -115	36 - 889	Poland	Zak, 1995 [17]
Metallurgical slag	8	10.8 - 38.8	2.7 - 21.8	7.3 - 63.3	/	Sofilic et al., 2004 [52]
Metallurgical slag	160	33 - 351	12 - 102	14 - 825	Poland	Zak et al., 1993 [19]
Metallurgical slag + dross ‡	43	10.0 - 436.0	9.5 - 55.6	75.7 - 649.6	Slovakia	Cabanekova, 2008 [53]

* Mentioned as maximum value

◇ Mentioned as typical values

□ Mentioned as average value

● Could contain samples reported by Zak et al. 1993 and Zak 1995

† Could contain boiler slag data and is converted from pCi/g

‡ Could contain doubles with Cabanekova 1996

Table 5-2: Exemption/clearance levels reported in EU-BSS | IAEA (equilibrium situation) and RP-122 part II (disequilibrium situation).

Radionuclide	EU-BSS | IAEA*	RP-122 part II
	Exemption/clearance level (Bq/kg)	Exemption/clearance level (Bq/kg)
^{238}U	1000	5000
^{226}Ra	1000	500**
^{210}Pb	1000	5000**
^{228}Ra	1000	5000**
^{228}Th	1000	500**
^{235}U	1000	1000**
^{40}K	10000	5000

* The activity concentration criterion of the EU-BSS | IAEA assumes equilibrium [4,54].
** To indicate that the derived clearance level also includes daughter nuclides [20].

Before use of non-ferrous slag can be allowed, the EU-BSS requires that the value of the activity concentration relative to the exemption/clearance levels is determined. In addition, the EU-BSS specifies a screening index called the activity concentration index (ACI) applicable for building materials containing these residues (Equation 5-1).

$$ACI = \frac{AC_{226\mathrm{Ra}}}{300\ Bq/kg} + \frac{AC_{232\mathrm{Th}}}{200\ Bq/kg} + \frac{AC_{40\mathrm{K}}}{3000\ Bq/kg}$$

Equation 5-1

With AC as activity concentration of the mentioned radionuclide expressed in Bq/kg.

According to the EU-BSS this index allows estimating the requirement that upon application of these building materials the public exposure is below the effective dose limit of 1 mSv a year. An ACI value below 1 assumes that the dose limit of 1 mSv a year is not exceeded. The application of metallurgical slags in building materials is gaining interest and the applications depend on the chemical composition, cooling path, availability, price, etc. [2]. Usage of metallurgical slags in tiles, in railway ballast, in roofing materials, in coloured glass and in cementitious materials are reported [2]. The main usage is as a raw material in asphalt and concrete mixtures for road construction – mainly for ferrous slag [2]. Recently, the application of non-ferrous slag as a binder to produce inorganic polymers building materials was reported [55]. Inorganic polymers (IPs) are novel types of building materials with lower CO_2 emissions in comparison to concrete [56]. IPs can be used in similar applications as

conventional concrete [57]. In addition, other reuse and recycle options are reported, like usage as sand blasting material, as reprocessing material for secondary metal recovery and for environmental remediation [2,58]. Despite these applications, still large fractions of slags currently end up on landfills [2].

A common feature of the listed studies on metallurgical slags in Table 5-1, is that the measurements represent a one-time sampling and that none of the considered studies follow the output of the process over a period of time. Therefore, no information is available to verify to which extent variations in the industrial process or in the origin of the incoming raw materials over time can impact the activity concentration of the produced non-ferrous slag. The current study, which focuses on non-ferrous fayalite slags produced in a secondary smelter facility for production of different types of non-ferrous metals, aims to address this aspect. The production during a one-month production period was monitored. Within this framework the activity concentrations of NORs are evaluated against the exemption/clearance levels of annex VII of the EU-BSS. The variation in activity concentration of the long-living natural radionuclides is discussed, as well as the (dis)equilibria which are present. Finally, the ACI is discussed since these slags are used for the production of IP building materials.

5.3. Methods and Materials

5.3.1. Samples

The samples in this study originate from a secondary smelting plant aimed at the production of different types of non-ferrous metals. The factory handles a broad range of primary and secondary raw materials from industries listed in annex VI of the EU-BSS as industries with naturally occurring radioactive materials [4]. The smelter facility is found under the category tin/lead/copper smelting in annex VI of the new EU-BSS. Non-ferrous fayalite slags are produced as by-product.

5.3.1.1. Non-Ferrous Fayalite Slag Samples

Every day, several smelting cycles are performed and with each cycle a different amount of slag is produced. These residues are the remaining after the recovery of non-ferrous metals from the feedstock by pyrometallurgical processes. Representative samples of slags from each smelting cycle were taken during a one-month period. The samples were collected directly from the liquid bath situated in the furnace. This implies that the sample is representative of the batch and that it is homogeneous. The produced fayalite slags were cooled by water quenching. In order to limit the number of samples for analysis and because the slags are discharged daily, one sample for each day was produced based on samples from several smelting cycles of that particular day. The relative contribution of each smelting cycle sample to the daily sample was

proportional to the slag production quantity of each smelting cycle (Equation 5-2).

$$Composition\ daily\ sample = \sum_{i=1}^{n} \frac{Quantity\ production\ batch\ i}{Quantity\ day\ production} * 100\%$$

Equation 5-2

All cycle samples were dry and milled to powders by disk milling. In total 31 slag mixtures were produced corresponding to 31 consecutive days of slag production. Each slag mixture dry mass varied between 80 g and 140 g. The samples of a first batch of slag samples were measured after a period of approximately 470 days after sample collection. Samples from a second batch (indicated as second batch), in total two fayalite slags samples, were sampled at a later date, prepared in the exact same way as the first batch and measured after a period of approximately 180 days after sample collection.

The slag samples are rich in aluminium oxides (typically 6 mass%)), iron oxides (typically 55 mass%) and silicon oxides (typically 23 mass%).

5.3.1.2. Flue Dust Samples

The flue dust is recovered by leading the off-gasses through fabric filter units. These are cleaned at regular time intervals by which the dust is transferred to dust silos for temporary storage. By the cleaning action and the subsequent fluidization of the dust for transport purposes, the dust is already mixed in the silos. Trucks are loaded directly from those silos. At several places of the truckload, grab samples are collected and mixed to form a homogeneous sample for measurements. Nine different batches of dust samples were monitored during the one-month production period, containing mainly Zn, and minor amounts of other non-ferrous metals. The dry mass of the collected samples ranged from 42 g to 76 g. The samples were measured after a period of approximately 470 days after sample collection.

5.3.1.3. Feedstock Samples

All feedstock materials are monitored upon arrival via a detection portal. As a result of this screening one type of feedstock material with elevated activities is selected for further investigations in the framework of this study. The considered feedstock material is mainly a metallic by-product of a primary non-ferrous metal producer, containing iron (> 70 %), and minor amounts of other metals. The radioactivity is primarily resulting from slag inclusions, which are difficult to separate from the metal phase. The considered feedstock material is a minor fraction of the total feedstock materials used in the production process. Samples for measurement were produced by mixing delivered lots (size from 25 to 50 tonnes) homogeneously by mobile cranes, and subsequently performing

several "coning & quartering" actions until a homogeneous and representative sample of about 500 kg is reached. This sample is further downsized by the same techniques using manual actions until a sample of circa 50 kg remains. Grab samples of this final sample were used for measurements. Five different batches of feedstock materials were monitored during the one-month production period. The dry mass of these samples ranged between 260 g and 570 g. The samples were measured after a period of approximately 470 days after sample collection.

5.3.2. Radiological Analysis

Measurements were performed on different HPGe-detectors of the Radionuclide Metrology Laboratory of JRC-Geel in Belgium. All detectors are located in the 225 m deep underground laboratory Hades located on the premises of the Belgian Nuclear Centre SCK•CEN in Mol, Belgium except for Ge-T5 which is located above ground. The detector details are listed in Table 5-3. The low background count rates of the underground detectors were in the order of 200 to 400 counts per day in the energy interval 40 to 2700 keV. The background count rate of individual peaks was mostly below 1 count per day. This low background is particularly important when measuring NORs that are known to be present in all detector systems. All samples for gamma-ray spectrometric analysis were transferred to radon tight Teflon® containers and stored for at least 21 days to reach secular equilibrium between ^{226}Ra and daughters. The slag and flue dust samples were positioned 2 mm above the endcap of each HPGe-detector except for detector Ge-8 where the samples were placed directly on the endcap. The feedstock samples were positioned 11 mm above the endcap of the HPGe-detector. The measurement times ranged from 2 to 7 days and the dead time was always below 1%.

Canberra's Genie 2000 software was used for data acquisition and spectrum analysis. The electron gamma shower National Research Council Canada (EGSnrc) [59] Monte Carlo code was used to calculate the full energy peak (FEP) efficiencies and the coincidence summing corrections. The Monte Carlo code input consists of the sample's measured dimensions, composition and density, and the detector set-up. Isotropic and uncorrelated emission of the gamma-rays was assumed in the simulations. A homogeneous distribution of radionuclides in the sample and of the sample material in the sample container were two other assumptions that were adopted in all the calculations.

The radionuclides occurring in natural decay series of ^{238}U and ^{232}Th, as well as ^{235}U and ^{40}K were investigated by their emitted gamma rays. An overview of the used gamma lines is found in Croymans et al. 2016 [60].

Table 5-3: HPGe detectors used for gamma-ray analysis.

	Ge-3	Ge-4	Ge-5	Ge-8	Ge-T5
Crystal type	P-type, coaxial	P-type, coaxial	P-type, planar	P-type, planar	P-type, coaxial
Relative efficiency	60%	100%	50%	19%	46%
Shielding	10 cm copper + 14 cm lead	7.5 cm copper + 15 cm lead	5 cm copper + 15 cm lead	5 cm copper + 15 cm lead	4 mm copper+ 10 cm lead
Top dead layer	0.7 mm	0.5 µm	0.5 µm	0.5 µm	0.6 mm
Samples measured	Slag 5, Flue dust samples	Slag 4, 6, 9, 11, 14, 20, 22, 26, 29, 31	Slag 1, 2, 3, 7, 12, 15, 17, 18, 19, 21, 23, 27,30	Slag 8, 10, 13, 16, 24, 25, 28	Feedstock materials
FWHM of QA at 661.6 keV	1.55	1.57	1.31	1.23	1.41
FWHM of QA at 1332 keV	1.89	1.96	1.75	1.64	1.86

A weighted mean of the activity was calculated for radionuclides with multiple gamma-rays. The activity of the different gamma-rays was taken into account. The Decay Data Evaluation Project (DDEP) website was used for the nuclear decay data [61].

The 186 keV peak is a doublet with contributions from ^{235}U (185.7 keV) and ^{226}Ra (186.2 keV). By subtracting the contribution from ^{226}Ra, from which the activity was determined from its daughters ^{214}Pb and ^{214}Bi, from the 186 keV doublet peak, the activity of ^{235}U is calculated. In addition, this result was confirmed by the other three main gamma lines of ^{235}U i.e. 143.8 keV, 163.4 keV and 205.3 keV. As natural isotopic abundance is expected for ^{235}U in these "non-nuclear" samples, one can see the measured $^{238}U/^{235}U$ activity ratio as a quality control of the measurement.

The activity concentration (in this paper meaning the activity per unit of mass) was determined by dividing the final activity determined for each radionuclide by the measured dry mass of the sample. All the activity concentrations were determined on the measurement date, mentioned in section 2.1 for each sample. Thus, no decay correction to the sampling date was made. The time of measurement between the first slag sample and the last slag sample was 42 days.

The uncertainties of the obtained activity concentrations were the combined standard uncertainties calculated according to the GUM (Guide to the expression of uncertainty in measurement) [62]. When combining several gamma-rays to one activity-value for one radionuclide and when combining activity-values from several daughters to one mother radionuclide using weighted means, the correlated parameters were excluded from the calculation of the uncertainty of the weighted mean and added separately afterwards in quadrature in order not to obtain unrealistic and far too low final uncertainties.

The ACI was calculated for slag 1 to 31 using the activity concentration of ^{226}Ra, ^{232}Th and ^{40}K (Equation 5-1). The EU-BSS assumes equilibrium between ^{232}Th and ^{228}Ac, and therefore the activity concentration of ^{228}Ac is used. The ACI calculation performed here assumes that the building material is constructed solely of the non-ferrous slag. Novel developments in IP production allow developing building materials solely out of non-ferrous fayalite slag [63].

Uncertainty of the ACI is calculated like in Equation 5-3.

$$\Delta(ACI) = \sqrt{\left(\frac{1}{300}\right)^2 \Delta(AC_{226Ra})^2 + \left(\frac{1}{200}\right)^2 \Delta(AC_{232Th})^2 + \left(\frac{1}{3000}\right)^2 \Delta\,(AC_{40K})^2}$$

Equation 5-3

Where AC*I* is the activity concentration index, *Δ(AC)* is the uncertainty of the activity concentration of the mentioned radionuclide.

5.4. Results and Discussion

Figure 5-1 and Figure 5-2 show the measured activity concentrations of radionuclides from the ^{232}Th and ^{238}U decay series in the slag mixtures. Table 5-4 shows the minimum and maximum activity concentrations, the ratio of the maximum over the minimum activity concentration and the ratio of different long living radionuclides over each other for feedstock material, flue dust and slag samples.

5.4.1. Assessment of Radiological Equilibrium in Samples

5.4.1.1. The ^{232}Th Decay Series

The activity concentrations of the relatively short-lived ^{224}Ra, ^{212}Pb, ^{212}Bi and ^{208}Tl (corrected for its branching) were equal within the measurement uncertainties. Their weighted mean value gave the activity concentration for ^{228}Th ($T_{1/2}$= 1.91 years). The activity concentration of the short-lived ^{228}Ac was

in equilibrium with its mother ^{228}Ra ($T_{1/2}$= 5.75 years). Looking at Table 5-4 the ratio of ^{228}Ra over ^{228}Th equals 1 in the feedstock material samples, flue dust samples and slag samples. For the slags, this equilibrium is not likely to have been established in the relatively short time (~470 days, two-thirds of the $T_{1/2}$ of ^{228}Th, and ~180 days, a quarter of the $T_{1/2}$ of ^{228}Th; for batch 1 and 2, respectively) between the production and the measurement. This means that Ra is not separated from Th during the industrial process of non-ferrous metal production. Th and Ra are both lithophilic and will therefore end up in the slag phase [64,65]. The affinity for silicates of both radionuclides confirms the unaffected equilibrium during the industrial process. Often in literature, equilibrium is assumed between ^{232}Th and ^{228}Ra, here the activity of ^{228}Ra is shown since this one is actually measured.

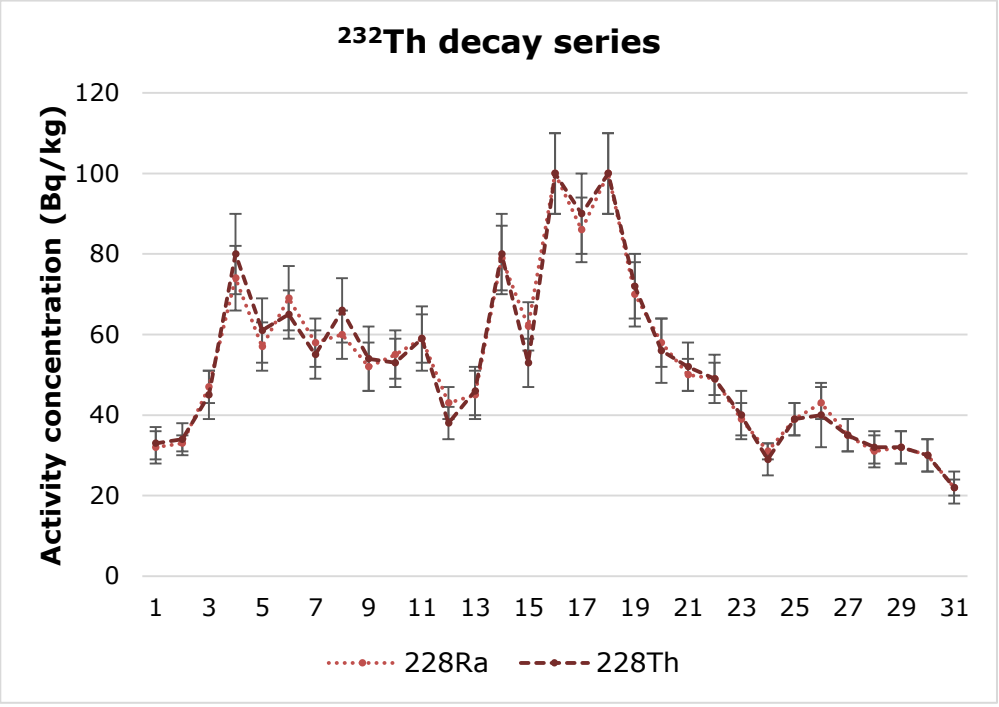

Figure 5-1: Activity concentration of 31 slag samples for the ^{232}Th decay series (coverage factor, k=2). Samples were collected at 31 consecutive days of slag production.

Table 5-4: minimum and maximum activity concentrations, ratio of the maximum over the minimum activity concentration and ratio of different long living radionuclides over each other for feedstock material, flue dust and non-ferrous fayalite slag samples (k=2).

Nuclide	Feedstock material (5 samples)			Flue dust (9 samples)		
	Activity concentration (Bq/kg)			Activity concentration (Bq/kg)		
	min	max	Ratio max/min	min	max	Ratio max/min
^{238}U	770 ± 90	2100 ± 300	2.7 ± 0.5	21 ± 8	50 ± 10	2 ± 1
^{226}Ra	410 ± 40	1600 ± 200	3.9 ± 0.6	0.8 ± 0.2	3.3 ± 0.2	4 ± 1
^{210}Pb	6000 ± 2000	22000 ± 7000	4 ± 2	300 ± 200	900 ± 300	3 ± 2
^{228}Ra	770 ± 70	2100 ± 200	2.7 ± 0.4	1.4 ± 0.2	2.8 ± 0.2	2.0 ± 0.3
^{235}U	27 ± 4	74 ± 8	2.7 ± 0.5	0.8 ± 0.2	2.3 ± 0.2	3 ± 1
^{228}Th	800 ± 100	2000 ± 400	2 ± 1	1.2 ± 0.2	3 ± 2	3 ± 2
^{40}K	10 ± 8	90 ± 10	9 ± 7	49 ± 6	210 ± 20	4.3 ± 0.7
^{228}Ra/^{228}Th	0.9 ± 0.2	1.0 ± 0.2		0.96 ± 0.09	1.5 ± 0.4	
^{238}U/^{226}Ra	1.2 ± 0.2	1.9 ± 0.3		10 ± 3	30 ± 10	
^{210}Pb/^{226}Ra	8 ± 3	20 ± 7		110 ± 30	900 ± 300	

Nuclide	Non-ferrous fayalite slag (31 samples)		
	Activity concentration (Bq/kg)		
	min	max	Ratio max/min
^{238}U	42 ± 4	180 ± 40	4.0 ± 1.0
^{226}Ra	14 ± 2	83 ± 8	5.9 ± 0.7
^{210}Pb	7 ± 4	90 ± 20	13 ± 7
^{228}Ra	22 ± 2	100 ± 10	4.5 ± 0.6
^{235}U	2.0 ± 0.4	8 ± 2	4 ± 1
^{228}Th	21 ± 2	100 ± 10	4.7 ± 0.5
^{40}K	26 ± 8	80 ± 10	3 ± 1
^{228}Ra/^{228}Th	0.9 ± 0.2	1.1 ± 0.2	
^{238}U/^{226}Ra	1.7 ± 0.4	7 ± 2	
^{210}Pb/^{226}Ra	0.14 ± 0.09	1.4 ± 0.5	

5.4.1.2. The ^{238}U Decay Series

For the ^{238}U series (Figure 5-2), the activity concentrations of ^{234}Th and ^{234m}Pa represent the activity concentration of ^{238}U, secular equilibrium is assumed since measurements of the samples took place approximately 470 days after the sample collection. The activity concentrations of ^{214}Pb and ^{214}Bi were equal within the measurement uncertainties so their mean value was taken as the activity for ^{226}Ra. The ^{226}Ra activity concentrations are for the slags a factor 1.7 ± 0.4 to 7 ± 2 lower than the activity concentration of ^{238}U (Table 5-4). This indicates an absence of equilibrium between ^{238}U and ^{226}Ra in the slags. This absence is surprising since U, Th and Ra, all are part of the first section of the ^{238}U decay series (^{238}U to ^{226}Ra) and are lithophilic elements [64,65]. So these elements have a high affinity for silicates and are expected to mainly end up in the slag phase.

This disequilibria is also present in the investigated feedstock material but less distinct, with a minimum and maximum ^{238}U/^{226}Ra ratio of 1.2 ± 0.2 and 1.9 ± 0.3 respectively (Table 5-4). Looking at another output material of the industrial process, the flue dust demonstrates an even more outspoken absence of equilibria with a minimum and maximum ^{238}U/^{226}Ra ratio of 10 ± 3 and 30 ± 10, respectively. It must be noted that the ^{238}U (maximum 50 ± 10 Bq/kg) and ^{226}Ra (maximum 3.3 ± 0.2 Bq/kg) activity concentrations of the flue dust samples are low in comparison with ^{238}U (minimum 42 ± 4 Bq/kg) and ^{226}Ra (minimum 14 ± 2 Bq/kg) activity concentrations of the slag samples (Table 5-4). In addition, per tonne slag approximately 25 kg of flue dust is produced. This means transport of ^{238}U and ^{226}Ra to the flue gasses is limited. The activity concentrations of ^{238}U and ^{226}Ra in the metallic fractions are low - this is confirmed by the company, however no data can be made publicly available. Regarding the lithophile properties of U and Ra and their limited absolute transport, it is believed that other sources of NORs which have a higher degree of disequilibrium than the measured feedstock material are present and consequently explain the relatively high level of disequilibria in the slag samples.

The activity concentrations ratios of ^{210}Pb over ^{226}Ra in the non-ferrous slags range between 0.14 ± 0.09 and 1.4 ± 0.5 (Table 5-4). In 9 cases, an absence of equilibrium is observed and the activity concentration of ^{210}Pb is lower than the activity concentration of ^{226}Ra. However, in slags 6 to 11, slags 17 to 23, slag 25 and slags 27 to 29 equal activity concentrations are measured (Figure 5-2). It is important to note that the observed equal activity concentrations of ^{226}Ra and ^{210}Pb cannot originate from the instalment of equilibrium of ^{210}Pb with ^{226}Ra during or after processing, since the half-life of ^{210}Pb is 22.23 years. Table 5-4 shows that for the flue dust the minimum and maximum ^{210}Pb/^{226}Ra ratios are 110 ± 30 and 900 ± 300, respectively, and for the feedstock material they are 8 ± 3 and 20 ± 7, respectively. So the absence of equilibrium is already present in the feedstock material but is less pronounced for the slag samples and more

pronounced for the flue dust samples. An enrichment in Pb concentration and enhanced levels of ^{210}Pb in dust samples in comparison to the used raw materials were also observed by Khater and Bakr, who studied the transport of ^{210}Pb transport in metallurgical industries [66]. The transport of Pb towards flue dust and fumes can be subscribed to the volatile nature of Pb. In addition, the ratio ^{210}Pb over ^{226}Ra in the slags samples is influenced by the transport of Pb towards the metallic phase i.e. the produced metal alloy. This transport is depending on the reduction potential in the furnace of the investigated smelter facility. Strong reducing conditions favor the transport of Pb towards the metal phase.

No ^{210}Pb was measured in slags 1 to 5 and the Minimum Detectable Activity (MDA) with a confidence limit of 95% was below 20 Bq/kg for slags 1 to 4 and 160 Bq/kg for slag 5. The MDA of slag 5 is higher due to the thicker dead layer of detector Ge-3, which impacts the FEP for the low-energy gamma-ray of ^{210}Pb.

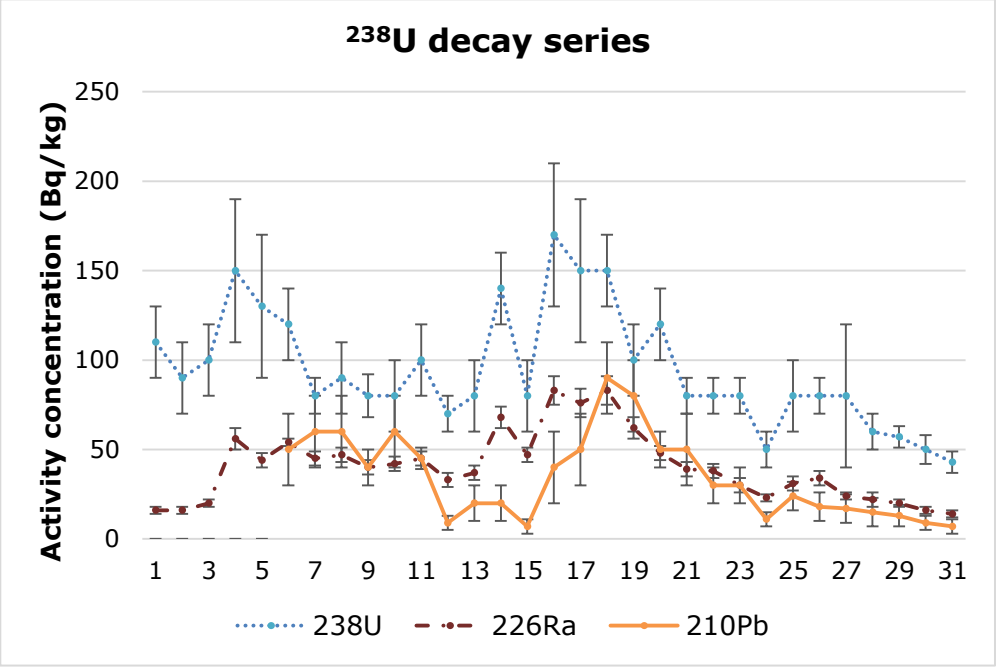

Figure 5-2: Activity concentration of 31 slag samples for the ^{238}U decay series (coverage factor, k=2). Samples were collected at 31 consecutive days of slag production.

The ratio of activity concentrations ^{238}U/^{235}U of all slags agreed within the uncertainties (except for slag 19) with the expected value of 21.6. The measured ^{238}U/^{235}U ratios (Figure 5-3) indicate therefore the expected natural

isotopic composition. This is an important quality control measure, which indicates that the gamma-spectrometric measurements were robust.

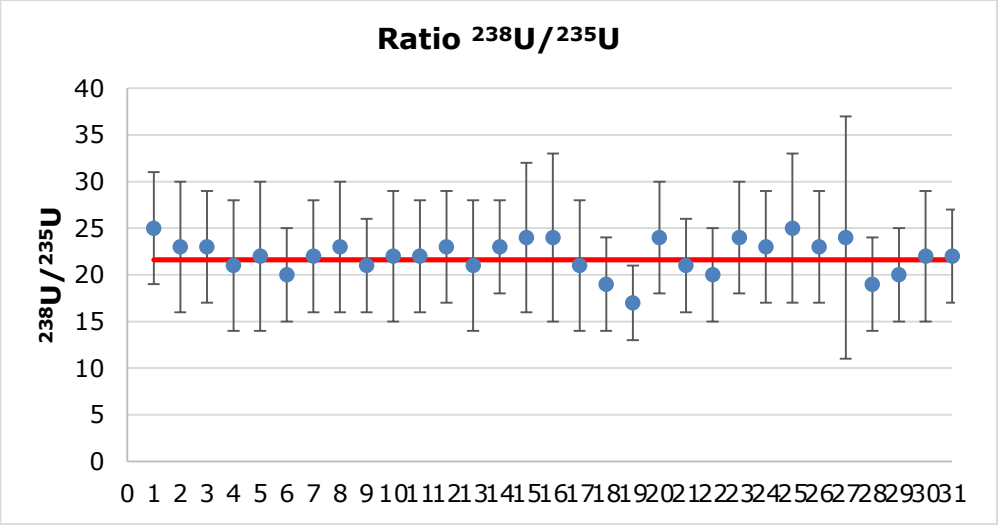

Figure 5-3: $^{238}U/^{235}U$ of slag 1 – slag 31, with ^{238}U via ^{234m}Pa (k=2). Red line indicates natural uranium ratio of 21.6. Samples were collected at 31 consecutive days of slag production.

5.4.1.3. ^{40}K

Potassium-40 is not a part of a decay series and has lithophilic properties (White, 2013). The ^{40}K activity concentrations in the slags vary between 26 ± 8 Bq/kg and 80 ± 10 Bq/kg (Figure 5-4 and Table 5-4).

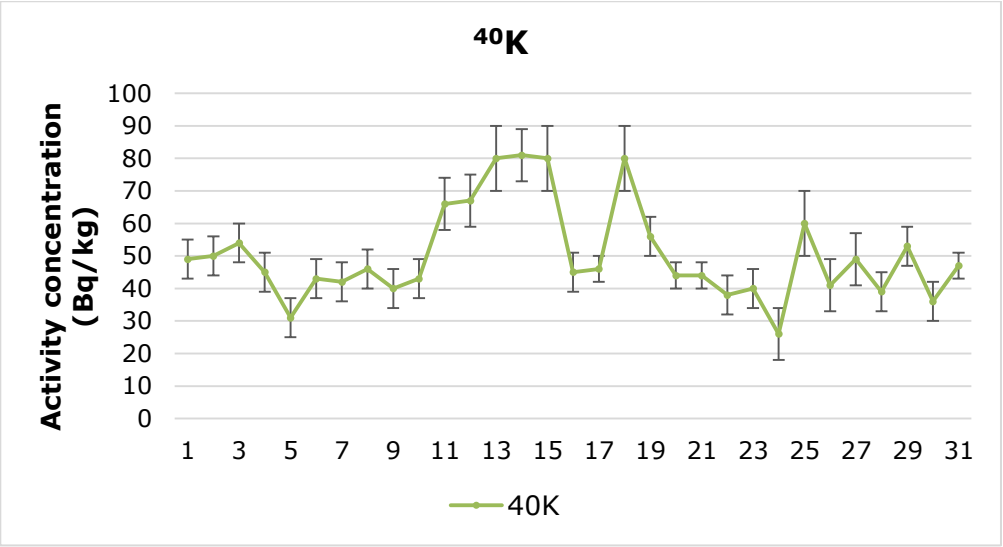

Figure 5-4: Activity concentration of slag 1 – slag 31 for ^{40}K (coverage factor, k=2). Samples were collected at 31 consecutive days of slag production.

5.4.2. Temporal Variation in the Activity Concentrations

The ratios of the maximum measured activity concentration over the minimum activity concentration for each long living radionuclide in the different materials (Table 5-4) indicate significant fluctuations. For the slags, the lowest ratio was 3 ± 1 for ^{40}K and the highest ratio was 13 ± 7 for ^{210}Pb whereas for the flue dust samples the lowest ratio was 2.0 ± 0.3 for ^{228}Ra and the highest ratios was 4.3 ± 0.7 for ^{40}K. The variations in the non-ferrous slag and flue dust samples can be explained as the smelter facility uses a mixture of primary and secondary raw materials. The radiological content of the input materials is strongly depending on the origin and as the data of the investigated feedstock material (Table 5-4) suggests also variations occur even when the origin of the input material is the same [67]. For the feedstock materials the lowest observed maximal/minimal ratio was 2 ± 1 for ^{228}Th and the highest observed ratio was 9 ± 7 for ^{40}K.

The selection, usage, ratios and amounts of the input material are driven by economic factors and optimized in function of the produced metals and a stable elemental composition in the slags and metals [68]. In addition, the company states that the amount of metals present in the input stream influences the quantity of slags and metals produced. Both quantities are also influenced by the process parameters. Therefore, differences occur between the production batches. The production batches are not aimed towards achieving an as low as possible activity concentration and the measured ratios differ significantly from unity even in the studied one-month period. It is clear that conclusions based on

the radiological characterisation of one day production or low frequency sampling over a larger period can be misleading. These measurements will only bear information on a specific time and not on the variation of the activity concentrations. Drawing conclusions based on a one-time sampling or low frequency sampling in order to ensure radiation protection of general public and workers should be performed cautiously. The authors recommend performing radiological measurements depending on the frequency of the discharge of the residues taking into account the complexity and variability of the facility/industry.

5.4.3. Comparison of Activity Concentrations with the Literature.

As discussed in the introduction and shown in Table 5-1, metallurgical slags can contain various amounts of NORs. Overall, the activity concentrations of the measured fayalite slags of this study are low compared with the metallurgical slags of Table 5-1. The quantity of slag per produced quantity of metal can vary depending on the production process. Gorai et al. (2003) estimated that for every tonne of copper 2.2 tonnes of slag is produced whereas Proctor et al. estimated that 220-370 kg blast furnace slag is produced per tonne of produced iron [69,70]. This in combination with the chemical characteristics of the slags and metals produced influences the transport of radionuclides and gives rise to enrichments or depletions in comparison with the input materials. Here, the slags originate from a secondary smelter facility, with a tonnage ratio of produced slags over metal above 1 and with scrap being the main input material for the recycling of metals. Since not all the feedstock contains enhanced concentrations of NORs, the result is that the activity concentration of the resulting slag is lower than the most active components in the feedstock.

5.4.4. Evaluation in function of Legislative Criteria

5.4.4.1. Evaluation considering the Exemption and Clearance Levels

Except for ^{210}Pb in the flue dust samples, all activity concentrations of the long living radionuclides in the slag and flue dust samples are below the EU-BSS | IAEA and RP-122 exemption/clearance levels (Table 5-2 and Table 5-4). This is in contrast with the feedstock materials for which all radionuclides – except for ^{235}U and ^{40}K - are above the exemption/clearance levels.

RP-122 part II specifies the exemption/clearance levels even when the secular equilibrium is absent via a summation rule. For slag 18 – having the highest observed activity concentrations - the result of this summation rule is 0.52 ± 0.03, well below the exemption/clearance level of 1.

5.4.4.2. Evaluation for Use as Building Material considering the ACI

Figure 5-5 shows the variation of the ACI when the fayalite slag is solely used (100%) to construct a building material. No day production batch exceeded the index value of 1, therefore every day production batch can be used as a building material. It must be noted that the highest observed activity concentrations (slag 18) are approximately a factor 12, 10 and 120 below the exemption/clearance levels of the EU-BSS for ^{226}Ra, ^{232}Th and ^{40}K, respectively, however the index has a value of approximately 0.8. So being well below the exemption/clearance levels does not necessarily imply that is in accordance with the limits applying to building materials.

Finally, it was observed that when only minor amounts of feedstock material, containing activity concentrations well above the EU-BSS exemption/clearance levels are used, the activity concentrations of the slags are below the exemption/clearance levels and the ACI value of 1 is not exceeded.

Portal monitoring provides valuable information on the input materials that could be of concern. Nevertheless, setting up holistic balances containing information on the activity concentration of all input materials per produced batch of output material can be difficult and cumbersome due to the complexity of industrial processes and large number of different input materials used. Therefore, one cannot exactly determine the impact of "elevated" feedstock materials so output monitoring in function of discharges provides the necessary information whether the residues are exempted or if they can be used in building materials considering the EU-BSS.

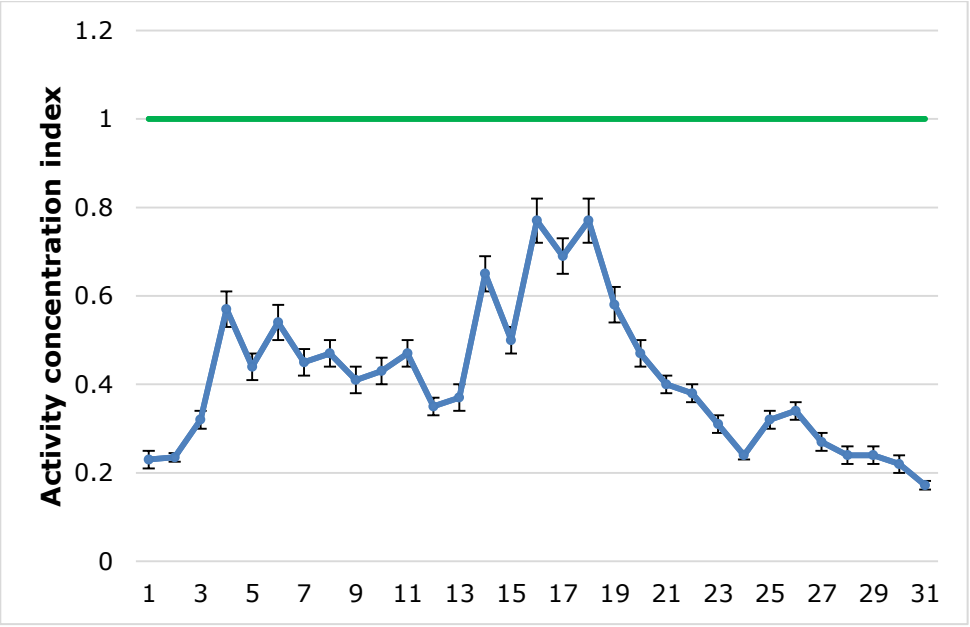

Figure 5-5: Activity concentration index (ACI) for slag 1 – 31 (k=2). Samples were collected at 31 consecutive days of slag production.

5.5. Conclusion

The current study monitored different materials processed in a non-ferrous smelter facility, which fits within the framework of the EU-BSS. Equilibria are discussed for the ^{232}Th and ^{238}U decay series. The ^{232}Th decay series was found to be in equilibrium for all the slags, measured feedstock material and flue dust. This was not the case for ^{238}U decay series due to lack of equilibrium in the feedstock material and the impact of the industrial process. The activity concentrations of the slags were all below the provided exemption/clearance levels of the EU-BSS and RP-122 part II, and are also low in comparison to slags reported in literature. The activity concentrations of the flue dust samples were all except for ^{210}Pb below the exemption/clearance levels. For the feedstock material only ^{40}K and ^{235}U were below the exemption/clearance levels. In addition, the ACI does not restrict the use of these non-ferrous slags to produce building materials.

Comparing the minimum and maximum observed activity concentrations for different radionuclides, differences up to a factor 13, 4.3 and 9 are registered for slag, flue dust and feedstock samples, respectively. These variations occur due to heterogeneity within the same input materials, and variation in input materials, input and output quantity and in the process parameters. The variations in activity concentrations indicate that using one-time sampling or

applying a low frequency of sampling can lead to misleading conclusions regarding the radiological output of a production process, in particular in complex systems. Consequently, drawing conclusions to ensure radiation protection should be performed cautiously and the complexity and variability of the facility or industry should be taken into account. Over the long time, production processes tend to change in time due to innovations, regulations and economic factors. These factors will impact both input and output and subsequently can also influence the radiological content of the residues. The frequency of the radiological monitoring should be optimized for a given plant in order to ensure radiation protection, especially when the residues are aimed towards reuse in public applications. The authors recommend monitoring depending on the frequency of the discharge of these residues.

5.6. Acknowledgements

The authors would like to thank the company for providing the samples and collaboration during this study. This work was supported by the European Commission within HORIZON2020 via the EURATOM project EUFRAT for transnational access. The authors would also like to acknowledge networking support by the COST Action TU1301.

5.7. References

[1] H.G. van Oss, 2011 Minerals Yearbook: Slag-Iron and Steel, 2013. http://minerals.usgs.gov/minerals/pubs/commodity/iron_&_steel_slag/myb1-2011-fesla.pdf.

[2] N.M. Piatak, M.B. Parsons, R.R. Seal, Applied Geochemistry Characteristics and environmental aspects of slag : A review, Elsevier Ltd, 2015. doi:10.1016/j.apgeochem.2014.04.009.

[3] National Slag Association, Common uses for slag, (2013). http://www.nationalslag.org/common-uses-slag (accessed May 22, 2016).

[4] European Commission, Laying down basic safety standards for protection against the dangers arising from exposure to ionising radiation, and repealing directives 89/618/Euratom, 90/641/Euratom, 96/29/Euratom, 97/43/Euratom and 2003/122/Euratom, Off. J. Eur. Union. (2014) 1–73.

[5] K. Leopold, D. Weiss, New approach to assessment and reduction of health risk and environmental impact originating from TENORM according to requirements of EU directive 96/29, 2003.

[6] T.P. Ryan, A. Janssens, E. Henrich, J.-L. Daroussin, Z.K. Hillis, E.I.M. Meijne, Industries giving rise to NORM discharges in the European Union - A review, in: Nat. Occur. Radioact. Mater. (NORM IV), 2004: pp. 169–185.

[7] M. Omar, NORM waste management in Malaysia, in: Int. Conf. Saf. Radioact. Waste Manag., 2000: pp. 89–92.

[8] B. Ismail, I.L. Teng, Y.M. Samudi, Relative radiological risks derived from different TENORM wastes in Malaysia, Radiat. Prot. Dosimetry. 147 (2011) 600–607.

[9] J.C. Gilmore, R.G. Jackson, Radiological hazards from deposits of Tin-smelting slag and the problems of site clearance and disposal, in: Proc. Eighth Int. Congr. Radiat. Prot. Int. Radiat. Prot. Assoc. Montr., 1992: pp. 1408–1411.

[10] M. Omar, M.S. Hamzah, A.K. Wood, Radioactive disequilibrium and total activity concentration of NORM waste, J. Nucl. Relat. Technol. 5 (2008) 47–56.

[11] K.M. Kontol, S.H.S.S. Ahmad, M. Omar, Radiological impact assessment for landfill disposal of NORM wastes in Malaysia, in: Nat. Occur. Radioact. Mater. (NORM V), 2007: pp. 355–359.

[12] M.A.A. Garcia, Caracterização Radioquímica E Impacto Radiológico Ambiental No Processamento De Cassiterita Para Produção, 2009.

[13] European Commission, Materials containing natural radionuclides in

enhanced concentrations - Report EUR 17625, 1997.

[14] R. Lehmann, Strahlenbelastung durch natürliche radionuklide in baumaterialien, fossilen brennstoffen und Dungemitteln, Bundesamt Für Strahlenshutz, Berlin. (1996) 135–156.

[15] A. Żak, K. Isajenko, B. Piotrowska, M. Kuczbajska, A. Ząbek, T. Sczygielski, Natural radioactivity of wastes, Nukleonika. 55 (2008) 387–391.

[16] M.A. Pires do Rio, E.C.S. Amaral, H.M. Fernandes, E.R.R. Rochedo, Environmental radiological impact associated with non-uranium mining industries: A proposal for screening criteria, J. Environ. Radioact. 59 (2002) 1–17. doi:10.1016/S0265-931X(01)00023-6.

[17] A. Zak, Exposure to radiation from the natural radionuclides indoors investigation of radioactivity of raws and building materials, Cent. Lab. Radiol. Prot. Bi-Annual Rep. 1994-1995. (1995) 51–55.

[18] J. Skowronek, B. Michalik, J. Dulewski, NORM in Polish industry, in: Proc. an Int. Conf. Held Szczyrk, Poland, 17–21 May 2004, 2004: pp. 1–9.

[19] A. Zak, M. Biernacka, J. Jagielak, P. Lipinski, Investigations of radioactivity of building raws and materials, Nukleonika. 38 (1993) 51–70.

[20] European Commission, Radiation protection 122 practical use of the concepts of clearance and exemption Part II application of the concepts of exemption and clearance to natural radiation sources, 2002.

[21] G.M. Crockett, K.R. Smith, W.B. Oatway, S.F. Mobbs, NRPB-W48 Radiological impact on the UK population of industries which use or produce materials containing enhanced levels of naturally occurring radionuclides Part II: The steel production industry, 2003.

[22] J.S. Hughes, M.P. Harvey, A Study on the Transport of Naturally-Occurring Radioactive Material HPA-RPD-036, 2008.

[23] A. Ene, A. Pantelica, Characterization of Metallurgical slags using low-level gamma-ray spectrometry and neutron activation analysis, Rom. J. Phys. 56 (2011) 1011–1018.

[24] J. Van Der Steen, Regulatory approaches for NORM residues in the Netherlands, in: Regul. Manag. Approaches Control Environ. Residues Contain. Nat. Occur. Radioact. Mater., 2004: pp. 61–73.

[25] L.A. Wendling, M.T. Binet, Z. Yuan, F. Gissi, D.J. Koppel, M.S. Adams, Geochemical and ecotoxicological assessment of iron- and steel-making slags for potential use in environmental applications, Environ. Toxicol. Chem. 32 (2013) 2602–2610. doi:10.1002/etc.2342.

[26] R. Taha, O. Sirin, H. Sadek, Beneficial use of Qatar's steel slag and gravel

deposits in road construction, Int. J. Waste Resour. 4 (2014) 1–7. doi:10.4172/2252-5211.1000167.

[27] T. Sofilic, D. Barisic, U. Sofilic, Natural radioactivity in steel slag aggregate, Arch. Metall. Mater. 56 (2011) 627–634. doi:10.2478/v10172-011-0068-y.

[28] B. Smodis, U. Repinc, L. Benedik, Identification and inventory of TENORM sources in Slovenia, Czechoslov. J. Phys. 56 (2006) 37–42.

[29] G. Tanase, M. Tanase, Natural radioactivity in iron and steel materials by low-level gamma spectrometry, Rom. J. Phys. 48 (2003) 363–368.

[30] M. Sahagia, A. Luca, A. Antohe, R. Ioan, M. Tanase, E. Garcia Torano, Comparison of analysis methods for the characterisation of the radioactive content of metallurgical slag used within the EURAMET-EMRP JRP IND04 metrometal, Rom. Reports Phys. 66 (2014) 649–657.

[31] J. Jeong, M. Baik, C. Park, T. Park, N. Ko, K.H. Yoon, A basic study on the radiological characteristics and disposal methods of NORM Wastes, J. Nucl. Fuel Cycle Waste Technol. 12 (2014) 217–233.

[32] Z.M. ALamoudi, F.G. ALmehmadi, Concentrations of the Naturally Occurring Radioactive Materials in waste samples from iron production the carbon filters used in Saudi Arabia, Life Sci. J. 10 (2013) 641–647. doi:10.1017/CBO9781107415324.004.

[33] K. Brodén, S.R. Ab, Y. Sandell, Radioactivity in commercially available metals, 2001.

[34] NORM4Building, Database of NORM4Building, (2016). http://norm4building.org/db/ (accessed July 1, 2016).

[35] T. Sofilić, D. Barišić, A. Rastovčan Mioč, U. Sofilić, Radionuclides in steel slag intended for road construction, J. Radioanal. Nucl. Chem. 284 (2010) 73–77. doi:10.1007/s10967-009-0431-x.

[36] T. Sofilić, D. Barišić, U. Sofilić, Monitoring of 137Cs in electric arc furnace steel making process, J. Radioanal. Nucl. Chem. 284 (2010) 615–622. doi:10.1007/s10967-010-0513-9.

[37] D. Xirouchakis, V. Manolakou, Properties of an EAf slag produced in Greece : a construction material for sustainable growth, 5th Int. Conf. Bitum. Mix. Pavements. (2011).

[38] H. Vanmarcke, J. Paridaens, P. Froment, J. Van Cauteren, C. Timmermans, C. Cosemans, F. Sassi, Identification and characterization of NORM industries in Belgium, in: Proc. IRPA12 12. Congr. Int. Radiat. Prot. Assoc. Strength. Radiat. Prot. Worldwide-Highlights, Glob. Perspect. Futur. Trends., 2010.

[39] F.A. Ugur, S. Turhan, H. Sahan, M. Sahan, E. Goren, F. Gezer, Z.

Yegingil, Investigation of the activity level and radiological impacts of naturally occurring radionuclides in blast furnace slag, Radiat. Prot. Dosimetry. 153 (2013) 502–508.

[40] S. Chinchón-payá, B. Piedecausa, S. Hurtado, M.A. Sanjuán, S. Chinchón, Radiological impact of cement , concrete and admixtures in Spain, Radiat. Meas. 46 (2011) 734–735. doi:10.1016/j.radmeas.2011.06.020.

[41] Ş. Turhan, Assessment of the natural radioactivity and radiological hazards in Turkish cement and its raw materials, J. Environ. Radioact. 99 (2008) 404–414. doi:10.1016/j.jenvrad.2007.11.001.

[42] T. Sofilic, D. Barišic, U. Sofilic, M. Đurokovic, Radioactivity of some building and raw materials used in Croatia, Polish J. Chem. Technol. 13 (2011) 23–27. doi:10.2478/v10026-011-0032-7.

[43] F. Puertas, M.M. Alonso, M. Torres-Carrasco, P. Rivilla, C. Gasco, L. Yagüe, J.A. Suárez, N. Navarro, Radiological characterization of anhydrous/hydrated cements and geopolymers, Constr. Build. Mater. 101 (2015) 1105–1112. doi:10.1016/j.conbuildmat.2015.10.074.

[44] R. Mustonen, Methods for evaluation of doses from building materials, Radiat. Prot. Dosimetry. 7 (1984) 235–238.

[45] M. Sharaf, M. Mansy, A. El Sayed, E. Abbas, Natural radioactivity and radon exhalaton rates in building materials used in Egypt, Radiat. Meas. 31 (1999) 491–495. doi:10.1017/CBO9781107415324.004.

[46] M. Gallyas, I. Torok, Natural radioactivity of raw materials and products in the cement industry, Radiat. Prot. Dosimetry. 7 (1984) 69–71. doi:10.1017/CBO9781107415324.004.

[47] H. Baltas, E. Kiris, İ. Ustabas, E. Yilmaz, M. Sirin, E. Kuloglu, B. Erdogan Gunes, Determination of natural radioactivity levels of some concretes and mineral admixtures in Turkey, Asian J. Chem. 26 (2014) 3946–3952. doi:10.1093/jae/ejm029.

[48] J. Pensko, Z. Stpiczynska, K. Blaton-Albicka, Emanating Power of Radon-222 Measured in Building Materials Original from Typical Building Materials Used in Poland Original from, in: CONF-780422 (VOL. 2), 1980: pp. 1407–1414.

[49] European Commission, Radiation protection 112 Radiological protection principles concerning the natural radioactivity of building materials, (1999) 1–16.

[50] H. Cabanekova, The concentration of natural radionuclides in various types of building materials in slovakia, J. Radioanal. Nucl. Chem. 209 (1996) 142–144.

[51] L.E. Muntean, C. Cosma, D. V. Moldovan, Measurement of natural radioactivity and radiation hazards for some natural and artificial building

materials available in Romania, J. Radioanal. Nucl. Chem. 299 (2014) 523–532. doi:10.1007/s10967-013-2837-8.

[52] T. Sofilic, D. Bariši, Ž. Grahek, Š. Cerjan-stefanovi, A. Rastov, B. Mio, Radionuclides in metallurgical products and waste, Acta Metall. Slovaca. 10 (2004) 29–35.

[53] H. Cabáneková, Building materials as the source of radiation load of Slovak population, 2008.

[54] IAEA, Application of the Concepts of Exclusion, Exemption and Clearance Safety Guide RS-G-1.7, 2004.

[55] Y. Pontikes, L. Machiels, S. Onisei, L. Pandelaers, D. Geysen, P.T. Jones, B. Blanpain, Slags with a high Al and Fe content as precursors for inorganic polymers, Appl. Clay Sci. 73 (2013) 93–102. doi:10.1016/j.clay.2012.09.020.

[56] J.L. Provis, Geopolymers and other alkali activated materials: why, how, and what?, Mater. Struct. 47 (2014) 11–25. doi:10.1617/s11527-013-0211-5.

[57] J.L. Provis, J.S.J. van Deventer, Alkali Activated Materials State-of-the-Art Report, RILEM TC 224-AAM, 1st ed., Springer Dordrecht Heidelberg New York London, 2014. doi:10.1007/978-94-007-7672-2.

[58] K.S. Al-jabri, A.H. Al-saidy, R. Taha, Effect of copper slag as a fine aggregate on the properties of cement mortars and concrete, Constr. Build. Mater. 25 (2011) 933–938. doi:10.1016/j.conbuildmat.2010.06.090.

[59] I. Kawrakow, E. Mainegra-Hing, F. Tessier, B.R.B. Walters, The EGSnrc C++ class library, NRC Rep. PIRS-898 (Rev A). (2009).

[60] T. Croymans, W. Schroeyers, P. Krivenko, O. Kovalchuk, A. Pasko, M. Hult, G. Marissens, G. Lutter, S. Schreurs, Radiological characterization and evaluation of high volume bauxite residue alkali activated concretes, J. Environ. Radioact. 168 (2017) 21–29. doi:10.1016/j.jenvrad.2016.08.013.

[61] Laboratoire national Henri Becquerel, Decay Data Evaluation Project, (2016). http://www.nucleide.org/DDEP.htm (accessed May 22, 2016).

[62] JCGM WG1, Evaluation of measurement data — Guide to the expression of uncertainty in measurement, 2008.

[63] L. Kriskova, P.T. Jones, H. Jannsen, B. Blanpain, Y. Pontikes, Synthesis and Characterisation of Porous Inorganic Polymers from Fayalite Slag., Slag Valoris. Symp. Zero Waste. 4 (2015) 227–230.

[64] B. Bourdon, S. Turner, G.M. Henderson, C.C. Lundstrom, Introduction to U-series Geochemistry, Rev. Mineral. Geochemistry. 52 (2003) 1–21.

[65] W.M. White, Chapter 7: Trace elements in Igneous processes, in: Geochemistry, 2013: pp. 259–313.

[66] A.E.M. Khater, W.F. Bakr, Technologically enhanced 210Pb and 210Po in iron and steel industry, J. Environ. Radioact. 102 (2011) 527–530. doi:10.1016/j.jenvrad.2011.02.002.

[67] IAEA, Extent of Environmental Contamination by Naturally Occurring Radioactive Material (NORM) and Technological Options for Mitigation - Technical reports series no. 419, 2003.

[68] T. Nakamura, K. Halada, Urban Mining Systems, 1st ed., Springer Japan, 2015.

[69] D.M. Proctor, K.A. Fehling, E.C. Shay, J.L. Wittenborn, J.J. Green, C. Avent, R.D. Bigham, M. Connolly, B. Lee, T.O. Shepker, M.A. Zak, Physical and chemical characteristics of blast furnace, basic oxygen furnace, and electric arc furnace steel industry slags, Environ. Sci. Technol. 34 (2000) 1576–1582. doi:10.1021/es9906002.

[70] B. Gorai, R.K. Jana, Characteristics and utilisation of copper slag - a review, Resour. Conserv. Recycl. 39 (2003) 299–313. doi:10.1016/S0921-3449(02)00171-4.

Chapter 6: Gamma Exposure from Building Materials – a Dose Model with Expanded Gamma Lines from Naturally Occurring Radionuclides Applicable in Non-Standard Rooms.

The results of this chapter have been published:

T. Croymans, F. Leonardi, R. Trevisi, C. Nuccetelli, S. Schreurs, W. Schroeyers, Gamma exposure from building materials - a dose model with expanded gamma lines from naturally occurring radionuclides applicable in non-standard rooms, Constr. Build. Mater. 159 (2017) 768–778.

Preface/Link with objectives: This chapter fits within objective 3 of this thesis and is focused on dose models for building materials. In order to assess safe use of building materials containing NORs, dose models can be used. The EU-BSS set a limit of 1 mSv per year and proposes a screening tool called the activity concentration index (ACI). Nevertheless, this ACI does not allow changing the building material characteristics and room properties. In addition, a limited set of gamma emission lines is considered in the ACI. The focus of this chapter is to study the impact of the gamma emmission intensity on the effective gamma dose in case of a rectangular room. Consequently, a novel dose calculation model was developed based on the Markkanen model (Section 2.6.4.1) in which an expanded set of gamma lines were used. Additionaly, this chapter compares different index and dose calculations relevant for the dose assessment within the European legislative framework applicable towards building materials.

6.1. Abstract

Building materials are a significant source of gamma rays exposure due to the presence of naturally occurring radionuclides (NORs). In order to protect the public from harmful radiation, the European basic safety standards (Council directive 2013/59/Euratom) [1] introduced a one-size-fits-all building(s) (materials) activity concentration index (ACI) based on a limited set of gamma lines. The ACI is considered *"as a conservative screening tool for identifying materials that may cause the reference level (i.e. 1 mSv/y) laid down in article 75(1) to be exceeded".* Regarding calculation of dose, many factors such as density and thickness of the building material, as well as factors relating to the type of building, and the gamma emission data need to be taking into account to

References at page 186

ensure accurate radiation protection. In this study, the implementation of an expanded set of 1845 gamma lines, related to the decay series of ^{238}U, ^{235}U and ^{232}Th as well as to ^{40}K, into the calculation method of Markkanen [2], is discussed. The expanded calculation method is called the Expanded Gamma Dose Assessment (EGDA) model. The total gamma emission intensity increased from 2.12 to 2.41 and from 2.41 to 3.04 for the ^{238}U and ^{232}Th decay series, respectively. In case of ^{40}K a decrease from 0.107 to 0.106 is observed. The ^{235}U decay series is added, having a gamma emission intensity of 3.1. In a standard concrete room, absorbed dose rates in air (D_A) per unit of activity concentration of 0.849, 0.256, 1.08, 0.0767 nGy/h per Bq/kg are observed. The use of weighted average gamma lines increased the D_A with 6.5 % and 1 % for the ^{238}U and ^{232}Th decay series, respectively. A decrease of 4.5 % is observed in the D_A of ^{235}U decay series when using the weighted average gamma lines in comparison to its non-averaged variant. The sensitivity of the EGDA model for density, wall thickness, presence of windows and doors and room size is investigated. Finally, a comparison of the index and dose calculations relevant for the dose assessment within the European legislative framework applicable towards building materials is performed. In cases where the ACI and density and thickness corrected dose calculation of Nuccetelli et al. [3] cannot provide guidance, the EGDA allows performing more accurate dose assessment calculations leading to effective doses which can be several 100 µSv/a lower.

6.2. Introduction

Building materials are a significant source of indoor gamma dose [4]. The importance to address the exposure originating from building materials is underlined in article 75 of the Euratom basic safety standards (EU-BSS) (Council directive 2013/59/Euratom), which must be transposed to national law by EU Member States before February 2018 [1]. This article states that "*The reference level applying to indoor external exposure to gamma radiation emitted by building materials, in addition to outdoor external exposure, shall be 1 mSv per year*". This European legislation was developed to establish basic standards, applicable in EU member states, for the protection against exposure of ionising radiation for workers and the general public. In a broader context, this legislation supports several launched initiatives of the European Commission for turning waste into a resource and promoting reuse and recycling with focus on the building industry in the framework of the Europe 2020 strategy [5–7]. In this context, the EU-BSS aims towards a safe use of by-products, originating from NORM (Naturally Occurring Radioactive Material)-processing industries, like metallurgical slags, fly and bottom ash, phosphogypsum and red mud. These residues are used or investigated to use in cement-based matrixes as supplementary cementitious materials (SCM) on a large scale [8–12]. In addition, more and more research is conducted to use these residues in cement alternatives which generate less CO_2, like inorganic polymers (IPs) [8–10]. This

fits with the aim to reduce the usage of primary resources. It is expected that future building materials used for dwellings will shift more and more towards these secondary raw materials that can potentially be rich in naturally occurring radionuclides (NORs): therefore the impact on the external gamma exposure of the use of these secondary raw materials needs to be assessed [10,13,14].

In order to assess the impact on external gamma exposure of building materials, different calculation methods, based on Monte Carlo simulations, integration and simple index and dose formulas, have been developed in the past [2,15–26]. Different dose assessment calculations have been developed based on gamma-ray attenuation and build-up factors [2,16,17,22,27]. These calculations allow specifying the physical parameters of the room and the material it is constructed out, in a straightforward way. The density and wall thickness are identified as the most critical parameters. Modifying these parameters, for the evaluation of non-standard rooms, can generate dose rate differences up to 40 % compared to a standard concrete room [27]. Seeking for a standardized approach, the EU-BSS [2] proposes a screening index, named activity concentration index (ACI). This index was originally developed by Markkanen [2] and is described in the technical guide Radiation Protection (RP)-112 [28]. The ACI is based on a number of assumptions that are not all necessarily valid. The ACI assumes a concrete room (400 cm x 500 cm x 280 cm) with a density of 2350 kg/m^3 and thickness of 20 cm for all surfaces (walls, floor and ceiling). In the last years, in order to get a reliable screening tool, that will allow for a realistic discrimination of building materials, a new density and thickness corrected index I(ρd) was developed by Nuccetelli et al. [3]. The available dose assessment models focus on the standard composition of concrete, however the increased usage of residues, which have an *a priori* chemical compositions differing from conventional raw materials (like OPC and gravel), can result in structures with very different compositions. Some models consequently apply a correction factor to compensate for the different composition [29]. In addition, disequilibrium in the ^{238}U and ^{232}Th decay series chain can be present for residues from NORM-processing industries. Information regarding disequilibrium can be valuable for gaining insight into environmental or industrial processes. However, when dealing with the dose assessments of building materials one should assess how meaningful the consideration of disequilibrium is. Up to now, to the authors' knowledge, in none of the existing dose calculations, disequilibrium situations are taken into account. In contrast, RP-122 [30] suggests using the highest activity concentration of a radionuclide present in a certain decay series to specify the activity concentration of that whole decay series. In none of the existing tools the presence of ^{235}U and its decay products is considered.

The above mentioned calculation methods have in common that they only use a fraction of the gamma emission lines known today. In practice, this means that often dose models use a specific set of major gamma lines or that the set of several major gamma lines is reduced to one or several averaged gamma lines

with the gamma intensity as weighing factor. Whereas, the gamma emission intensity of this averaged gamma line is the sum of the individual gamma emission intensities. This technique is performed to provide simplicity. However, progress has been made in the characterization of the gamma emissions of radionuclides. The Laboratoire National Henri Becquerel has built an online database providing continuously updated information on the gamma emission lines of a wide range of radionuclides that allows going beyond this simplified approach [31]. Implementation of this database into a dose calculation method allows a more accurate safety assessment to evaluate if construction products can be used from a radiation protection point of view [3]. Both sample parameters, like density and composition, as well as room parameters like thickness of the walls, ceiling and floor, number of walls present, the sample composition of each wall etc. impact the final received dose [15,27]. An adaptable dose assessment calculation allows taking these parameters into account.

Using an flexible dose or index calculation, in contrast to a screening index, for the evaluation of building materials fits better with the 1 mSv dose requirement of article 75 of the EU-BSS [2], in particular when dealing with non-standard room and building material parameters. In addition, the implementation of non–standard room and building material parameters deals with the requirement of annex VII of the EU-BSS [2], that states "*The calculation of dose needs to take into account other factors such as density, thickness of the material as well as factors relating to the type of building and the intended use of the material (bulk or superficial)*". The current study implements improvements, based on scientific data available in literature, into the existing and validated Markkanen room model [2]. A sensitivity analysis of the different parameters impacting the calculated absorbed dose rate in air is performed. For the different improvements implemented in the dosimetric evaluation, the impact and practicality for industrial implementation is discussed.

6.3. Materials & Methods:

6.3.1. Materials

For the evaluation of the dose model the composition of concrete, defined by NIST [32], is used, except when mentioned differently.

6.3.2. Model

6.3.2.1. Model Description

To assess the absorbed dose rate in air (D_A), the room model of Markkanen [2] (see Equation 6-1) is used.

$$D_A = 5.77\text{x}10^{-7}\ \frac{AC\,\rho}{4\pi}\sum_i \gamma_i \left(\frac{\mu_{en}}{\rho}\right)_i E_i \int B_i \frac{\mathrm{e}^{-\mu_i s}}{l^2}\mathrm{dV}$$

Equation 6-1

With D_A the absorbed dose rate in air in Gy/h, *AC* the activity concentration of a radionuclide incorporated in the material of concern in Bq/kg, ρ the density of the material in kg/m^3, γ_i the gamma intensity of gamma line *i*, $(\mu_{en}/\rho)_i$ the energy absorption coefficient in air for gamma energy E_i in cm^2/g, E_i the photon energy in MeV, μ_i the linear attenuation coefficient of the material for gamma energy E_i in cm^{-1}, B_i the dose build up factor (see Equation 6-2) calculated via the Berger's formula, l the distance between the point of detection (x_p, y_p, z_p) and the point of integration in cm (see Equation 6-4) and *s* the fraction of l within the top layer in cm (see Equation 6-3). The total absorbed dose rate in air is the sum of the absorbed dose rate in air calculated from ceiling, floor and each wall. The $(\mu_{en}/\rho)_i$ is a polynomial best fit achieved from the data reported by Martin [33] using the data of Hubbell and Seltzer [34].

$$B_i = \ 1 + C(E_i)\mu_i s e^{D(E_i)\mu_i s}$$

Equation 6-2

In literature different *C* and *D* parameters are proposed by different authors. In the model described here, the values of *C* and *D* proposed by Pelliccioni [35] are used. These are calculated for the energy spectrum via logarithmic and exponential best-fit function respectively by using the concrete parameters described by Pelliccioni [35] at 7 mean free paths (MFP).

$$s = \ \left|\frac{z}{z_p - z}\right| l$$

Equation 6-3

$$l = \ \sqrt{(x_p - x)^2 + (y_p - y)^2 + (z_p - z)^2}$$

Equation 6-4

In order to convert the D_A to effective dose a conversion factor of 0.7 Sv/Gy is used [28]. This conversion factor is used for all gamma emitters and originates from the UNSCEAR 2000 report [4]. This conversion factor is used in the dose calculations considered in this article and is consequently used for comparison reasons. Nevertheless, nuclide specific conversion factors have been suggested by Krstic and Nikezic [36].

The model assumes a homogeneous sample composition and a homogeneous distribution of the radionuclides throughout the composed materials. In addition, a standard room is used as a reference throughout the paper. The standard room size was described by Koblinger [15] as measuring 400 cm x 500 cm x 280 cm and adopted by RP-112 [28]. Here a standard thickness of walls, floor and ceiling of 20 cm is assumed. Neither doors nor windows are present and the point of detection (x_p, y_p, z_p) is set at the middle of the room. Whereas, Koblinger suggested a density of 2320 kg/m^3, RP-112 suggests a density of 2350 kg/m^3 [15,28]. The value of 2350 kg/m^3 is used here as a standard.

No background correction is assumed when calculating the D_A.

All calculations are performed by a combination of Microsoft® excel and R® [37]. The input parameters are submitted in Microsoft® excel whereas the further treatment of the input data is performed by Microsoft® excel and R®.

6.3.2.2. Selection of the Number of Gamma Lines.

In order to check the impact of the number of gamma lines, a comparison of the absorbed dose rate in air is made between different dose assessment models for a standard room. The Markkanen [2], Mustonen [22], ISS room model [23] and the model developed in this study, further called Expanded Gamma Dose Assessment (EGDA) model, are compared. Different versions of the EGDA model are evaluated depending on the number of gamma lines used for the dose assessment. 'EGDA>1%', 'EGDA>0.1%', 'EGDA>0%' take into account all gamma lines which have a gamma emission intensity (including the branching factor) above respectively 1 %, 0.1 % and 0 % when considering gamma emission lines from the ^{238}U, ^{232}Th and ^{235}U decay series and ^{40}K. In addition, two variants of 'EGDA>0.1%' are discussed. In one variant the emission gamma lines of ^{238}U and ^{232}Th (except for the 2614 keV gamma emission line since this emission line represents approximately 38 % of the dose rate of the ^{232}Th decay series) of 'EGDA>0.1%' are converted to one weighted average gamma emission line. This variant is indicated in Table 6-1 by the suffix "averaged". In the second variant, the emission gamma lines which have a gamma emission intensity lower than 0.1 % are converted to one weighted average gamma line for ^{238}U, ^{232}Th and ^{235}U. This variant is indicated in Table 6-1 as "EGDA+". Details on each model are provided in Table 6-1. Since not all the details necessary for the calculations were present in the original paper of Markkanen [2] and Mustonen [22], updated values were used (details in Table 6-1). This is indicated by a suffix "updated". In addition, a second variant of the ISS room model, which makes use of the Berger parameters described by Pelliccioni [35] instead of the Berger parameters of Markkanen [2], is discussed. This variant is indicated with the infix "Pelliccioni" whereas the original ISS room model is indicated with the infix "original". For readability, abbreviations of the dose

model names are provided in Table 6-1 and Table 6-5. These abbreviations are used further throughout the chapter.

Table 6-1: Overview of the different dose calculation models and their parameters used to evaluate the absorbed dose rate in air.

Model	Markkanen original	Markkanen updated	Mustonen updated	ISS original room model	ISS Pelliccioni room model
Concrete composition	Markkanen 1995 [2]	Ordinary Portland concrete (NIST)	Ordinary Portland concrete (NIST)	Ordinary Portland concrete (NIST)	Ordinary Portland concrete (NIST)
Energy absorption coefficient in air	Markkanen 1995 [2]	Best fit from Martin 2006 [33]	Best fit from Martin 2006 [33]	Hubbell 1982 [38]	Hubell 1982 [38]
Density (kg/m^3)	2350	2350	2350	2350	2350
Linear attenuation coefficient	From Markkanen 1995 [2]	XCOM [39]: ordinary Portland concrete (NIST)	XCOM [39]: ordinary Portland concrete (NIST)	Hubbell 1982 [38]	Hubbell 1982 [38]
Gamma emission energy and intensity	Markkanen 1995 [2]	Mustonen 1984 [22]	Mustonen 1984 [22]	NuDat website [40]	NuDat website [41]
Berger Parameters	Markkanen 1995 [2]	Best fit of Pelliccioni 1989 [35]	Best fit of Pelliccioni 1989 [35]	Best fit of Markkanen 1995 [2]	Best fit of Pelliccioni 1989 [35]
Number of gamma lines ^{238}U	1	1	24	19*	19*
Gamma emission intensity ^{238}U* **	2.12	2.12	2.12	2.41	2.41
Number of gamma lines ^{232}Th	2	2	20	14*	14*
Gamma emission intensity ^{232}Th* **	2.41	2.41	2.41	2.63	2.63

Table 6-1 (Continuation): Overview of the different dose calculation models and their parameters used to evaluate the absorbed dose rate in air.

Model	**Markkanen original**	**Markkanen updated**	**Mustonen updated**	**ISS original room model**	**ISS Pelliccioni room model**
Number of gamma lines ^{40}K	1	1	1	1	1
Gamma emission intensity ^{40}K	0.107	0.107	0.107	0.107	0.107
Number of gamma lines ^{235}U	-	-	-	-	-
Gamma emission intensity ^{235}U* **	-	-	-	-	-
Model abbreviation	$Mark_{orig}$	$Mark_{upd}$	$Must_{upd}$	ISS_{orig}	ISS_{Pelli}

Model	**EGDA>1%**	**EGDA>0.1%**	**EGDA>0.1% averaged**	**EGDA+**	**EGDA>0%**
Concrete composition	Ordinary Portland concrete (NIST)	Ordinary Portland concrete (NIST)	Ordinary Portland concrete (NIST)	Ordinary Portland concrete (NIST)	Ordinary Portland concrete (NIST)
Energy absorption coefficisent in air	Best fit from Martin 2006 [33]	Best fit from Martin 2006 [33]	Best fit from Martin 2006 [33]	Best fit from Martin 2006 [33]	Best fit from Martin 2006 [33]
Density (kg/m^3)	2350	2350	2350	2350	2350
Linear attenuation coefficient	XCOM [39] : ordinary Portland concrete (NIST) or IP	XCOM [39]: ordinary Portland concrete (NIST) or IP	XCOM [39]: ordinary Portland concrete (NIST) or IP	XCOM [39]: ordinary Portland concrete (NIST) or IP	XCOM [39]: ordinary Portland concrete (NIST) or IP

Table 6-1 (Continuation): Overview of the different dose calculation models and their parameters used to evaluate the absorbed dose rate in air.

Model	**EGDA>1%**	**EGDA>0.1%**	**EGDA>0.1% averaged**	**EGDA+**	**EGDA>0%**
Gamma emission energy and intensity	DDEP website [31]	DDEP website [31]	DDEP website [31]	DDEP website [31]	DDEP website [31]
Berger Parameters	Best fit of Pelliccioni 1989 [35]	Best fit of Pelliccioni 1989 [35]	Best fit of Pelliccioni 1989 [35]	Best fit of Pelliccioni 1989 [35]	Best fit of Pelliccioni 1989 [35]
Number of gamma lines ^{238}U	82	87	1*	87 + 1**	761
Gamma emission intensity ^{238}U* **	2.19	2.36	2.36	2.41	2.41
Number of gamma lines ^{232}Th	36	110	2*	110 + 1**	349
Gamma emission intensity ^{232}Th* **	2.76	2.98	2.98	3.04	3.04
Number of gamma lines ^{40}K	1	1	1	1	1
Gamma emission intensity ^{40}K	0.106	0.106	0.106	0.106	0.106
Number of gamma lines ^{235}U	47	128	1*	128 + 1**	734
Gamma emission intensity ^{235}U* **	2.78	3.04	3.04	3.1	3.1

* 87, 109 and 128 gamma emission lines are converted to 1 for ^{238}U, ^{232}Th and ^{235}U, respectively
** 674, 239 and 606 gamma emission lines are converted to 1 for ^{238}U, ^{232}Th and ^{235}U, respectively
*** The gamma emission intensity is the sum of the individual gamma-ray emission energies.

6.3.2.3. Role of the Build-Up Factor

The impact of the build-up factor (B) was evaluated for a standard room by using different sets of Berger parameters C and D to calculate the D_A per unit of activity concentration. The Berger parameters as described by Markkanen [2] and by Pelliccioni [35] were compared. In addition, the case without Berger parameters (C=D=0) is evaluated, meaning the role of build-up factor is neglected. The latter case is indicated by the suffix "B = 1" in Table 6-4.

6.3.2.4. Role of the Presence Disequilibria in the ^{232}Th, ^{238}U and ^{235}U Decay Series.

For model 'EGDA>0.1%' the contribution of long living radionuclides and their progeny to the total absorbed dose rate in air per unit of activity concentration for the decay series of ^{238}U and ^{232}Th is evaluated. The ^{238}U decay chain is divided into 3 subchains: i.e. ^{238}U-part (^{238}U to ^{230}Th), ^{226}Ra-part (^{226}Ra to ^{214}Po) and ^{210}Pb-part (^{210}Pb to ^{210}Po). Similar, the ^{232}Th decay chain is divided into ^{232}Th-part (only ^{232}Th), ^{228}Ra-part (^{228}Ra to^{228}Ac) and ^{228}Th-part (^{228}Th to ^{208}Tl). The absorbed dose rate in air of ^{235}U is evaluated in the framework of the ratio of AC of ^{238}U/^{235}U i.e. 21.6 as expected value for non-diluted/enriched samples. No disequilibrium is considered in case of ^{235}U decay series as (dis)equilibrium in this decay series is often not reported.

6.3.2.5. Impact of Sample Specific Composition

The impact of the sample composition on the dose rate is compared by simulating a room constructed out of fayalite slag based inorganic polymers (FSIPs). FSIPs have different chemical, physical and structural properties than concrete. The characteristics of FSIPs are described by Kriskova et al. [41], Onisei et al. [42] and Iacobescu et al. [43]. The sample composition differs from concrete consequently leading to the usage of different linear attenuation coefficients. The attenuation coefficients are calculated for each gamma emission energy via the XCOM program [48]. The sample specific coherent mass attenuation coefficient of XCOM is therefore converted to the sample specific linear attenuation coefficient.

6.3.3. Sensitivity Analysis

A sensitivity analysis of the parameters impacting the absorbed dose rate in air is performed. The studied parameters are density, wall thickness, presence of windows and doors and room size. All parameters are compared to the standard parameters of a standard concrete room as defined in Section 6.3.2.1.

6.3.3.1. Density

The impact of the wall density on the D_A is tested for a standard room with density varying stepwise (step size of 100 kg/m^3) between 1000 kg/m^3 and 3500 kg/m^3, corresponding to the density of hollow bricks up to the density of high density concrete.

6.3.3.2. Wall Thickness

In a standard concrete room the wall thickness is assumed to be 20 cm. However, depending on the usage, thinner or thicker walls are required. The impact of the wall thickness on the D_A in the standard room is tested with wall thickness varying stepwise (step size of 5 cm) between 5 cm and 80 cm while keeping floor and ceiling thickness constant at 20 cm.

6.3.3.3. Room Size

The impact of the room size on the D_A is tested for a concrete room. A square room is simulated with the length of the wall varying stepwise (step size of 100 cm) between 100 cm and 1000 cm for a room height of 280 cm and between 100 cm and 1183.2 cm for a room height of 200 cm.

6.3.3.4. Presence of Windows and Doors

The EU-BSS assumes a standard room without the presence of windows and doors. This is a strict approach but not realistic. The impact of the presence of windows or doors of different surfaces is tested. Tests are conducted for surfaces of 1 m^2, 2 m^2 and 4 m^2 positioned in the middle or the corner of a wall or ceiling. The imaginary dose rate originating of the specific window/door surface is subtracted from the dose rate of the wall without any window/door.

6.3.4. Comparison of Index and Dose Assessment Tools.

A comparison is made of the most used index and dose calculations relevant for the dose assessment within the European legislative framework applicable towards building materials. More details regarding these different index and dose calculations are shown in Table 6-2 or can be found in the respective references.

The index-values calculated via ACI and the density and thickness corrected index (I(ρd)) are compared using the AC of different types of residues and cement shown in Table 6-3 [1–3]. The obtained dose of the Markkanen original, density and thickness corrected (D(ρd)) and EGDA>0% dose calculations are compared using the same AC [2,3,30]. In addition, to the standard density of 2350 kg/m^3 and standard thickness of 20 cm, six different scenarios are tested with varying density and thickness (Table 6-4). In the comparisons, it is

assumed that the residues are solely used to construct a building material, this because recent studies [44,45] indicate the applicability of building materials without the use of any additives like cement, sand, gravel, etc. The AC values originate from Nuccetelli et al. (2015) [10]. In all cases the exposure time is 7000 h.

Table 6-2: Overview of the parameters of the index and dose calculations used in the European legislative framework applicable towards building materials.

	Index calculation		**Dose calculation**		
	ACI	**I(ρd)**	**Markkanen original**	**D(ρd)**	**EGDA>0%**
Geometry	Floor, ceiling, 4 walls	Floor, ceiling, 4 walls	Floor, ceiling, 4 walls	Floor, ceiling, 4 walls	Floor, ceiling, 4 walls
Size geometry (cm^3)	400 x 500 x 280*	400 x 500 x 280	400 x 500 x 280	400 x 500 x 280	(Flexible) Here 400 x 500 x 280
Wall thickness (cm)	20	Flexible	20	Flexible	Flexible
Density (kg/m^3)	2350**	Flexible	2350**	Flexible	Flexible
Background correction	50 nGy/h***	50 nGy/h	0.348 mSv	0.245 mSv	0.245 mSv
Composition	Concrete	Concrete	Concrete	Concrete	(Flexible) Here Concrete
Reference(s)	EU-BSS [1]; RP-112[28]; Markkanen [2]	Nuccetelli et al. 2015[3]	EU-BSS [1]; RP-112 [28]; Markkanen [2]	Nuccetelli et al. [3]	

* In Markkanen [2] size is 12 x 7 x 2.8 m^3 with thickness of 0.2 m

** In Markkanen [2] density is 2320kg/m^3

*** In Markkanen [2] background is 70 nGy/h

Table 6-3: Activity concentrations (Bq/kg) of ^{226}Ra, ^{232}Th and ^{40}K present in different residues and cement. Data are average values of database from Nuccetelli et al. 2015 [10]

Material type	**^{226}Ra (Bq/kg)**	**^{232}Th (Bq/kg)**	**^{40}K (Bq/kg)**
Furnace slags	147	42	258
Bottom ash and fly ash	207	80	546
Phosphogypsum	381	22	71
Bauxite residue	337	480	205
Cement	42	32	214

Table 6-4: Description of 6 different scenarios which are described by a specific set of density and thickness. The scenarios are used for the comparison of the models of Table 6-2

Scenario number	**1**	**2**	**3**	**4**	**5**	**6**
Thickness (cm)	10	10	18	25	40	40
Density (kg/m^3)	1400	3000	3000	1400	1400	3000

6.4. Results and Discussion

In Section 6.4.1 the different absorbed dose rates in air per unit of activity concentration for ^{238}U, ^{232}Th, ^{40}K and ^{235}U obtained by different dose assessment models are compared. This section discusses the impact of working with averaged gamma emission lines as well as the impact of the build-up factor and the radiological equilibria.

Based on this comparison, the most practical EGDA model with the highest gamma emission intensity is selected and in Section 6.4.2 a sensitivity analysis of this model is performed by changing wall thickness and density, room size and the presence of windows and doors. Throughout Section 6.4.1 and 6.4.2 the impact of the sample composition is quantified.

Section 6.4.3 deals with the application of the model focussing on the dosimetric evaluation, the impact and the practicality for industrial implementation. Consequently, a comparison is performed of the most used index and dose calculations relevant for the dose assessment within the European legislative framework applicable towards building materials.

6.4.1. Model

6.4.1.1. Impact of the Number of Gamma Lines

Table 6-5 shows the D_A per unit of activity concentration for ^{238}U, ^{232}Th, ^{40}K and ^{235}U of the different models described in Table 6-1. The different models assume a concrete standard room unless indicated else by suffix FSIP.

Table 6-5: Overview of the absorbed dose rate in air per unit of activity concentration (nGy/h per Bq/kg) for ^{238}U, ^{232}Th, ^{40}K and ^{235}U calculated by different dose assessment calculation models described in Table 6-1.

	^{238}U	**^{232}Th**	**^{40}K**	**^{235}U**
Model abbreviation	**Dose rate in air (D_A) (nGy/h per Bq/kg)**	**Dose rate in air (D_A) (nGy/h per Bq/kg)**	**Dose rate in air (D_A) (nGy/h per Bq/kg)**	**Dose rate in air (D_A) (nGy/h per Bq/kg)**
$Mark_{orig}$	0.908	1.06	0.0767	-
$Mark_{orig\ B=1}$	0.3845	0.5	0.0408	-
$Mark_{upd}$	0.893	1.02	0.0778	-
$Mark_{upd\ B=1}$	0.383	0.501	0.0407	-
$Must_{upd}$	0.84	0.999	0.0778	-
$Must_{upd\ B=1}$	0.0405	0.51	0.0407	-
ISS_{orig}	0.894	1.138	0.0767	-
ISS_{Pelli}	0.869	1.109	0.0767	-
EGDA>1%	0.76	0.967	0.0767	0.228
EGDA>0.1%	0.826	1.06	0.0767	0.25
EGDA>0.1% $_{B=1}$	0.395	0.535	0.0401	0.0819
EGDA>0.1% FSIP	0.838	1.07	0.0784	0.234
EGDA>0.1%$_{aver}$	0.88	1.07	0.0767	0.239
EGDA>0.1%$_{aver\ B=1}$	0.368	0.51	0.0401	0.0725
EGDA+	0.85	1.08	0.0767	0.255
EGDA>0%	0.849	1.08	0.0767	0.256

Suffix 'orig' (original): Data of the original paper are used as shown in Table 6-2.
Suffix 'upd' (updated): Updated data, as shown in Table 6-2, are used with the original calculation method.
Suffix 'B=1' (build-up factor = 1): The Berger parameters are set to zero. This means the role of the build-up factor is negligible.
Suffix 'aver' (averaged): Several gamma lines are reduced to a single weighted average gamma emission line.
Suffix 'Pelli' (Pelliccioni): the Berger parameters as described by Pelliccioni 1989 are used.
FSIP: The chemical composition of the room components is set to the FSIP chemical composition.

Comparing the D_A between $Mark_{orig}$ and $Mark_{upd}$, an increase of 1.7 % and 3.8 % is observed for ^{238}U and ^{232}Th, respectively, in favour of the $Mark_{orig}$ model. In case of ^{40}K, a decrease of 1.4 % is observed in favour of the $Mark_{orig}$ model. This deviation in D_A is due to the usage of different Berger parameters and a different concrete composition in the two models (Table 6-1).

The 24 emission gamma lines of ^{238}U and the 19 gamma emission lines (2614 keV-line is excluded) of ^{232}Th of the Mustonen model are converted to a single weighted average gamma emission line for ^{238}U and ^{232}Th in the Markkanen model.

Comparing $Mark_{upd}$ with $Must_{upd}$, a 6 % and 2 % increase in D_A is observed for ^{238}U and ^{232}Th, respectively. This increase is solely due to usage of averaged gamma lines in the Markkanen model. In case of ^{235}U a decrease in the D_A of 4.6 % (4.9 %) is observed for the 'averaged EGDA' variant. The differences are solely due to the usage of energy specific attenuation coefficients and energy specific C and D Berger parameters as the total gamma intensity stays equal.

When comparing the EGDA models with $Mark_{upd}$, $Must_{upd}$ and the ISS room models one can see that the number of gamma lines used is much higher (Table 6-1). When more gamma lines are included in the EGDA model the gamma emission intensity also increases for ^{238}U, ^{232}Th and ^{235}U, leading to higher D_A when comparing EGDA>1%, EGDA>0.1% and EGDA>0%. However, the gamma emission intensity of the ISS room model is smaller than the gamma emission intensity of EGDA>0% for ^{238}U and ^{232}Th (Table 6-1), still the D_A of the ISS room model is higher than the D_A of EGDA>0% (Table 6-5). The usage of a set of averaged gamma-lines in the ISS room models tends to increase the D_A, as discussed above. In addition, the usage of other B in the ISS_{orig} (Table 6-1) also impacts the D_A, this is discussed in Section 6.4.1.2.

The EGDA>0% model uses all the gamma lines available originating from ^{238}U, ^{232}Th, ^{235}U and ^{40}K. In total 1845 gamma lines are used in the calculation by model EGDA>0% whereas in model EGDA>0.1% 326 gamma lines are used. The gamma emission intensity of EGDA>0.1% is 2.1 %, 2.0 % and 1.9 % lower than EGDA>0% for ^{238}U, ^{232}Th and ^{235}U, respectively. Nevertheless, when using a higher number of gamma lines also the calculation time increases. In order to limit the calculation but still consider the maximum gamma emission intensity, the extra gamma lines of EGDA>0% in comparison to EGDA>0.1% are converted to 3 weighted average gamma lines; one line for ^{238}U, ^{232}Th and ^{235}U. This approach is incorporated in the EGDA+ model (Table 6-1). The difference in D_A between EGDA+ and EGDA>0% is limited to plus 0.001 nGy/h per Bq/kg for ^{238}U and minus 0.001 nGy/h per Bq/kg for ^{235}U. In case of ^{232}Th no difference was observed.

6.4.1.2. Impact of the Build-Up Factor.

Table 6-5 shows the D_A for several models. Comparing the D_A of the "B=1" variants with the non-unity originals, a significant decreases in the D_A is present. For example, in the case of EGDA>0.1% the "B=1" variant has an D_A which is approximately 52 %, 50 %, 48 % and 67 % lower for ^{238}U, ^{232}Th, ^{40}K and ^{235}U, respectively. The presence of the B is consequently important when calculating the D_A. The ISS_{Pelli} model differs only from the ISS_{orig} model by the usage of the data of Pelliccioni instead of the data of Markkanen to calculate the B. Comparing both models, the D_A per unit of activity concentration of the ISS_{Pelli} model is 2.8 % and 2.6 % lower for ^{238}U and ^{232}Th, respectively, in case of a standard concrete room.

6.4.1.3. Impact of Disequilibrium in the ^{232}Th, ^{238}U and ^{235}U Decay Series.

Considering the decay series of ^{238}U: the ^{238}U-part, ^{226}Ra-part and ^{210}Pb-part of the decay chain represent respectively approximately 0.93 %, 99 % and 0.067 % of the total external absorbed gamma dose rate in air per unit of activity concentration of the whole ^{238}U decay series, in the case of a standard concrete room. The lifespan of a building material will not allow reestablishing the equilibrium between the ^{238}U-part and ^{226}Ra-part. Looking solely at the lifespan aspect, it would be meaningful to treat both parts of the decay chain separately. However, this is not always feasible since one must be able to measure ^{238}U, ^{234}Th or ^{234}Pa. Using in this case the AC of ^{226}Ra for the whole decay series will only introduce a small bias since the ^{238}U-part and ^{210}Pb-part contribute less than 1 % to the total D_A of the ^{238}U decay series. On the other hand using the AC of ^{238}U for ^{226}Ra and its decay products would have a large impact as ^{226}Ra-part represents 99 % of the D_A of the ^{238}U decay series. The suggestion of RP-122 to use the highest AC present in the decay series would overestimate the gamma dose rate when the AC of ^{238}U or ^{210}Pb is larger than the AC of ^{226}Ra. Due to the small contribution of the ^{210}Pb-part to the gamma dose (i.e. 0.067%), the activity concentration of ^{226}Ra is used for the ^{210}Pb-part of the decay series in this study. The half-life of ^{222}Rn allows radon exhalation from the building material which decreases the external absorbed gamma dose rate in air. De Jong and Van Dijck [18] showed that the external absorbed gamma dose rate in air decreased on average with 9 % and 5 % for gypsum and concrete used in the Netherlands, respectively. In addition, the EU-BSS [1] treats the radon exposure (from soil and building materials) separately from the gamma exposure linked to building materials. For this reason all the EGDA models do not consider radon and are therefore stricter in terms of gamma ray exposure.

Considering the decay series of ^{232}Th: the ^{232}Th-part, ^{228}Ra-part and ^{228}Th-part of the decay chain represent respectively approximately 0.004 %, 39.6 % and

60.4 % (Table 6) of the total external absorbed gamma dose rate in air per unit of activity concentration of the whole ^{232}Th decay series in the case of a standard concrete room. Disequilibria in the ^{232}Th decay chain are complex and insights in the production process of NORM-residues can provide useful information. In the case of complete Th-separation, the equilibrium will install within a timeframe of 40 years in the Th-bearing residue. Whereas, in the Ra-bearing residue the activity will fade away. The lifetime of building materials can be considered to cover this timespan. Being strict, it is best not to consider disequilibrium and consider the highest activity concentration that is possible and use for the complete (so 100 %) D_A calculation of the ^{232}Th decay series. An adequate determination of the activity concentration is recommended to assess whether or not disequilibria are present. In addition, it is assumed in this study that no ^{220}Rn exhalation from the building material takes place as the half-life of ^{220}Rn is relatively short (55.8 sec).

To the authors' knowledge the decay series of ^{235}U is considered in none of current dose assessments tools available. However, taking into account all the gamma emission intensities above 0.1 %, the absorbed dose rate in air is 0.250 nGy/h per Bq/kg for a standard concrete (Table 6-5). This is above the D_A of ^{40}K on a Bq/kg level. However, framing this ^{235}U D_A in a broader context, when the natural abundance of U is respected the AC of ^{235}U is 0.0463 times the AC of ^{238}U. So in reality the contribution of the D_A of ^{235}U is of limited consequence, except when high activity concentrations of ^{238}U are present. When no ^{235}U is measured, the authors recommend using 0.0463 times the AC of ^{238}U to implement the dose originating from ^{235}U. Within the ^{235}U decay series, disequilibrium situations can also be present but these are not considered here.

Table 6-6: Absorbed dose rate in air (D_A) per unit of activity concentration (nGy/h per Bq/kg) of the long-living radionuclides and their progeny of the ^{238}U and ^{232}Th decay series in case of the EGDA>0.1% model.

Concrete standard room					
^{238}U Decay series			**^{232}Th Decay series**		
	D_A (nGy/h per Bq/kg)	**% Contribution**		**D_A (nGy/h per Bq/kg)**	**% Contribution**
^{238}U Part	0.0077	0.931	**^{232}Th Part**	4.1E-05	0.004
^{226}Ra Part	0.82	99.002	**^{228}Ra Part**	0.42	39.583
^{210}Pb Part	0.00055	0.067	**^{228}Th Part**	0.64	60.413

6.4.1.4. Impact of Sample Specific Composition

The impact of the sample composition is studied by comparing EGDA>0.1% and EGDA>0.1% FSIP. An increase in the D_A of 1.4 %, 0.9 % and 2.1 % is observed for ^{238}U, ^{232}Th and ^{40}K when FSIP is used instead of concrete. On the contrary, in case of ^{235}U, a decrease in the D_A of 6.8 % is observed. It has to be noted that here solely the linear attenuation coefficients are changed. A change of sample composition implies also changing the energy and MFP-dependent B, due to the interdependency between the composition, the energy and the MFP. However, the study of this aspect is outside the scope of this paper.

6.4.1.5. Selection of EGDA>0% Model

The EGDA>0% model uses the highest gamma emission intensity and makes use of all the nuclear data on an individual base. Consequently, this approach is the more accurate one and is selected for the performance of a sensitivity analysis in section 6.4.2.The *C* and *D* Berger parameters described by Pelliccioni (1989) [35] are used for the calculations. The presence of gamma emission by ^{235}U is considered and disequilibrium situations can be considered when necessary.

6.4.2. Sensitivity Analysis of EGDA>0% Model

6.4.2.1. Impact of the Wall Thickness Calculated by the EGDA>0% Model.

Figure 6-1 shows the relative change (%) in D_A for different thicknesses relative to the wall thickness of 20 cm for ^{238}U, ^{232}Th, ^{40}K and ^{235}U in a standard concrete room. It is observed that the relative decrease in D_A occurs rapidly with decreasing wall thickness. In case of a wall thickness of 5 cm, a relative decrease of 27.4 %, 27.6 %, 28.9 % and 21.1 % is observed for ^{238}U, ^{232}Th, ^{40}K and ^{235}U, respectively. In case of a wall thickness of 80 cm, a relative increase of 6.1 %, 7.4 %, 7.7 % and 1.1 % is observed for ^{238}U, ^{232}Th, ^{40}K and ^{235}U, respectively. However, a plateau in the increase of the D_A is observed. The percentage increase of the D_A between 20 cm and 25 cm thickness is below 1 % for ^{235}U whereas for the other radionuclides this is approximately 3 %. From a thickness of 40 cm, the increase in the D_A is below 1 % per increase in 5 cm thickness for all the radionuclides. According to Risica et al. (2001) [27] this plateau originates from self-absorption effects.

As the floor thickness is not varied the contribution of the walls to the D_A will increase with the thickness. The contribution of the smaller wall (400 cm) will increase with approximately 5 % relative to the larger wall (500 cm) when increasing the wall thickness from 5 cm to 80 cm.

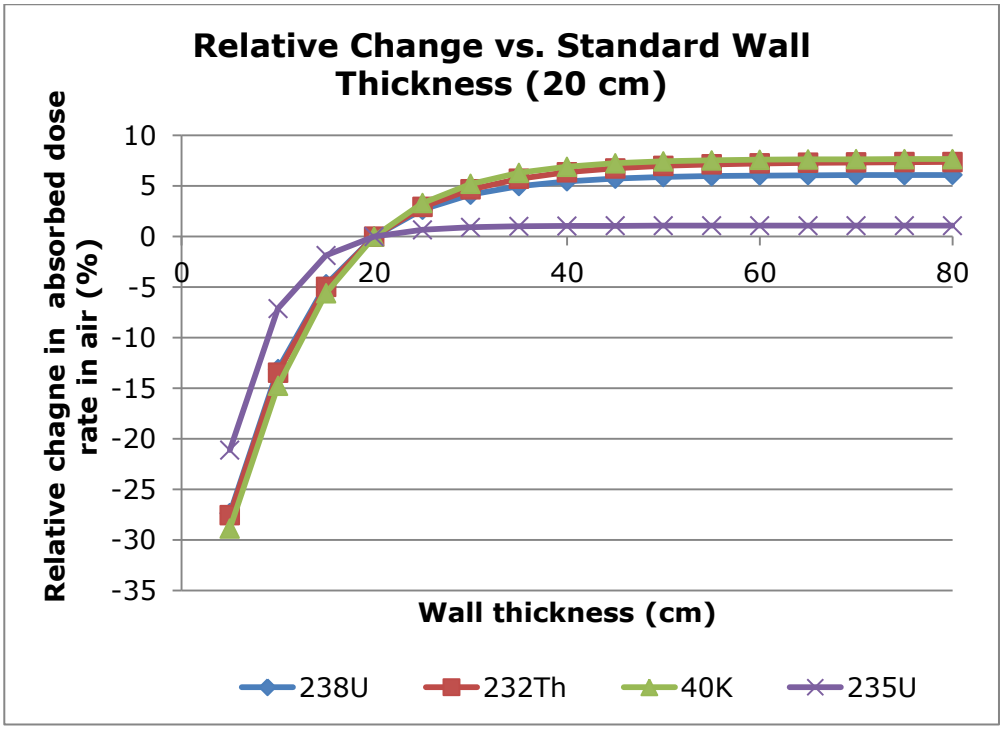

Figure 6-1: Relative change in the absorbed dose rate in air (D_A) for a standard concrete room with varying thickness (5-80 cm) vs. a standard concrete room with wall thickness of 20 cm for ^{238}U, ^{232}Th, ^{40}K and ^{235}U. Relative change: ($D_A thickness_X$ – $D_A thickness_{20\ cm}$)/($D_A thickness_{20\ cm}$ x 100).

6.4.2.2. ***Impact of the Density Calculated by EGDA>0% Model.***

Figure 6-2 shows the difference in D_A for different densities relative to the standard density of 2350 kg/m^3 for ^{238}U, ^{232}Th, ^{40}K and ^{235}U in a standard concrete room with thickness of 20 cm. At densities lower than 2350 kg/m^3 a relative decrease in D_A is observed whereas a relative increase is observed at densities higher than 2350 kg/m^3. In case of a density of 1000 kg/m^3, a relative decrease of 34 %, 35 %, 38 % and 20 % is observed for ^{238}U, ^{232}Th, ^{40}K and ^{235}U, respectively. In case of a density of 3500 kg/m^3, a relative increase of 9 %, 10 %, 11 % and 2 % is observed for ^{238}U, ^{232}Th, ^{40}K and ^{235}U, respectively. With increasing densities, the total number of radionuclides present in the material will increase leading to higher D_A. With decreasing densities the contrary is true.

With increasing densities, the relative contribution of the floor and ceiling to total dose rate decreases with approximately 1 % whereas the dose rate of the walls increases slightly. This effect is observed for the different radionuclides.

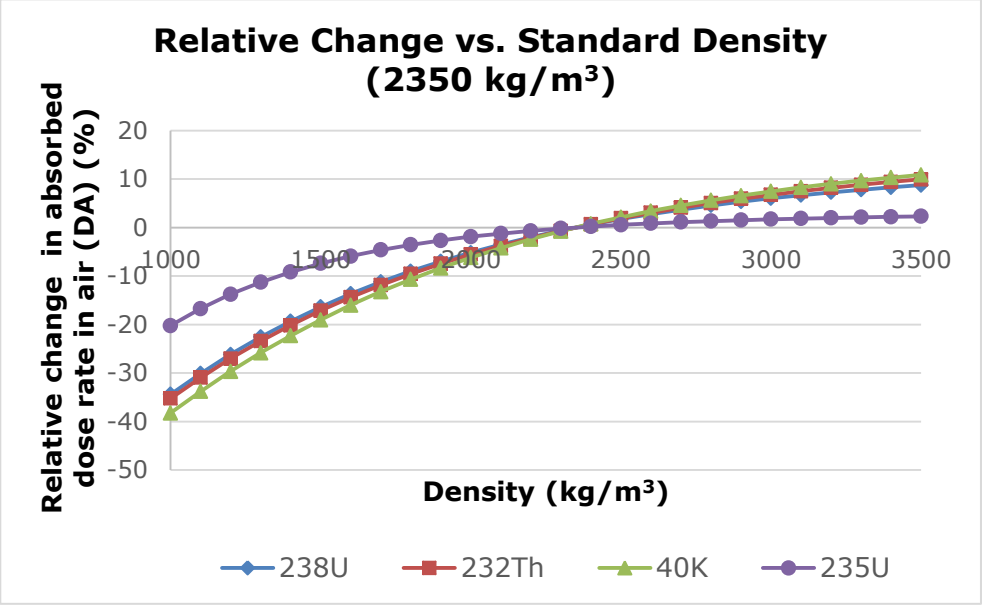

Figure 6-2: Relative difference of the absorbed dose rate in air (D_A) for a standard concrete room with varying density (1000-3500 kg/m^3) vs. a standard concrete room with density of 2350 kg/m^3 for ^{238}U, ^{232}Th, ^{40}K and ^{235}U. Relative change: ($D_A$density$_X$ – $D_A$density$_{2350\ kg/m^3}$)/($D_A$density$_{2350\ kg/m^3}$ x 100).

6.4.2.3. Impact of the Room Size Calculated by the EGDA>0% Model

Figure 6-3 shows the difference in D_A for different room sizes relative to the standard room size (400 x 500 x 280 cm^3) for ^{238}U, ^{232}Th, ^{40}K and ^{235}U in a standard concrete room. It is observed that the relative decrease in D_A occurs with decreasing room size. In case of a room size of 2.8 m^3, a relative decrease of 4 %, 4 %, 4 % and 3 % is observed for ^{238}U, ^{232}Th, ^{40}K and ^{235}U, respectively. In case of a room size of 280 m^3, a relative increase of 5 %, 6 %, 6 % and 2 % is observed for ^{238}U, ^{232}Th, ^{40}K and ^{235}U, respectively. With increasing room size, the person standing in the room is surrounded by more material. Consequently, the total number of radionuclides present in the room will also increase, leading to higher D_A. With decreasing room size the contrary is true.

Figure 6-3 also shows that the influence of the room size affects the radionuclides differently.

Next to changing the room surface, the impact of the room height is studied. At small room volumes (below approximately 15 m^3), the D_A of ^{232}Th is lower in case of a height of 200 cm than in case of a height of 280 cm. For a room area of 1 m^2 a difference of approximately 2.3 %, 2.5 %, 2.7 % and 1.2 % difference for respectively ^{238}U, ^{232}Th, ^{40}K and ^{235}U is observed. However, at room size larger than 15 m^3 the impact of height on the D_A is reverted. At a room volume of 280 m^3, an increase in the D_A of 1.7 %, 2.0 %, 2.1 % and 0.5 % for respectively ^{238}U, ^{232}Th, ^{40}K and ^{235}U is observed in favour of the room height of 200 cm .

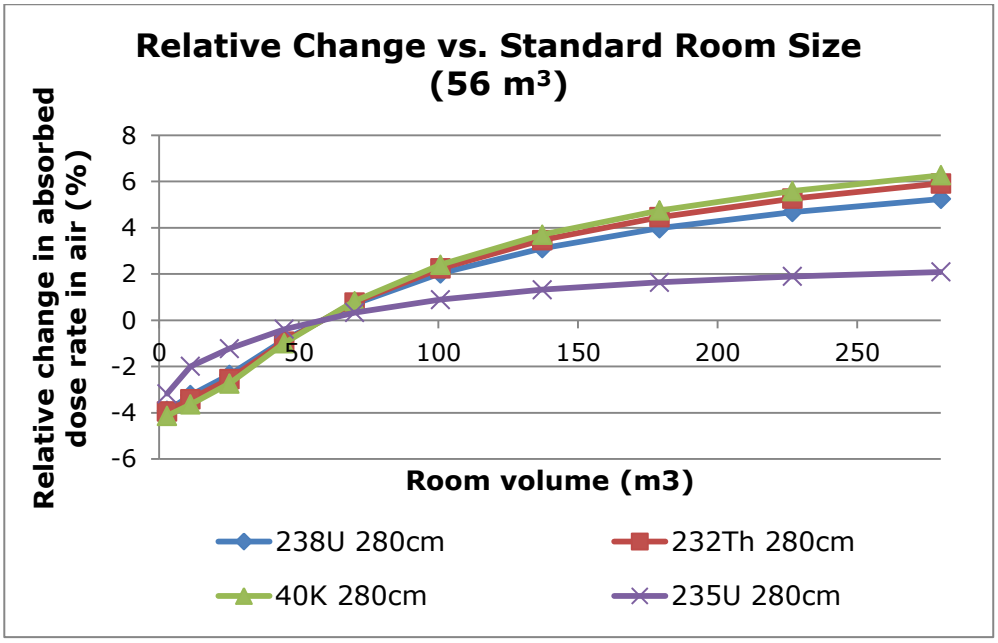

Figure 6-3: Relative difference of the absorbed dose rate in air for a standard concrete room with varying room size (2.8 - 280 m^3) vs. a standard concrete room with room size of 56 m^3 for ^{238}U, ^{232}Th, ^{40}K and ^{235}U. Relative change: $(D_A volume_X - D_A volume_{56\ m3})/(D_A volume_{56\ m3} \times 100)$

6.4.2.4. ***The Impact of the Presence of Windows and Doors by the EGDA>0% Model.***

Table 6-7 shows the percentage of deviation in the D_A of the different room components in comparison to the standard concrete room. With increasing size of the window or door surface the D_A of the component decreases. For example, in wall one the D_A decreases with approximately 12 % in case of a window of 100 cm x 100 cm whereas this decrease is approximately 37 % for a window of 200 cm x 200 cm. In both cases the windows are positioned in the middle of wall. Nevertheless, the position of the surface in the component plays an important role. In wall 2, the D_A decreases for approximately 41 % when the window is positioned in the middle of the wall. When the same window is positioned in the corner, the D_A decreases with 26 % in comparison to a standard concrete room. In addition, it must be noted that in the case of a standard concrete room wall 1, wall 2 and the floor/ceiling contribute for approximately 9.5 %, 14.5 % and 26 % respectively to the total D_A of the room. The final influence on the D_A due to the presence of a window in the ceiling will be larger than for a window in wall 1.

Table 6-7: % Deviation in dose rate for different window surfaces located in the middle or the corner of Wall 1 (400 cm x 280 cm), Wall 2 (500 x 280 cm) and the ceiling (400 cm x 500 cm) in comparison to respectively Wall 1, Wall 2 and the ceiling without the presence of windows.

	Window 100 cm x 100 cm		**Window 100 cm x 200 cm**		**Window 200 cm x 200 cm**	
	Middle	**Corner**	**Middle**	**Corner**	**Middle**	**Corner**
	% Deviation in absorbed dose rate in air (D_A) originating from wall 1 (400 cm x 280 cm) with a window in comparison wall 1 without a window					
^{238}U	-11.8	-7.3	-22.5	-21.1	-43.2	-36.6
^{232}Th	-11.8	-7.3	-22.5	-21.1	-43.1	-36.6
^{40}K	-11.7	-7.4	-22.4	-21	-43	-36.6
^{235}U	-12.1	-7.2	-23	-21.4	-43.9	-36.7
	% Deviation in absorbed dose rate in air (D_A) originating from wall 2 (500 cm x 280 cm) with a window in comparison to wall 2 without a window					
^{238}U	-11.7	-4.5	-21.9	-19.9	-41.1	-26.4
^{232}Th	-11.6	-4.5	-21.8	-19.9	-41	-26.4
^{40}K	-11.5	-4.6	-21.7	-19.8	-40.7	-26.4
^{235}U	-12.2	-4.3	-22.6	-20.4	-42.2	-26.1
	% Deviation in absorbed dose rate in air (D_A) originating from a ceiling (500 cm x 400 cm) with a window in comparison to a ceiling without a window					
^{238}U	-14.6	-2.2	-22.8	-6.4	-40.8	-17.3
^{232}Th	-14.4	-2.3	-22.5	-6.4	-40.4	-17.2
^{40}K	-13.9	-2.2	-21.7	-6.3	-39.2	-16.9
^{235}U	-15.7	-2.1	-23.9	-6.1	-42.5	-16.9

6.4.3. Comparison of Index and Dose Calculations.

Table 6-8 shows different index and dose values for 5 types of building materials calculated via different models described in Table 6-2. It must be noted that different authors and models use different background reductions like mentioned in Table 6-2. In addition, in all calculations it is assumed that both the walls as the floor/ceiling have the same density and thickness. The ACI calculation is a non-flexible calculation and assumes a density of 2350 kg/m^3 and walls of 20 cm thick and is considered as a reference for comparison since this is screening tool prescribed by the EU-BSS. Looking at a building material with density of 2350 kg/m^3 and thickness of 20 cm, the index value of the ACI is higher than the index-value of I(ρd) except for the phosphogypsum composition.

In case of building materials lighter than 2350 kg/m^3 and thinner than 20 cm building materials, the ACI overestimates the index-value in comparison to I(ρd) (scenario 1). In scenario 2 and 3, the building material is thinner than 20 cm and heavier than 2350 kg/m^3. In scenario 2, solely overestimations by the ACI are observed. In scenario 3, an overestimation by the ACI only occurs in case of bauxite residue and cement. In contrast, an underestimation occurs in case of furnace slags, bottom and fly ashes and phosphogypsum. In scenarios 4 and 5, the building material is lighter than 2350 kg/m^3 and thicker than 20 cm. In scenario 4, the ACI overestimates the index value in comparison to I(ρd). In scenario 5, an overestimation by the ACI occurs in case of bauxite residue. In contrast, an underestimation occurs in case of furnace slags, bottom and fly ashes, phosphogypsum and cement. Looking at building materials heavier than 2350 kg/m^3 and thicker than 20 cm, the ACI underestimates the index-value (scenario 6).

Table 6-8: Overview of the index-values and effective dose (mSv/a) of the index and dose calculations used in the European legislative framework for different building materials consisting of residues or cement.

Index								
Model	**ACI**	**I(pd)**						
Furnace slags	0.788	0.384	0.628	0.811	0.77	0.678	0.822	1.006
Bottom ash and fly ash	1.269	0.609	0.997	1.290	1.225	1.077	1.307	1.602
Phosphogypsum	1.405	0.719	1.171	1.510	1.434	1.264	1.529	1.864
Bauxite residue	3.592	1.657	2.710	3.509	3.330	2.928	3.554	4.355
Cement	0.385	0.18	0.295	0.382	0.363	0.319	0.387	0.476
Thickness (cm)	20	10	10	18	20	25	40	40
Density (kg/m^3)	2350	1400	3000	3000	2350	1400	1400	3000
Scenario number		1	2	3		4	5	6
Dose								
Model	**Mark$_{orig}$ (mSv/a)**	**D(pd) (mSv/a)**						
Furnace slags	0.726	0.238	0.549	0.745	0.704	0.606	0.755	0.916
Bottom ash and fly ash	1.293	0.521	1.017	1.329	1.264	1.108	1.346	1.604
Phosphogypsum	1.592	0.659	1.237	1.595	1.521	1.342	1.614	1.905
Bauxite residue	3.825	1.841	3.190	4.043	3.865	3.437	4.087	4.796
Cement	0.206	-0.019	0.128	0.222	0.202	0.155	0.227	0.304
Thickness (cm)	20	10	10	18	20	25	40	40
Density (kg/m^3)	2350	1400	3000	3000	2350	1400	1400	3000
Scenario number		*1*	*2*	*3*		*4*	*5*	*6*

Table 6-8 (Continuation): Overview of the index-values and effective dose (mSv/a) of the index and dose calculations used in the European legislative framework for different building materials consisting of residues or cement.

Dose							
Model	**EGDA>0% (mSv/a)**						
Furnace slags	0.238	0.557	0.736	0.697	0.59	0.712	0.813
Bottom ash and fly ash	0.52	1.029	1.317	1.254	1.083	1.279	1.441
Phosphogypsum	0.661	1.252	1.577	1.506	1.313	1.533	1.710
Bauxite residue	1.830	3.192	3.971	3.798	3.337	3.868	4.323
Cement	-0.019	0.132	0.219	0.199	0.148	0.207	0.257
Thickness (cm)	10	10	18	20	25	40	40
Density (kg/m^3)	1400	3000	3000	2350	1400	1400	3000
Scenario number	1	2	3		4	5	6

In scenario 1, the ACI underestimates the index-value, it is recommended to use the I(ρd) when that ACI index value is above 1. As in scenario 3 and 5, the ACI can over- or underestimate the index value it is best to use the I(ρd). As the density and thickness parameters of scenario 2 and 4 correspond to the parameters of scenario 3 and 4 respectively, it is best to also use the I(ρd) for scenario 2 and 4. For scenario 6, the ACI underestimates the index value and from a radioprotection point of view I(ρd) is recommended.

As underestimations by the $Mark_{orig}$ model (corresponds to ACI) in comparison to D(ρd) (corresponds to I(ρd)) occur in scenario 2, 3, 5 and 6, it is recommended from a radioprotection point of view, to use the D(ρd) calculation. In other scenarios, it is recommended to use the D(ρd) calculation when the effective dose approximates 1 mSv/a.

Comparing the D(ρd) with EGDA>0% one can see that the D(ρd)-dose-values are for all scenarios higher than the ones calculated via EGDA>0% except for scenario 1 and 2, which have a low wall thickness. In both scenarios, the EGDA>0% gives an effective dose which is solely a few µSv/y higher. In scenario 3, 4, 5 and 6 the EGDA>0% gives a dose which is from the order of 10 µSv/y to several 100's µSv/a lower. Therefore, in these scenarios, in case of an effective dose close to 1mSv calculated by D(ρd), the authors recommend using a more detailed dose assessment model like EGDA>0% to more accurately assess the dose. It must also be noted that in this comparison the density and thickness of the walls and floor/ceiling are all equal. This can be different in reality and can affect the dose significantly. In addition, one has to take into account that a room size larger than 400 cm x 500 cm x 280 cm gives rise to a dose increase like discussed in Section 6.4.2.3. In addition, the presence of windows and doors will also impact this background correction as well as the different sample compositions.

Regarding the different residues, the AC of a residue can vary according to the input, process parameters, etc. [13,46]. Therefore, one cannot draw conclusions from the index and dose values of Table 6-8 on the usage of these classes of residues as building material but a case by case approach should be performed.

6.5. Conclusion

The current study provides a dose calculation assessment based on the original dose calculation of Markkanen with expanded number of gamma lines and higher total gamma intensity. It is shown that working with averaged gamma lines increases the absorbed dose rate in air for ^{238}U and ^{232}Th with 6.1 % and 0.9 % respectively in case of a standard concrete room. In contrast, a decrease of 4.6 % is determined in case of ^{235}U.

The presence of the build-up factor increases the absorbed dose rate in air and plays an important role in the final obtained dose received from building materials. In case the build-up factor is absent, a decrease in absorbed dose rate in air of 52 %, 50 %, 48 % and 67 % for ^{238}U, ^{232}Th, ^{40}K and ^{235}U respectively is observed. In case of the ISS_{Pelli} model, the use of the Pelliccioni Berger parameters lowered the absorbed dose rate in air with 2.8 % and 2.6 % for ^{238}U and ^{232}Th respectively, in comparison with the ISS_{orig} model, which uses the Berger parameters described by Markkanen. Further improvements on the accuracy of the B and consequently the absorbed dose rate in air can be made by working with build-up factors customized towards the chemical composition of the building material with for example a geometric progression approach [47].

The developed EGDA>0% model is complementary to the existing ACI/original Markkanen model and I(ρd)/D(ρd) index/dose calculations which prove relevant for the dose assessment within the European legislative framework applicable towards building materials. Due to its simplicity, the authors recommend to perform a first screening by using the ACI proposed by the EU-BSS in the case of building materials thinner than 20 cm or lighter than 2350 kg/m^3. In the case of a building material thicker than 20 cm or heavier than 2350 kg/m^3, the authors propose to use the D(ρd) calculation tool of Nuccetelli et al. [3] in case of standard room sizes. In case the resulting dose of this calculation exceeds 1 mSv/a one should perform a more detailed dose assessment. The EGDA>0% model can be used for these specific cases. The EGDA>0% model also allows coping with non-standard room sizes or the presence of doors and windows. The model does not consider the dose originated by ^{222}Rn exhalation resulting in an overestimation of the total external gamma dose originating from building materials.

A sensitivity analysis was performed of the EGDA>0% model. The main factors that contribute to increase the absorbed dose rate in air in comparison to a standard concrete room (Volume of 56 m^3; density of 2350 kg/m^3; wall/floor/ceiling thickness of 20 cm) are:

- Increasing density; in case of 3500 kg/m^3 an increase of 9 %, 10 %, 11 % and 2 % for ^{238}U, ^{232}Th, ^{40}K and ^{235}U respectively is observed.
- Increasing thickness; in case of 80 cm thick walls an increase of 6 %, 7 %, 8 % and 1 % for ^{238}U, ^{232}Th, ^{40}K and ^{235}U respectively is observed.
- Increasing volume; in case of a room volume of 280 m^3 an increase of 5 %, 6 %, 6 % and 2 % for ^{238}U, ^{232}Th, ^{40}K and ^{235}U respectively is observed.

The main factors that contribute to decrease the absorbed dose rate in air in comparison to a standard concrete room are:

- Decreasing density; in case of 1000 kg/m^3 a decrease of 34 %, 35 %, 38 % and 20 % for respectively ^{238}U, ^{232}Th, ^{40}K and ^{235}U is observed.
- Decreasing thickness; in case of 5 cm thick walls a decrease of 27 %, 28 %, 29 % and 21 % for ^{238}U, ^{232}Th, ^{40}K and ^{235}U respectively is observed.
- Decreasing volume; in case of a room volume of 2.8 m^3 a decrease of 4 %, 4 %, 4 % and 3 % for ^{238}U, ^{232}Th, ^{40}K and ^{235}U respectively is observed.
- Presence of windows or doors; in case of one window of 2 x 2 m in wall 1 a decrease of 4 % for ^{238}U, ^{232}Th, ^{40}K and ^{235}U is observed.

In addition, the shape of the room can also impact the absorbed dose rate in air. Also the position and size of the window or door in the wall will impact the final absorbed dose rate in air. Larger windows positioned in the middle of the wall lead to a lower absorbed dose rate in air. The implementation of the chemical composition in the model via the attenuation coefficients showed limited effects on the absorbed dose rate in air. For a standard room an increase of 1.4 %, 0.9 % and 2.1 % is observed for ^{238}U, ^{232}Th and ^{40}K in case of a FSIP sample composition in comparison to a concrete sample composition. In contrast, a decrease of 6.8% in case of ^{235}U is observed.

Although the Markkanen room model is widely spread and used as a conservative screening tool in European legislation, the uncertainty of the method should be assessed. The expansion proposed here extends the model with validated scientific data but does not take care of the uncertainty. The uncertainty assessment is a topic for further research.

6.6. Acknowledgement

This work was supported by the COST Action TU1301.

6.7. Addenda

The addenda provides additional information which was not included in the published article but used in the calculations of the EGDA models.

6.7.1. C and D Berger Parameters

The EGDA models use the C and D Berger parameters described by Pelliccioni (1989) in order to assess the build-up factor (*B*) [35]. These *C* and *D* Berger parameters are shown in Table 6-9. A best fit through the available data points is performed via a logarithmic (Equation 6-5) and exponential (Equation 6-6) fit function for C and D, respectively. The R-squared value is above 0.99 and 0.98 for the fit of C and D, respectively.

$$C = -0.465ln(E) + 4.4462$$

Equation 6-5

$$D = \frac{0.09738}{e^{0.001E}}$$

Equation 6-6

With E the energy in keV.

Table 6-9: Overview of the C and D Berger parameters as described in Pelliccioni (1989) [35].

E (keV)	C	D
30	0.105	-0.038
100	1.6	0.036
200	1.97	0.079
500	1.55	0.066
660	1.5	0.047
800	1.3	0.047
1000	1.24	0.033
1250	1.12	0.025
2000	0.89	0.014
4000	0.6	0.004
6000	0.46	0.001
8000	0.37	0.002
10000	0.32	0.001

6.7.2. Concrete Composition

The composition of concrete is used as the standard composition for performing calculations. However this concrete composition is in most cases not specified. Therefore the EGDA models make use of the concrete composition provided by NIST [32]. This composition is shown in Table 6-10.

Table 6-10: Composition of Portland concrete. Data from NIST [32].

Element	Fraction by mass (mass%)
H	0.01
C	0.001
O	0.529107
Na	0.016
Mg	0.002
Al	0.033872
Si	0.337021
K	0.013
Ca	0.044
Fe	0.014

6.7.3. Linear Attenuation Coefficients

Based on this concrete composition the linear attenuation coefficients are calculated via the XCOM program [39]. XCOM is a program which allows to generate μ of atoms, compounds and mixtures ($Z<100$) within the energy range of 1 keV to 100 GeV. The composition and energy lines of interest (in Figure 6-4 as " additional energies in MeV") are used as an input (shown in Figure 6-4). The output is the mass attenuation coefficient of concrete which is then converted to the linear attenuation coefficient using the density of the material.

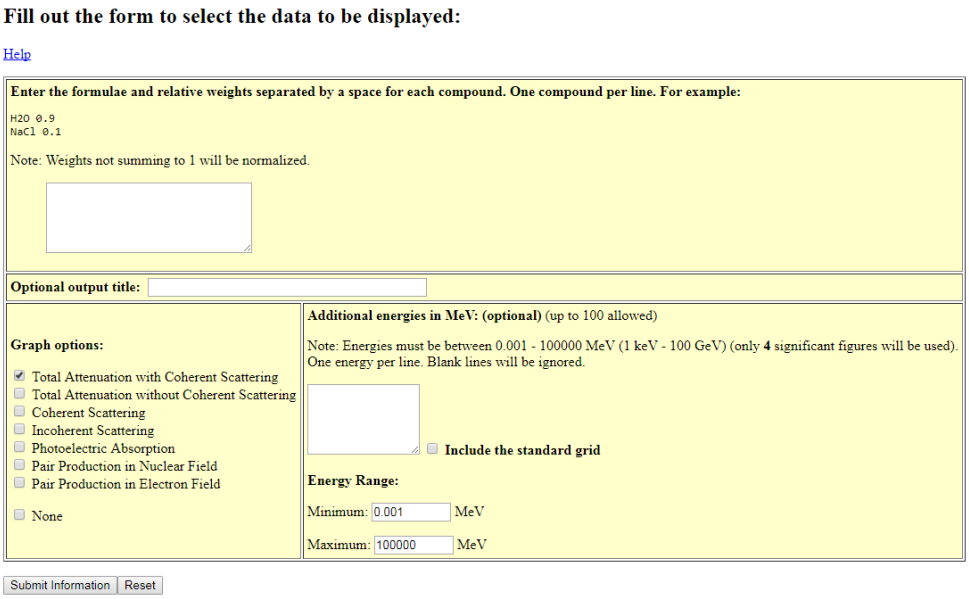

Figure 6-4: Graphical representation of input page of the XCOM program to calculate attenuation coefficients of a compound. Screenshot from NIST-XCOM [39].

6.8. References

[1] European Commission, Laying down basic safety standards for protection against the dangers arising from exposure to ionising radiation, and repealing directives 89/618/Euratom, 90/641/Euratom, 96/29/Euratom, 97/43/Euratom and 2003/122/Euratom, Off. J. Eur. Union. (2014) 1–73.

[2] M. Markkanen, Radiation Dose Assessments for Materials with Elevated Natural Radioactivity, Finish Cent. Radiat. Nucl. Safety. Rep. STUK-B-STO 32. (1995) 1–41.

[3] C. Nuccetelli, F. Leonardi, R. Trevisi, A new accurate and flexible index to assess the contribution of building materials to indoor gamma exposure, J. Environ. Radioact. 143 (2015) 70–75. doi:10.1016/j.jenvrad.2015.02.011.

[4] United Nations, Sources and Effects of Ionizing Radiation United Nations Scientific Committee on the Effects of Atomic Radiation UNSCEAR 2000 Report to the General Assembly, with Scientific Annexes VOLUME I: SOURCES, 2000.

[5] European Commission, Communication from the commission to the European Parliament, the council, the European economic and social committee and the committee of the regions A resource-efficient Europe - Flagship initiative under the Europe 2020 Strategy COM(2011) 21, (2011).

[6] European Commission, Communication from the commision Europe 2020 A strategy for smart, sustainable and inclusive growth COM(2010) 2020 final, (2010).

[7] European Commission, Communication from the commission to the european Parliament, the council, the european economic and social committee and the committee of the regions Roadmap to a resource efficient Europe COM(2011) 571 final, (2011).

[8] W. Schroeyers, T. Croymans-Plaghki, S. Schreurs, Towards a holistic approach for risk assessment when reusing slag with enhanced NORM content in building materials, 4th Int. Slag Valoris. Symp. (2015).

[9] Y. Pontikes, R. Snellings, Cementitious binders incorporating residues, in: Handb. Recycl., 2014: p. 219–229,. doi:10.1016/B978-0-12-396459-5.00016-7.

[10] C. Nuccetelli, Y. Pontikes, F. Leonardi, R. Trevisi, New perspectives and issues arising from the introduction of (NORM) residues in building materials: A critical assessment on the radiological behaviour, Constr. Build. Mater. 82 (2015) 323–331. doi:10.1016/j.conbuildmat.2015.01.069.

[11] R. Siddique, I.M. Khan, Supplementary Cementing Materials, 1st ed.,

Springer-Verlag Berlin Heidelberg, 2011. doi:10.1017/CBO9781107415324.004.

[12] D.V. Ribeiro, J.A. Labrincha, M.R. Morelli, Use of Calcined Bauxite Waste as a Supplementary Cementitious Material: Study of Pozzolanic Activity, J. Mater. Sci. Eng. 4 (2014) 172–178.

[13] T. Croymans, I. Schreurs, M. Hult, G. Marissens, H. Stroh, G. Lutter, S. Schreurs, W. Schroeyers, Variation of natural radionuclides in non-ferrous fayalite slags during a one-month production period, J. Environ. Radioact. 172 (2017) 63–73. doi:10.1016/j.jenvrad.2017.03.004.

[14] R. Trevisi, S. Risica, M. D'Alessandro, D. Paradiso, C. Nuccetelli, Natural radioactivity in building materials in the European Union: A database and an estimate of radiological significance, J. Environ. Radioact. 105 (2012) 11–20. doi:10.1016/j.jenvrad.2011.10.001.

[15] L. Koblinger, Calculation of exposure rates from gamma sources in walls of dwelling rooms, Health Phys. 34 (1978) 459–463.

[16] E. Stranden, Radioactivity of building materials and the gamma radiation in dwellings, Phys. Med. Biol. 24 (1979) 921–930.

[17] S. Righi, S. Verità, P.L. Rossi, M.F. Maduar, A dose calculation model application for indoor exposure to two-layer walls gamma irradiation: the case study of ceramic tiles, Radiat. Prot. Dosimetry. 171 (2016) 545–553. doi:10.1093/rpd/ncv476.

[18] P. de Jong, W. van Dijk, Modeling gamma radiation dose in dwellings due to building materials., Health Phys. 94 (2008) 33–42. doi:10.1097/01.HP.0000278509.65704.11.

[19] J. Deng, L. Cao, X. Su, Monte Carlo simulation of indoor external exposure due to gamma-emitting radionuclides in building materials, Chinese Phys. C. 38 (2014) 108202. doi:10.1088/1674-1137/38/10/108202.

[20] M. Zeeshan Anjum, S.M. Mirza, M. Tufail, N.M. Mirza, Z. Yasin, Natural radioactivity in building materials: dose determination in dwellings using hybrid Monte Carlo-deterministic approach, Int. Conf. Nucl. Data Sci. Technol. (2007) 1–4. doi:10.1051/ndata:07187.

[21] N.M. Mirza, S. Mirza, A Shape and Mesh Adaptive Computational Methodology for Gamma Ray Dose from Volumetric Sources, Radiat. Prot. Dosimetry. 38 (1991) 307–314. doi:10.1093/oxfordjournals.rpd.a081106.

[22] R. Mustonen, Methods for evaluation of doses from building materials, Radiat. Prot. Dosimetry. 7 (1984) 235–238.

[23] C. Nuccetelli, S. Risica, M.D. Alessandro, R. Trevisi, Natural radioactivity in building material in the European Union : robustness of the activity

concentration index I and comparison with a room model, J. Radiol. Prot. 32 (2012) 349–358. doi:10.1088/0952-4746/32/3/349.

[24] V. Manić, G. Manić, D. Nikezic, D. Krstic, Calculation of Dose Rate Converstion Factors for 238U, 232Th and 40K in Concrete Structures of Various Dimensions, With Application To Nis, Serbia, Radiat. Prot. Dosimetry. 152 (2012) 361–368.

[25] V. Manić, D. Nikezic, D. Krstic, G. Manić, Assessment of indoor absorbed gamma dose rate from natural radionuclides in concrete by the method of build-up factors, Radiat. Prot. Dosimetry. 162 (2014) 609–617. doi:10.1093/rpd/nct358.

[26] B. Chen, Q. Wang, W. Zhuo, Assessment of gamma dose rate in dwellıngs due to Decoratıve stones., Radiat. Prot. Dosimetry. 166 (2015) 1–4. doi:10.1093/rpd/ncv256.

[27] S. Risica, C. Bolzan, C. Nuccetelli, Radioactivity in building materials: room model analysis and experimental methods., Sci. Total Environ. 272 (2001) 119–126.

[28] European Commission, Radiation protection 112 Radiological protection principles concerning the natural radioactivity of building materials, (1999) 1–16.

[29] R. Mustonen, Methods for evaluation of radiation from building materials, Radiat. Prot. Dosimetry. 7 (1985) 235–238.

[30] European Commission, Radiation protection 122 practical use of the concepts of clearance and exemption Part II application of the concepts of exemption and clearance to natural radiation sources, 2002.

[31] Laboratoire national Henri Becquerel, Decay Data Evaluation Project, (2016). http://www.nucleide.org/DDEP.htm (accessed May 22, 2016).

[32] NIST, Composition of Concrete, Portland, (n.d.) 1. http://physics.nist.gov/cgi-bin/Star/compos.pl?matno=144 (accessed November 5, 2016).

[33] J.E. Martin, Physics for radiation protection, 2nd ed., WILEY-VCH Verlag GmbH & Co. KGaA, 2006.

[34] J.H. Hubbell, S.M. Seltzer, Tables of X-Ray mass attenuation coefficients and mass energy-absorption coefficients 1 keV to 20 MeV for Elements Z=1 to 92 and 48 Additional substances of Dosimetric Interest., Http://Physics.Nist.Gov/Xaamdi. (1996). doi:http://physics.nist.gov/xaamdi.

[35] M. Pelliccioni, Fondamenti fisici della radioprotezione, Pitagora, 1989.

[36] D. Krstic, D. Nikezic, Calculation of Indoor Effective Dose factors in Ornl Phantoms Series Due to Natural Radioactivity in Building Materials,

Health Phys. 97 (2009) 299–302.

[37] R Development Core Team, R: A language and environment for statistical computing. R Foundation for Statistical Computing, Vienna, Austria., (2008). http://www.r-project.org.

[38] J.H. Hubbell, Photon mass attenuation and Energy-absorption coefficients from 1 keV to 20 Mev, Int. J. Appl. Radiat. Isot. 33 (1982) 1269–1290.

[39] M.J. Berger, J.H. Hubbell, S.M. Seltzer, J. Chang, J.S. Coursey, R. Sukumar, D.S. Zucker, K. Olsen, XCOM: Photon Cross Sections Database, NIST Stand. Ref. Database 8. (2010) 1–5. http://www.nist.gov/pml/data/xcom/.

[40] IAEA, NuDat, (n.d.). http://www.nndc.bnl.gov/nudat2/.

[41] L. Kriskova, P.T. Jones, H. Jannsen, B. Blanpain, Y. Pontikes, Synthesis and Characterisation of Porous Inorganic Polymers from Fayalite Slag., Slag Valoris. Symp. Zero Waste. 4 (2015) 227–230.

[42] S. Onisei, K. Lesage, B. Blanpain, Y. Pontikes, Early Age Microstructural Transformations of an Inorganic Polymer Made of Fayalite Slag, J. Am. Ceram. Soc. 9 (2015) 1–9. doi:10.1111/jace.13548.

[43] R.I. Iacobescu, V. Cappuyns, T. Geens, L. Kriskova, S. Onisei, P.T. Jones, Y. Pontikes, The influence of curing conditions on the mechanical properties and leaching of inorganic polymers made of fayalitic slag, Front. Chem. Sci. Eng. (2017) 208–213. doi:10.1007/s11705-017-1622-6.

[44] M. Marangoni, L. Arnout, L. Machiels, L. Pandelaers, E. Bernardo, P. Colombo, Y. Pontikes, C. Jantzen, Porous, Sintered Glass-Ceramics from Inorganic Polymers Based on Fayalite Slag, J. Am. Ceram. Soc. 99 (2016) 1–7. doi:10.1111/jace.14224.

[45] T. Hertel, B. Blanpain, Y. Pontikes, A Proposal for a 100 % Use of Bauxite Residue Towards Inorganic Polymer Mortar, J. Sustain. Metall. 2 (2016) 394–404. doi:10.1007/s40831-016-0080-6.

[46] IAEA, Extent of Environmental Contamination by Naturally Occurring Radioactive Material (NORM) and Technological Options for Mitigation - Technical reports series no. 419, 2003.

[47] Y. Harima, Validity of the Geometric-Progression Formula in approximating Gamma-Ray Buildup Factors, Nucl. Sci. Eng. 5 (1986) 24–35.

Chapter 7: Experimental Determination of Linear Attenuation Coefficients: Design of Narrow Beam Set-Up

Preface/Link with objectives: This chapter fits within objective 4 of this thesis and is focused on the design of a narrow beam set-up to experimentally determine the linear attenuation coefficient (μ) of fayalite slag based inorganic polymers (FSIPs). In addition, it would be favorable to perform the experimental measurements within an acceptable timeframe of 1 to 2 days and with uncertainties of below 5 % in the energy range of 0.6 to 2.5 MeV.

7.1. Introduction

This chapter deals with the development and technical aspects of a set-up for determining μ. At first a perfect narrow beam set-up was developed, as shown in Figure 7-2. Several parameters, like for example the scattered acceptance angle absorber thickness, measurement time and the characteristics of the source and collimators, needed to be taken into account for the development of a narrow beam set-up (Section 2.7). These parameters and the practical challenges encountered during the development of the narrow beam set-up are discussed in the next sections and lead to adapting the original set-up (Section 7.2 to 7.7). The set-up with adaptions is shown in Figure 8-1. Chapter 8 deals with the measurement of the μ of the FSIPs at different energies. The concepts linked to gamma-ray shielding were explained in Section 2.7. As a reminder, the law of Lambert-Beer is shown in Equation 7-1.

$$I = I_0 B\, e^{-\mu x}$$

Equation 7-1

With I the photon intensity after passing through an absorber, I_o the initial photon intensity, B the build-up factor, x the thickness of the absorber material in cm and μ the linear attenuation coefficient in cm^{-1}.

7.2. Scattering

A narrow beam set-up is designed in such a way that the amount of scattered photons able to reach the detector is reduced to a minimum, in order to make the impact of scattered photons negligible (Section 2.7.2.2). Absorber thickness, detector surroundings and the scattered acceptance angle have an influence on the number of scattered photons reaching the detector (this aspect is discussed in the next section). The absorber thickness should ideally be kept small so that

References at page 205

multiple scattering is reduced to a minimum. So ideally, a scattered photon interacts only once with the absorber and does not reach the detector afterwards. Consequently, the detector should be well surrounded by a shielding material so that scattered photons cannot reach the detector. In order to reduce the scattering even more, the set-up can be placed in such a manner that a distance is kept between the walls of the room and the detector [1]. An example of such a particular configuration is shown in Figure 7-1. In this way the (scattered)photons cannot scatter back via the surroundings towards the

detector. From a practical point of view, this was not possible in the attenuation set-up developed here. For safety and practical reasons the whole set-up was located in a Pb shield of 10 cm thickness and with an internal liner of 4 mm Cu resulting in a maximum source-detector distance of 23.4 cm (Figure 7-2). Comparing this set-up with other set-ups in the literature, the source-detector distance of this set-up is shorter. For example, in Singh et al. (2008) this distance is 70 cm and in Davisson and Evans (1951) it is 125 cm [1,2].

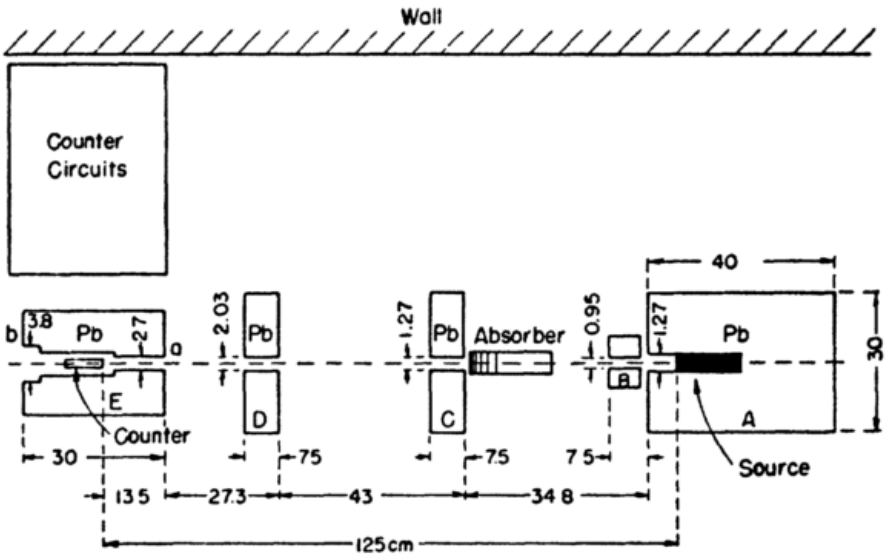

Figure 7-1: Set-up of Davisson and Evans (1951) with all dimensions shown in cm [1].

This limited distance impacts the thickness and apertures of the collimators in order to obtain an acceptable scattered acceptance angle.

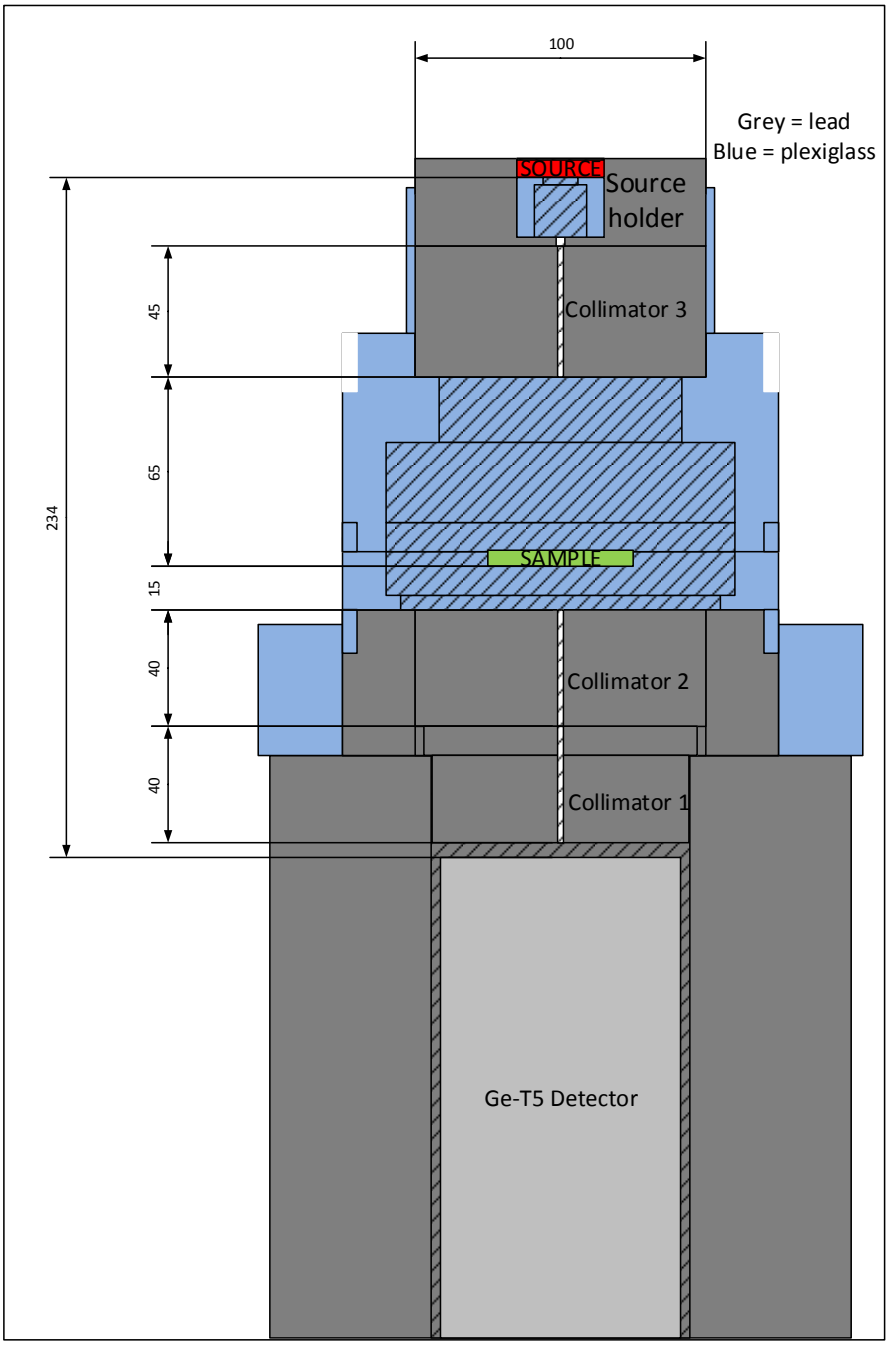

Figure 7-2: Graphical representation of the narrow beam set-up developed for experimental determination of the linear attenuation coefficients. The hashed areas indicate a hollow opening inside the shield or sample holder.

7.3. Scattered Acceptance Angle θ_{sc}

The scattered acceptance angle, θ_{sc}, characterizes the narrowness of the beam coming from the source towards the detector. This angle is defined as the sum of the incidence divergence, θ_{in}, and exit beam collimation, θ_{out}, as shown in Figure 7-3 [3].

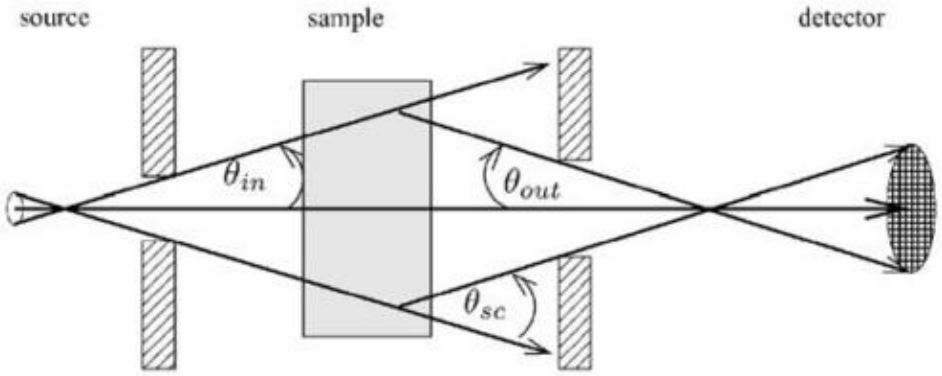

Figure 7-3: Schematic representation of scattered acceptance angle. Figure from Midgley (2006) [3].

In order to work with a narrow beam geometry the scattered acceptance angle should be sufficiently small to guarantee a build-up factor (B) equal or close to 1. Nevertheless, the B does not solely depend on the size of the scattered acceptance angle but also on the absorber thickness and its chemical composition. When B differs from 1, the calculation of the μ becomes more cumbersome. The tipping point between a good (B=1) and bad geometry (B>1) is hard to quantify (Section 2.7.2.2, and Equation 2-22). The effect of the total scatter acceptance angle and the absorber thickness on B is illustrated in Figure 7-4 for high volume fly ash concrete and in Figure 7-5 for water. It can be seen that B increases with both absorber thickness and scatter acceptance angle. For example, in case of the different fly ash samples (Figure 7-4), the value of B is below 1.01 when the absorber thickness is in the range from close to 1 up to 4.5 mean free paths (MFPs – being the average distance a photon travels between collisions with atoms of the target material) at a scattered acceptance angle of 3.57°. Whereas, when the scattered acceptance angle is 12.49°, the value of B is below 1.01 when the MFP is less than 2. The number of MFPs at which B starts increasing also depends on the sample composition. In case of a scatter acceptance angle of 3.57°, B starts increasing around an absorber thickness of approximately 4.5 MFP for fly ash whereas this is 3.5 MFP for water. Gopal and Savnjeevaiah (1973) studied for carbon and lead the impact of the number of MFPs (μx - the linear attenuation coefficient μ multiplied by the absorber thickness x), as a conclusion they define a criterion that when MFP is

kept below 1 a narrow beam geometry can be considered and multiple scattering is limited [4]. In addition, Singh Man (2018) stated that the number of mean free paths for low Z_{eff} materials (Z_{eff}<20) in the energy range of 661 keV – 1332 keV should be below 0.5 when performing attenuation measurements [5].

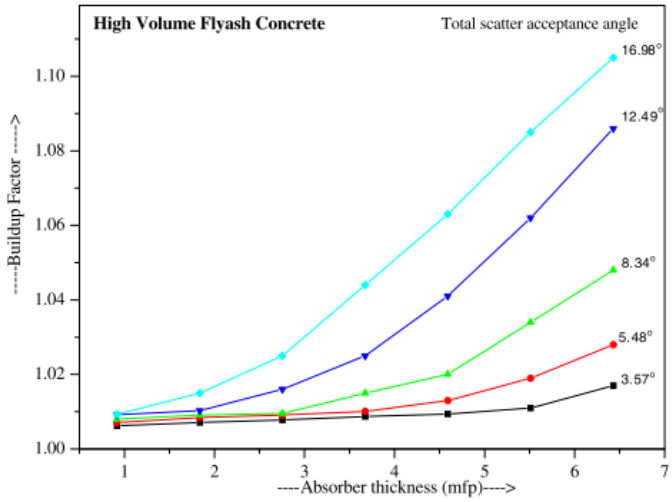

Figure 7-4: Variation of build-up factor with absorber thickness (MFP – mean free path) for different scatter acceptance angles in high volume fly ash concrete. Figure from Singh et al. (2008) [2].

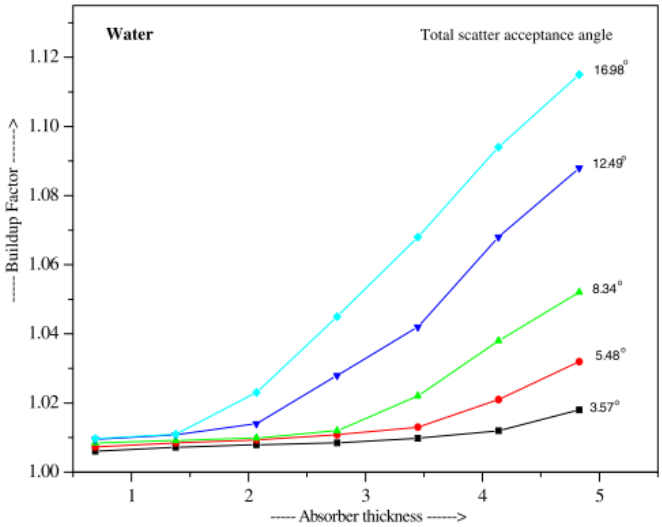

Figure 7-5: Variation of build-up factor with absorber thickness (MFP – mean free path) for different scatter acceptance angles in water. Figure from Singh et al. (2008) [2].

In addition, the source energy also plays a role, Midgley (2006) studied the effect of the scattered acceptance angle in function of energy [3]. A scatter to primary ratio (SPR) between 0.5 and 1.0 % leads to an acceptable fraction (0.5 – 1.0 %) of scattering – corresponding to a narrow beam configuration. Equation 7-2 was used to calculate the SPR. In case of incoherent scattering (i.e. Compton scattering; Section 2.7.1.2), higher energies require a smaller scattered acceptance angle in order to fit the SPR range of 0.5 to 1.0 % as illustrated in Figure 7-6 [3]. In Chapter 8, μ is determined for energies between 0.6 and 2.5 MeV. For this energy range an angle of 4° leads to acceptable level of scattering. It must be noted that for the selected energies of Chapter 8, the coherent scattering (i.e. no energy transfer occurs and the only the direction of the photon changes) fraction is negligible.

$$SPR = \frac{I_{coh}+I_{Inc}}{I_{tot}} x100$$

Equation 7-2

With I_{coh} the intensity (counts) of the coherent scattering fraction, I_{inc} the intensity (counts) of the incoherent scattering fraction and I_{tot} the total intensity (counts).

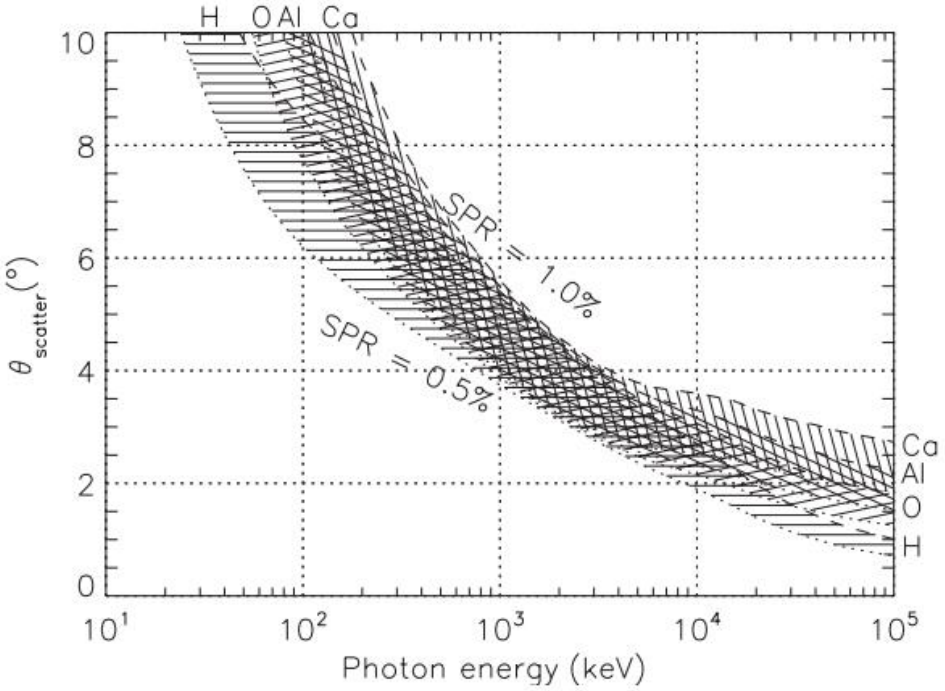

Figure 7-6: Scatter acceptance angles in function of energy with SPR between 0.5 and 1.0% for incoherent scattering. Figure from Midgley (2006) [3].

In addition, the source-detector distance and the collimator apertures influence the scattered acceptance. In case of the set-up developed in this work, which is depicted in Figure 7-2, collimators with apertures up to 2 mm had a scattered acceptance angle of less than 4°. These apertures are small in comparison to the reported apertures in literature. In the study of Davisson and Evans (1951), the apertures vary between 0.95 and 2.03 cm, and in the study of Singh et al. (2008) these vary between 0.4 and 0.9 cm [1,2]. In addition, the aperture opening also impacts the count rate as shown in Table 7-1. The count rate increases when the aperture of the collimators increases. For example in case of 661.6 keV the count rate increases from 0.05302 to 0.2003 s^{-1} when the aperture increases from 1 mm to 2 mm, respectively.

Table 7-1: Impact of collimator aperture on count rate at 661.6 keV without absorber. The measurement time was 1.5 h with set-up of Figure 7-2.

Collimator aperture (mm)	**Count rate (s^{-1})**
	661.6 keV
1	0.05302
1.5	0.1126
2	0.2003

As the 2 mm aperture had the highest count rate and a scattered acceptance angle of 2.8° it was selected for use in the initial experimental determination of the μ. Nevertheless, some encountered practical problems led to the usage of even larger apertures in the final experiments. In the next sections (Section 7.4 to 7.7) these practical problems are discussed.

7.4. Distribution of the Activity in the Source

Three sources were used for the determination of the linear attenuation coefficient i.e. ^{60}Co, ^{137}Cs and ^{226}Ra. All sources were produced by Eckert & Ziegler. The diameter of the active area was 3, 3 and 5 mm for ^{60}Co, ^{137}Cs and ^{226}Ra, respectively. At first, the sources were placed directly in a custom made Pb source holder with an aperture of approximately 3 mm. However, the radioactivity in drop deposited (so-called) point sources is not completely located in a "point". It is also not homogeneously spread in the source area as shown in the autoradiograph in Figure 7-7. Consequently, small differences in positioning the source could impact the count-rate and consequently influence the linear attenuation coefficient as discussed in Section 7.5. Table 7-2 shows the effect on the count-rate when rotating the source holder in relation to the first collimator (i.e. collimator 1 in Figure 7-2) on the count rate in case of ^{137}Cs. In the case with three collimators with aperture of 1.5 mm the count rate changed by -12 % after a 90 ° rotation. After increasing the aperture of the upper collimator from 1.5 mm to 2 mm, there was still a difference of 10 % observed in the count rate when rotating the source (Set 2 in Table 7-2). Larger collimator openings would impact the scattered acceptance angle and were therefore (initially) not an option. Instead, an additional plexiglass holder to support the source was placed in the Pb source holder(Set 3 in Table 7-2). This holder enlarged the distance between the source and the first collimator, consequently omitting the effect of the heterogeneous activity distribution. From Table 7-2 it can be seen that with this plexiglass holder (Set 3) the impact of rotating the source on the count rate is negligible.

Table 7-2: Measured count-rates from a ^{137}Cs source before and after rotating the source 90°.

Set of collimators	Degrees (°)	Count rate 661 keV (s^{-1})	Relative difference with 0° (%)
Set 1	0°	0.152	0
	90°	0.133	-12.1
Set 2	0°	0.155	0
	90°	0.171	10.3
Set 3	0°	0.134	0
	90°	0.133	-0.1

Set 1: Three collimators with aperture of 1.5 mm.
Set 2: Two collimators with aperture of 1.5 mm and top collimator (closest to

source) with aperture of 2 mm.

Set 3: Collimators of set 2, additional plexi holder to position the source higher in the Pb source holder (Figure 7-2).

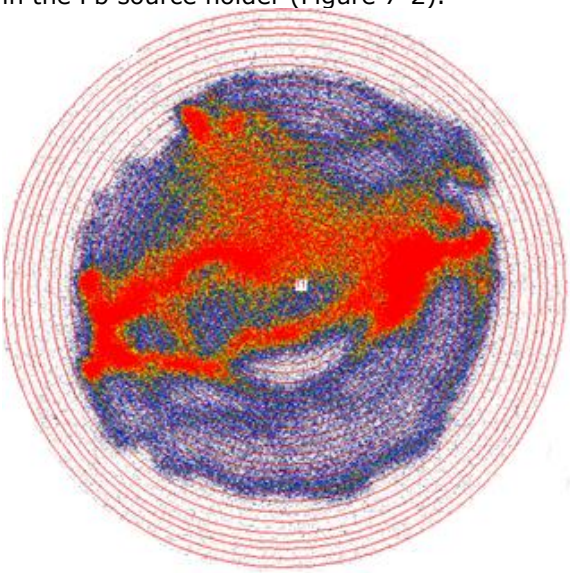

Figure 7-7: Distribution of alpha activity in a drop deposited point source. Figure from Pommé (2017) [6]. The outer (ring) diameter is 3.4 cm.

7.5. Relevance of Counting Statistics, Absorber Thickness and Measurement Time for the Determination of the Linear Attenuation Coefficient

In case of the set-up as shown in Figure 7-2 with collimator apertures of 2 mm, the count rate was 0.2003 s^{-1} for ^{137}Cs (Table 7-1). Good counting statistics (preferable below <1% statistical uncertainty – corresponding to 10 000 counts) are required. In case of a set-up equipped with collimators of 2 mm aperture and a ^{137}Cs source of 372 kBq performing a blanco measurement (i.e. measuring air), approximately 13 hours were required to achieve 10 000 net-counts in the 662 keV peak. When a sample containing shielding material is measured the measurement time will increase, depending on the characteristics of the sample, in order to reach 10 000 counts.

Nevertheless, good counting statistics do not necessarily imply a low relative uncertainty of μ. The uncertainty on the linear attenuation coefficient ($\Delta\mu$), derived from Equation 2-23, is shown in Equation 7-3.

$$\Delta\mu = \frac{1}{x}\sqrt{\left(\frac{\Delta I_0}{I_0}\right)^2 + \left(\frac{\Delta I}{I}\right)^2 + \left(ln\frac{I_0}{I}\right)^2\left(\frac{\Delta x}{x}\right)^2}$$

Equation 7-3

With μ the linear attenuation coefficient in cm^{-1}, x the thickness of the absorber material in cm, I_o the initial photon intensity, I the photon intensity after passing through an absorber. It must be noted that the uncertainty of B is not included in the calculation. In the literature B is often not considered when calculating μ [7–10]. So it is assumed that B equals 1.

The relative uncertainty of μ is shown in Equation 7-4.

$$\frac{\Delta\mu}{\mu} = -\frac{\sqrt{\left(\frac{\Delta I_0}{I_0}\right)^2+\left(\frac{\Delta I}{I}\right)^2+\left(ln\frac{I_0}{I}\right)^2\left(\frac{\Delta x}{x}\right)^2}}{\ln(\frac{I_0}{I})}$$

Equation 7-4

With μ the linear attenuation coefficient in cm^{-1}, x the thickness of the absorber material in cm, I_o the initial photon intensity, I the photon intensity after passing through an absorber.

In case of a 5.91 mm thick Al disc, a peak area of 10 000 and 11 268 counts in I and I_0, respectively, corresponded with a relative uncertainty of 11.5 % in the linear attenuation coefficient (Table 7-3). If counts increase by a factor 10, the relative uncertainty decreases to 3.6 %. If the counts increase by a factor 100, it reduces the relative uncertainty to 1.4 %. These intensities were chosen in accordance with the μ of aluminum at 661 keV i.e. 0.201 cm^{-1}.

Table 7-3: Impact of counts on relative uncertainty of μ. With μ of 0.201 cm^{-1} (aluminium at 661 keV).

I_0 (counts)	11268	112680	1126800
I (counts)	10000	100000	1000000
Δμ/μ (%)	11.5	3.6	1.4

Next to counting statistics, the uncertainty also depends on the thickness of the sample as shown in Equation 7-3. Thicker samples lead to lower uncertainties. However, the effect of multiple scattered gamma-rays increases with sample thickness, as discussed in Sections 7.2 and 7.3. so it comes down to an optimization problem like explained by Gopal and Sanjeevah (1973) [4].

In addition, in order to keep the same statistical uncertainty with thicker samples, the measurement time needs to be increased. This longer

measurement time in its turn could lead to an accuracy problem in case of the ^{60}Co peaks. The half-life of ^{60}Co is 5.2 years. In a time period of two weeks this could lead to a lower count rate of approximately 0.5 % between the start and the end of the measurement. This 0.5 % decrease in count rate consequently impacts the accuracy of the μ experimentally determined via a logarithmic function. This effect is illustrated in Table 7-4, here, I_0 is the reference case. Whereas, in case of I_0 x 0.995 and I_0 x 1.005 the count rate of I_0 is multiplied by 0.995 and 1.005, respectively. This leads to a difference of 0.5 % in the count rate, which in its turn leads to a difference between 5 and 6 % in the μ of I_0 x 0.995 and I_0 x 1.005 in comparison with the original I_0 (Table 7-4). The count rate of the shield is kept constant in all cases.

Table 7-4: Impact of deviations in the count rate on the linear attenuation coefficient μ in case of ^{60}Co (1173 keV). Numbers based on the μ of 1173 for aluminum i.e. 0.1526 cm^{-1}.

Intensity of blanco	**Counts I_0**	**Counts I**	**μ (cm^{-1})**	**Relative difference in μ (%)**
I_0	15000	13706	0.1526	0
I_0 x 0.995	14925	13706	0.1441	-5.654
I_0 x 1.005	15075	13706	0.1610	5.419

In order to deal with this side-effect of long measurement times, a correction factor for both the measurement time as well as for the reference date (like in Equation 3-2) was used to calculate the intensities. For the measurement time this correction factor is:

$$CFt_{mx} = \frac{\lambda_x t_m}{1 - e^{-\lambda_x t_m}}$$

Equation 7-5

With CFt_{mx} the correction factor for the measurement time for radionuclide x, λ_x is the decay constant of radionuclide x and t_m, the real clock time of the measurement.

In case of the reference date this correction factor is:

$$CFt_{dx} = e^{\lambda_x t_d}$$

Equation 7-6

With CFt_{dx} the correction factor for the reference date for radionuclide x, λ_x is the decay constant of radionuclide x and t_d, the decay time (i.e. the time between the measurement date and the reference date (the data at which t is set to zero)).

These correction factors mathematically correct for the decay occurring during the measurement and during the difference of the start date of the measurement with and without absorber and thereby enable longer measurement times. However, except for the obvious drawback of long measurements time of reduced output, long measurement times also raises issues about the stability of the system. It is much preferred to try to limit a single measurement to about 1 day in order to ensure background (changes in cosmic rays flux and radon-concentration in the lab), electronics (changes in the grid and temperature) and mechanical stability (unexpected vibrations due to work). These stability considerations were taken into account for the measurements. The set-up was located in an air conditioned and temperature controlled lab equipped with radon monitors. The detector was connected to a UPS system to provide a stable electrical feed.

7.6. Degradation of the Collimators

The set-up was constructed in such a way that the collimators could be well aligned. The upper collimator and source holder could also be removed easily to change the sample. The collimators were produced out of Pb, which is a soft material. Due to this material characteristic, change in the collimators' dimensions can occur over time which could become deleterious in case of very small aperture dimensions.

7.7. Usage of larger Apertures – Final Design

Regarding the long measurement time and the requirement of good counting statistics, it was decided to use larger apertures for the experimental determination of the μ. Consequently, the set-up was adapted with apertures of 3, 3 and 5 mm for collimator 1, 2 and 3, respectively (Figure 8-1 Section 8.3.3.5). Furthermore, the source was moved closer to the detector by reducing the height of the collimators. Collimators 1 and 3 were reduced to 1.5 cm and collimator 2 to 2.7 cm. Consequently, the source-detector distance was reduced to 21.5 cm. The use of larger apertures and a reduced source-detector distance lead to a higher scattered acceptance angle of 7.5°. This set-up is shown in Figure 8-1. The blanco count rate of the measured energies in case of ^{60}Co, ^{137}Cs and ^{226}Ra is shown in Table 7-5. For ^{137}Cs the count rate increased with a factor 130 in comparison to the previous set-up with collimator apertures of 2 mm (Table 7-1).

Table 7-5: Overview of count rate (s^{-1}) of final set-up of Figure 8-1 (Section 8.3.3.5) in case of no absorber for gamma-ray energies of ^{60}Co, ^{137}Cs and ^{226}Ra.

Radionuclide	**Energy (keV)**	**Count rate (s^{-1})**
^{137}Cs	661.6	25.9
^{60}Co	1173	47.0
	1332	50.2
^{226}Ra	609	7.0
	1120	5.7
	1765	6.2
	2204	1.8
	2447	0.5

As shown in Figure 7-4 and Figure 7-5, it is important to keep the number of mean free paths low to meet the requirement of *B* equal to 1. Consequently, thin samples are favourable to measure in terms of *B*. When changing a sample, only the upper collimator needs to be taken out and could abrade over time. For this reason this collimator had a wider aperture of 5 mm. This 5 mm aperture is also larger than the aperture of the source holder of 3 mm. The performance of the novel set-up was validated by experimentally determining the μ of an Al-disc (thickness of 5.91 ± 0.02 mm) of which the μ are well documented. Table 7-6 shows that the test results obtained using the Al-disc agreed very well with the data from XCOM. The uncertainty for the energies 661.6, 1173, 1132, 609, 1120, 1765 and 2204 keV was below 5%. In case of 2447 keV the relative uncertainty was approximately 8%.

Table 7-6: Overview of the measurement time, tabulated μ values for aluminum and measured μ values for aluminum.

Nuclide	Energy (keV)	Measurement time (hours)	μ Al tabulated (XCOM) (cm^{-1})	μ Al measured (cm^{-1}) (k=1)	Relative uncertainty (%) (k=1)
^{137}Cs	661.6	20	0.201	0.202 ± 0.002	1.0
^{60}Co	1173	20	0.153	0.150 ± 0.001	0.9
	1332	20	0.144	0.142 ± 0.001	1.0
^{226}Ra	609	40	0.208	0.208 ± 0.003	1.2
	1120	40	0.157	0.157 ± 0.003	1.8
	1765	40	0.124	0.123 ± 0.003	2.1
	2204	40	0.111	0.117 ± 0.005	4.1
	2447	40	0.106	0.111 ± 0.009	7.9

7.8. Conclusion

A set-up has been developed and validated for the measurement of linear attenuation coefficients (μ). The set-up was developed to perform measurements with low uncertainties and within the order of 1 to 2 days. In case of ^{60}Co and ^{137}Cs, measurements of 20 hours lead to relative uncertainties of below 1%. In case of ^{226}Ra, the measurement time was 40 hours due to the lower count rates. For ^{226}Ra, the relative uncertainties were below 8 %. The set-up was validated by means of an Al-disc.

7.9. References

[1] C.M. Davisson, R.D. Evans, Measurements of Gamma-Ray absorption coefficients, Phys. Rev. 81 (1951) 404–411.

[2] S. Singh, A. Kumar, C. Singh, K.S. Thind, G.S. Mudahar, Effect of finite sample dimensions and total scatter acceptance angle on the gamma ray buildup factor, Ann. Nucl. Energy. 35 (2008) 2414–2416. doi:10.1016/j.anucene.2008.08.008.

[3] S. Midgley, Angular width of a narrow beam for X-ray linear attenuation coefficient measurements, 75 (2006) 945–953. doi:10.1016/j.radphyschem.2006.01.008.

[4] S. Gopal, B. Sanjeevaiah, A method to determine the gamma-ray attenuation coefficients, Nucl. Instruments Methods Phys. Res. Sect. A Accel. Spectrometers, Detect. Assoc. Equip. 107 (1973) 221–225.

[5] K. Singh Mann, Measurement of exposure buildup factors : The influence of scattered photons on gamma-ray attenuation coefficients, Nucl. Inst. Methods Phys. Res. A. 877 (2018) 1–8. doi:10.1016/j.nima.2017.08.047.

[6] S. Pommé, Autoradiography - Personal Communication, 2017.

[7] N. Singh, K.J. Singh, K. Singh, H. Singh, Comparative study of lead borate and bismuth lead borate glass systems as gamma-radiation shielding materials, Nucl. Instruments Methods Phys. Res. Sect. B Beam Interact. with Mater. Atoms. 225 (2004) 305–309. doi:10.1016/j.nimb.2004.05.016.

[8] S. Singh, A. Kumar, D. Singh, K.S. Thind, G.S. Mudahar, Barium-borate-flyash glasses: As radiation shielding materials, Nucl. Instruments Methods Phys. Res. Sect. B Beam Interact. with Mater. Atoms. 266 (2008) 140–146. doi:10.1016/j.nimb.2007.10.018.

[9] K. Singh, H. Singh, V. Sharma, R. Nathuram, A. Khanna, R. Kumar, S.S. Bhatti, H.S. Sahota, Gamma-ray attenuation coefficients in bismuth borate glasses, Nucl. Instruments Methods Phys. Res. Sect. B Beam Interact. with Mater. Atoms. 194 (2002) 1–6. doi:10.1016/S0168-583X(02)00498-6.

[10] I. Akkurt, H. Akyildirim, B. Mavi, S. Kilincarslan, C. Basyigit, Gamma-ray shielding properties of concrete including barite at different energies, Prog. Nucl. Energy. 52 (2010) 620–623. doi:10.1016/j.pnucene.2010.04.006.

Chapter 8: Fayalite Slag Based Inorganic Polymers as Gamma-Ray Shielding Material.

The results of this chapter will be submitted for publication in an international refereed scientific journal in the field of attenuation coefficients. The most suited journal is: "Radiation Physics and Chemistry".

Tom Croymans, Gerd Marissens, Guillaume Lutter, Remus Ion Iacobescu, Yiannis Pontikes, Mikael Hult, Sonja Schreurs, Wouter Schroeyers

Link with objectives: This chapter fits within objective 4 of this thesis and is focused on the gamma-ray shielding capabilities of fayalite slag based inorganic polymers (FSIPs). In this chapter, a building material is developed solely out of fayalite slag (FS) by means of alkali activation. The produced FSIP was produced without the usage of any virgin raw materials, like cement. The linear attenuation coefficient (μ) of the FSIP has been determined experimentally with a narrow beam geometry set-up. In addition, the μ of the FSIP was simulated by means of Monte Carlo simulations (MCSs) and by XCOM. The simulated μ's of the FSIP were compared with the ones of conventional high density concretes (HDCs). The half-value was calculated and the effective atomic number (Z_{eff}) is calculated.

8.1. Abstract

High-density concrete (HDC) is widely used in a broad range of sectors for its gamma-ray shielding properties and high density. The incorporated aggregates are added to improve shielding and are typically iron or barium bearing. These aggregates are expensive and usually originate from primary ores. Use of secondary resources for the production of alternative materials to replace HDC without compromising the quality of the end-product, could enable the production of a cost attractive, sustainable alternative.

In this study, a new shielding material is designed based only on fayalite slag (FS), a by-product of the non-ferrous industry. For the production of an inorganic polymer (IP), an alternative that generates less CO_2 than ordinary concrete building materials, fayalite slag (FS) was mixed with an alkali activating solution and pressed and stored at room temperature.

The linear attenuation coefficients (μ) were experimentally determined with ^{60}Co (1173 and 1332 keV), ^{137}Cs (661.6 keV) and ^{226}Ra (609, 1120, 1765, 2204 and 2447 keV) gamma-ray sources. In addition, theoretical simulations were

References at page 229

performed using Monte Carlo simulations using the Electron Gamma Shower national research council of Canada (EGSnrc) program for ^{60}Co, ^{137}Cs, ^{226}Ra and for the energies of 1.5, 2, 3, 4, 5 and 6 MeV. The obtained results are compared with the linear attenuation coefficients from conventional HDCs. In addition, other parameters like effective atomic number and half value layer are calculated. In conjunction with the above, the compressive strength of the inorganic polymer was tested.

The simulated results show that the FSIP attenuates better than ordinary, hematite-serpentine, ilmenite-limonite and basalt-magnetite concrete. However, barite, ilmenite, steel scrap, and steel-magnetite concrete attenuate better than the FSIP. Looking at the Z_{eff} values, only steel scrap, and steel-magnetite concrete have a higher effective atomic number (Z_{eff}) than FSIP over the whole energy range of 0.01 MeV to 1000 MeV. Agreement between experimental and simulated results was within 2 % for ^{60}Co and ^{137}Cs, and within 11 % for ^{226}Ra in case of the FSIP.

In conclusion, FSIPs were found to perform comparably to existing gamma-ray shielding materials in the market, but with a lower expected mineral cost. In addition a much reduced generation of CO_2 is expected. Therefore, these results suggest that fayalite slag based inorganic polymers can find applications as gamma-ray shielding material.

8.2. Introduction

Gamma-ray shielding materials are designed to attenuate gamma-rays and thereby protect the surroundings. These materials find their application in nuclear, medical and storage facilities. The atomic number and the density of the shielding materials are related to their ability to scatter and absorb gamma-rays, and via these interactions attenuate radiation [1,2]. Although any material can be used as a shielding material, dense materials consisting of elements with high atomic number are preferred [1,2]. Nevertheless, an optimum between economical, mechanical, physical and shielding parameters will determine the choice of a suitable shielding material [1].

Concrete is widely used for shielding against radiation mainly due to its easy handling and structural properties [1]. In order to save space and increase the attenuation of gamma-rays, natural or synthetic aggregates bearing iron or barium are typical used as additives [1]. These aggregates are expensive; for example in 2016, the cost for barite and iron-scrap were 198 and 192 dollars per tonne, respectively [3]. Furthermore, aggregates of natural origin and the production of cement require the exploitation of raw materials. Each of these conventional cement and iron or barium bearing aggregate mixtures have certain drawbacks in terms of processing, handling, availability, durability, safety or cost [1]. Better shielding materials based on lead or uranium exist, but

their associated costs are even higher [1,4]. As metallurgical slags also contain large amounts of elements with a high atomic number, these slags are potential raw materials for shielding. Metallurgical slags are produced in large quantities worldwide and more and more research has been conducted to valorize these by-products [5–16]. Slags have been proven to be good precursors for the production of inorganic polymers (IP), an alternative for ordinary concrete building materials that generates less CO_2 [14–16]. CO_2 emissions linked to this class of materials are estimated to be between 30 and 80% lower in comparison to cement [17].

IPs are produced by mixing a solid precursor with an alkali activating solution creating a paste that hardens to form an amorphous 3D structure. Depending on the precursor, the structure varies. Most known 3D structures are alkali-alumino-silicate polymers although other structures exist in which Fe is incorporated in the structure [11,17,18]. These structures consist of rich iron-silicate sources with limited aluminum content. High iron-bearing slags are investigated as starting materials for these 3D structures [5–12]. Research is ongoing to clarify the role of iron in these structures [18–21]. Regarding the high volume of iron rich slag produced worldwide (i.e. approximately 50 million tonnes) the production of IPs forms a potential and highly interesting pathway for valorizing these slags in a primary-resource-reducing way [22]. However the use of IPs as gamma-ray shielding material is a new and unexplored field.

In order to valorize and upcycle slags as a gamma-ray shielding building material other aspects need to be considered. Slags can contain elevated levels of naturally occurring radionuclides (NORs) and their use in/as building materials can have certain legal limitations due to the Euratom Basic Safety Standards, Council Directive 2013/59/Euratom (EU-BSS) [23]. The EU-BSS sets a 1 mSv/a gamma dose exposure threshold level in terms of public exposure. Consequently, this dose limit needs to be respected in order to allow valorization of industrial by-products - like slags - as building materials. Nevertheless, this is certainly not valid for all slags [23]. This radiological aspect is addressed by Croymans et al. (2017) for a fayalite slag as a raw material, in addition an overview of the activity concentrations of the NORs in different metallurgical slags is presented [23]. Other industrial by-products known to be potentially enriched in NORs, like fly ash, electric arc furnace slag and blast furnace slag have been used in the development of shielding materials, but only as glass or in cement mixtures [24–26]. Next to the NOR-content, the leaching of heavy metals needs to be investigated prior to the valorization of industrial by-products as building material [27,28].

To be able to compare the gamma-ray shielding properties of different materials, the attenuation coefficient (μ) is a fundamental parameter. This coefficient has been investigated for elements [29] but also for a wide range of materials like alloys [30,31], biological materials [32], glasses [24], minerals

[33], composite and building materials [34–36]. Berger and Hubbell (1987/1999) developed a database, named XCOM. This database is made online available to enable the calculation of mass attenuation coefficients for elements, compounds and mixtures from 1 keV to 100 GeV [37,38]. This database can be used in MC simulation programs. Today, also Monte Carlo (MC) codes for radiation transport allow calculations of μ as an integral part of simulating custom experimental radiological set-ups. Such usage is, however, more complex and labor intensive in comparison to XCOM.

In this study, IPs were produced solely from iron-rich fayalite slags. So in this design the slag took the role as primary attenuator instead of the aggregates. But it also took the role as binder, thereby replacing expensive (natural) aggregates and cement, making their exploitation unnecessary for this application. The attenuation coefficients of fayalite slag based inorganic polymers (FSIPs) were determined experimentally and compared with theoretical values obtained via MC simulations using the Electron Gamma Shower national research council of Canada (EGSnrc) MC code. The obtained attenuation coefficients and compressive strengths were compared with cement-mineral based shielding materials described in literature. The linear attenuation coefficients of those materials were also calculated using EGSnrc. The results were also compared with Geant4 results reported in the literature [39]. In addition, the effective atomic number and half value layer were calculated for the different high density concretes (HDCs) and FSIP.

8.3. Materials and Methods

8.3.1. Sampling, Sample Preparation and Analysis of Precursor Material

The samples in this study originate from a secondary smelting plant, which produces non-ferrous fayalite slags as a by-product during the production of different types of non-ferrous metals. Water-quenched (WQFS) and slowly cooled fayalite slags (SCFS) were used for the production of inorganic polymers (IPs). The difference between both slags is the cooling path, leading to a higher crystalline phase for the SCFS. Mineralogy of the WQFS and SCFS samples was determined using a Philips Analytical PW 1710 diffractometer with Cu K_α radiation operating at 45 kV and 30 mA. The measurement included a stepwise scan over a range of 5-70° 2θ with steps of 0.02° 2θ per 2 seconds. Qualitative analysis was performed with the "X'pert HighScore Plus" PANalytical software (PANalytical, Almelo, The Netherlands). Quantitative results were obtained adopting the Rietveld method using the "Topas® Academic" software.

WQFS samples were milled using an attritor mill (Wiener & Co N.V.) and sieved afterwards with a vibratory sieve shaker AS 200 (Retsch) equipped with a 80 µm sieve. D(50) of the milled powder was 8.65 µm. The SCFS were reduced in size

by hand until they were small enough to fit in a disk mill pulverisette 13 (Fritsch). The milled fraction was sieved according to the EN 196-1 norm by a vibratory sieve shaker AS 200 (Retsch). The EN 196-1 grain size distribution is used in the production of the FSIPs.

8.3.2. Production of Inorganic Polymer and Analysis

The WQFSs were used as binder because the high amorphous content; the SCFSs were used as aggregate. The FSs were activated using a 50-50 mass% 6M sodiumhydroxide-sodiumsilicate activating solution and mixed in binder/aggregate/activating solution ratios of 1/4.2/0.4. They were then pressed with a hydraulic laboratory press MIGNON SSN/EA (Nannetti) at 100 bar into 3 cuboid and 8 cylindrical shapes. It must be noted that produced IPs are mortars and not concretes.

The cuboid samples were stored for 28 days at 20 °C and 60 % humidity and used for compressive strength testing. This was found by Iacobescu et al. (2017) to be the most optimum curing conditions for these systems [27]. Average dimensions of these samples were 50.3 ± 0.1 mm, 50.2 ± 0.1 mm, and 19.3 ± 0.4 mm. The cuboid samples were polished prior to the uniaxial compressive strength test, performed with a Schenck Trebel apparatus with head displacement of 1 mm/s.

The cylindrical samples were selected for experimental determination of the attenuation factor and no specific requirements of temperature and humidity were chosen for storage. The height of the cylindrical samples varied between 6.43 ± 0.05 mm and 18.86 ± 0.03 mm and these samples had a typical diameter of 50.0 ± 0.1 mm. The density of the produced FSIPs varied between 2.96 ± 0.02 g/cm^3 and 3.10 ± 0.01 g/cm^3. The highest density was observed for the thickest samples. The density was calculated from the dimensions, measured with a Vernier caliper (precision of 0.03 mm) or Mitutoyo Micrometer (precision of 0.001 mm), and the mass with an analytical balance (Sartorius MSX (SE EA)) (precision of 0.1 mg).

From the produced batch, 1 sample was milled by means of a mortar and pestle and used to determine the chemical composition of the FSIP. The composition was determined by Vlaamse Instelling Technologisch Onderzoek (VITO) in Mol, Belgium with a high performance energy dispersive XRF spectrometer with polarized X-ray excitation geometry (HE XEPOS, Spectro Analytical Systems, Kleve, Germany). This instrument is equipped with a 50 W tungsten end-window tube (max. 60 kV, 2 mA) and a Silicon Drift Detector.

8.3.3. Narrow Beam Gamma-Ray Attenuation Set-Up and Experimental Determination of Linear Attenuation Coefficients

A narrow beam gamma-ray attenuation set up was developed and used for experimental determination of the attenuation coefficients of the IP samples.

8.3.3.1. Radioactive Sources

So-called point sources (Eckert & Ziegler) of ^{60}Co, ^{137}Cs and ^{226}Ra were used for the measurements. The active area is 3 mm in case of the ^{60}Co and ^{137}Cs sources and 5 mm for the ^{226}Ra source. The total activity of each radionuclide at the time of measuring was 382, 372 and 315 kBq for ^{60}Co (1173 and 1332 keV) ^{137}Cs (662 keV) and ^{226}Ra (609, 1120, 1765, 2204 and 2447 keV), respectively. Attenuation coefficients corresponding to the respective energies of these sources were determined experimentally. The energies of ^{60}Co and ^{137}Cs were measured together by stacking the sources.

8.3.3.2. Gamma-ray Detector

A low-background coaxial HPGe detector with a relative efficiency of 46 % (FWHM: 1.41 at 662 keV and 1.86 at 1332 keV) was used for the measurements. This detector is located in the Radionuclide Metrology Laboratory at the European Commission's Joint Research Centre in Geel, Belgium. The detector has a deadlayer thickness of about 0.6 mm and a 1.7 mm thick aluminum window.

8.3.3.3. Validation of attenuation measurement

It is known that the effect of multiple scattered gamma-rays reaching the detector increases with sample thickness [40]. In order to make this effect negligible, the sample thickness was selected to meet the requirement of the number of mean free paths being below 1, as proposed by Gopal and Sanjeevah (1973) [41]. A high purity Al disc with thickness of 5.91 ± 0.02 mm was used to check the performance of the set-up prior to measuring unknown samples. The obtained μ values of these validation measurements agreed within the relative uncertainty - up to 16% (k=2) for ^{226}Ra - with the expected theoretical values of μ for Al (Table 8-1). The higher uncertainties of ^{226}Ra are due to the low count rate leading to low counting statistics.

Table 8-1: Overview of measurement time and linear attenuation coefficients of aluminum to validate the set-up.

Radionuclide	Energy (keV)	Measurement time (hours)	μ Al tabulated (XCOM) (cm^{-1})	μ Al measured (cm^{-1}) (k=2)
^{137}Cs	661.6	20	0.201	0.202 ± 0.004
^{60}Co	1173	20	0.153	0.150 ± 0.002
	1332	20	0.144	0.142 ± 0.002
^{226}Ra	609	40	0.208	0.208 ± 0.006
	1120	40	0.157	0.157 ± 0.006
	1765	40	0.124	0.123 ± 0.006
	2204	40	0.111	0.117 ± 0.010
	2447	40	0.106	0.111 ± 0.018

8.3.3.4. Samples for attenuation measurement

Out of the 8 produced disc-shaped FSIP samples, 2 were selected as absorber to measure the μ experimentally. The thin (thinnest of all produced) sample has a thickness of 6.43 ± 0.05 mm and a density of 2.96 ± 0.02 g/cm^3. The other sample has a thickness of 17.65 ± 0.07 mm and a density of 3.10 ± 0.01 g/cm^3.

Gopal and Sanvnjeevaiah (1973) reported the the number of MFPs should be below 1 when performing attenuation measurements [41]. Singh Man (2018) defined a more strict criterion within the energy range of 662 to 1332 keV the number of MFPs for low Z_{eff} materials (Z_{eff}<20) should be below 0.5 MFP when performing attenuation measurements [42].

In case of the two FSIP samples the number of MFPs was below 0.5 in the energy range of 609 keV to 2447 keV.

The thickness of each sample selected for experimental determination of the linear attenuation coefficient was determined with a Mitutoyo Micrometer (precision of 0.001 mm).

8.3.3.5. Experimental Set-Up

A diagram of the narrow beam gamma-ray attenuation set-up is shown in Figure 8-1. The set-up shown in Figure 8-1 is situated in a shield consisting of 4 mm Cu and 10 cm of low-activity Pb. The sources were enclosed in a lead container with an aperture of 3 mm in the direction of the detector. The collimators (collimator 1 and 2) closest to the detector had each an aperture of 3 mm, whereas the

collimator closest to the source had an aperture of 5 mm. The distance between the bottom of the source and the detector was 21.5 cm. The total scatter acceptance angle was slightly larger than the recommended value of 4° of Midgley (2006) i.e. 7.5° [43]. Consequently, it was important to measure thin samples [40,41,43]. The spectrum was measured for 20 hours when measuring ^{60}Co and ^{137}Cs to record at least 10^6 counts (both I and I_0) corresponding with a maximum relative uncertainty (k=1) of 2 % for the linear attenuation coefficient in case of ^{60}Co and ^{137}Cs. For ^{226}Ra, the measurement time was 40 hours per measurement. However, due to the low count rate lower intensities were obtained, leading to higher uncertainties up to 10 %. To investigate the heterogeneity of the absorber, 5 different measurements of each sample were made; the sample was repositioned each time. The measured values of μ are reported with their corresponding relative combined standard deviation in Table 8-4.

Data acquisition and peak area analysis were performed using Canberra's Genie 2000 software.

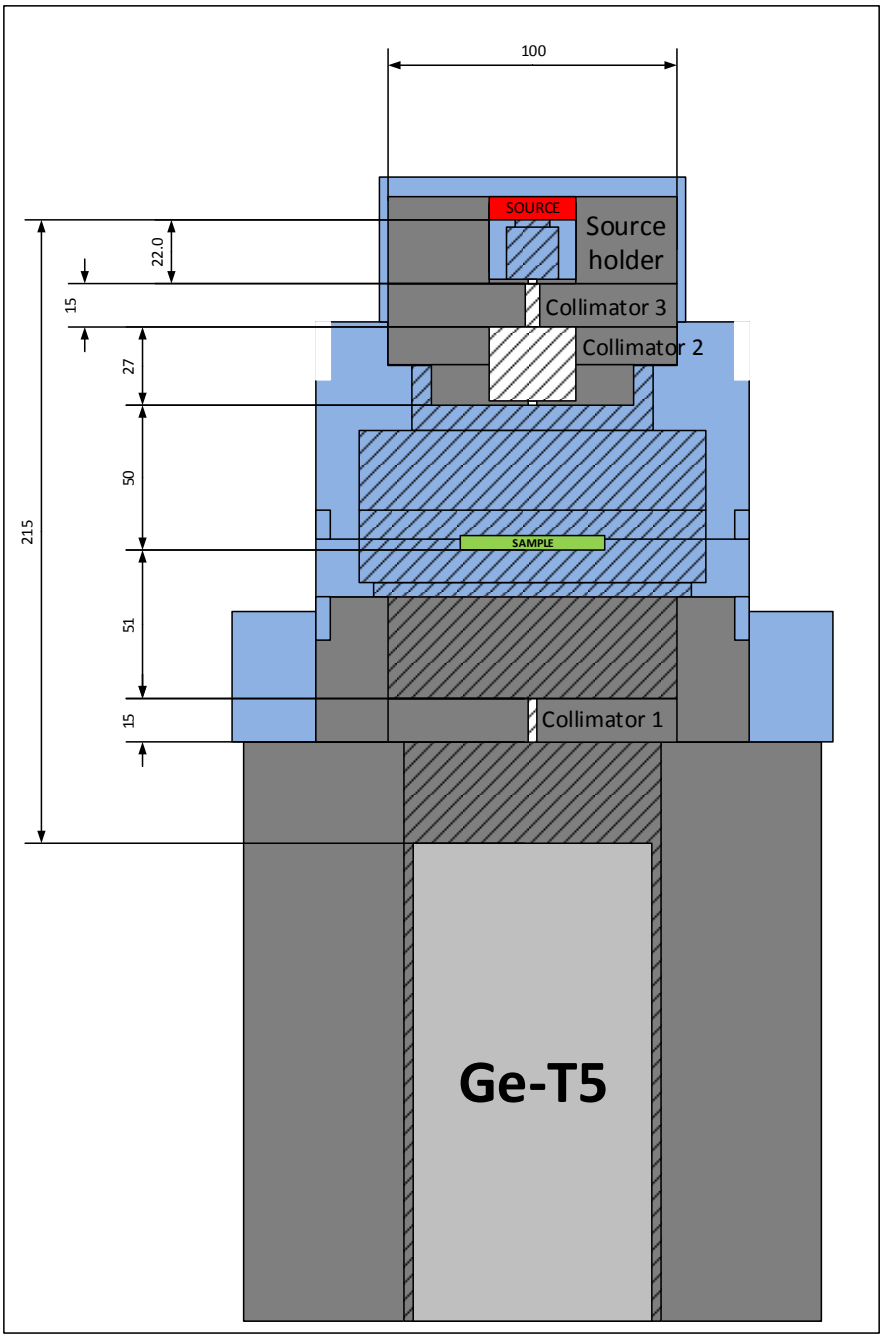

Figure 8-1: Schematic overview of the narrow beam set-up for determination of linear attenuation coefficient. The hashed areas indicate a hollow opening inside the shield or sample holder.

8.3.4. Calculations

The linear attenuation coefficient (μ) is a measure for the probability that a photon will interact with a given material per unit path length. μ is calculated via the law of Lambert-beer. The calculation is shown in Equation 8-1.

$$\mu = \frac{\ln(\frac{I_0}{I})}{x}$$

Equation 8-1

With I the photon intensity after passing through an absorber, I_o the initial photon intensity, x the thickness of the absorber material in cm and μ the linear attenuation coefficient in cm^{-1}.

The uncertainty on the linear attenuation coefficient is calculated as shown in Equation 8-2

$$\Delta\mu = \frac{1}{x}\sqrt{\left(\frac{\Delta I_0}{I_0}\right)^2 + \left(\frac{\Delta I}{I}\right)^2 + \left(ln\frac{I_0}{I}\right)^2\left(\frac{\Delta x}{x}\right)^2}$$

Equation 8-2

The half value layer (*HVL*) is calculated as shown in Equation 8-3. The half value layer is the thickness of the absorber material required to decrease the intensity of a photon beam to half its initial value [2].

$$HVL = \frac{\ln(2)}{\mu}$$

Equation 8-3

A composite material is not characterized by a single atomic number (Z) in case of photon interactions, but by a weighted atomic number, called the effective atomic number (Z_{eff}). The partial photon interaction processes of the individual elements of the composite material are used as weighting factor. Consequently, the Z_{eff} is dependent on the photon energy. The Z_{eff} of a composite material at a given energy corresponds to the atomic number of a single element interacting in a similar way with the photons at that given energy. The Z_{eff} of the HDCs and FSIPs were calculated in the range of 0.01 to 1000 MeV via the Auto-Z_{eff} software developed by Taylor et al. (2012) [44].

8.3.5. Simulated Linear Attenuation Coefficients

8.3.5.1. EGSnrc

Monte Carlo simulations were performed using the hpge3 user code developed for the general purpose simulation program EGSnrc, Lutter et al. (2017) [45,46]. The coupled transport of electrons and photons is simulated in the energy region of 1 keV to 20 000 keV. Photon interactions taken into account were pair and triplet production, Compton scattering, photo-electric absorption and Rayleigh scattering. Photon cross sections of the XCOM database were used. For electron transport the default settings were used [47]. In order to reduce the simulation time, a photon cut and electron cut function, with an energy threshold value of 100 keV below the initial source energy, were implemented in the EGSnrc code for materials composed of Pb. All EGSnrc simulations were performed based on the set-up of Davisson and Evans (1951) [48]. Scoring was done in the detector and the photon energy spectra had a 0.3 keV resolution. The detector dimensions were increased in order to obtain a better efficiency and in this way reducing the simulation time as fewer events need to be simulated. The detector diameter and height were 14 and 40 cm, respectively. Various HDC materials as well as the produced FSIPs were simulated for different energies, shown in Table 8-5. The composition and density of the HDCs can be found in the study of Bashter (1997), except for barite concrete the composition and density of NIST is used [49,50]. The FSIPs chemical composition can be found in Table 8-2. FSIPs were simulated with a density of 2.96 and 3.10 g/cm^3. All simulations were performed in tenfold, each with a different seed. The reported uncertainty is the statistical uncertainty. The number of events was selected so that for each simulation the total number of counts registered in the full energy peak was at least 500 000.

Simulations were compared with Geant4 simulations performed in the study of Singh et al. (2014) [39]. Here, also a narrow beam set-up was simulated. No details on the simulation parameters were provided.

8.4. Results and Discussion

8.4.1. XRD-results

The amorphous content of the WQFS and SCFS were 75 and 27 %, respectively. The crystalline phase of the WQFS consists out of fayalite (22 %) and hercynite (3 %). In case of the SCFS, the crystalline phase consisted out fayalite (69 %) and magnetite (4 %).

8.4.2. XRF-results

Table 8-2 shows the most relevant oxides present in the sample with a normalized mass%. The chemical composition of the FSIP is a combination of the WQFS, SCFS and the sodium silicate activating solution. The XRF-results suggest that the slags are rich in Fe, Si and Al, the three elements necessary for the production of iron-alumino-silicate IPs. The uncertainty of the determined mass% for Na, Mg, Al and Si is in the order of 30 %, for the other elements the uncertainty is lower than 30 %.

Table 8-2: Chemical composition in mass% FSIP (fayalite slag based inorganic polymer).

	Chemical composition (mass%)										
	FeO	**SiO_2**	**Na_2O**	**Al_2O_3**	**CaO**	**ZnO**	**CrO**	**PbO**	**MnO**	**CuO**	**SnO**
FSIP	51.4	33.1	4.9	4.1	2.6	2.3	0.5	0.2	0.4	0.4	0.1

8.4.3. Density and Compressive Strength of IP

The compressive strength of the FSIP was compared to the compressive strength of different concrete-based radiation shielding structures reported by Kaplan (1989) (Table 8-3) [1]. The produced cuboid inorganic polymer showed a 28-day compressive strength of 25 ± 2 MPa. In comparison to the different HDCs, the FSIP's compressive strength fitted with the compressive strength range of the barite, ilmenite, hematite and magnetite concretes i.e. 24.8-42.2, 20.6-75.3, 16.2-89.3 and 19.2-42.8 MPa, respectively. The compressive strengths of the limonite, ferrophosphous and steel concrete were higher i.e. 40.4, 30.4 and 76.0 MPa, respectively. Nevertheless, according to Kaplan (1989) the required compressive strength of concrete for radiation shielding depends on the circumstances it is used in, but a 28-day strength of 20 MPa is generally adequate [1]. So their use as precast structures opens up a possibility to safely use these FSIPs in public spaces from a compressive strength point of view.

Table 8-3: Density and compressive strength of different types of high density concrete and of the produced IP in this study (k=1). Concrete data from Kaplan (1989) [1].

	Density (g/cm^3)	Compressive strength (MPa)
Barite concrete [1]	3.5-3.7	24.8-42.2
Ilmenite concrete [1]	3.49-3.92	20.6-75.3
Limonite concrete [1]	2.96	40.4
Hematite concrete [1]	3.73-4.2	16.2-89.3
Ferrophosphous concrete [1]	4.65	30.4
Magnetite concrete [1]	3.41-4.38	19.2-41.8
Steel concrete [1]	6.3	76
FSIP	3.10 ±0.01	25 ± 2

8.4.4. Attenuation Coefficients

Table 8-4 shows the experimentally obtained values of μ for the two produced FSIP samples with a density of 2.96 g/cm^3 and 3.10 g/cm^3. Here, the reported uncertainty was the standard deviation of 5 measurements. The results obtained with the designed set-up were in very good agreement with the values obtained via EGSnrc. In case of ^{60}Co and ^{137}Cs, differences up to 2 % were obtained. In case of ^{226}Ra, differences between 1 and 11 % were obtained. In general, both the simulated and the experimental (except for 2204 and 2447 keV) μ values of the denser FSIP (3.10 g/cm^3) were a few percent higher meaning that the denser material will attenuate photons better.

Table 8-4: Linear attenuation coefficient of fayalite slag inorganic polymer (FSIP) with density of 2.96 and 3.1 g cm^{-3} determined in this study using EGSnrc, XCOM and experimental measurements (the standard deviation of 5 measurements is given for the experimental values, k=1).

	FSIP (2.96 g cm^{-3})		**FSIP (3.10 g cm^{-3})**	
Energy (keV)	**μ EGSnrc (cm^{-1})**	**μ EXP (cm^{-1})**	**μ EGSnrc (cm^{-1})**	**μ EXP (cm^{-1})**
609	0.232 ± 0.002	0.223 ± 0.003	0.243 ± 0.002	0.244 ± 0.001
661	0.223 ± 0.002	0.228 ± 0.004	0.234 ± 0.001	0.232 ± 0.001
1120	0.173 ± 0.002	0.174 ± 0.004	0.181 ± 0.002	0.183 ± 0.001
1173	0.169 ±0.001	0.171 ± 0.001	0.177 ± 0.001	0.177 ± 0.001
1332	0.159 ± 0.001	0.161 ± 0.002	0.166 ± 0.001	0.167 ± 0.001
1765	0.137 ± 0.002	0.140 ± 0.004	0.143 ± 0.001	0.146 ± 0.001
2204	0.123 ± 0.001	0.134 ± 0.005	0.130 ± 0.002	0.133 ± 0.001
2447	0.118 ± 0.001	0.131 ± 0.006	0.122 ± 0.001	0.130 ± 0.004

Table 8-5 shows the experimentally and computationally obtained μ values of the different HDCs and FSIP samples. The experimental μ values originate from the study of Bashter (1997) [49], the Geant4 simulated μ values originate from the study of Singh et al. (2014) [39]. The EGSnrc simulated μ values are from this study.

Comparing the μ values of EGSnrc and Geant4, the absolute values of the relative difference were for all the investigated energies of the HDCs below 20 % except for ordinary concrete-6000 keV (21 %) and steel scrap concrete-5000 keV (34 %). The absolute values of the relative difference between the EGSnrc simulated μ values of the HDCs and the experimentally obtained μ values of Bashter (1997) were also below 20 %. In case of Geant4, this difference was below 10 %. Bashter (1997) reported that for the experimental μ values of the HDC the uncertainty was within 10 % (but not specified per measurement) [49]. In the literature, differences up to 38 % are reported between the experimentally determined μ values and calculated μ values [34,35,51,52].

Table 8-4 shows that the EGSnrc and experimental results are in good agreement. The EGSnrc results allow comparing the produced FSIP (3.10 g/cm^3) with the different HDCs in the energy region of 1000 keV to 6000 keV (Table 8-5). Consequently, the FSIP (3.10 g/cm^3) attenuates between 23-28 %, 16-20 %, 4-7 % and 0-5 % better than ordinary, hematite-serpentine, ilmenite-limonite and basalt-magnetite concrete, respectively. Barite, ilmenite, steel scrap, and steel-magnetite concrete attenuate between 5-24 %, 12-15 %, 28-36 % and 62-75 %, respectively, better than the FSIP (3.10 g/cm^3). The steel containing concretes shield significantly better than the other HDCs and the

FSIP. It must be noted that due to the steel usage, steel containing concretes are costly i.e. 192 dollar per tonne in 2016 [3].

Table 8-5: Linear attenuation coefficients of ordinary (OR) concrete, hematite-serpentine (HS) concrete, ilmenite-limonite (IL) concrete, basalt-magnetite (BM) concrete, ilmenite (IT) concrete, steel scrap (SS) concrete, steel-magnetite (SM) concrete, barite (BA) concrete and faylite slag inorganic polymer (FSIP) reported in literature and determined by calculations and by experiments.

	OR (2.3 g cm^{-3})			**HS (2.5 g cm^{-3})**			**IL (2.9 g cm^{-3})**		
Energy (keV)	**μ EGSnrc (cm^{-1})**	**μ Geant4 (cm^{-1})**	**μ EXP (cm^{-1})**	**μ EGSnrc (cm^{-1})**	**μ Geant4 (cm^{-1})**	**μ EXP (cm^{-1})**	**μ EGSnrc (cm^{-1})**	**μ Geant4 (cm^{-1})**	**μ EXP (cm^{-1})**
1500	0.120	0.141	0.164	0.128	0.126	0.124	0.146	0.149	0.159
2000	0.104	0.112	0.116	0.111	0.108	0.105	0.126	0.123	0.118
3000	0.084	0.089	0.099	0.094	0.095	0.093	0.106	0.103	0.101
4000	0.071	0.082	0.087	0.082	0.083	0.088	0.091	0.09	0.092
5000	0.066	0.062	0.078	0.074	0.078	0.08	0.086	0.087	0.086
6000	0.061	0.074	0.078	0.068	0.078	0.082	0.082	0.087	0.086
Ref	This work	Singh et al. (2014) [39]	Bashter (1997) [49]	This work	Singh et al. (2014) [39]	Bashter (1997) [49]	This work	Singh et al. (2014) [39]	Bashter (1997) [49]

Table 8-5 (continuation): Linear attenuation coefficients of ordinary (OR) concrete, hematite-serpentine (HS) concrete, ilmenite-limonite (IL) concrete, basalt-magnetite (BM) concrete, ilmenite (IT) concrete, steel scrap (SS) concrete, steel-magnetite (SM) concrete, barite (BA) concrete and faylite slag inorganic polymer (FSIP) reported in literature and determined by calculations and by experiments.

	BM (3.05 g cm^{-3})			**IT (3.5 g cm^{-3})**			**SS (4 g cm^{-3})**		
Energy (keV)	**μ EGSnrc (cm^{-1})**	**μ Geant4 (cm^{-1})**	**μ EXP (cm^{-1})**	**μ EGSnrc (cm^{-1})**	**μ Geant4 (cm^{-1})**	**μ EXP (cm^{-1})**	**μ EGSnrc (cm^{-1})**	**μ Geant4 (cm^{-1})**	**μ EXP (cm^{-1})**
1500	0.157	0.152	0.139	0.176	0.181	0.2	0.202	0.202	0.196
2000	0.134	0.122	0.11	0.152	0.151	0.154	0.173	0.192	0.208
3000	0.111	0.106	0.095	0.126	0.126	0.128	0.147	0.162	0.179
4000	0.095	0.092	0.082	0.111	0.112	0.115	0.13	0.147	0.158
5000	0.088	0.088	0.085	0.103	0.106	0.112	0.121	0.162	0.172
6000	0.085	0.077	-	0.099	0.102	-	0.117	0.112	-
Ref	This work	Singh et al. (2014) [39]	Bashter (1997) [49]	This work	Singh et al. (2014) [39]	Bashter (1997) [49]	This work	Singh et al. (2014) [39]	Bashter (1997) [49]

Table 8-5 (continuation): Linear attenuation coefficients of ordinary (OR) concrete, hematite-serpentine (HS) concrete, ilmenite-limonite (IL) concrete, basalt-magnetite (BM) concrete, ilmenite (IT) concrete, steel scrap (SS) concrete, steel-magnetite (SM) concrete, barite (BA) concrete and faylite slag inorganic polymer (FSIP) reported in literature and determined by calculations and by experiments.

	SM (5.11 g cm^{-3})			**BA (3.35 g cm^{-3})**			**FSIP (3.1 g cm^{-3})**		
Energy (keV)	**μ EGSnrc (cm^{-1})**	**μ Geant4 (cm^{-1})**	**μ EXP (cm^{-1})**	**μ EGSnrc (cm^{-1})**	**μ Geant4 (cm^{-1})**	**μ EXP (cm^{-1})**	**μ EGSnrc (cm^{-1})**	**μ Geant4 (cm^{-1})**	**μ EXP (cm^{-1})**
1500	0.256	0.238	0.22	0.165	-	-	0.157	-	-
2000	0.222	0.205	0.203	0.142	-	-	0.135	-	-
3000	0.187	0.19	0.184	0.123	-	-	0.113	-	-
4000	0.166	0.169	0.18	0.111	-	-	0.097	-	-
5000	0.156	0.164	0.174	0.108	-	-	0.092	-	-
6000	0.15	0.147	-	0.106	-	-	0.086	-	-
Ref	This work	Singh et al. (2014) [39]	Bashter (1997) [49]	This work	-	-	This work	-	-

Figure 8-2 shows the half (HVL) of the different HDCs and FSIP in function of different energies. The HVL allows easily comparison of the shielding capabilities of different materials as they constitute a more tangible measure, due to their expression in cm. The EGSnrc data are used to calculate the HVL. Consequently, the same relative differences between the FSIP and other HDCs are obtained, as reported in case of Table 8-5. In terms of cm, the FSIP requires a thickness of approximately 4.5 in order to reduce the initial intensity of a beam of photons with a factor 2, at an energy of 1.5 Mev. In case of 6 MeV, this thickness becomes approximately 8 for a reduction with a factor 2.

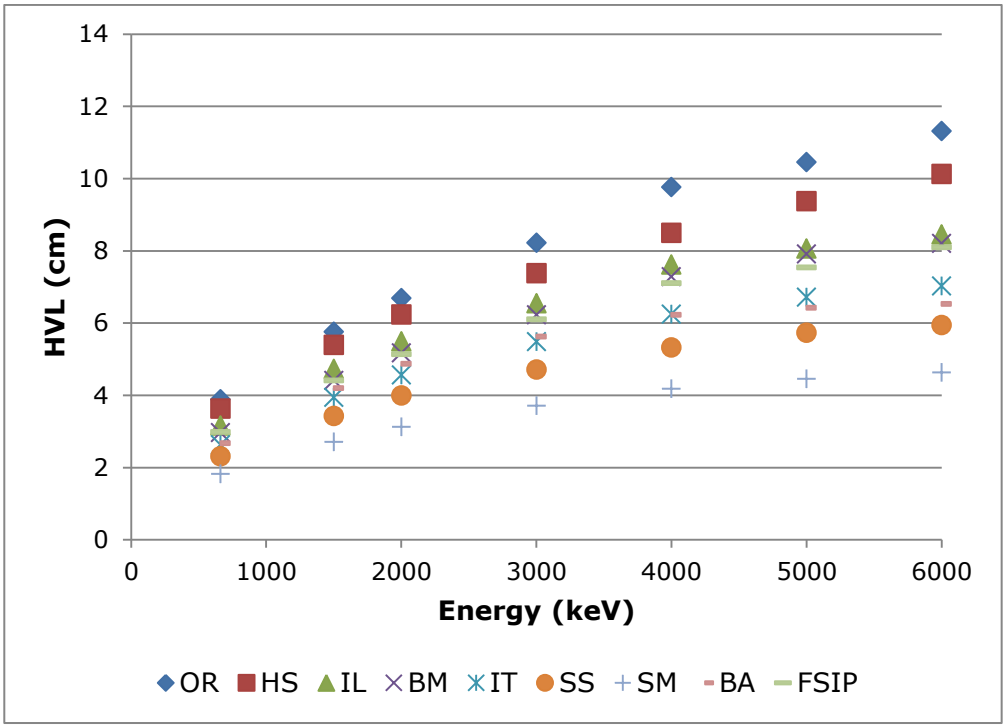

Figure 8-2: Half value layer (cm) in function of energy (keV) of ordinary (OR) concrete, hematite-serpentine (HS) concrete, ilmenite-limonite (IL) concrete, basalt-magnetite (BM) concrete, ilmenite (IT) concrete, steel scrap (SS) concrete, steel-magnetite (SM) concrete, barite (BA) concrete and faylite slag inorganic polymer (FSIP).

The Z_{eff} is often used to easily compare different shielding materials at a well-defined energy. Figure 8-3 shows the calculated Z_{eff} of the different HDCs and FSIP. Comparing the Z_{eff} of the produced FSIP with density of 3.1 g/cm^3 with values of the conventional HDCs over the energy range of 0.01 MeV to 1000 MeV, it can be seen that the FSIP has a higher Z_{eff} of between 34-45 %, 15-30 %, 14-26 %, 2-12 % and 2-11 % in comparison to ordinary, hematite-serpentine, basalt-magnetite, ilmenite-limonite and ilmenite concrete. Steel

scrap and steel-magnetite concrete have a higher Z_{eff} of between 1-9 % and 17 -24 % than FSIP over the whole energy range. In the range where the Compton scattering is dominant i.e. between 0.3 MeV and 3 MeV the Z_{eff} of the FSIP and steel scrap concrete are nearly identical i.e. approximately 13.25.

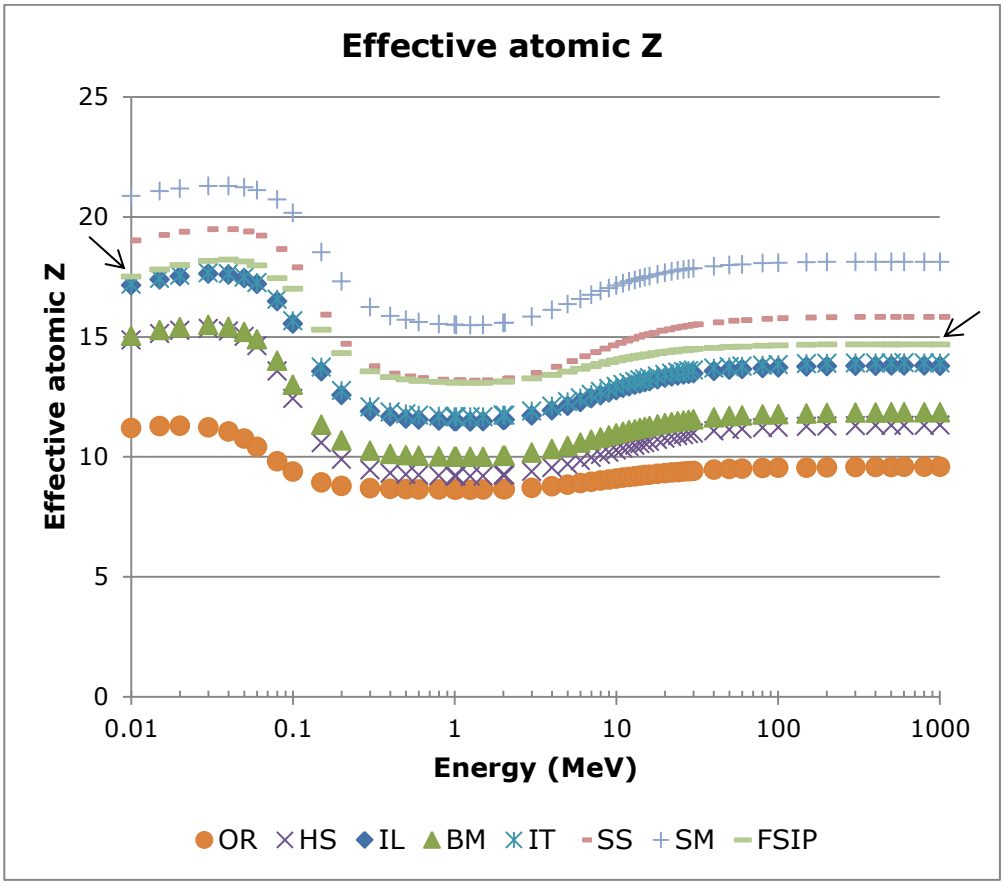

Figure 8-3: Z_{eff} in function of energy for ordinary (OR) concrete, hematite-serpentine (HS) concrete, ilmenite-limonite (IL) concrete, basalt-magnetite (BM) concrete, ilmenite (IT) concrete, steel scrap (SS) concrete, steel-magnetite (SM) concrete and faylite slag inorganic polymer (FSIP) (highlighted with arrow).

8.5. Cost of Minerals

The aggregates typically used in HDCs are expensive and have various cost prices; (Table 8-6) for example in 2016 the cost for barite, iron-scrap, ilmenite and iron-ore were 198, 192, 105 and 82.41 dollars per tonne, respectively, whereas the cost for sand and gravel was 8.8 dollar per tonne [3]. The cost of cement in 2016, is estimated at 111 dollars per tonne [3]. According to United States Geological Surveys (USGS), the cost for iron and steel slags (although

here non-ferrous slag is used, this cost gives an indication) was 19.5 dollars per tonne in 2016 [3]. The mineral cost of these slags is between 5 to 10 times lower than the ilmenite, iron scrap and barite mineral. Slags cost approximately 5 times less than cement and approximately twice as much as sand and gravel. For the production of FSIP an activating solution is required which is costly for example 250 kg of sodium silicate costs over 1000 dollars [53].

The usage of slags to produce HDC structures can be an interesting pathway from an economical point of view if the cost of the activating solutions can reduced, if quantities required for the activation can be reduced or if other cheaper alternatives can be used for the activation.

Table 8-6: Overview cost for different minerals used in (High density) concretes. Data from USGS (2017) [3].

Mineral	**Cost of mineral 2016 (dollars per ton)**
Cement	111
Barites	198
Iron-scrap	192
Ilmenite	105
Sand and gravel	8.8
Iron-ore	82.41
Iron and steel slag	19.5

8.6. Activation Products

During the operation in nuclear facilities the concrete shielding as well as metallic parts (like reinforcement bars) can become activated over time which can lead to the formation of solid radioactive waste [54]. Like other iron bearing HDCs, the FSIP developed here has a high iron content which can lead to production of long-living ^{60}Co ($T_{1/2}$ = 5.3 a) radionuclides. Next to ^{60}Co other activation products can be produced, e.g. ^{152}Eu, ^{22}Na, ^{133}Ba,… depending on the chemical composition of the shield [54]. Sonck et al. (2000) reported that the considerable differences of activation can be expected in different installations [54]. Also the cost related to decommission can vary largely. One must be aware of this aspect and this forms a topic of further research.

8.7. Conclusion

For application in gamma-ray shielding materials, the developed FSIP can be a competitive alternative for conventional HDCs. Looking at the simulated EGSnrc linear attenuation coefficients; the FSIP attenuates up to 28% better than ordinary, hematite-serpentine, ilmenite-limonite and basalt-magnetite concrete.

Barite, ilmenite, steel scrap, and steel-magnetite concrete attenuate better (in the range of 5 to 75 %) than the FSIP. Looking at the Z_{eff}-values solely, steel scrap and steel-magnetite concrete have a higher Z_{eff} of between 1- 24 % than FSIP over the whole energy range of 0.01 MeV to 1000 MeV. In the same energy range, the Z_{eff} is between 2 and 45 % higher in comparison to ordinary, hematite-serpentine, basalt-magnetite, ilmenite-limonite and ilmenite concrete. The experimental data and the EGSnrc data were in good agreement with each other in case of the FSIP i.e. within 2 % for ^{60}Co and ^{137}Cs, and within 11 % for ^{226}Ra.

Comparing the Z_{eff} of the produced FSIP with density of 3.1 g/cm^3 with values of the conventional HDCs over the energy range of 0.01 MeV to 1000 MeV, it can be seen that the FSIP has a higher Z_{eff} of between 34-45 %, 15-30 %, 14-26 %, 2-12 % and 2-11 % in comparison to ordinary, hematite-serpentine, basalt-magnetite, ilmenite-limonite and ilmenite concrete, respectively. Steel scrap and steel-magnetite concrete have a higher Z_{eff} of between 1-9 % and 17 -24 %, respectively, than FSIP over the whole energy range.

From a compressive strength point of view, the FSIP is on the lower end in comparison with existing HDCs. Nevertheless, the strength of 25 MPa of FSIP is considered to be adequate for structural shielding applications [1].

The mineral cost of ferrous and steel slag (although here non-ferrous slag is used, this cost gives an indication) is between 5 to 10 times lower than the ilmenite, iron scrap and barite mineral. Slags cost approximately 5 times less than cement and approximately twice as much as sand and gravel. Consequently, from an economic point of view the FSIP is competitive with existing HDCs and even with ordinary concrete when the cost of the activating solution is excluded. Furthermore, the use of FS both as binder and aggregate does not require the exploitation of natural resources in contrast with the conventional cement-aggregate mixtures.

The commonly used barium and iron aggregates used in cement mixtures have their drawbacks in terms of processing, handling, availability, durability, safety or cost [1]. Nevertheless, the proposed FSIP design of this study needs to be further investigated to check the long-term properties and the drawbacks in the design, like radiation induced damage or heat induced thermal stresses. The cost can be reduced by optimizing the used activating solution.

8.8. Acknowledgements

The authors are grateful to Mark Van Noyen, Eddy Pauwels, Stephaan Cauwbergs and Danny De Smet (European Commission) for the production of the narrow beam set-up. This work was supported by the European Commission within HORIZON2020 via the EURATOM project EUFRAT.

8.9. References

[1] M.F. Kaplan, Concrete radiation shielding, 1st ed., Longman Scientific & Technical, 1989.

[2] J.E. Martin, Physics for radiation protection, 2nd ed., WILEY-VCH Verlag GmbH & Co. KGaA, 2006.

[3] USGS, Commodity Statistics and Information - nonfuel minerals, (2017). https://minerals.usgs.gov/minerals/pubs/commodity/ (accessed October 1, 2017).

[4] V.K. Orlov, Y. a. Metelkin, a. a. Maslov, Extra-Heavy Concrete and Cermet: Protective Materials with Enhanced γ-Ray Absorption, At. Energy. 117 (2015) 243–250. doi:10.1007/s10512-015-9917-5.

[5] K. Komnitsas, D. Zaharaki, V. Perdikatsis, Geopolymerisation of low calcium ferronickel slags, J. Mater. Sci. 42 (2007) 3073–3082.

[6] K. Komnitsas, D. Zaharaki, V. Perdikatsis, Effect of synthesis parameters on the compressive strength of low-calcium ferronickel slag inorganic polymers, J. Hazard. Mater. 161 (2009) 760–768.

[7] I. Maragkos, I.P. Giannopoulou, D. Panias, Synthesis of Ferronickel slag-based geopolymers, Miner. Eng. 22 (2009) 196–203.

[8] M.B. Ogundiran, H.W. Nugteren, G.J. Witkamp, Immobilisation of lead smelting slag within spent aluminate-fly ash based geopolymers., J. Hazard. Mater. 248–249 (2013) 29–36. doi:10.1016/j.jhazmat.2012.12.040.

[9] S. Onisei, Y. Pontikes, T. Van Gerven, G.N. Angelopoulos, T. Velea, V. Predica, P. Moldovan, Synthesis of inorganic polymers using fly ash and primary lead slag., J. Hazard. Mater. 205–206 (2012) 101–10. doi:10.1016/j.jhazmat.2011.12.039.

[10] Y. Pontikes, L. Machiels, S. Onisei, L. Pandelaers, D. Geysen, P.T. Jones, B. Blanpain, Slags with a high Al and Fe content as precursors for inorganic polymers, Appl. Clay Sci. 73 (2013) 93–102. doi:10.1016/j.clay.2012.09.020.

[11] L. Machiels, L. Arnout, P.T. Jones, B. Blanpain, Y. Pontikes, Inorganic polymer cement from fe-silicate glasses: Varying the activating solution to glass ratio, Waste and Biomass Valorization. 5 (2014) 411–428. doi:10.1007/s12649-014-9296-5.

[12] S. Onisei, K. Lesage, B. Blanpain, Y. Pontikes, Early Age Microstructural Transformations of an Inorganic Polymer Made of Fayalite Slag, J. Am. Ceram. Soc. 9 (2015) 1–9. doi:10.1111/jace.13548.

[13] K. Komnitsas, D. Zaharaki, Geopolymerisation: A review and prospects for the minerals industry, Miner. Eng. 20 (2007) 1261–1277.

doi:10.1016/j.mineng.2007.07.011.

[14] C. Shi, P. V. Krivenko, D. Roy, alkali activated cements and concretes, Taylor & Francis, NY, USA, 2006.

[15] S. a. Bernal, J.L. Provis, A. Fernandez Jiminez, P. V. Krivenko, E. Kavalerova, M. Palacios, C. Shi, Binder Chemistry - high-calcium alkali - activated materials, in: J.L. Provis, J.S.J. van Deventer (Eds.), Alkali Act. Mater., 2014: pp. 59–92.

[16] Y. Pontikes, R. Snellings, Cementitious binders incorporating residues, in: Handb. Recycl., 2014: p. 219–229,. doi:10.1016/B978-0-12-396459-5.00016-7.

[17] J.S.J. Van Deventer, J.L. Provis, P. Duxson, D.G. Brice, Chemical research and climate change as drivers in the commercial adoption of alkali activated materials, Waste and Biomass Valorization. 1 (2010) 145–155. doi:10.1007/s12649-010-9015-9.

[18] S. Simon, G.J.G. Gluth, A. Peys, S. Onisei, D. Banerjee, Y. Pontikes, The fate of iron during the alkali-activation of synthetic (CaO-)FeO_x-SiO_2 slags: An Fe *K* -edge XANES study, J. Am. Ceram. Soc. (2017) 1–12. doi:10.1111/jace.15354.

[19] D.S. Perera, J.D. Cashion, M.G. Blackford, Z. Zhang, E.R. Vance, Fe speciation in geopolymers with Si/Al molar ratio of ~ 2, J. Eur. Ceram. Soc. 27 (2007) 2697–2703. doi:10.1016/j.jeurceramsoc.2006.10.006.

[20] J.L. Bell, W.M. Kriven, Formation of an iron-based inorganic polymer (geopolymer), in: D. Singh, W.M. Kriven (Eds.), Mech. Properites Perform. Eng. Ceram. Compos. IV., John Wiley & Sons, 2010: pp. 301–311.

[21] P.N. Lemougna, K.J.D. MacKenzie, G.N.L. Jameson, H. Rahier, U.F. Chinje Melo, The role of iron in the formation of inorganic polymers (geopolymers) from volcanic ash: a 57Fe Mössbauer spectroscopy study, J. Mater. Sci. 48 (2013) 5280–5286. doi:10.1007/s10853-013-7319-4.

[22] National Slag Association, Common uses for slag, (2013). http://www.nationalslag.org/common-uses-slag (accessed May 22, 2016).

[23] T. Croymans, I. Schreurs, M. Hult, G. Marissens, H. Stroh, G. Lutter, S. Schreurs, W. Schroeyers, Variation of natural radionuclides in non-ferrous fayalite slags during a one-month production period, J. Environ. Radioact. 172 (2017) 63–73. doi:10.1016/j.jenvrad.2017.03.004.

[24] S. Singh, A. Kumar, D. Singh, K.S. Thind, G.S. Mudahar, Barium-borate-flyash glasses: As radiation shielding materials, Nucl. Instruments Methods Phys. Res. Sect. B Beam Interact. with Mater. Atoms. 266 (2008) 140–146. doi:10.1016/j.nimb.2007.10.018.

[25] M. Maslehuddin, a. a. Naqvi, M. Ibrahim, Z. Kalakada, Radiation shielding properties of concrete with electric arc furnace slag aggregates and steel shots, Ann. Nucl. Energy. 53 (2013) 192–196. doi:10.1016/j.anucene.2012.09.006.

[26] M. Kurudirek, I. Türkmen, Y. Özdemir, A study of photon interaction in some building materials: High-volume admixture of blast furnace slag into Portland cement, Radiat. Phys. Chem. 78 (2009) 751–759. doi:10.1016/j.radphyschem.2009.03.070.

[27] R.I. Iacobescu, V. Cappuyns, T. Geens, L. Kriskova, S. Onisei, P.T. Jones, Y. Pontikes, The influence of curing conditions on the mechanical properties and leaching of inorganic polymers made of fayalitic slag, Front. Chem. Sci. Eng. (2017) 208–213. doi:10.1007/s11705-017-1622-6.

[28] N.M. Piatak, M.B. Parsons, R.R. Seal, Characteristics and environmental aspects of slag: A review, Appl. Geochemistry. 57 (2015) 236–266. doi:10.1016/j.apgeochem.2014.04.009.

[29] J.H. Hubbell, Photon mass attenuation and energy-absorption coefficients, Int. J. Appl. Radiat. Isot. 33 (1982) 1269–1290.

[30] K. Sidappe, G. Nayak, K.M. Balkrishana, N. Lingappa, Experimental effective atomic numbers for the photoelectric process in some alloys at 84 and 145 keV, Nucl. Sci. Eng. 93 (1986) 57–61.

[31] V.P. Singh, N.M. Badiger, Gamma ray and neutron shielding properties of some alloy materials, Ann. Nucl. Energy. 64 (2014) 301–310. doi:10.1016/j.anucene.2013.10.003.

[32] N.C. Yang, P.K. Leichner, W.G. Hawkins, Effective atomic numbers for low energy total photon interaction in human tissues., Med. Phys. 14 (1987) 159–766.

[33] I. Han, L. Demir, M. Şahin, Determination of mass attenuation coefficients, effective atomic and electron numbers for some natural minerals, Radiat. Phys. Chem. 78 (2009) 760–764. doi:10.1016/j.radphyschem.2009.03.077.

[34] E. Yilmaz, H. Baltas, E. Kiris, İ. Ustabas, U. Cevik, A.M. El-Khayatt, Gamma ray and neutron shielding properties of some concrete materials, Ann. Nucl. Energy. 38 (2011) 2204–2212. doi:10.1016/j.anucene.2011.06.011.

[35] I. Akkurt, C. Basyigit, S. Kilincarslan, B. Mavi, The shielding of gamma rays by concretes produced with barite, Prog. Nucl. Energy. 46 (2005) 1–11. doi:10.1016/j.pnucene.2004.09.015.

[36] A. Un, F. Demir, Determination of mass attenuation coefficients, effective atomic numbers and effective electron numbers for heavy-weight and normal-weight concretes., Appl. Radiat. Isot. 80 (2013) 73–77.

doi:10.1016/j.apradiso.2013.06.015.

[37] M.. Berger, J.H. Hubbell, XCOM: Photon cross sections database, Web Version 1.2. (n.d.).

[38] L. Gerward, N. Guilbert, K. Bjorn Jensen, H. Levring, X-ray absorption in matter. Reengineering XCOM, Radiat. Phys. Chem. 60 (2001) 23–24. doi:10.1016/S0969-806X(00)00324-8.

[39] V.P. Singh, M.E. Medhat, N.M. Badiger, Utilization of Geant4 Monte Carlo simulation method for studying attenuation of photons in normal and heavy concretes at high energy values, J. Radioanal. Nucl. Chem. 300 (2014) 325–331. doi:10.1007/s10967-014-2984-6.

[40] S. Singh, A. Kumar, C. Singh, K.S. Thind, G.S. Mudahar, Effect of finite sample dimensions and total scatter acceptance angle on the gamma ray buildup factor, Ann. Nucl. Energy. 35 (2008) 2414–2416. doi:10.1016/j.anucene.2008.08.008.

[41] S. Gopal, B. Sanjeevaiah, A method to determine the gamma-ray attenuation coefficients, Nucl. Instruments Methods Phys. Res. Sect. A Accel. Spectrometers, Detect. Assoc. Equip. 107 (1973) 221–225.

[42] K. Singh Mann, Measurement of exposure buildup factors : The influence of scattered photons on gamma-ray attenuation coefficients, Nucl. Inst. Methods Phys. Res. A. 877 (2018) 1–8. doi:10.1016/j.nima.2017.08.047.

[43] S. Midgley, Angular width of a narrow beam for X-ray linear attenuation coefficient measurements, 75 (2006) 945–953. doi:10.1016/j.radphyschem.2006.01.008.

[44] M.L. Taylor, R.L. Smith, F. Dossing, R.D. Franich, Robust calculation of effective atomic numbers: The Auto-Zeff software, Med. Phys. 391 (2012) 1769–2491. doi:10.1118/1.3689810.

[45] G. Lutter, M. Hult, F. Tzika, H. Stroh, G. Marissen, Gamma-ray spectrometry analysis software environment, Appl. Radiat. Isot. (2017) 1–5. doi:10.1016/j.apradiso.2017.06.045.

[46] I. Kawrakow, E. Mainegra-Hing, F. Tessier, B.R.B. Walters, The EGSnrc C++ class library, NRC Rep. PIRS-898 (Rev A). (2009).

[47] I. Kawrakow, D. Rogers, The EGSnrc code system: Monte Carlo simulation of electron and photon transport., 2011.

[48] C.M. Davisson, R.D. Evans, Measurements of Gamma-Ray absorption coefficients, Phys. Rev. 81 (1951) 404–411.

[49] I.I. Bashter, Calculation of radiation attentuation coefficients for shielding concretes, Ann. Nucl. Energy. 24 (1997) 1389–1401.

[50] J.H. Hubbell, S.M. Seltzer, Tables of X-Ray mass attenuation coefficients

and mass energy-absorption coefficients 1 keV to 20 MeV for Elements Z=1 to 92 and 48 Additional substances of Dosimetric Interest., Http://Physics.Nist.Gov/Xaamdi. (1996). doi:http://physics.nist.gov/xaamdi.

[51] N. Singh, K.J. Singh, K. Singh, H. Singh, Comparative study of lead borate and bismuth lead borate glass systems as gamma-radiation shielding materials, Nucl. Instruments Methods Phys. Res. Sect. B Beam Interact. with Mater. Atoms. 225 (2004) 305–309. doi:10.1016/j.nimb.2004.05.016.

[52] O. Gencel, A. Bozkurt, E. Kam, T. Korkut, Determination and calculation of gamma and neutron shielding characteristics of concretes containing different hematite proportions, Ann. Nucl. Energy. 38 (2011) 2719–2723. doi:10.1016/j.anucene.2011.08.010.

[53] Merck, Sodium silicate in solution, (2018). http://www.merckmillipore.com/BE/fr (accessed January 14, 2018).

[54] M. Sonck, N. Buls, A. Hermanne, G. Eggermont, Radiological and Economic Impact of Decommissioning Charged Particle Accelerators, 2000.

General conclusions and outlook

In 2016, 4.6 billion tonnes of cement were produced for usage in construction materials. It is estimated that the cement sector contributes between 5 and 8 % of the global anthropogenic CO_2 emission. In addition, cement and concrete require the exploitation of raw materials like sand, gravel, limestone etc. In contrast, by-products like metallurgical slags, bauxite residue, phosphogypsum, fly and bottom ashes, are typically used in low value applications or stockpiled. These by-products can be valorized in the production of construction materials, possibly with novel processes like alkali activation, which allow incorporation rates of up to nearly 100 % of these by-products. Consequently, these by-products are ready to replace cement and concrete and to reduce the exploitation of raw materials. However, some of these by-products can be of radiological concern. Due to industrial processing of primary or secondary raw materials, naturally occurring radionuclides, being the radionuclides of the ^{238}U, ^{235}U and ^{232}Th decay series and ^{40}K, can concentrate or dilute in the produced (by-) products. In this framework, radiological measurements and dose assessments provide valuable information on the safe usage of these construction materials. This aspect is also handled in the European basic safety standards (EU-BSS) (Council Directive 2013/59/Euratom) by introducing the activity concentration index (ACI) and setting a dose criterion of 1 mSv/a for public exposure.

This thesis deals with the valorization of two Fe-rich industrial by-products, being bauxite residue (BR) and non-ferrous fayalite slag (FS), in construction materials and considers specifically the radiological point of view. The activity concentrations (AC) of the radionuclides of the ^{238}U, ^{232}Th and ^{235}U decay series and ^{40}K of BR containing concretes and FS were studied. Dose assessments were performed in case of occupational and public exposure. A novel more accurate model has been developed to better assess the gamma exposure from building materials. Finally, a building material solely based on FS was developed and studied in terms of its gamma-ray shielding capabilities.

BR originates from the aluminum production and over 2.7 billion tonnes of BR are stockpiled. Consequently, it is desirable to find a viable reuse option. In Chapter 4, BR containing concretes, containing up to 90 mass% of BR, have been analyzed by means of gamma-ray spectrometry using HPGe detectors in combination with Monte Carlo simulations. In contrast to the "standard" analysis of ^{226}Ra, ^{228}Ac and ^{40}K, a thorough analysis of the whole decay series of ^{238}U and ^{232}Th was performed. Disequilibrium was found in the ^{238}U decay series with AC up to 110 ± 20 Bq/kg for the ^{238}U-part, 90 ± 20 Bq/kg for the ^{226}Ra-part and

120 ± 60 Bq/kg for the ^{210}Pb-part. Equilibrium was present in the ^{232}Th decay series; with activity concentrations up to 120 ± 20 Bq/kg. Activity concentrations up to 4.3 ± 0.5 Bq/kg and 90 ± 20 Bq/kg were obtained for ^{235}U and ^{40}K respectively.

In addition in Chapter 4, a dosimetric study in terms of their use both as civil engineering material (e.g. streets) and as a building material was performed for these BR containing concretes. In terms of public exposure, the studied BR concretes can, from a radiological perspective, be safely used in both streets and playgrounds (ACI_{sp} - dose criterion of 0.1 mSv/a) as well as in building materials (ACI_{BM} - dose criterion of 1 mSv/a) with levels up to 90 mass% BR. In terms of occupational exposure, the studied BR concretes can be safely used in road construction (RP-122 - dose criterion of 0.3 mSv/a) up to 90 mass% BR whereas for building material construction this is up to 60 mass% BR (RP-122 - dose criterion of 0.3 mSv/a). **Consequently, from a radiological perspective, mixtures containing high mass% of BR can be a reuse option.** However, prior to usage a holistic approach is recommended. Depending on the final application specific chemical (e.g. leaching), physical (e.g. density) and mechanical (e.g. freeze thaw resistance) properties need to be taken into account. The radon release from these materials can also be a topic of further research. In addition, it must be noted that the studied BR originates from one facility, which may use bauxite ores from one particular origin, and from one particular production batch. Variations in the NOR-content of industrial facilities is an interesting topic for further research and was studied in Chapter 5 in case of FS.

FS are currently used in various applications like tiles, railway ballast, roofing materials, sand blasting material. Nevertheless, their use can be stimulated by developing applications with a higher valorization value like for example building materials or materials with niche applications i.e. gamma-ray shielding materials. Chapter 5 provides an intensive literature search on the AC of different NORs present in slags. It was shown that the AC of NORs varies between 2 and 130 000 Bq/kg in literature. Even, within the same type of slags the AC varied significantly, for example in case of tin slags ACs between 230 and 130 000 Bq/kg were reported. In Chapter 5, the NORs present in FS of a secondary smelter facility, a NORM-processing industry according to the EU-BSS, were monitored daily during a one month production period. In the ^{238}U decay series, the AC ranged between 42 ± 4 and 180 ± 40 Bq/kg for the ^{238}U-part, between 14 ± 2 and 83 ± 8 Bq/kg for the ^{226}Ra-part and between 7 ± 4 and 90 ± 20 Bq/kg for the ^{210}Pb-part. Equilibrium was present in the ^{232}Th decay series; with activity concentrations varying between 21 ± 2 and 100 ± 10 Bq/kg. ACs between 2.0 ± 0.4 and 8 ± 2 Bq/kg, and between 26 ± 8 and 80 ± 10 were obtained for ^{235}U and ^{40}K, respectively. The ACs of the slags were all below the provided exemption/clearance levels of the EU-BSS and RP-122, and are also low in comparison to slags reported in literature. In addition, the

ACs of flue dust samples and feedstock materials were measured. The activity concentrations of the flue dust samples were all except for ^{210}Pb below the exemption/clearance levels. For the feedstock material only ^{40}K and ^{235}U were below the exemption/clearance levels.

Comparing the minimum and maximum observed activity concentrations for different radionuclides, differences up to a factor 13, 4.3 and 9 were registered for respectively slag, flue dust and feedstock samples. These variations occur due to heterogeneity within the same input materials, and variation in input materials, input and output quantity and in the process parameters. **Consequently, one-time measurements can provide a misleading image in terms of radiation protection. The output frequency of a production process as well as the complexity of the process should be considered.** In addition, over the long term, production processes tend to change in time due to innovations, regulations and economic factors and can lead to changes in the radiological content of input and output materials. Therefore, care must be taken prior to drawing conclusions whether or not a whole class of materials is safe or not especially when these materials will be used in or as building materials. It is recommended to incorporate this variability into the legislation in order to assure public safety. As a future research project, the variability in other industries or plants can be monitored and can lead to recommendations for radiological monitoring in function of an industrial sector. Finally, it must be noted that according to the ACI, there were no restrictions in using building materials solely produced out of FS, in case of the 31 batches studied.

However, the ACI is based on a specific set of building material and room parameters i.e. a concrete (2350 kg/m^3) room of 280 cm x 400 cm x 500 cm consisting only out of walls of 20 cm thick. These parameters are not necessary valid for all types of building materials and rooms, and will depend on the final application. In Chapter 6, a dose model was developed, called the expanded gamma dose assessment (EGDA) model. This model allows taking into account building and room parameters. A sensitivity analysis was performed for the decay series of ^{238}U, ^{232}Th, ^{235}U and ^{40}K. The EGDA>0% model showed that parameters like density, thickness, room volume and the presence of windows and/or doors can impact the absorbed dose rate in air (D_A) up to 38 % in comparison to the standard considered room of the ACI. In addition, the EGDA>0% model uses all the gamma emission lines and up to date nuclear data linked to NORs, also the ones of the ^{235}U decay series, which is not evaluated before. Consequently, in comparison with the ACI calculation method, the total gamma emission intensity was increased from 2.12 to 2.41 and from 2.41 to 3.04 for the ^{238}U and ^{232}Th decay series, respectively in case of the EGDA>0% model. In case of ^{40}K a decrease from 0.107 to 0.106 was observed. In case of the ^{235}U decay series the gamma emission intensity was 3.1 .It was shown that working with averaged gamma lines instead of individual gamma lines can impact the D_A up to 6.1 % - depending on the considered NOR.

In addition, Chapter 6 compared the developed EGDA>0% model, the I(ρd)/D(ρd) formula and ACI in a set of different scenarios with varying density (1400 to 3000 kg/m^3) and thicknesses (10 to 40 cm). The ACI can lead to both over- and underestimations of the effective dose and consequently restrict valorization of safe building materials or wrongly allow building materials with doses above the 1 mSv/a threshold. Also, using a flexible dose or index calculation, in contrast to a screening index, for the evaluation of building materials fits better with the 1 mSv/a dose requirement of article 75 of the EU-BSS, in particular when dealing with non-standard room and building material parameters. In addition, the implementation of non–standard room and building material parameters deals with the requirement of annex VIII of the EU-BSS, that states "*The calculation of dose needs to take into account other factors such as density, thickness of the material as well as factors relating to the type of building and the intended use of the material (bulk or superficial)*". **Therefore, Chapter 6 suggests initially performing a density and thickness corrected dose calculation formula. When needed, more advanced dose model calculations, like the developed EGDA>0% model are recommended.**

The EGDA>0% model could be further improved by considering customized build-up factors. These customized build-up factors should consider the chemical composition of the building material and be adapted in function of the number of mean free paths per gamma emission energy. The method of geometric progression should be considered for this improvement. In addition, further improvements can be performed by taking into account the energy dependence of the dose coversion factors. The different dose calculation methods lack to provide an uncertainty to the calculated results. Uncertainty estimates provide a topic of further research and would benefit the legislators and industry.

The use of fayalite slag based inorganic polymers (FSIPs) as gamma-ray shielding material was studied in Chapters 7 and 8. In this framework a dedicated set-up was developed to experimentally determine the linear attenuation coefficients (μ) at energies varying between 0.6 and 2.5 MeV. The set-up allowed performing measurements within 1 to 2 days with an uncertainty of below 8 %. Additionally, simulations were performed by the EGSnrc MC code and XCOM. The experimental and simulated results showed to be in very good agreement with each other i.e. a maximum relative difference of 11 % between XCOM or EGSnrc and the experimental μ values. In addition, the FSIP was compared with conventional high density concretes (HDCs) in the energy range of 1.5 to 6 MeV. Relatively, the FSIP attenuates between 23-28 %, 16-20 %, 4-7 % and 0-5 % better in comparison to ordinary, hematite-serpentine, ilmenite-limonite and basalt-magnetite concrete, respectively. Barite, ilmenite, steel scrap, and steel-magnetite concrete attenuate between 5-24 %, 12-15 %, 28-36 % and 62-75 %, respectively, better than the FSIP. Nevertheless, it must be noted that the mineral cost of slags was lower than that of minerals used in

HDCs. For example, the mineral cost of ferrous and steel slag (although here non-ferrous slag is used, this cost gives an indication) was between 5 to 10 times lower than the ilmenite, iron scrap and barite mineral. **So, the developed FSIP performs comparably to conventional gamma-ray shielding materials, but with a smaller expected mineral cost.** In order to guarantee a safe usage as a gamma-ray shielding material, further research needs to be conducted in terms of long-term properties and possible drawbacks in the design like sensitivity to thermal stresses, heat transfer, radiation damage, etc. Like for BR concretes a holistic approach of FSIPs is recommended in function of the final application. In order to improve the shielding capabilities, by-products of higher density and/or containing heavier elements are interesting for further research. Next to gamma-ray shielding, neutron shielding could be an additional niche market in which inorganic polymers can become an alternative to conventional HDCs. Regarding the high Fe-content (51 mass% FeO), neutron activation of Fe, which can lead to the production of radioactive ^{60}Co, must be taken into account. A detailed study of other possible activation products is also recommended for further research.

To conclude, alkali activated materials based on by-products are gradually finding their way into the construction industry. However, the activity concentrations of NORs could limit their usage. Especially, since the public opinion is highly sensible to everything linked to the term radioactivity. It was shown in this PhD thesis that this concern is not always valid. However, one must be aware that dedicated monitoring proves valuable since variations in the NOR content in by-products occur. Next to monitoring, assessment of the gamma dose linked to building materials must be optimized towards the parameters of the building material and its final application. Next to the ACI, more accurate models exist which are flexible in terms of room and building material parameters. One such alternative is the developed EGDA>0% model which allows to better understand and assess whether or not building materials (containing by-products) are safe from a radiation protection perspective. Additionally in this general framework, high-tech niche applications, like gamma-ray shielding materials, could be a trigger for general acceptance of by-product containing construction materials. To end, the usage of by-products in building materials allows reducing the usage of cement and virgin raw materials, and is a step forward towards a more sustainable world.

Algemeen besluit en vooruitzicht

In 2016 werd er 4,6 miljard ton cement geproduceerd voor het gebruik als constructiemateriaal. De bijdrage van de cementsector aan de wereldwijde antropogene CO_2-uitstoot wordt geschat tussen de 5 en 8 %. Daarnaast wordt de ontginning van grondstoffen zoals zand, kiezel, kalksteen etc vereist voor de productie van cement en beton. Anderzijds worden bijproducten zoals metallurgische slakken, bauxite residue, fosforgips, vlieg- en bodemassen, typisch gebruikt in laagwaardige toepassingen, of worden ze opgeslagen. Deze bijproducten kunnen worden gevaloriseerd in de productie van constructiematerialen, dewelke via nieuwe processen, zoals alkali-activatie, toelaten om deze bijproducten voor bijna 100 % te incorporeren. Bijgevolg zijn deze bijproducten klaar om cement en beton te vervangen en om de ontginning van grondstoffen te verminderen. Vanuit radiologisch standpunt kunnen sommige van deze bijproducten een bezorgdheid vormen. Omwille van industriële verwerking van primaire of secundaire grondstoffen, kunnen natuurlijk voorkomende radionucliden, zijnde de radionucliden van de ^{238}U, ^{235}U en ^{232}Th vervalreeksen, alsook ^{40}K, zich ophopen of verdunnen in de geproduceerde (bij)producten. In dit algemeen kader kunnen radiologische metingen en dosisbepalingen waardevolle informatie verschaffen voor het veilige gebruik van constructiematerialen. Dit aspect wordt ook behandeld in de Europese veiligheidsstandaarden (Council Directive 2013/59/Euratom) door het introduceren van een activiteitsconcentratieindex (ACI) en door het zetten van een dosislimiet van 1 mSv/a voor publieke blootstelling.

Deze thesis behandelt vanuit radiologisch standpunt, de valorizatie van twee ijzerrijke industriële bijproducten, zijnde bauxite residue (BR) en non-ferro fayalite slak (FS), in constructiematerialen. De activititeitsconcentraties van de radionucliden behorend tot de ^{238}U, ^{235}U en ^{232}Th vervalreeksen, alsook ^{40}K van BR-bevattende betonstalen en FS werden bestudeerd. Dosisbepalingen werden uitgevoerd in functie van beroepsmatige en publieke blootstelling. Een nieuw, meer accuraat dosismodel werd ontwikkeld, om zo beter de gammablootstelling, komende van bouwmaterialen te bepalen. Uiteindelijk werd een bouwmateriaal ontwikkeld dat enkel bestaat uit FS. Dit werd bestudeerd in het kader van zijn gammastralingsafschermingscapaciteiten.

BR is afkomstig van de aluminiumproductie en momenteel is meer dan 2,7 miljard BR opgeslagen. Bijgevolg is het wenselijk om een leefbare hergebruikoptie te vinden voor BR. In hoofdstuk 4 werden BR-bevattende betonstalen, met BR niveaus tot en met 90 massa%, geanalyseerd door middel van gammaspectrometrie, gebruikmakend van HPGe detectoren, in combinatie met Monte Carlo simulaties. In tegenstelling tot de "standaard" analyse van

^{226}Ra, ^{228}Ac en ^{40}K, vonden robuuste analyses van de gehele ^{238}U en ^{232}Th vervalreeksen plaats. Er werd een onevenwicht vastgesteld in de ^{238}U vervalreeks met maximale activiteitsconcentraties van 110 ± 20 Bq/kg voor het ^{238}U-deel, 90± 20 Bq/kg voor het ^{226}Ra-deel en 120 ± 60 Bq/kg voor het ^{210}Pb-deel. Er werd een evenwicht vastgesteld in de ^{232}Th vervalreeks, met maximale activiteitsconcentraties van 120 ± 20 Bq/kg. De maximale activiteitsconcentraties voor ^{235}U en ^{40}K waren respectievelijk 4,3 ± 0,5 Bq/kg en 90 ± 20 Bq/kg.

Daarnaast werd er in hoofdstuk 4 een dosimetrische studie van de BR-bevattende betonstalen uitgevoerd, in functie van hun gebruik als civiel materiaal (e.g. straten) en als bouwmateriaal. In termen van publieke blootstelling kunnen de bestudeerde BR-bevattende betonstalen veilig gebruikt worden in straten en speelpleinen (ACI_{BM} – dosislimiet van 0,1 mSv/a), alsook in bouwmaterialen (ACI_{BM} – dosislimiet van 1 mSv/a). In termen van beroepsmatige blootstelling kunnen de bestudeerde BR-bevattende betonstalen veilig gebruikt worden in wegconstructie (RP-122 – dosislimiet van 0,3 mSv/a) tot en met niveaus van 90 massa% BR. In het geval van bouwmaterialen (RP-122 – dosislimiet van 0,3 mSv/a) kunnen deze betonstalen veilig gebruikt worden tot en met niveaus van 60 massa% BR. **Bijgevolg kunnen vanuit een radiologisch perspectief mengsels, die een hoog massa% aan BR bevatten, een hergebruik optie vormen.** Echter is een holistische benadering aangewezen vooraleer over te gaan tot het gebruik. Afhankelijk van de uiteindelijke toepassing dient er rekening gehouden te worden met specifieke chemische (e.g. uitloging), fysieke (e.g. dichtheid) en mechanische (e.g. vries-dooi bestendigheid) eigenschappen. De hoeveelheid radon, die uit deze materialen ontsnapt, kan ook een interessant onderwerp zijn voor verder onderzoek. Daarnaast dient er opgemerkt te worden dat de bestudeerde BR stalen afkomstig zijn van één welbepaalde productiebatch van één faciliteit, dewelke mogelijk bauxite ertsen gebruikt van één bepaalde oorsprong. Variaties in de hoeveelheden aan natuurlijke voorkomende radionucliden in industriële faciliteiten is ook een interessant onderwerp voor verder onderzoek. Dit werd bijgevolg dan ook bestudeerd voor FS in hoofdstuk 5.

FS wordt momenteel gebruikt in verscheidene toepassingen, zoals tegels, spoorwegballast, roofingmateriaal en zandstraalmateriaal. Desalniettemin kan het gebruik van FS gestimuleerd worden door het ontwikkelen van toepassingen met een hogere valorisatiewaarde, zoals bijvoorbeeld bouwmaterialen of materialen met nichetoepassingen. In hoofdstuk 5 werd een doorgedreven literatuurstudie uitgevoerd omtrent de activiteitsconcentratie van verschillende natuurlijk voorkomende radionucliden in metallurgische slakken. In deze literatuurstudie werd aangetoond dat de activiteitsconcentratie van natuurlijk voorkomende radionucliden varieert tussen 2 en 130 000 Bq/kg. Zelfs binnen hetzelfde type van slakken varieerde de activiteitsconcentratie significant, voor tinslakken werden bijvoorbeeld activiteitsconcentraties tussen de 230 en 130

000 Bq/kg gerapporteerd. Verder werd in hoofdstuk 5 de aanwezigheid van natuurlijk voorkomende radionucliden in FS gemonitord gedurende een productieperiode van één maand. Deze FS waren afkomstig van een secundaire smelterfaciliteit die volgens de EU-BSS valt onder NORM-verwerkende industrie. In de ^{238}U vervalreeks varieerde de activiteitsconcentratie tussen 42 ± 4 en 180 ± 40 Bq/kg voor het ^{238}U-deel, tussen 14 ± 2 en 83 ± 8 Bq/kg voor het ^{226}Ra-deel en tussen 7 ± 4 en 90 ± 20 Bq/kg voor het ^{210}Pb-deel. Er werd evenwicht vastgesteld in de ^{232}Th vervalreeks met activiteitsconcentraties tussen 21 ± 2 en 100 ± 10 Bq/kg. Activiteitsconcentraties tussen 2,0 ± 0,4 en 8 ± 2 Bq/kg, en tussen 26 ± 8 en 80 ± 10 werden vastgesteld voor respectievelijk ^{235}U en ^{40}K. De activiteitsconcentraties van de slakken lagen allemaal onder de vrijgaveniveaus van de EU-BSS en RP-122. Bovendien zijn deze activiteitsconcentraties ook laag in vergelijking met de slakken, gerapporteerd in de literatuur. Naast de slakken werden ook vliegassen en inputmaterialen gemeten De activiteitsconcentraties van de vliegassen lagen allemaal onder het vrijgaveniveau, behalve voor ^{210}Pb. Voor de inputmaterialen lagen enkel ^{40}K en ^{235}U onder de vrijgaveniveaus.

Wanneer de minimum en maximum geobserveerde activiteitsconcentraties van de verschillende radionucliden werden vergeleken, werden er verschillen tot en met een factor 13; 4,3 en 9 vastgesteld voor respectievelijk de slak, vliegas- en inputmateriaalstalen. Deze variaties zijn te wijten aan de heterogeniteit van dezelfde inputmaterialen, de variatie in de inputmaterialen, de input- en outputhoeveelheden en de procesparameters. **Bijgevolg kan een eenmalige meting een misleidend beeld geven in het kader van radioprotectie. De outputfrequentie en de complexiteit van een productieproces dienen in rekening gebracht te worden.** Bovendien hebben productieprocessen de neiging te veranderen doorheen de tijd omwille van innovatie, regelgeving en economische factoren. Hierdoor kunnen ook wijzigingen voorkomen in de radiologische karakteristieken van de input- en outputmaterialen. Bijgevolg moet er met enige voorzichtigheid omgegaan worden met concluderen dat een gehele klasse van materialen al dan niet veilig is voor gebruik als bouwmateriaal. Daarnaast wordt er aanbevolen om deze variabiliteit te incorporeren in de wetgeving om publieke veiligheid te garanderen. Als een toekomstig onderzoeksproject kan de variabiliteit van radionucliden gemonitord worden in andere industrieën of faciliteiten. Dit kan leiden tot aanbevelingen omtrent de radiologische monitoring van bepaalde industriële sectoren. Tenslotte waren er voor de 31 gemeten slakken geen restricties in het gebruik als bouwmateriaal, aldus de ACI.

Het dient opgemerkt te worden dat de ACI gebaseerd is op een specifieke set van eigenschappen, gelinkt aan de kamer en het bouwmateriaal i.e. een betonnen (2350 kg/m^3) kamer van 280 cm x 400 cm x 500 cm die enkel bestaat uit muren van 20 cm dikte. Deze eigenschappen zijn niet noodzakelijk geldig voor alle type bouwmaterialen en kamers. Zij hangen af van de uiteindelijke

toepassing. In hoofdstuk 6 werd een dosismodel ontwikkeld, genaamd "expanded gamma dose assessment (EGDA) model". Dit model brengt de bouwmateriaal- en kamereigenschappen in rekening. Een sensiviteitsanalyse werd uitgevoerd voor de ^{238}U, ^{232}Th, ^{235}U vervalreeks en ^{40}K. Deze analyse met het EGDA>0% model toonde aan dat parameters zoals dichtheid, dikte, volume van de kamer en de aanwezigheid van ramen en/of deuren de in lucht geabsorbeerde dosis (D_A) tot 38 % kunnen beïnvloeden, in vergelijking met de standaardkamer gebruikt door de ACI. Daarnaast maakt het EGDA>0% model gebruik van alle gammastralingemissielijnen en up-to-date nucleaire data, gelinkt aan de de natuurlijk voorkomende radionucliden. Bovendien werd ook de data, gelinkt aan de ^{235}U vervalreeks, beschouwd. Bijgevolg steeg, in vergelijking met de ACI berekeningsmethode, de intensiteit van gammastralingemissie van 2,12 naar 2,41 en van 2,41 naar 3,04 voor respectievelijk de vervalreeks van ^{238}U en ^{232}Th bij het EGDA>0% model. Voor ^{40}K werd er een daling van 0,107 naar 0,106 vastgesteld van de intensiteit van de gammastralingemissie. Voor de ^{235}U vervalreeks was de intensiteit van gammastralingsemissie 3,1. Door te werken met gemiddelde gammastralingemissielijnen in plaats van individuele gammastralingemissielijnen kon een verschil in de D_A tot 6,1 % - afhankelijk van het beschouwde radionuclide – worden vastgesteld.

Daarnaast werden in hoofdstuk 6 het ontwikkelde EGDA>0% model, de I(ρd)/D(ρd) formule (vergelijkingen 2-15 en 2-16) en de ACI met elkaar vergeleken voor verschillende scenario's met variërende dichtheid (1400 tot 3000 kg/m^3) en dikte (10 tot 40 cm). Het gebruik van de ACI kan zowel tot onder- als overschattingen van de effectieve dosis leiden. Hierdoor kan de valorisatie van veilige bouwmaterialen beperkt worden, alsook het verkeerdelijk toelaten van bouwmaterialen met een dosis boven de 1 mSv/a grens. Bovendien past het gebruik van een flexibele dosis of indexberekening, in tegenstelling tot de screeningsindex, beter met de 1 mSv vereiste van artikel 75 van de EU-BSS voor het evalueren van bouwmaterialen. Dit in het bijzonder wanneer het gaat over niet-standaard parameters van het bouwmateriaal en de kamer. De vereiste van annex VIII van de EU-BSS zijnde: *"Bij de dosisberekening dient rekening te worden gehouden met andere factoren zoals dichtheid, dikte van het materiaal en factoren die betrekking hebben op het soort gebouw en het beoogde gebruik van het materiaal (bulk of oppervlakte)."* wordt daarnaast beter behandeld door de implementatie van niet-standaard bouwmateriaal- en kamerparameters. **Om deze reden wordt in hoofdstuk 6 voorgesteld om initieel een dichtheid- en diktegecorrigeerde dosisberekening uit te voeren met behulp van formules. Wanneer nodig kunnen meer geavanceerde dosismodellen, zoals het ontwikkelde EGDA>0% model, worden gebruikt.**

Het EGDA>0% model kan verder verbeterd worden door aangepaste build-up factoren te beschouwen. Deze aangepaste build-up factoren kunnen best de

chemische samenstelling in rekening nemen en gebruik maken van mean free paths, aangepast per gamma emissie energie. Voor deze verbetering kan de methode van geometrische progressie overwogen worden. Daarnaast kan het in rekening brengen van energieafhankelijke dosisconversiefactoren het model verder verbeteren. De verschillende dosisberekeningsmethodes missen onzekerheidsberekeningen. Het bepalen van de onzekerheid is een onderwerp voor toekomstig onderzoek en het zou de wetgeving alsook de industrie ten goede komen.

In hoofdstuk 7 en 8 werd het gebruik van anorganische polymeren op basis van fayalite slakken (FSIPs) als gammastralingsafschermingsmateriaal bestudeerd. Binnen dit kader werd een opstelling ontwikkeld om experimenteel lineaire attenuatiecoefficiënten (μ) te bepalen in het energiebereik tussen 0,6 en 2,5 MeV. De opstelling liet toe om metingen uit te voeren binnen 1 tot 2 dagen met een onzekerheid onder de 8 %. Daarnaast werden er simulaties uitgevoerd met behulp van EGSnrc Monte Carlo berekening en XCOM. De experimentele en gesimuleerde resultaten kwamen goed overeen i.e. een maximum relatief verschil van 11 % tussen XCOM of EGSnrc en de experimentele μ waarden. Daarnaast werd de FSIP vergeleken met verschillende types conventionele hogedichtheidsbeton in het energiebereik van 1,5 tot 6 MeV. Relatief gezien, verzwakte de FSIP gammastraling tussen de 23-28 %, 16-20 %, 4-7 % en 0-5 % beter dan respectievelijk ordinair, hematiet-serpentijn, ilmeniet-limoniet en basalt-magnetiet beton. Bariet, ilmeniet, staalschroot en staal-magnetiet beton verzwakten de gammastraling respectievelijk tussen de 5-24 %, 12-15 %, 28-36 % en 62-75 % beter dan de FSIP. Echter dient er opgemerkt te worden dat de minerale kostprijs van de slakken lager is dan deze van mineralen, gebruikt voor hogedichtheidsbeton. Zo is bijvoorbeeld de minerale kost van ferro- en staalslakken (hoewel er hier non-ferro slakken werden gebruikt, kan deze kost als een indicatie dienen) tussen de 5 tot 10 keer lager dan die van ilmeniet, staalschroot en bariet. **Dus het ontwikkeld FSIP heeft vergelijkbare attenuatie-eigenschappen met conventionele gammastralingafschermingsmaterialen, maar met een lagere verwachte kost.** Om het veilig gebruik als gammastralingafschermingsmateriaal te kunnen garanderen, is verder onderzoek vereist naar de eigenschappen op lange termijn, en de mogelijke tekortkomingen in het design, zoals de gevoeligheid voor thermische stress, warmteoverdracht, stralingsschade etc. Net zoals voor de BR-bevattende betonstalen, wordt dus een holistische benadering aanbevolen, in functie van het uiteindelijke gebruik. Om de afschermingseigenschappen verder te verbeteren, zijn andere bijproducten met een hogere dichtheid en/of met zwaardere elementen interessant om te bestuderen. Naast afschermingseigenschappen voor gammastraling, kan afscherming tegen neutronen ook een interessante nichemarkt vormen waarin anorganische polymeren een alternatief kunnen vormen voor hogedichtheidstbeton. Gezien de hoge ijzerfractie (51 massa% FeO) dient er

rekening gehouden te worden met de neutronactivatie van Fe, wat kan leiden tot de productie van radioactief ^{60}Co. Een gedetailleerde analyse omtrent andere mogelijke activatieproduction kan een interessant onderwerp zijn voor verder onderzoek.

Ter conclusie: alkali-geactiveerde materialen, opgebouwd uit bijproducten, vinden geleidelijk hun weg in de constructie-industrie. Echter kan de mogelijke bezorgdheid omtrent de radiologische eigenschappen hun gebruik beperken. In het bijzonder, gezien de publieke opinie zeer gevoelig is aan alles wat gelinkt is aan radioactiviteit. In deze PhD-thesis werd er aangetoond dat deze bezorgdheid zeker niet altijd terecht is. Echter moet men er zich van bewust zijn dat toegewijde monitoring waardevol kan zijn, omwille van de variabiliteit in de natuurlijk voorkomende radionucliden in bijproducten. Naast de monitoring, dienen gammadosisbepalingen van bouwmaterialen geoptimaliseerd te worden, in kader van de eigenschappen van het bouwmateriaal en zijn uiteindelijke toepassing. Naast de ACI bestaan er accuratere modellen, die bovendien flexibel zijn, in termen van de eigenschappen, het bouwmateriaal en de beschouwde kamer. Een mogelijk alternatief is het ontwikkelde EGDA>0% model, dewelke beter toelaat om te begrijpen en te bepalen of bouwmaterialen (die bijproducten bevatten) veilig zijn, vanuit het radioprotectief perspectief. Binnen dit algemeen kader kunnen hoogtechnologische toepassingen, zoals gammastralingafschermingsmaterialen, een trigger zijn voor het algemeen aanvaarde gebruik van bijproducten in bouwmaterialen. Tenslotte kan het gebruik van bijproducten in bouwmaterialen, het gebruik van cement en onontgonnen grondstoffen verminderen, om zo een stap vooruit te zetten naar een duurzamere wereld.

List of publications

2017:

Book Chapter:

T. Kovacs, G. Bator, W. Schroeyers, J.A. Labrincha, F. Puertas, M. Hegedus, D. Nicolaides, M.A. Sanjuán, P. Krivenko, I.N. Grubesa, Z. Sas, B. Michalik, M. Anagnostakis, I. Barisic, C. Nuccetelli, R. Trevisi, T. Croymans, S. Schreurs, N. Todorovic, D. Vaiciukyniene, R. Bistrickaite, A. Tkaczyk, K. Kovler, R. Wiegers, R. Doherty, From raw materials to NORM by-products, in: W. Schroeyers (Ed.), Nat. Occur. Radioact. Mater. Constr., 2017: pp. 135–182.

Paper:

T. Croymans, W. Schroeyers, P. Krivenko, O. Kovalchuk, A. Pasko, M. Hult, G. Marissens, G. Lutter, S. Schreurs, Radiological characterization and evaluation of high volume bauxite residue alkali activated concretes, J. Environ. Radioact. 168 (2017) 21–29.

G. Lutter, I.V. Schreurs, T. Croymans, W. Schroeyers, S. Schreurs, M. Hult, G. Marissens, H. Stroh, F. Tzika, A low-energy set-up for gamma-ray spectrometry of NORM tailored to the needs of a secondary smelting facility, Appl. Radiat. Isot. (2017) 1–5.

T. Croymans, I. Schreurs, M. Hult, G. Marissens, H. Stroh, G. Lutter, S. Schreurs, W. Schroeyers, Variation of natural radionuclides in non-ferrous fayalite slags during a one-month production period, J. Environ. Radioact. 172 (2017) 63–73.

P. Krivenko, O. Kovalchuk, A. Pasko, T. Croymans, M. Hult, G. Lutter, N. Vandevenne, S. Schreurs, W. Schroeyers, Development of alkali activated cements and concrete mixture design with high volumes of red mud, Constr. Build. Mater. 151 (2017) 819–826.

T. Croymans, F. Leonardi, R. Trevisi, C. Nuccetelli, S. Schreurs, W. Schroeyers, Gamma exposure from building materials - a dose model with expanded gamma lines from naturally occurring radionuclides applicable in non-standard rooms, Constr. Build. Mater. 159 (2017) 768–778.

Conference material:

T. Croymans, F. Leonardi, R. Trevisi, C. Nuccetelli, S. Schreurs, W. Schroeyers, Gamma exposure from building materials – a dose model with expanded gamma lines from NORs applicable in non-standard rooms, in: FINAL Symposium COST

NETWORK "NORM4Building" (Use of by-products in construction: dealing with natural radioactivity), Rome, Italy – From 06 June to 08 June 2017, 2017. [Abstract & Presentation – cat: C2]

W. Schroeyers, K. Gijbels, T. Croymans, N. Vandevenne, B. Mast, B. Vandoren, Y. Pontikes, F. Leonardi, C. Nuccetelli, R. Trevisi, S. Schreurs, Impact assessment of the use of NORM residues in alkali activated materials for building applications:, in: EU NORM symposium 2017, London, United Kingdom – From 02 October to 05 October 2017, 2017. [Abstract & Presentation – cat: C2]

2016

Conference material:

N. Vandevenne, B. Mast, E. Thijssen, G. Reggers, R. Carleer, T. Croymans, Y. Pontikes, S. Schreurs, W. Schroeyers, Developing waste-based inorganic polymers for radioactive waste encapsulation: A leaching study, in: NuMat2016 Nucl. Mater. Conf. Montpellier - Fr. 7-10/11/2016, 2016. [Presentation – cat: C2]

W. Schroeyers, N. Vandevenne, K. Gijbels, B. Mast, T. Croymans, B. Vandoren, Y. Pontikes, S. Schreurs, Using NORM containing construction materials as an immobilization matrix for waste, in: 8th EAN-NORM Work. Stock. - Sweden, 5-7/12/2016, 2016. [Abstract & Presentation – cat: C2]

T. Croymans, I. Vandael Schreurs, M. Hult, G. Marissens, H. Stroh, G. Lutter, S. Schreurs, W. Schroeyers, Variation of natural radionuclides in non-ferrous fayalite slags during a one-month production period, in: V. Terr. Radioisot. Environ. Int. Conf. Environ. Prot. Veszprém - Hungary, 19-20/05/2016, 2016. [Abstract & Presentation – cat: C2]

2015:

Conference proceedings:

W. Schroeyers, T. Croymans, S. Schreurs, Towards a holistic approach for risk assessment when reusing slag with enhanced norm content in building materials, in: Roceedings 4th Int. Slag Valoris. Symp., 2015: pp. 309–314. [Proceedings paper – cat: C1]

Conference material:

S. Schreurs, R. Carleer, J. Yperman, Y. Pontikes, M. Hult, K. Vanreppelen, J. Maggen, S. Vanderheyden, T. Croymans, N. Vandevenne, W. Schroeyers, Targeted treatment of selected waste streams to produce added value materials, in: Top. Day Deal. with Environ. Contam. from Response to Risk Assessment, SCK-CEN, Mol - Belgium, 26/11/2015, 2015. [Presentation – cat: C2]

W. Schroeyers, T. Croymans-Plaghki, S. Schreurs, Towards a holistic approach for risk assessment when reusing slag with enhanced NORM content in building materials, 4th Int. Slag Valoris. Symp. (2015). [Presentation – cat: C2]

W. Schroeyers, G. Xhixha, N. Vandevenne, F. Mantovani, T. Croymans, M. Stals, S. Schreurs, On site measurement strategies for the characterization of NORM, in: Ital. Radon NORM Work. (IRANOW2015), Salerno, Italy, 11-17/10/2015, 2015. [Abstract – cat: C2]